

Role of metallic nanoclusters in catalysis for fuel cell feed gas purification and hydrogen storage

Krstić, Marjan

Doctoral thesis / Disertacija

2016

Degree Grantor / Ustanova koja je dodijelila akademski / stručni stupanj: **University of Split, Faculty of Science / Sveučilište u Splitu, Prirodoslovno-matematički fakultet**

Permanent link / Trajna poveznica: <https://urn.nsk.hr/urn:nbn:hr:166:827385>

Rights / Prava: [In copyright](#) / [Zaštićeno autorskim pravom.](#)

Download date / Datum preuzimanja: **2024-04-20**

Repository / Repozitorij:

[Repository of Faculty of Science](#)

University of Split
Faculty of Science
Biophysics Doctoral Programme

Marjan Krstić

**Role of metallic nanoclusters in
catalysis for fuel cell feed gas
purification and hydrogen storage**

Doctoral thesis

Split, 2016

Sveučilište u Splitu
Prirodoslovno-matematički fakultet
Poslijediplomski sveučilišni doktorski studij
Biofizika

Marjan Krstić

**Uloga metalnih nanoklastera u katalizi
za pročišćavanje pogonskog plina
gorivnih ćelija i spremanje vodika**

Doktorski rad

Split, 2016.

Sveučilište u Splitu, Prirodoslovno-matematički fakultet

Odjel za fiziku, Poslijediplomski sveučilišni doktorski studij Biofizika

”Uloga metalnih nanoklastera u katalizi za pročišćavanje pogonskog plina gorivnih ćelija i spremanje vodika”

Doktorski rad autora Marjana Krstića kao dio obaveza potrebnih da se dobije doktorat znanosti, izrađen pod vodstvom mentora prof. dr. dr. h. c. Vlaste Bonačić-Koutecký i prof. dr. sc. Paška Županovića

Dobiveni akademski naziv i stupanj: doktor prirodnih znanosti iz polja fizike

Povjerenstvo za ocjenu i obranu doktorskog rada u sastavu:

1. prof. dr. sc. Ante Bilušić, redoviti profesor
2. prof. dr. sc. Franjo Sokolić, redoviti profesor
3. dr. sc. Anita Kriško, viši znanstveni suradnik
4. dr. sc. Mile Ivanda, znanstveni savjetnik (zamjenski član)

1. _____

2. _____

3. _____

Potvrđuje da je disertacija obranjena dana _____

Voditelj studija: prof. dr. sc. Paško Županović

Predsjednik Vijeća studija: prof. dr. dr. h. c. Vlasta Bonačić-Koutecký

ACKNOWLEDGMENTS

I would like to express my sincere gratitude to all the people who was with me, supported me and helped during the fruitful research time of the last 5 years and preparation of this thesis. First, I am endlessly grateful to the Prof. Vlasta Bonačić-Koutecký, for the continuous support of my Ph.D study and related research, for her motivation, patience and immense knowledge. By accepting me into her research group she showed an infinite faith in me and gave me an opportunity to work on such interesting topics in the field of the nanocluster catalysis. I appreciate all the research related discussions we had, where she motivated me by always asking challenging questions. She steered me in the right direction whenever she thought it was needed but gave me the freedom and showed me the trust to express myself and give my own contribution to the research. I must admit that I am really lucky to be supervised by such intelligent, widely-talented and educated person she is. Furthermore, I have to say special thanks to the thesis co-mentor Prof. Paško Županović, who showed me an incredible world of physics. He was always there for me, believed in me and guide me throughout entire master's education and Ph.D study.

All this would not be possible without numerous experimental collaborations. Therefore, I feel a special need to thank to Prof. Thorsten M. Bernhardt, Prof. Sandra M. Lang and Sandra U. Förtig from University of Ulm for initiating and proposing new challenges as well as stimulating discussions in the research direction of fuel cell feed gas purification. The hydrogen storage research direction would not be such a success without the experimental collaboration with Prof. Richard A. J. O'Hair, Athanasios Zavras and Dr. George N. Khairallah from University of Melbourne and Prof. Philippe Dugourd, Dr. Rodolphe Antoine, Dr. Marion Girod, Dr. Luke MacAleese, Prof. Jérôme Lemoine, Dr. Steven Daly and Dr. Philippe Maitre from University of Lyon. Without their precious and insightful comments, hard question, encouragement and support it would not be possible to conduct this research, so one sincere thanks goes to all of them.

I also thank my fellow coworkers, especially Željka Sanader for the continuous support, help and discussions as well as for all the fun we have had in the last five years working together.

Finally, the last but not the least, I must acknowledge gratitude to my parents, sister, brother, other members of family and all my dear friends for providing me with unfailing support and continuous encouragement throughout my work on the research, writing the thesis and my life in general.

University of Split

Faculty of Science

Ph.D. thesis

**ROLE OF METALLIC NANOCLUSTERS IN CATALYSIS FOR FUEL CELL
FEED GAS PURIFICATION AND HYDROGEN STORAGE**

Marjan Krstić

Thesis performed at:

- Center of excellence for science and technology - Integration of Mediterranean region (STIM) at Interdisciplinary center for Advanced science and technology (ICAST), University of Split

Abstract:

Catalytic reactivity of the small transition and coinage metal nanoclusters have been theoretically studied in context of (1) advancing fuel cell technology by developing cost-effective techniques to improve quality of the feed gas as well as (2) safe storage and release of hydrogen in its gaseous state at room temperatures and pressures. In order to address the challenge concerning the improvement the quality of fuel cell feed gas reactions of small ruthenium cationic nanoclusters with CO and H₂ has been performed. The origin of the selectivity and outstanding activity of small ruthenium nanoparticles in the catalytic CO methanation reaction has been identified. The second aim of this dissertation is to advance materials for hydrogen storage and their release technology. For this purpose a gas-phase study of fragmentation and catalytic activity of ligated coinage metal hydride nanoclusters has been performed. The theoretical findings based on density functional theory (DFT) are strongly supported by experimental results through international cooperation. Within thesis we demonstrated that powerful combination of density functional theory and experimental investigations can contribute to intelligently developed new materials and procedures to overcome the challenges hampering worldwide application of fuel cells as "green" technology of the future.

(100 pages, 25 figures, 1 table, 115 references, 2 appendices, original in English)

Thesis deposited in:

- National and University Library in Zagreb
- University Library in Split
- Library of the Faculty of Science, University of Split

Keywords: fuel cells, feed gas purification, ruthenium clusters, hydrogen storage and release, coinage metal hydrides, density functional theory

Supervisor: Paško Županović, Ph.D./Full professor

Supervisor: Vlasta Bonačić-Koutecký, Dr. Dr. h. c./Full professor

Reviewers:

1. Ante Bilušić, Ph.D./Full professor
2. Franjo Sokolić, Ph.D./Full professor
3. Anita Kriško, Ph.D.

Thesis accepted: 30.11.2016.

Sveučilište u Splitu

Prirodoslovno-matematički fakultet

Doktorski rad

**ULOGA MALIH METALNIH NANOKLASTERA U KATALIZI ZA
PROČIŠĆAVANJE POGONSKOG PLINA GORIVNIH ČELIJA I
SPREMANJE VODIKA**

Marjan Krstić

Rad je izrađen u:

- Centru izvrsnosti za znanost i tehnologiju - Integracija Mediteranske regije (STIM) pri Interdisciplinarnom centru za naprednu znanost i tehnologiju (ICAST), Sveučilište u Splitu

Sažetak:

Katalitička reaktivnost malih nanoklastera prijelaznih metala teorijski je istraživana u kontekstu (1) unaprjeđenja tehnologije gorivnih članaka razvijajući jeftine tehnike poboljšanja kvalitete pogonskog plina kao i (2) sigurne pohrane i otpuštanja vodika u plinovitom stanju na atmosferskoj temperaturi i tlaku. Da bi riješili problem nedovoljne kvalitete pogonskog plina gorivnih članaka istraživale su se reakcije malih rutenijevih nanoklastera s CO i H₂. Izvor selektivnosti i izvrsne aktivnosti malih rutenijevih čestica u katalitičkoj CO metanacijskoj reakciji je identificiran. Drugi cilj ove disertacije je unaprjeđivanje materijala za tehnologiju pohrane i otpuštanja vodika. U tu svrhu provela su se istraživanja fragmentacije i katalitičke aktivnosti ligandiranih metalnih hidridnih nanoklastera. Naša teorijska istraživanja bazirana na teoriji funkcionala gustoće su potvrđena eksperimentalnim rezultatima priznatih istraživačkih grupa kroz međunarodnu suradnju. Unutar ove teze demonstrirali smo da moćna kombinacija našeg teorijskog istraživanja potvrđena eksperimentalnim istraživanjima može doprinijeti inteligentnom razvoju novih materijala i procedura da bi se nadišli problemi koji sprječavaju široku primjenu gorivnih čelija kao "zelene" tehnologije budućnosti.

(100 stranica, 25 slika, 1 tablica, 115 literaturnih navoda, 2 priloga, jezik izvornika: engleski jezik)

Rad je pohranjen u:

- Nacionalnoj sveučilišnoj knjižnici u Zagrebu
- Sveučilišnoj knjižnici u Splitu
- Knjižnica Prirodoslovno-matematičkog fakulteta na Sveučilištu u Splitu

Ključne riječi: gorivni članci, pročišćavanje pogonskog plina, rutenijevi klasteri, spremanje i otpuštanje vodika, hidridi kovinskih metala, teorija funkcionala gustoće

Mentor: prof. dr. sc. Paško Županović, redoviti profesor

Komentor: prof. dr. dr. h. c. Vlasta Bonačić-Koutecký, redoviti profesor

Ocjenjivači:

1. prof. dr. sc. Ante Bilušić, redoviti profesor
2. prof. dr. sc. Franjo Sokolić, redoviti profesor
3. dr. sc. Anita Kriško, viši znanstveni suradnik

Rad prihvaćen: 30.11.2016.

Contents

ABSTRACT	1
LIST OF PUBLICATIONS RELEVANT TO THE THESIS	4
I. INTRODUCTION	5
1 Fuel cell technology challenges	6
1.1 Fuel cell feed gas quality	7
1.2 Hydrogen storage	7
2 Historical overview of nanoparticle catalysts and role of transition and noble metal clusters in catalysis	8
3 Ruthenium nanoclusters and their role in fuel cell feed gas purification . . .	10
4 Silver, gold and copper hydrides and their role in hydrogen storage	11
5 Theoretical methods	13
5.1 Density functional theory	14
5.2 Lowest energy structures, transition states and energy profiles	15
5.3 Molecular dynamics in the ground and excited state, simulated annealing	16
5.4 Structural characterization	17
6 Complementary experimental approaches	18
II. THE STRUCTURE AND GOALS OF THE THESIS	20
1 Ruthenium nanoclusters and their role in fuel cell feed gas purification . . .	20
2 Silver, gold and copper hydrides and their role in hydrogen storage	22
III. RUTHENIUM NANOCLUSTERS AND THEIR ROLE IN FUEL CELL FEED GAS PURIFICATION	34
1 Gas-Phase Synthesis and Structure of Wade-Type Ruthenium Carbonyl and Hydrido Carbonyl Clusters	35
2 The Origin of the Selectivity and Activity of Ruthenium-Cluster Catalysts for Fuel-Cell Feed-Gas Purification: A Gas-Phase Approach	40
IV. SILVER, GOLD AND COPPER HYDRIDES AND THEIR ROLE IN HYDROGEN STORAGE	46
1 ESI/MS investigation of routes to the formation of silver hydride nanocluster dications $[\text{Ag}_x\text{H}_{x-2}\text{L}_y]^{2+}$ and gas-phase unimolecular chemistry of $[\text{Ag}_{10}\text{H}_8\text{L}_6]^{2+}$	47
2 Formation and Characterisation of the Silver Hydride Nanocluster Cation $[\text{Ag}_3\text{H}_2((\text{Ph}_2\text{P})_2\text{CH}_2)]^+$ and Its Release of Hydrogen	57

CONTENTS

3	Ligand-induced substrate steering and reshaping of $[\text{Ag}_2(\text{H})]^+$ scaffold for selective CO_2 extrusion from formic acid	66
4	Selectivity Effects in Bimetallic Catalysis: Role of the Metal Sites in the Decomposition of Formic Acid into H_2 and CO_2 by the Coinage Metal Binuclear Complexes $[\text{dppmMM}'(\text{H})]^+$ (submitted)	75
CONCLUSIONS AND OUTLOOK		80
APPENDIX		83
1	Composition dependent selectivity in the coadsorption of H_2O and CO on pure and binary silver-gold clusters	84
2	Water activation by small free ruthenium oxide clusters	91
CURRICULUM VITAE		98
LIST OF PUBLICATIONS		99

ABSTRACT

The electrochemical energy conversion mediated by fuel cells is one of the most promising technologies for achieving sustainable and "green" environmentally compatible source of energy. In the fuel cells energy is produced by the reaction of hydrogen and oxygen through catalytic process on platinum nanoparticles with water as a sole byproduct. The worldwide application of the hydrogen fuel cells as the clean, renewable source of energy is hindered by the challenges that still have to be overcome. Two most prominent challenges for fuel cells applications are electricity generation in decentralized small-scale households and in transportation, due to the low quality of the hydrogen fuel cell feed gas and insufficient density and safety of the currently available hydrogen storage technology, respectively.

In this thesis, catalytic reactivity of the small transition and coinage metal nanoclusters have been theoretically investigated in context of (1) advancing fuel cell technology by developing cost-effective techniques to improve quality of the feed gas as well as (2) safe storage and release of hydrogen in its gaseous state at room temperatures and pressures. The theoretical findings based on density functional theory (DFT) are strongly supported by experimental results through international cooperation.

(1) In order to address the challenge concerning the improvement the quality of fuel cell feed gas reactions of small ruthenium cationic nanoclusters with CO and H₂ has been theoretically investigated in combination with gas-phase experiments. This has been stimulated by previous findings that very small oxide-supported ruthenium nanoparticles with 0.9nm in diameter can be active and selective catalysts for the CO methanation reaction. However, the exact mechanism of the reaction has not been proposed yet.

For this purpose the reaction of Ru_n⁺ (n=4-6) with CO has been investigated theoretically and experimentally. Interestingly, only one specific product for each cluster size, Ru₄(CO)₁₄⁺, Ru₅(CO)₁₆⁺ and Ru₆(CO)₁₈⁺ have been produced showing particular stability of these complexes. Moreover, density functional theory provided detail structural characterization of these previously unknown carbonyl complexes which are in perfect agreement with the geometries predicted by Wade's electron counting rules. Following investigation of the reaction of Wade-type carbonyl complexes Ru₄(CO)₁₄⁺ and Ru₆(CO)₁₈⁺ with hydrogen shows that up to three CO molecules can be replaced with hydrogen molecules bound to the ruthenium cluster in dissociated form. Newly formed hydrido carbonyl complexes preserve total ligand count also corresponding to the Wade cluster sizes. These findings presented the starting point to study reactivity of several basic chemical transformations such as hydrogenation of the carbon monoxide and methanation reaction.

In this context the next aim of the thesis was to discover the origin of the selectivity and outstanding activity of small ruthenium nanoparticles in the catalytic CO methanation reaction with relevance to the hydrogen fuel cell feed gas purification. The aim is to prevent deactivation of the platinum nanoparticles on the anode and cathode within the fuel cell.

We focus on small nanoclusters as model systems (e.g. Ru_4^+ and Ru_6^+). The density functional theory is employed to construct reaction profiles and provide mechanistic insight into reaction route involving the formation of the formyl-type intermediate. From these studies three fundamental properties of small ruthenium nanoclusters are identified which are responsible for its catalytic activity and selectivity: (i) high reactivity towards CO in comparison to the CO_2 ; (ii) promotion of the cooperatively CO and H_2 coadsorption and dissociation, thus prohibiting CO poisoning; and (iii) the presence of low coordinated ruthenium atom centers forming few Ru-Ru bonds. Apparently, only catalysts containing very small ruthenium nanoclusters will satisfy all three conditions. These conceptual insights also opened a new route for transferring model system results to guide the intelligent design strategies for catalytic materials for fuel cell feed gas purification. In the future we propose to employ intrazeolite anchored Ru carbonyl and hydridocarbonyl complexes, in particular $\text{Ru}_6(\text{CO})_{18}$ and $\text{H}_4\text{Ru}_4(\text{CO})_{12}$ previously synthesized in condensed phase, as a new catalytic system for fuel cell feed gas purification by methanation of CO.

(2) The second aim of this dissertation is to advance materials for hydrogen storage and their release technology. For this purpose a gas-phase study of ligated coinage metal hydride nanoclusters has been performed. Combination of extensive *ab initio* theoretical calculations and multistage mass spectrometry experiments have been carried out in two directions. First, fragmentation chemistry of the ligand protected silver hydride clusters $[\text{Ag}_{10}\text{H}_8\text{L}_6]^{2+}$ and $[\text{Ag}_3\text{H}_2\text{L}]^+$ where $\text{L}=(\text{Ph}_2\text{P})_2\text{CH}_2$ (dppm) has been investigated with aim to study hydrogen release triggered by ligands loss or induced by irradiation with light.

Concerning fragmentation chemistry, series of different liganded silver hydride cluster sizes are experimentally accessible through collision-induced dissociation in the ion-trap. DFT calculations are used to examine how cluster geometry is changed during sequential loss of ligands triggering loss of the all hydrogen atoms from the silver core. Initial loss of two ligands and following loss of additional ligand is calculated to be endothermic. Loss of these three ligands induces structural changes in the silver core leading eventually to the subsequent loss of all hydrogen atoms which is calculated to be slightly exothermic. Moreover, theoretical calculations allows for structural characterization of the triatomic silver hydride nanocluster. Molecular dynamic simulations are performed to probe the fragmentation channels in the ground and first excited state. Finding that formation and release of hydrogen can be induced by irradiation with light is important in context of metal hydrides as a hydrogen storage medium. These findings are fully supported by mass spectroscopy experiments.

Second, of particular importance is investigation of catalytic reactions of $[\text{Ag}_2\text{HL}]^+$ and binuclear complexes $[\text{dppmMM}'(\text{H})]^+$ where M, M' = Ag, Au and Cu with formic acid to selectively release H_2 and CO_2 . The determination of mechanism responsible for decomposition of formic acid achieved within this thesis has huge application potential. In this contributions to the thesis the role of the different ligands as well as different metal sites in homo- and heterometallic liganded hydride clusters are systematically studied in order to gain insight into reaction mechanism and optimize the catalyst for the decomposition of formic acid to hydrogen and carbon dioxide in context of important application in hydrogen storage and *in situ* generation of H_2 . First, the role of the ligand in binuclear silver hydride cation has been investigated. It has been shown that the role of ligand is crucial for developing a two-step catalytic cycle where appropriate choice of the ligand switches on the reactivity by keeping subunit intact consisting from $\text{Ag}_2\text{H}(\text{P}_2)(\text{CH}_2)$. Furthermore, the investigation of the role of different metals and metal centers in the same reaction allowed for systematic search for the

optimum cost-effective coinage bimetallic hydrides. It has been shown that improvement of the catalytic cycle efficiency up to two orders of magnitude occurs for ligated Cu_2H or Au_2H in comparison to the ligated silver hydride can be achieved. It is concluded that the copper homobinuclear catalyst performs the best concerning hydrogen release from formic acid and overall costs in context of hydrogen storage. The value of these fundamental gas-phase studies is that they allow to gain insights through theoretical investigation and serve to stimulate experimental approaches not only in gas phase but also in solution. Therefore, the results presented in this thesis inspired experiments in solution in which the release of hydrogen has been observed almost instantly. Eventually two concepts have emerged: (i) different metal centers and different ligands can have a vital role in activation of the catalyst towards the substrate and (ii) gas-phase experiments can be used to direct the search for novel metal cluster catalysts that will be also catalytically active in solution.

Altogether, the both aims of this theses has been achieved by contributing (1) to develop procedures for purification of fuel cell feed gas via ruthenium nanoclusters and (2) to design ligated small noble metal hydrides which can drive the hydrogen release important for hydrogen storage.

MARJAN KRSTIĆ

The following publications constitute the main part of the thesis:

1. S. M. Lang, S. U. Förtig, T. M. Bernhardt, M. Krstić, V. Bonačić-Koutecký: "Gas-Phase Synthesis and Structure of Wade-Type Ruthenium Carbonyl and Hydrido Carbonyl Clusters", *J. Phys. Chem. A* 118 (37), 8356-8359, **2014**
2. S. M. Lang, T. M. Bernhardt, M. Krstić, V. Bonačić-Koutecký: "The Origin of the Selectivity and Activity of Ruthenium-Cluster Catalysts for Fuel-Cell Feed-Gas Purification: A Gas-Phase Approach", *Angew. Chem. Int. Ed.* 53 5467-5471, **2014**
3. M. Girod, M. Krstić, R. Antoine, L. MacAleese, J. Lemoine, A. Zavras, G. N. Khairallah, V. Bonačić-Koutecký, Ph. Dugourd, and R. A. J. O'Hair: "Formation and characterisation of the silver hydride nanocluster cation $[\text{Ag}_3\text{H}_2((\text{Ph}_2\text{P})_2\text{CH}_2)]^+$ and its release of hydrogen", *Chemistry-A European Journal* 20 (50), 16626-16633, **2014**
4. A. Zavras, G. N. Khairallah, M. Krstić, M. Girod, S. Daly, R. Antoine, Ph. Maitre, R. J. Mulder, S.A. Alexander, V. Bonačić-Koutecký, Ph. Dugourd and R. A. J. O'Hair: "Ligand-induced Substrate Steering and Reshaping of $[\text{Ag}_2(\text{H})]^+$ Scaffold for Selective CO_2 Extrusion from Formic Acid", *Nature Communication*, 7:11746, **2016**
5. M. Krstić, A. Zavras, G. N. Khairallah, Ph. Dugourd, V. Bonačić-Koutecký, R. A. J. O'Hair: "ESI/MS Investigation of Routes to the Formation of Silver Hydride Nanocluster Dications $[\text{Ag}_n\text{H}_{n-2}\text{L}_m]^{2+}$ and Gas-phase Unimolecular Chemistry of $[\text{Ag}_{10}\text{H}_8\text{L}_6]^{2+}$ ", *Int. J. of M. Spec.* **2016**, doi:10.1016/j.ijms.2016.05.022
6. A. Zavras, M. Krstić, Ph. Dugourd, V. Bonačić-Koutecký, R. A. J. O'Hair: Selectivity Effects in Bimetallic Catalysis: Role of the Metal Sites in the Decomposition of Formic Acid into H_2 and CO_2 by the Coinage Metal Binuclear Complexes $[\text{dppmMM}'(\text{H})]^+$, submitted, **2016**

The following publications are included in the appendix:

1. I. Fleischer, D. M. Popolan, M. Krstić, V. Bonačić-Koutecký, T. M. Bernhardt: "Composition dependent selectivity in the coadsorption of H_2O and CO on pure and binary silver-gold clusters", *Chem. Phys. Lett.* 565, 74, **2013**
2. S. M. Lang, T. M. Bernhardt, M. Krstić, V. Bonačić-Koutecký: "Water activation by small free ruthenium oxide clusters", *Phys. Chem. Chem. Phys.* 16 (48), 26578-26583 **2014**

I. INTRODUCTION

A fuel cell has been invented in 1839 by William Robert Grove[1][2]. Nevertheless, it took over a century for the first commercial use of fuel cell by National Aeronautics and Space Administration (NASA) in their space missions in the early 1960s. Fuel cell was used as a reliable power source to provide electricity in the satellites and space capsules using only hydrogen and oxygen. Fuel cells have potential to become "green" technology providing clean source of energy in the future compared to other energy conversion and storage systems (e.g. batteries or photovoltaic, thermoelectric, thermionic energy and fossil fuels) due to its high efficiency, high energy production per occupied unit volume and ability to provide large power outputs. Many different types of fuel cells exist which use broad variety of fuels (hydrogen, methane, ethanol) to provide electricity in direct chemical conversion to electrical energy, but the most common type of fuel cell today is low-temperature proton-exchange membrane fuel cell (PEMFC)[3]. Fuel cells produce electrical energy and heat in the electrochemical conversion of hydrogen and oxygen to water as only product by catalytic processes on the platinum nanoparticles deposited on the surface of anode and cathode[3][4]. Wide spread use of PEMFC in decentralized small-scale residential applications as well as in the transportation has still not been achieved due to the several technical disadvantages that still have to be overcome. Two most prominent challenges are related to 1) improving quality of fuel cell feed gas and 2) insufficient large density (mass to volume ratio) of currently available hydrogen storage devices.

Therefore, this dissertation focuses on these two areas closely related to fuel cell technology and its application in domestic surroundings as well as in transportation. These are:

- 1) Improvement of fuel cell feed gas purification by investigation of the origin of selectivity and activity of nanocluster catalysts which are responsible for removal of CO. Recently discovered oxide-supported ruthenium particle catalysts are very promising feed gas "cleaning" materials but the reason why they exhibit such excellent performance still remains an open question. This was stimulation to become involved in this research direction and to study reactivity and selectivity properties of small cationic ruthenium clusters in context of feed gas purification with the aim to increase durability of PEMFC. In the Introduction part of this thesis, gas phase ruthenium clusters will be presented as model systems that promote selective catalytic CO methanation reaction and fundamental properties of these clusters will be identified which provide conceptual mechanistic insight into the methanation reaction.
- 2) Hydrogen storage, which represents key issue for future worldwide use of fuel cells for clean, environmentally compatible technology. Due to their possible advantages as future clean source of energy in comparison with presently widespread technology based on fossil fuels (e.g. natural gas, crude oil, petroleum, coal, etc.), hydrogen storage is highly active research area worldwide. The fact, that only few atoms of noble metal clusters in specific surrounding can have unexpected and extraordinary reactive properties stimulated us to

become involved in this research direction. Within this dissertation we focused on the role of Ag_2H and Ag_3H_2 under influence of different ligands serving as protection and stabilizers in context of selective extrusion of CO_2 from formic acid for which it is necessary to achieve release of H_2 either by heating or irradiation by light.

In this thesis above mentioned issues have been addressed by extensive theoretical investigation of reactivity of small metallic nanoclusters in the context of catalysis. Gas phase approach offers advantage because it can provide insight into the molecular-level conceptual aspects of the reactions as well as structure-reactivity relationship and aid the future design of improved catalyst materials. Therefore, theoretical contribution using first-principle density functional theory (DFT) has a triple role:

- i) to determine energy steps of catalytic reactions and catalytic cycles;
- ii) recognition of reaction mechanism;
- iii) stimulation of experimental realization of theoretically predicted reaction steps.

Therefore, Introduction is composed from six sections:

- 1 Fuel cell technology challenges
- 2 Historical overview of nanoparticle catalysts and role of transition and noble metal clusters in catalysis
- 3 Ruthenium nanoclusters and their role in fuel cell feed gas purification
- 4 Silver, gold and copper bimetallic hydrides and their role in the hydrogen storage
- 5 Theoretical methods
- 6 Complementary experimental approaches

The chapter II. under the name "THE STRUCTURE AND GOALS OF THE THESIS" presents detailed discussion of the results and it is composed of two parts. First part is devoted to the topic of "Ruthenium nanoclusters and their role in fuel cell feed gas purification". The publications relevant for this research direction are listed under chapter III. The second part of the chapter II. presents results of the "Silver, gold and copper bimetallic hydrides and their role in the hydrogen storage". Therefore, section II.2. contains discussion of the results published in four separate papers but thematically linked contributions in context of hydrogen release for hydrogen storage applications.

The appendix of this thesis contains two additional publications. The topic of first publication is the reactivity of small threenuclear homo- and heterometallic silver-gold clusters towards carbon-monoxide and water molecules. The second contribution is focused on the small free ruthenium clusters, Ru_x^+ ($x = 2-5$), and ruthenium oxide clusters, Ru_xO_y^+ ($x = 2-5$, $y = 1-2$) and their reactivity towards water molecules in context of an efficient hydrogen transfer reaction from the water molecules to the oxygen atoms of the ruthenium oxide clusters.

1 Fuel cell technology challenges

Fuel cell is a device that consist of three main parts: the anode, the electrolyte and the cathode. The anode and the cathode are electrodes that are mostly composed of gold or platinum and its alloy nanoparticles deposited on carbon paper[5]. Metal nanoparticles serve as catalysts to promote oxidation reactions and produce positively charged hydrogen ions (H^+) and electrons (e^-). The hydrogen ions travel through the electrolyte from the anode to the cathode of the fuel cell. At the same time, electrons are extracted to the external

circuit, producing direct current electricity, which can be used to power different devices. At the cathode, hydrogen cations, electrons and oxygen are recombined together to produce water in the steam phase and heat that can also be used for practical applications. Gold and platinum nanoparticles in electrodes are easily deactivated (poisoned) by even small amounts of carbon monoxide (CO), present in the fuel cell feed gas, which deactivates the electrodes reducing durability of PEM fuel cell. Another challenge linked to fuel cell applications, especially in transportation, is realization of safe storage and release of hydrogen on demand at room temperatures and atmospheric pressure during operation of fuel cell. These are the problems which solution will determine the future viability of fuel cells.

1.1 Fuel cell feed gas quality

Today, hydrogen is mainly produced in industrial facilities by steam reformation or partial oxidation of fossil fuels (e.g. methane)[6] over Ni-catalysts, which beside hydrogen, produce other compounds, carbon monoxide (1-8%), carbon dioxide (10-20%)[7] and water(30%). Since CO is undesired in the fuel cell feed gas it has to be effectively removed from the hydrogen-rich gas mixture. One procedure to achieve CO removal is to promote reaction of CO with hydrogen, which is also present in the feed gas (50%) to produce methane (CH_4) in catalytic reaction of methanation. Water, carbon dioxide and methane do not influence gold or platinum electrodes inside the PEMFC. However, present CO_2 in the feed gas can either react with hydrogen to produce CH_4 during methanation reaction leading to intolerable need of hydrogen in the feed gas or produce additional amounts of CO in the reverse water-gas shift reaction. Therefore, key concept is to find systems with 100% selectivity towards CO compared with CO_2 and high activity for CO methanation reaction to produce methane and water, thus successfully minimizing CO poisoning in the fuel cell which will elongate its durability and increase viability.

1.2 Hydrogen storage

Hydrogen technology is one of the most attractive "green" technologies, since hydrogen is easily available on Earth in abundant resources from oceans in the form of water. Moreover, it is not associated with increasing of CO_2 amount released in the atmosphere which produces "greenhouse effect", which is disadvantage of traditional hydrocarbons as source of energy[8][9]. Combustion of hydrogen produces only clean water. Presently available technologies of hydrogen storage in its natural gas phase (pressurized) or in the liquid phase (cooled below 33K) are not practical[10][11] due to the safety issues and storage tank technology, which requires finding other ways of low-cost, efficient, safe and compact hydrogen storage has to be proposed. Beside standard techniques of hydrogen storage under high pressures and very low temperatures, other material based hydrogen storage approaches have been recently investigated. Material based storage can be accomplished using sorbent materials, metal hydrides and chemical hydrogen storage materials. In this thesis focus will be on interaction of metal hydrides and chemical hydrogen storage materials in the form of formic acid.

2 Historical overview of nanoparticle catalysts and role of transition and noble metal clusters in catalysis

Today, catalysts are applied in numerous industrial production processes worldwide and its economical value is so significant that it is difficult to estimate. Some of the typical examples are chemical manufacturing, crude oil processing, pharmaceutical production, etc. Catalysts can have enormous influence in alternative source of energy such as in PEMFC or in conversion of biomass to useful liquid and gas fuels. Another practical applications of catalysts are for the environmental issues in context of reduction of atmospheric pollutants as in the car exhaust catalyst or in the degradation processes of toxic wastewater pollutants to harmless compounds.

Despite the role of the catalysis in the modern society[12][13], approach for development of new catalysts and improvement of existing ones remains the same over large period of time. This is typically phenomenological approach and follows procedure where numerous number of different compounds are prepared by the means of combinatorial techniques and tested for activity and reactivity in the relevant reactions[14][15]. Nevertheless, many excellent catalysts have been prepared which have been applied in different industries worldwide. However, key scientific insight of the reaction steps in the processes taking place on the active sites of the catalysts is still missing. Lack of these informations can be obstacle for the future direct design of new or improvement of the existing catalyst materials.[16]

Because of this historical, experimental efforts and practical applications, first catalytic systems investigated were always on metal oxide support. Surface-science approach has shown that the chemical bond between adsorbed molecules and support is similar to the bonds formed by adsorbed molecules to the metallic clusters[17], indicating that size-selected clusters can be good model systems to study the processes occurring on the supported catalysts.[18] Gas phase studies have been introduced because in spite of many experiments the mechanism of the reactions is much more difficult to determine when several factors which cannot be separated are present, which is the case with support.[19] Observation that charged atoms in the metallic clusters are active heterogeneous catalysts stimulated researchers to enter this new field of "free" catalytic nanoparticles where it was possible to produce exact number of atoms and desired ionic charge of the model system exhibiting unique electronic properties.[20][21][22] This direction allowed to elucidate leading features of the catalytic reaction mechanisms of these species and to unravel close structure-reactivity relations for those isolated systems providing insight into the molecular reaction processes and compare them with those taking place in supported systems.[23] Gas phase investigation on "free" metallic clusters also opens new possibilities for synthesis routes for mass scale catalysts production. Furthermore, small isolated clusters of atoms can be novel model systems in two ways. Since cluster sizes and corresponding charges are well defined, they can be easily theoretically described, and in combination with mass spectrometry, provide adequate description of unknown reaction steps taking place in catalytic cycle.[24] Another advantage of gas phase clusters is that they generally have much different, almost unique reactivity and unexpected properties, which can be used for finding of new catalytic routes. Otherwise these routes would have never been found because they might be hidden under influence of the support. As the field of catalyst research will be further advanced, the understanding why small nanoparticles may be responsible for main proportion of the activity of the heterogeneous catalysts becomes increasingly important.[25]

Nevertheless, although gas phase theoretical and experimental research have some advantages over condensed phase there is still a lot of criticism of this methods in the term of investigation of catalytic processes present. One of the main critics is that due to the different Coulomb charge of the metal cluster ions in vacuum, as well as the counter-ions or solution, clusters are more reactive to the reactants than their condensed phase analogue. Therefore, concerns are that gas phase studies might not represent the real mechanisms, energetics or kinetics happening in the condensed phase, and there can not be direct transfer of findings from the gas phase models and experiments to the real supported catalysts.[19][26] On the other hand there are examples of the combination of extensive gas phase theoretical research complemented with gas phase experiments where previous condensed phase research has been confirmed, and even more detailed insight into reaction mechanism were gained that were not possible within study of supported catalyst. It is interesting to emphasize that recently one such example has been presented by us.[27] Therefore, future development and improvement of novel catalysts will depend on insights from the investigation of the small gas phase clusters and its activity and selectivity in the studied reactions.

Transition metal oxides are often used as catalyst or catalysts support materials. One of widely used catalyst in numerous industrially important processes is vanadium oxide. To understand the underlying reasons of their significant reactivity gas phase studies have been performed. The results of these studies implicated that radical oxygen center is responsible for selective oxidation processes such as oxidation of ethylene (C_2H_4) [28][29] or thermal activation of methane (CH_4) which is present only for the given stoichiometries. Radical oxygen centers found in gas phase studies has also been confirmed in numerous experimental investigations of the supported V_2O_5 and VO_3 systems for different catalytic reactions.[30]

Furthermore, for the studies of the role of oxygen radical centers in the oxidation of CO, C_2H_4 and C_2H_2 in the heterogeneous oxidation catalysts zirconium oxide clusters as a model system was used.[31][32] Combination of theoretical and experimental efforts showed that out of whole range of cationic clusters only $(ZrO_2)_x^+$ with $x=2-5$ promote transfer of an oxygen atom to the CO to produce CO_2 . [33] The calculated energy profile for the $Zr_2O_4^+$ showed that the oxidation reaction of CO proceeds via bonding of carbon atom of carbon monoxide to the oxygen radical center of zirconium oxide cluster which involves relatively low barriers. The overall reaction is exothermic by 1.65 eV. Similar investigations have been done for the anionic $(ZrO_x)_{2x+1}^-$ species in context of oxidation reactions. These findings related to oxygen radical centers and charge state have conceptual implications for the design of future catalysts.[34]

Titanium oxide is also important in the context of the catalysis since it is commonly utilizes both as a active material and support. It has been shown that TiO_2 support influence the gold nanoparticles in the synthesis of the aromatic compounds.[35] Moreover, titanium dioxide by itself can cleave the $N=N$ double bond in some cases.[36] Since titanium and zirconium have similar valence electron shells a series of the combined gas phase theoretical simulations and experiments have been done. The studies designed to investigate the reactive mechanisms of titanium oxide cationic clusters with CO, C_2H_2 , C_2H_4 and C_3H_6 has been performed.[37][32] The authors conclude that $Ti_2O_4^+$ and in some extent TiO_2^+ exhibit preferential oxygen loss when they are interacting to reactants. DFT calculations have showed that both catalysts have spin unpaired electron localized creating an oxygen radical center with the elongated bond. Calculated reaction profiles and MD simulations that the cluster oxidizes the reactants studied while the regeneration of the oxygen atom can be

achieved by the reaction of titanium oxides with N_2O .

History of nanoparticle catalysts dates almost 30 years back in time when Haruta *et al.* first produced metal-oxide supported gold nanoparticles smaller than 10 nm in the diameter[38][39]. It has been shown that these novel gold nanoparticles are highly active for hydrogen and carbon monoxide oxidation even at low temperatures as -70 Celsius degrees. Moreover, they found out that this enhanced catalytic activity can be tuned by changing the support due to interaction of gold with transition metal-oxides. This unexpected catalytic activity of supported gold nanoparticles has drawn superior attention and opened new area of a search for novel "green" nanocluster catalysts for industrially relevant catalytic processes. Further size-dependent studies of supported gold nanoclusters in the sub-nanometer regime showed even more unexpected dependence of the chemical activity on the number of gold atoms in metallic cluster. For example, cluster of seven gold atoms deposited on magnesium oxide support showed no catalytic activity in the oxidation of CO to CO_2 compared to Au_{8-20} which are proven to be very active[40]. These first discoveries stimulated worldwide scientific community to investigate gold nanoparticles in context of catalytic processes as one of the most frequently studied system. Beside gold nanoclusters, other catalytically active metallic nanoclusters such as silver, iron, palladium, copper, etc., have been extensively investigated theoretically and experimentally in the gas phase or at support as well as in the zeolites[40][41][23][42]. These investigations included numerous factors: size-dependence, structures of the metallic clusters, morphology, different supports with or without defects, different ligands, ionic charge, etc[43][44][45].

Recently, silver and copper clusters have also attracted worldwide interest mainly due to their photoluminescent properties[46] as well as possible catalytic application,[47] e.g. for the oxygen reduction reaction taking place on the cathode inside fuel cells or in the context of hydrogen storage. More detailed discussion about coinage metal hydride clusters is under the chapter I.4.

3 Ruthenium nanoclusters and their role in fuel cell feed gas purification

Ruthenium was discovered by Karl Ernst Claus in 1844 and belongs to a rare transition metal which together with iron and osmium compose group 8 of chemical elements in the periodic table. Due to similar physical and chemical properties it is related to the platinum-group metals (PGM) consisting from rhodium, palladium, osmium, iridium and platinum. Annual production of ruthenium is estimated to be about 20 tonnes. Most ruthenium extracted from the ores is used for electronic devices and catalysts.

Ruthenium complexes such as Ru-containing organic dyes and sensitizers are known to absorb light in the visible regime and have been actively investigated in context of solar energy technologies. Ligated ruthenium-based compounds have been used for light absorption in dye-sensitized solar cells as a promising new low-cost solar cell materials.[48] Moreover, ruthenium is also a versatile catalyst and its alloys are used in Fischer-Tropsch (FT) reaction.[49] Within FT process CO and H_2 are converted into gas and liquid hydrocarbon chains which is important route for the production of diesel and petrol fuels. Even though it is used industrially for the last 70 years exact mechanism of FT process still needs clarification.

The simplest Fischer-Tropsch reaction is methanation of carbene monoxide where 3 H_2 molecules reacts with CO to produce CH_4 and H_2O molecule. This reaction is a promising for removal of CO from fuel cell feed gas which is produced by steam reformation of fossil fuels (e.g. methane).[6] Carbon monoxide acts as a poison to the platinum or platinum alloys nanoparticles on the anode of the fuel cell decreasing the durability of the PEMFC device.[50] However, hydrogen rich reformat feed gas also contains up to 15% of carbon dioxide which can also react catalytically with hydrogen to form CH_4 in the methanation reaction or to form CO in the reverse water-gas shift reaction.[7] Both of these reactions are undesired since the first one leads to loss of hydrogen used as fuel and second produces additional amounts of CO. It is known that metal-oxide-supported ruthenium catalysts promote methanation reaction involving CO and CO_2 .

For the application of ruthenium as fuel cell feed gas purification catalysts a novel cost-efficient catalyst based on ruthenium nanoparticles with high activity and selectivity have to be developed. Recently, Al_2O_3 and zeolite supported ruthenium nanoparticles in the size regime from 0.9 to 3 nm has been experimentally produced and tested for activity and selectivity of CO/ CO_2 methanation reaction. It has been shown that selectivity and activity depends on ruthenium particle size. While highest relative activity of CO methanation reaction has been detected for nanoparticles of 1.9 nm (~ 320 atoms), selectivity of CO versus CO_2 methanation was only 80%. Reducing the size of the supported ruthenium nanoparticle to the 0.9 nm (~ 30 atoms) increased CO methanation selectivity to 100% but relative activity of the reaction was reduced by factor of 2. Thus, small ruthenium nanoclusters under 1nm in diameter are promising CO methanation catalysts. However, the origin of their high activity and selectivity for the methanation was still unknown. Therefore, several major challenges within this thesis will be addressed. They involve:

- i) evolution of selectivity and activity at even smaller sub-nanometer cluster sizes in the regime where "each atom counts",
- ii) identification of small cluster sizes responsible for higher activity compared to ruthenium nanoparticles composed of few hundreds atoms,
- iii) identification of fundamental properties responsible for origin of outstanding selectivity and activity in the methanation reaction,
- iv) understanding of the reaction steps in the methanation reaction mechanism (identification of all intermediates and corresponding barrier heights in the catalytic cycle) and
- v) finding the mechanism of C-O bond breaking which might be an important reaction step for methanation reaction.

4 Silver, gold and copper hydrides and their role in hydrogen storage

The noble or coinage metals (silver, gold and copper) form metal hydride complexes with wide range of different architectures through interaction of metal and hydrogen as well as metal hydrides with ligands. Metal atoms in these complexes are almost always monovalent with d-electrons energetically accessible having impact on their bonding and reactivity. These two metals form covalent metal-hydrogen bonds due to relatively low electropositivity. Moreover, combined theoretical and experimental investigations have shown that hydrogen can mimic the coinage metals in the small clusters. It is interesting to notice that in all

these metal hydrides there is the presence of at least one hydride bridge as a motive. First studies of coinage metal hydrides have focused mainly on copper hydrides in context of catalysis, but in the last decade study of gold and silver hydrides have accelerated and thus new catalytic reactions have been found. First indirect evidence of the formation of the silver hydrides from silver salts and hydrogen in the solutions was in the middle 1950s[51] but it took almost 50 years to provide direct experimental evidence of existence and stability of gas phase silver hydrides. In fact, the first direct evidence of silver-only hydride was published in 2010 by Liu et al. as ligated octanuclear silver hydride with the Ag₈H core synthesized in tetrahydrofuran (THF) solution.[52] This complex exhibited a remarkably stable structure where single hydrogen atom is in the center of the tetracapped tetrahedron silver shell within icosahedral skeleton formed by 12 selenium atoms of the 6 surrounding ligands. Structural characterization such as hydrogen bonding site and Ag-Ag bond lengths has been performed using NMR spectroscopy. Furthermore, catalytic activity of these first ligated silver hydrides in processes of C-C bond formation from allylic halides have been proved by the means of collision-induced dissociation (CID).[53][54] In the following years further investigation of the silver-containing heterogeneous catalysts have shown their importance in the processes such as alcohol dehydrogenation by γ -alumina-supported silver clusters[55] and methane activation by the zeolite H-ZSM-5 modified by the silver.[56] This unique potential of noble metal hydrides to promote important chemical reactions inspired the theoretical design and experimental synthesis of other ligand-stabilized silver and gold hydride complexes. One important class of silver hydride structures are phosphine-silver hydrides. These complexes were first prepared in solution and isolated by the O’Hair group in 2013 and analyzed by electrospray ionization mass spectrometry (ESI-MS).[57] Structural assignment to the peaks in the mass spectra have been attributed to the [Ag₃H(L₂)₃]²⁺, [Ag₃H(Cl)(L₂)₃]⁺, [Ag₃(Cl₂)(L₂)₃]⁺ and [Ag₁₀(H)₈(L₂)₆]²⁺. Furthermore, application of the X-ray and neutron diffraction analysis to these new type of silver hydrides revealed the binding of the hydride and chloride ligands to silver clusters as the μ_3 -bridging mode with bisphosphine ligands bridging two neighboring silver atoms. Additional CID studies of the isolated complexes in the gas phase gave insight to the fragmentation channels and ability to produce other smaller phosphine-silver hydride species.

Only several years before synthesis and isolation of the silver-only hydrides, namely in 2008, gold-only hydride ([(IDipp)AuH], IDipp=1,3-bis(2,6-diisopropylphenyl)-imidazol-2-ylidene) has been synthesized in solution and isolated for the first time.[58] NMR and X-ray spectroscopy confirmed structural properties with hydrogen atom binding in this gold hydride species as terminal hydride complex. This results has been additionally confirmed by IR spectrum measurements which displayed a band at 1976 cm⁻¹, which is a characteristic of the presence of terminal hydrogen atom in this (IDipp)AuH hydride studied. Finally, stability of this first gold-only hydride was studied in 2015 and it was found that it will decompose after several hours in C₆D₆ solution exposed to the air at room temperature but it will be stable under inert atmosphere or when transformed to the solid state.[59] Neutral phosphine-gold hydride has not been reported up to now, but ligated (μ -hydrido)digold cation has been reported in 2009 by Lean, Le Floch and co-workers. NMR spectroscopy displayed that deuterium atom is bridging two (Xantphos-Phosphole)gold(I) fragments.[60] All previously discussed metal hydrides have had d¹⁰ metal centers. But similar to platinum(II) hydride complexes, Bochmann et al. managed to synthesize the stable gold hydride with Au(III) oxidation state exhibiting d⁸ electronic configuration.[61] Gold-hydrogen bonds in

all of these complexes are not weak and additional stabilization during synthesis can be achieved by proper choice of ligand. These Au(I) and Au(III) containing hydrides has been identified as catalysts[62] or as reaction intermediates[63] in numerous reactions.

In comparison with other coinage metals, copper is metal that forms hydrides easily. Already in 1844, Wurtz reported a red-brown crystal compound that has been characterized as copper hydride.[64] In the following 35 years Berthelot and Wurtz exchanged several scientific publications with evidences whether or not the compound synthesized by Wurtz is copper hydride.[65][66][67]. Eventually Wurtz managed to end the debate with arguments for his original statement and thanked Berthelot for bringing attention to its discovery.[68] In the following years many other scientists have been studying copper hydrides using different techniques such as X-ray powder diffraction[69], neutron diffraction[70], and NMR experiments[71]. The conclusion was that copper hydrides are not stable and they decompose to its components within a day at ambient temperature[72]. Lately, DFT computational studies of copper hydrides found that oligomers of $[\text{CuH}]_n$ ($n=3-6$) exhibit stable, planar ring structures.[73][74]. Furthermore, *ab initio* calculations of $[\text{Cu}_2(\mu\text{-H})_2]$ have been performed and showed no direct Cu-Cu bonds but delocalized copper and hydrogen centers bonding.[75] Similar to other noble metal hydrides, copper also produces neutral and ionic phosphine ligated hydride complexes, including binuclear copper hydride, which showed to be thermally sensitive.[76][77] The first copper hydride isolated in pure molecular form was $[(\text{Ph}_3\text{P})\text{CuH}]_6$ which exhibits distorted octahedron copper centers each with one phosphine ligand and hydrogen atoms bridging two neighboring copper atoms.[78][79][80] Similar to gold, copper also formates ligand protected hydrides with N-heterocyclic carbene and cyclic alkylamino carbene ligands.[81][82] Recently, larger stable copper hydride clusters containing 7, 8, 20, 28 and 32 copper atoms have also been synthesized and characterized by the means of DFT, NMR and X-ray spectroscopy.[83][84][85][86][87] All of these copper hydrides are part of the many different chemical reactions where they play an important role as reactive intermediate or catalyst. Such of these reactions are: CO conversion to methanol[88], hydrosilation catalysis of ketons, imines and enones[89][90], hydroalkylation[91] and hydrogen release upon irradiation with sunlight.[85]

Altogether, findings that noble metals, mainly silver (gold and copper) have stable hydrides stimulated us to engage in study of small ligated noble metal hydrides in context of hydrogen storage and release for applications in transportation due to their high H % weight content. Different aspects of material based hydrogen storage possibilities will be thus presented in chapter IV of this theses.

5 Theoretical methods

Molecules consist of nuclei and electrons, so theoretical and computational chemistry utilize computers to solve approximately Schrödinger equation allowing to determine the structures and other physical and chemical properties of molecules and other complex systems such as solids. In this work theoretical quantum chemistry (QC) simulations in the framework of density functional theory (DFT) are used to determine structures, absolute and relative interaction energies, reactivity, vibrational frequencies, electronic charge distribution, dipoles, higher multipole moments, absorption and emission spectra as well as collision cross sections.

5.1 Density functional theory

One of the most widespread and versatile method today for the theoretical investigation of the ground state properties of relatively large molecular systems (up to several hundreds atoms) is density functional theory. It is a computational quantum mechanical method based on electron density, instead of wave function, to solve many-body Schrödinger equation for molecular system of interest. It is based on the two Hohenberg–Kohn theorems[92] which states that i) the ground state properties of many-electron system are uniquely determined by an electron density that depends on only 3 spatial coordinates and ii) the electron density that minimizes the total energy is the exact ground state density. Using this two theorems Walter Kohn and Lu Jeu Sham, transformed the Schrödinger equation in the well known Kohn-Sham equation of fictitious system of non-interacting electrons that generate the same electron density as any real system of interacting electrons, hence introducing the new aspect in DFT in 1965.[93] Therefore, when electron density of molecular system under study is determined, all ground state properties of the "real" system can be predicted easily. To be able to solve the molecular system of interest, functionals (functions of another function), which in this case is the spatially dependent electron density, have to be used.

The Kohn–Sham equation is defined by a local fictitious external one-particle potential in which the non-interacting electrons move, called the Kohn–Sham potential. However, the exchange-correlation part of Kohn–Sham potential is unknown, so it has to be adequately approximated.

Numerous exchange-correlation (XC) functionals have been introduced to describe different molecular properties such as ground state energy, binding energies, vibrational frequencies, ionization potentials, optical properties, etc. In this work three functionals (hybrid B3LYP[94][95][96], generalized gradient approximation (GGA) PBE functional[97] and Coulomb-attenuated cam-B3LYP functional[98]) have been used that are proven to be adequate for ground state structural determination and reaction profiles, as well as infrared (IR) and ultraviolet-visible (UV-vis) absorption spectra of systems studied involving ruthenium cation clusters and ligated silver hydrides (e.g. ruthenium carbonyl and hydrido carbonyl clusters, $\text{dppmAg}_3\text{H}_2^+$, dppmAg_3^+ , $\text{dppmAg}_2\text{H}^+$, $\text{dppmAg}_2(\text{O}_2\text{CH})^+$ where dppm stands for bis(diphenylphosphino)methane ligand), formic acid, etc.

Beside right choice of XC functional for the proper description of the system studied special care has to be used when choosing atomic basis set. It is a finite set of basis functions used to describe atomic orbitals. Linear combination of atomic orbitals (LCAO) centered on each atomic nucleus is than used to describe Kohn-Sham orbitals. There are hundreds of basis sets published using linear combination of Gaussian functions since it is computational easier to calculate integrals and overlap, leading to huge computational savings which means that more complex systems can be theoretically described. In this work only few carefully chosen basis sets such as def2-SVP and def2-TZVP[99][100] were used to correctly describe structures, absolute and relative energies of catalytic steps and excited state properties. During most molecular bonding, only valence electrons take part in it and determine many chemical properties such as bond strengths, bond lengths, polarizabilities, electron affinities, and ionization potentials, as well as molecular geometries. Therefore, introduction of effective core potentials (ECP) for heavier elements led to significant reduction of computational costs and speed up of calculations.[101] ECP is a useful mean to replace the core electrons in the calculation with an effective potential, eliminating the need for the core basis functions.

Furthermore these pseudopotentials may be used to describe relativistic effects which are largely confined to the core as in the case of ruthenium, silver and specially gold atoms using relativistic effective core potentials (RECP).

For the simulation of optical properties of the investigated systems, mainly absorption and emission spectra, the time-dependent DFT (TDDFT) is used. TDDFT is natural extension of DFT to determine excited state properties which are based on time-dependent external potential.[102] It has been proven that there is direct correlation of time-dependent electron density and time-dependent external potential. This means that electron density of the non-interacting electrons placed in the time-dependent Kohn-Sham potential behave the same as the many-body interacting electrons of the "real" system in the presence of time-dependent external field. This extension of the DFT method allows to determine excited state energies, intensities of the transitions between ground and excited states, corresponding dipole moments for that transitions, excited state geometries, etc. For some of the investigated systems special attention has to be made to properly choose the exchange-correlation functional to correctly describe excited state properties. One of the typical example of such functional is cam-B3LYP[98], a hybrid functional that has long-range correction to treat correctly Coulomb interaction for charge transfer excitations which can be underestimated in the case of plain B3LYP or some other functional.

5.2 Lowest energy structures, transition states and energy profiles

In the catalytic reactions, for every catalytic cycle or chemical process an energy profile along the reaction pathways, where reactants are transformed into products, is composed of series of local minima and corresponding transition states (TS) between them. Usually, all local minima and TS are presented by energies with respect to the initial energy of the system, along the reaction pathways in the form of the energy surface. The height of every transition state is called "activation energy" for that particular catalytic step. Overall, catalytic cycle can be either exothermic or endothermic, so additional heat is released or needed within the individual catalytic step, respectively. Exothermicity and endothermicity is based on the difference of the total energy of the final product and the initial total energy of the investigated system. Therefore, if the energy of products is lower than the energy of reactants the catalytic process is exothermic and if the energy of products is higher than that of reactants it is endothermic.

The extensive search for all local minima and specially for TS, presented in typical energy profile is computationally time demanding. This is based on the full optimization of the corresponding structures using gradient minimization techniques. All stationary points found during optimization are characterized as local minima or transition state by calculation of their vibrational frequencies. If the structure of interest has all of its $3N-6$ (N - number of atoms in the system) vibrational frequencies positive it corresponds to the local minima, and if there is one negative vibrational mode present it represents one of the transition states. Optimization of the molecular structure is purely mathematical problem. The system is varied until minimum of desired function for that system is not found. In our case coordinates of the atoms in molecule are the object of variation and the function of minimization is the energy of the system. Since nuclei of the atoms are approximately 1000-100000 times heavier than electron the Born-Oppenheimer approximation can be applied. Optimization is performed iteratively with the following steps:

- i) geometry coordinates of chemical structure is prepared, either in Cartesian coordinates or Z-matrix form;
- ii) for given geometry structure electron density is found using single point QC calculation in the framework of DFT;
- iii) for the determined electron density first and/or second derivatives of energy (gradients, Hessian matrix) are calculated in analytical or numerical manner. Gradient vector \mathbf{g} is defined as partial derivation of energy function with respect to the n-dimensional coordinate vector where $n=3N-6$ if calculation is done in internal coordinates or $n=3N$ if Cartesian coordinates are used.
- iv) based on the calculated energy gradients, atoms are moved to the new position obeying classical Newton equations along the direction defined with $-\mathbf{g}$. Step size for next structure in geometry optimization procedure can be also adjusted to speed up the calculation. For example at the beginning of the local minimum search step size can be large (since gradients are also large) and closer to the energy minimum step size could be reduced.
- v) for this new coordinates of atoms in the molecule, electron density is determine once again using single point DFT calculations.

Steps iii-v are repeated until convergence is achieved, which means that optimization is accomplished if the change in energy of system, electron density, step size and/or Newton forces acting on the atoms in the molecule are reduced below desired thresholds.

Transition state optimization proceeds in the same manner as optimization of the local minima, but the additional condition corresponding to first order saddle point on the potential energy surface (PES) is introduced. In order to be computationally efficient, starting input geometry for TS search has to be very close to the real transition state or search will not be effective. Numerous strategies to deal with this obstacles have been developed but still it can be difficult to locate the TS of interest due to the complexity of the PES or numerical instabilities of the mathematical algorithms applied.

Nevertheless, to address difficulties and speed up search for local minima and transition states of the molecular systems the molecular dynamics or simulated annealing can be utilized.

5.3 Molecular dynamics in the ground and excited state, simulated annealing

Molecular dynamics is a form of computer simulation developed in the late 1950s[103][104] to study time evolution of the movements of atoms within the molecules for a defined period of time. Trajectories are determined numerically solving Newton’s equations of motion for atoms on energy surface. Forces (negative gradient of the potential energy) acting on atoms are calculated for every time step by means of density functional theory. The available energy in the system is distributed between kinetic and potential energy, thus molecules are able to overcome barriers between minima if the barrier heights are lower than the kinetic energy. If the system undergoing MD simulation have enough high energy which is closely related to the temperature of the system ranging from several hundreds to thousands K, the simulation will sample multiple minima on PES around the starting point. Number of minima that will be sampled are related to the time step for integrating Newtons equations (usually from 0.1 to 0.5 femtoseconds) and total number of steps giving the total time of the simulation (up to pico- or nanoseconds). To sample more minima on the PES multiple MD simulations can be

utilized with different starting geometries sampled by some probability function e.g. Wigner distribution function. Different local minima may be found by minimizing the structures of selected configurations at suitable intervals during MD allowing for more systematic search for the global minimum. Even though this procedure can help in the search for the lowest energy structure it does not necessarily ensure that the global minimum will be found since the internal energy determined by the initial system energy or simulation temperature does not overcome barriers larger than itself.

MD in excited state is usually performed to understand the photo-induced reactions in photoactive molecules. When the light is absorbed the molecule is in its excited state. As a consequence of the excitation usually a rearrangement or photochemical reaction such as isomerization or bond breaking is observed. MD in excited state proceeds in a similar manner as a ground state molecular dynamics with difference that forces acting on the nuclei are calculated as a negative gradient of the potential energy of the excited state of the molecule at that time step. The Born-Oppenheimer approximation is valid as long as the excited state and ground state PES are not too close to each other. If that is not the case, e.g. when S_0 and S_1 approach each other during MD simulation we have to consider explicitly the probability of electron hopping from one PES to the another.[105][106] This is the case in many systems of interest therefore non-adiabatic dynamic simulation has to be performed.[107]

Simulating annealing (SA) is another method that allows the search for the local (or global) minimum. The name "annealing" comes from the solid state physics applied to growing crystals. If the cooling of the hot piece of metal is done very slow large single crystals can be formed in it which represents the global energy minimum of the solid state. Contrary, rapid cooling produces local minimum, a "distorted" solid. Compared to the MD simulation initial temperature is always chosen to be high, from 2000-3000K.[108] Then a normal MD simulation is initiated and the temperature is slowly reduced. At the beginning of the simulation molecule is allowed to move over large areas on the PES due to the high temperature, but later, it becomes trapped in the local minimum as the temperature is decreased. If the "cooling" of the system is done very slowly for an infinite time the found minimum will be global minimum. In practice, due to the limiting computational resources, SA simulation is very short again and only the local area is sampled.

5.4 Structural characterization

Often, it is a case that in experiments system under study is synthesized by the different techniques in solution or in gas phase and properties of interest are measured. In that situation some informations about experimental system such as atomic mass or subunits (metallic cluster core and number of ligands) of the full systems can be determined by the means of mass spectrometry but complete structure of the system is not known. When the lowest energy structure is found theoretically additional characterization has to be done to be sure that it corresponds to global minimum and to the structure of the system studied experimentally. Structural characterization is usually done comparing some simulated spectroscopic properties such as infrared (IR) spectra and/or UV-vis absorption spectra with experimentally measured ones.

Infrared spectroscopy (or vibrational spectroscopy) is based on the property that molecules absorb specific frequencies that are characteristic of their structure.[109] Frequency of the absorbed photons in the infrared part of the electromagnetic spectra matches the transition

energy of the bond or group that vibrates. These resonant frequencies and matching energies are determined by the molecular PES, masses of atoms or groups and the associated vibronic coupling. A molecule can vibrate in numerous ways and each way is one vibrational mode. If a molecule have N atoms and molecules are nonlinear, they have $3N-6$ degrees of vibrational modes while linear molecules have $3N-5$.

The infrared spectrum of molecule sample is relatively easy to obtain. It is recorded by passing a beam of a light in the infrared part of the spectrum through the sample. If the frequency of the IR light is equivalent to the energy of a bond or collection of bonds an absorption occurs.[110] Examination of the light transmitted through the sample reveals the absorbed energy at each frequency or wavelength. This method is usually used to identify the compounds containing covalent bonds by matching recorded absorption bands with previously known characteristic vibrational bands of bonds and functional groups in terms of intensity and frequency. Common procedure is to compare experimentally obtained spectra with the simulated one using *ab initio* calculations, e.g. DFT, to confirm the structure of interest. IR spectroscopy is thus a reliable technique widely used in both organic and inorganic chemistry as well as in industry and research.

Ultraviolet-visible spectroscopy (UV-vis) is yet another absorption spectroscopy technique where electrons within atoms and molecules undergo electronic transitions from ground state to excited state.[111] The absorption frequency matches the energy between the occupied molecular orbital and unoccupied molecular orbital. This method is commonly used in analytical chemistry to determine the molecular system of interest by comparison of experimental and theoretically simulated spectra because the wavelengths of absorption peaks can be correlated with electronic transitions of the characteristic bonds or functional groups. However, this method is also widely used in the investigation of the optical properties of the molecular complexes[112] or new materials for applications such as biological imaging and solar cells.[113]

6 Complementary experimental approaches

Our theoretical studies supported by complementary experimental investigations performed by international experimental groups is a key component of this thesis. Theoretical calculations can be performed but experiments are the one which confirms or denies the theoretical predictions. In experiments, first step is to prepare metallic nanoclusters. Different approaches exists. For example, in the case of fuel cell feed gas purification experiments, gas-phase ruthenium cation clusters were prepared by sputtering of Ru metal targets by high-energy Xe ion beams.[114] The produced mixture of different size clusters were then mass selected by the quadrupole mass filter and guided to the ion trap prefilled with helium buffer gas and reactant gases CO or CO/D₂. After the reaction time of up to several seconds the products are extracted, mass analyzed and detected with the quadrupole mass filter and channeltron electron amplifier. In this case, theoretical structural characterization has been performed in a following way. First, we optimized the bare Ru cation clusters to find global minimum for each cluster size. The help of MD "on the fly" simulations in the ground state and simulated annealing was utilized in the global minimum search if needed. Furthermore, these geometries of bare nanoclusters were used as a starting point for the reoptimization of the initially constructed geometries of ruthenium carbonyl and ruthenium hydrido carbonyl

clusters. Complete reaction profiles for the CO methanation reaction were constructed by full optimization using gradient minimization techniques and stationary points were characterized as minima or transition states by calculating the vibrational frequencies.

In the case of series of experiments concerning hydrogen storage research direction, initial complexes were synthesized in solution and subsequently transferred to the gas-phase by electrospray ionization (ESI). Ion molecule reactions, collision or light (laser) induced dissociation and mass analysis of fragments or reaction intermediates during catalytic cycle were performed in the series of ion traps and mass analyzers.[115] This setup allowed to control complete catalytic cycle and determine masses of all reaction intermediates as well as final reaction constants and efficiencies. DFT calculations of all local minima and corresponding transition states in between them enabled us to construct reaction profiles and determine relative energies and enthalpy of catalytic cycles. By direct comparison of experimentally determined reaction coefficients and calculated stabilization energies as well as relative heights of transition states it is possible to order different catalysts in term of catalytic efficiency. CID and LID experiments are used to induce and record all possible fragmentation channels while the manifold of *in silico* MD simulations in the ground and excited state at high temperature produces the measurable equivalent by counting number of trajectories exhibiting same fragments.

As it can be seen all theoretically predicted values and properties have experimental counterpart. Therefore, combination of these two makes powerful tool to study catalytic reactions in the gas phase with possibility to transfer the gained knowledge towards real catalytic materials with superior performance.

II. THE STRUCTURE AND GOALS OF THE THESIS

1 Ruthenium nanoclusters and their role in fuel cell feed gas purification

In order to provide the answers to the open questions concerning fuel cell feed gas purification the gas-phase ruthenium cation clusters Ru_n^+ ($n=4-6$) as model systems have been investigated using first-principle density functional theory calculations in combination with ion-trap mass spectrometry. Cationic clusters have been selected since previous experiments on deposited ruthenium nanoparticles on metal oxide supports have shown positive charge on the Ru nanoclusters. Joint theoretical and experimental results allowed to provide 1) structural characterization of gas-phase Wade-type ruthenium carbonyl and hydrido carbonyl clusters and 2) elucidation of the origin of the selectivity and activity of ruthenium-cluster catalysts for fuel cell feed gas purification including determination of step-by-step reaction mechanism and the C-O bond breaking mechanism as described in chapter III.

Within chapter III.1) First principle DFT calculations (for details cf. Chapter I.5) was employed to determine structural properties of the ruthenium carbonyl ($\text{Ru}_4(\text{CO})_{14}^+$, $\text{Ru}_5(\text{CO})_{16}^+$, $\text{Ru}_6(\text{CO})_{18}^+$) and hydrido carbonyl ($\text{H}_5\text{Ru}_4(\text{CO})_{12}^+$) cation clusters which exhibited particular stabilities due to valence electron (VE) count of 18 for each metal atom. This remarkable structural stability can be closely linked to effective atomic number (EAN) rule and is in accordance with the geometries predicted by Wade's electron counting rule that relates the electronic properties of the carbonyl clusters to the geometric structures. Original Wade's rules predict for $\text{Ru}_4(\text{CO})_{14}^+$ a tetrahedral structure, for $\text{Ru}_5(\text{CO})_{16}^+$ trigonal bipyramid and for $\text{Ru}_6(\text{CO})_{18}^+$ bicapped tetrahedron, which is in perfect agreement with the results of DFT calculations. They can be characterized by specific position of CO molecules in so called μ_1 - and μ_2 -atop positions described in chapter III.1. Corresponding calculated average CO binding energies are 1.89, 1.83 and 1.79 eV, respectively. For the hydrido carbonyl cluster $\text{H}_5\text{Ru}_4(\text{CO})_{12}^+$ two CO molecules can be replaced by H_2 molecules while additional hydrogen atom is bound to the metal core in order to balance positive charge of the cluster leading to the perfect closed electronic shell configuration. All 5 hydrogens are bound dissociatively in the μ_2 -configuration bridging two neighboring Ru atoms assuming C_{2v} symmetry.

III.2) In order to find origin of selectivity and activity of ruthenium cluster catalysts in context of fuel cell feed gas purification DFT calculations in combination with ion-trap mass spectrometry were employed to investigate reactivity of the gas-phase ruthenium clusters Ru_n^+ ($n=4-6$) with CO within methanation reaction. First, origin of the CO/ CO_2 selectivity has been studied. It has been found that ruthenium clusters strongly bind carbon monoxide

II. THE STRUCTURE AND GOALS OF THE THESIS

(calculated binding energy $E_b(\text{Ru}_4^+-\text{CO})=1.76$ eV) while it is almost nonreactive toward the carbon dioxide ($E_b(\text{Ru}_4^+-\text{CO}_2)=0.45$ eV) thus preventing unwanted hydrogen consuming CO_2 methanation. Moreover, strong binding of CO also explains pronounced stability of the ruthenium carbonyl cation clusters.

Second, origin of the catalytic activity of the small ruthenium nanoparticle has been investigated. It has been demonstrated that in spite of the calculated high binding energy of the CO to the metal cluster compared to the binding energy of H_2 ($E_b(\text{Ru}_4^+-\text{CO})=1.76$ eV vs. $E_b(\text{Ru}_4^+-\text{H}_2)=0.66$ eV, $E_b(\text{Ru}_6^+-\text{CO})=1.69$ eV vs. $E_b(\text{Ru}_6^+-\text{H}_2)=0.59$ eV) the co-adsorption of hydrogen is possible and thus CO poisoning does not occur. In addition, ion-trap mass spectrometry experiments also showed that CO actively promotes hydrogen co-adsorption because complexes of $\text{Ru}_4(\text{CO})_{11}\text{D}_7^+$ and $\text{Ru}_6(\text{CO})_{15}\text{D}_8^+$ have been identified. In contrast, at most four and two D atoms participate in reactions of ruthenium Ru_4^+ and Ru_6^+ clusters, respectively, without presence of CO. Theoretical results provided complete insight into the origin of this cooperative effect. DFT clearly show that hydrogen is dissociatively bound to the metal cluster core in the hydrido carbonyl complexes with dissociation energy being 0.2 eV more exothermic when the CO molecule is bound at the same Ru atom than without pre-adsorbed CO. Furthermore, the preferred site of dissociative adsorption of H_2 in carbonyl clusters has been determined. Tetrahedral Ru_4^+ has all equivalent Ru atoms and each forms three Ru-Ru bonds with neighboring atoms, but bicapped tetrahedral Ru_6^+ contains atomic centers with three, four and five bonds to other ruthenium centers. Therefore, in the case of $\text{Ru}_6(\text{CO})_{17}\text{H}_2^+$ the hydrogen is bound dissociatively to the Ru center forming three bounds to the surrounding Ru atoms as the most stable structure while centers with more metal-metal bonds are 0.41 and 0.52 eV less stable. Hence, these low-coordinated metal atoms which are the most abundant in the very small nanoparticles in addition to the cooperative effects are the origin of the high activity.

Finally, CO methanation reaction mechanism has been studied by the means of density functional theory calculations. The trigonal prismatic Ru_6^+ , having all equivalent atoms bound to three other Ru atoms has been chosen as an excellent reaction model where CO and H_2 are co-adsorbed on the same active metal center of the cluster. The stabilization energy of co-adsorbed species are 2.3 eV for the undissociated H_2 molecule and 2.54 eV if the H_2 is dissociated. The following step from the co-adsorbed species is either direct C-O bond breaking which renders to be unfeasible since calculated energy barrier exceeds the binding energy of the CO and H_2 to the Ru cluster, or hydration of the carbon atom to form the formyl-type intermediate (HCO) which is calculated to be energetically most favorable mechanism. Formyl formation proceeds over the barrier of 1.36 eV and overall is exothermic by 1.58 eV. The second hydrogen molecule introduced in the system bounds to the oxygen atom of the formyl intermediate to form water molecule and the methyne (CH) ligand. Subsequent binding of two additional H_2 molecules are required to form methane (CH_4) which is then liberated from the Ru_6^+ cluster, yielding overall reaction to be exothermic by 4.52 eV. Reaction mechanism proceeding over formyl-type intermediate is in an excellent agreement with the IR spectroscopic studies which previously identified HCO as a intermediate of the CO methanation of the ruthenium catalyst supported on the Al_2O_3 . Additionally, more complex reaction pathway starting from the experimentally observed $\text{Ru}_4(\text{CO})_{13}\text{H}_2^+$ hydrido carbonyl cluster has been calculated which has been shown to proceed along mechanistically and energetically similar pathway over formyl formation. In both cases all the calculated barrier heights are smaller than the initial energy of the reactants.

Altogether, these model studies have been shown to be an important step for conceptual mechanistic insight into recently discovered excellent performance of the supported ruthenium particle catalysts in context of the fuel cell feed gas purification. These findings open possibility for transferring model results to guide design of novel catalytic materials for feed gas purification with improved efficiency.

The following key fundamental properties for new generation of ruthenium based catalysts can be defined: a) high reactivity towards CO in contrast to inertness to CO₂ as a precondition of the selectivity; b) promotion of the hydrogen co-adsorption and dissociation on the ruthenium carbonyl clusters and c) preference of ruthenium clusters with the presence of Ru active centers forming a low number of metal-metal bonds. Only very small Ru clusters satisfy these three conditions. Therefore, the proposal is to study intrazeolite anchored Ru carbonyl clusters as one additional step to the real improved catalysts for fuel cell feed gas purification by CO methanation.

2 Silver, gold and copper hydrides and their role in hydrogen storage

Hydrogen storage is one of the important technologies that can boost worldwide application of energy efficient hydrogen fuel cells as source of clean energy. The goal of this research direction is improvement of the hydrogen storage technology and release of hydrogen mediated by ligated coinage metal hydrides. In Chapter IV, the combination of DFT methods and mass spectrometry is presented as powerful tool for:

- 1) synthesis of silver hydrides and gaining insight into triggered release of the hydrogen in the ground state by ligand loss and structural change of the silver cluster core,
- 2) studying hydrogen release from the small ligated silver cluster in the excited state by irradiation with light,
- 3) investigation of the catalytic selective decomposition of the formic acid to the H₂ and CO₂ by dppm ligated binuclear silver hydride in context of application in hydrogen storage, and
- 4) optimization of the performance and cost efficiency of the [dppmMM'(H)]⁺ (M, M'=Ag, Au, Cu) complexes for the selective decarboxylation of the HO₂CH to release hydrogen.

Within chapter IV.1) DFT calculations give an insight into structural changes and energetics of the silver cluster core upon sequential ligands loss leading to the triggered loss of 8 coordinated hydrogen atoms as 4 hydrogen molecules in the series of reaction steps: [Ag₁₀H₈L₆]²⁺ → [Ag₁₀H₈L₄]²⁺ + 2L → [Ag₁₀H₈L₃]²⁺ + L → [Ag₁₀L₃]²⁺ + 4H₂, where L=(Ph₂P)₂CH₂ (dppm). These fragmentation reactions are interesting since they represent a change from a ionic ligated silver hydride cluster to the metallic cluster after release of hydrogen. The previously optimized geometric structure of [Ag₁₀H₈L₆]²⁺ served as a starting point for removal of two ligands, that bind only via 1 phosphine atoms, from the metal hydride core and re-optimization of the [Ag₁₀H₈L₄]²⁺. The silver core of this initial ligated silver hydride contains a symmetric bicapped square antiprism with two different hydride coordination modes with 4 μ₂ and μ₃ hydrogen atoms. Fully re-optimized structure of [Ag₁₀H₈L₄]²⁺ have two rotated mutually connected pentagonal rings as a silver core with the same coordination modes of the hydride ligands. Removal of the additional dppm ligand does not induce structural change of the hydride silver core but triggers hydrogen release producing only silver dication [Ag₁₀L₃]²⁺. The structure of this ligated metallic-only

nanocluster has once again transformed silver core formed by trigonal bipyramid capped by additional 5 silver atoms. DFT calculations show that initial loss of two ligands requires 2.9 eV and the loss of the next ligand requires additional 1.9 eV which is in a good agreement with the experiments where loss of the ligands are happening under CID processes. Eventually, structural changes in the silver core led to the loss of all hydrogen atoms which is exothermic by 0.2 eV, also fully supported by experimental finding where loss of hydrogen has been proven to happen spontaneously.

Experimental approach in this contribution provided procedure for synthesis of the $[\text{Ag}_{10}\text{H}_8\text{L}_6]^{2+}$ from the precursor structure in the solution. Following combination of multistage mass spectrometry (MS^n) under CID condition and electrospray ionization mass spectrometry allows for production and identification as well as giving insight to fragmentation chemistry of the broad range of the dppm ligated silver hydride clusters such as $[\text{Ag}_x\text{H}_{x-2}\text{L}_y]^{2+}$ where $x=9-15$ and $[\text{Ag}_x\text{H}_{x-1}\text{L}_y]^+$ where $x=1,2$ and 4. In conclusion, theoretical studies complemented by multistage mass spectrometry showed that CID triggered sequential ligand loss drives the hydrogen release from the silver core suggesting that related reactions might also happen at the surfaces of the silver nanoparticles.

Chapter IV.2) presents DFT study in combination with mass and action spectrometry of the small silver hydride cluster $[\text{Ag}_3\text{H}_2\text{L}]^+$ where $\text{L}=\text{dppm}$ and its gas-phase fragmentation as well as H_2 formation and release when irradiated with light. Structural characterization and absorption spectrum analysis has been performed for precursor $[\text{Ag}_3\text{H}_2\text{L}]^+$, product ion $[\text{Ag}_3\text{L}]^+$ and protonated ligand $[\text{L}+\text{H}]^+$. After extensive search for the lowest energy structure of precursor cation, TD-DFT calculation and comparison with UV-Vis action spectrum confirmed planar subunit of triangular Ag_3 cluster with two hydrogen in the μ_2 -configuration stabilized by dppm ligand through its both phosphorus atoms. Moreover, theoretical calculation showed that equilibrium structure of the S_1 state differs from the one in the ground state with two hydrogen atoms inserted into Ag-Ag bonds. Calculated absorption spectrum have two dominant bands at 270 nm and 250 nm corresponding to transitions to S_1 and S_8 excited state mainly in $\text{Ag}_3\text{H}_2\text{-P}_2$ subunit. To characterize the $[\text{Ag}_3\text{L}]^+$ the main product after photoactivation of $[\text{Ag}_3\text{H}_2\text{L}]^+$ the same procedure was used which showed that absorption spectrum exhibit two bands between 200 and 300 nm. Experiments confirmed the characteristics of the absorption spectra but are only slightly red-shifted compared to theory. This small shift can be caused by the relative positions of the phenyl rings in the dppm ligand in experimental setup which has been shown to influence the spectroscopic pattern.

To study fragmentation channels of the initial complex $[\text{Ag}_3\text{H}_2\text{L}]^+$ molecular dynamics simulations have been performed in the ground and first excited state. MD "on the fly" simulation in the ground state (S_0) shows that main fragmentation channel is loss of AgH which is in agreement with experimental finding of $[\text{AgL}]^+$ product observed after CID where two AgH or Ag_2H_2 fragments (also found in MD simulation as a possible channel) are lost. Minor channel for H_2 loss is also found in the ground state. These fragmentation channels in the ground state could be qualitatively explain by the nature of HOMO which have a node between two Ag atoms capped by dppm ligand. The fact that all simulations were performed at 2400K confirms the high stability of the initial ion.

More importantly, to investigate LID experimental finding which showed hydrogen formation and release, complementary MD simulation in the first excited state S_1 has been carried out. Molecular dynamics showed that the main fragmentation channel is indeed formation of H_2 and its release which can be qualitatively explained by the nature of leading

excitation for S_1 state (HOMO \rightarrow LUMO transition). LUMO contains two nodes which separates each hydrogen atom from the Ag_3 ligated cluster indicating that H_2 release might occur. The mechanism for the hydrogen release, first involves weakening of the Ag-Ag and Ag-H bonds corresponding to the equilibrium structure of the S_1 state, making formation of the H_2 complex easy, following by its release. Only other minor fragmentation channel in the first excited state also shows AgH fragmentation, very similar to the one in the ground state. Experiments performed with $[Ag_3D_2L]^+$ complex showed in the mass spectra all fragments found in the all MD simulations confirming that dppm ligand is not the source of hydrogen or AgH released and fragmented under LID and CID conditions.

The possibility that $[Ag_3H_2L]^+$ ion could be regenerated by the reaction of $[Ag_3L]^+$ with hydrogen were also investigated theoretically and experimentally. DFT calculated reaction profile showed that overall reaction is slightly exothermic by 0.37 eV but it includes overcoming the barrier of 0.61 eV which does not permit the reaction to occur. Experiment showed no reaction of hydrogen with $[Ag_3L]^+$ in the gas phase confirming theoretical findings.

Finally, the findings presented in this contribution on the gas-phase model of the dppm ligated cation silver nanocluster may be the general route for the photo-release of hydrogen in the excited state from ligated metal hydrides and could be governed by the influence of the ligand.

Focus of the chapter IV.3) is on the binuclear silver hydride cation $[Ag_2H]^+$ and how to functionalize it with a appropriate choice of phosphine ligand to achieve the selective catalysed decomposition of formic acid to H_2 and CO_2 with potential application in areas such as hydrogen storage and generation of *in situ* hydrogenation sources for reduction of organic substrates. $[Ag_2H]^+$ subunit can be structurally manipulated to switch on the protonation of formic acid, as a key step to release hydrogen.

The powerful combination of DFT calculations with gas-phase ion molecule reactions (IMR), CID, infrared and ultraviolet action spectroscopy has been employed to examine the role of different ligands (L) in decarboxylation of the formic acid catalysed by the $[LAg_2H]^+$. The systems have been studied which included following ligands: a) no ligand, b) $L=PPh_3$, c) $L=2xPPh_3$, d) $L=bis(diphenylphosphino)methane$ (dppm), e) $L=bis(diphenylphosphino)benzene$ (dppbz) and f) $L=bis(diphenylphosphino)ethane$ (dppe). Theoretical and experimental study showed no catalytic decomposition in the reaction with formic acid for the first three systems a), b) and c). Experimentally, only formation of the Lewis adduct of the two, one and none formic acid molecules have been observed, respectively. DFT optimized structures of these silver hydrides showed that in this case Ag-Ag bond is elongated with phosphine ligands bound almost linearly with the binuclear silver hydride thus preventing activation of the hydrogen release. In the case of the systems d), e) and f) ligand has the role to shorten the bond between silver atoms which weakens the Ag-H bonds. P-Ag-H angle is also deviated from linearity which allows for the formic acid to bind easily, react and release H_2 .

Furthermore, for the system d) with the dppm ligand structural characterization of the $[dppmAg_2H]^+$ and $[dppmAg_2(O_2CH)]^+$ in the gas-phase has been performed by comparison of the simulated IR and UV absorption spectra with infrared multiple photon dissociation (IRMPD) and UV action spectroscopy. IR spectrum of the $[dppmAg_2H]^+$ clearly shows characteristic bands of the μ_2 bridging coordination of the hydride which is predicted by the optimised structures. Theoretical calculations were performed with D3 dispersion correction which reduced the distances between two parallel aromatic rings, preventing their mobility.

II. THE STRUCTURE AND GOALS OF THE THESIS

A good match was observed for both structures and both experimental methods with DFT and TD-DFT calculations thus the structural assignment is unambiguous.

To gain insight into reaction steps of the catalytic cycle for the decarboxylation of the formic acid mediated by dppm ligated silver hydride (d) a reaction mechanism has been determined in the framework of the DFT. Overall catalytic cycle of the reaction can be divided into two steps: 1) ion-molecule reaction of formic acid with silver hydride to produce $[\text{dppmAg}_2(\text{O}_2\text{CH})]^+$ and H_2 which is exothermic process with barriers that lie below the energy of the separated reactants, and 2) decarboxylation of the $[\text{dppmAg}_2(\text{O}_2\text{CH})]^+$ to complete catalytic cycle which is endothermic process with high barriers needing additional heat to be introduced to the system through CID process. Indeed, for step 1 calculations showed that the binding energy of the cis-formic acid to the silver hydride is 0.24 eV, followed by the H_2 activation barrier of 0.18 eV to produce very stable $[\text{dppmAg}_2(\text{O}_2\text{CH})]^+$ complex after release of hydrogen which is exothermic by 0.95 eV. Step 2 of the catalytic cycle involves breaking of one Ag-O bonds via the barrier of 1.7 eV followed by decarboxylation which proceeds over the barrier of 1.86 eV to release CO_2 . Theoretically determined mechanism is in agreement with experimental finding where IMR for step 1 is happening spontaneously while step 2 requires additional energy through multiple collisions with the helium gas during CID process. All three ligands d) dppm, e) dppbz and f) dppe promote the reaction of selective decarboxylation of formic acid to hydrogen and carbon dioxide molecule with the following efficiency: d) \approx e) \gg f), which is in agreement with DFT determined barrier height for all three systems. These gas-phase results also stimulated solution-phase experiments where it has been shown that the same reaction occurs at the temperature of 70 °C and evolution of both H_2 and CO_2 was observed.

Altogether, we showed that the combined gas-phase theoretical and experimental approach is valuable to systematically explore factors that control reactivity in a catalytic cycle. We demonstrated that ligand choice is one of the crucial factors in this reaction having influence on the silver hydride geometry thus switching on the protonation of the hydride in the case of dppm, dppbz and dppe ligands. Finally, two concepts have emerged: i) ligands can have a vital role in the activation of the metal cluster and its reactivity towards substrate and ii) fundamental gas-phase (theoretical and experimental) investigations can be employed to direct the search for new types of metal complexes in context of catalytic reactions. These two concepts allowed us to systematically achieve selective release of hydrogen and extrusion of carbon dioxide from formic acid, an important process for application in hydrogen storage technology.

Chapter IV.4) presents extension of the work presented under IV.3). In this contribution, the role of metal sites for activity and selectivity of the coinage metal binuclear complexes $[\text{dppmMM}'(\text{H})]^+$ (M or M' = Ag, Au, Cu) in context of decomposition of formic acid to hydrogen and carbon dioxide. Systematic study of the silver, gold and copper homobinuclear and heterobinuclear ligated hydride allows for developing a deeper understanding of bimetallic catalysis through possibility to examine each of the metal center.

Combination of the extensive DFT calculations coupled with multistage mass spectrometry will provide means to evaluate cooperative effects between the metal centers which influence both catalytic steps of H_2 release and CO_2 extrusion from HO_2CH . DFT calculated reaction profiles for all hetero- and homobimetallic hydride complexes provide insight into how reactivity is modulated by the nature of metal centers. In all metal center combinations step 1 of the catalytic cycle is exothermic with all TS barrier heights under the energy

of separated reactants. TS structure in all cases for step 1 exhibit similar geometry where one metal center acts as a binding site for the oxygen atom of the trans form of the formic acid while the other site contains the hydride which is being protonated. Initial complex of homobimetallic hydrides with stabilized formic acid has following order in term of the well depth: $[\text{dppmAu}_2(\text{H})]^+$ (-1.08 eV) > $[\text{dppmCu}_2(\text{H})]^+$ (-0.73 eV) > $[\text{dppmAg}_2(\text{H})]^+$ (-0.24 eV). For the complexes with mixed bimetallic centers formic acid can bind either of the two metal atoms. A comprehensive analysis of all possible sites of attack revealed that the favorable site for binding of formic acid is copper atom in the case of $[\text{dppmCuAg}(\text{H})]^+$ and $[\text{dppmCuAu}(\text{H})]^+$ and gold atom in the case of $[\text{dppmAgAu}(\text{H})]^+$. This is consistent with the relative reactivity order of the homobimetallic hydride complexes.

The DFT calculations for the step 2 of the catalytic cycle shows that both metal atoms play a role in the mechanism of decarboxylation. This process involves overcoming of two barriers, the breaking of one M-O bond to isomerize the O,O-bridged formate to its O-bound form and decarboxylation to produce O-bound $[\text{dppmMM}'(\text{H})(\text{OCO})]^+$ complex, which then releases CO_2 . In this case detailed analysis of all possible TS and intermediates was performed for $[\text{dppmCuAg}(\text{H})]^+$, which showed that most favored site of hydride attack is at silver atom.

MS mass spectroscopy experiments started with coordinated formates $[\text{dppmMM}'(\text{O}_2\text{CH})]^+$ which were then transferred into gas-phase via ESI method. CID of these species generated $[\text{dppmMM}'(\text{H})]^+$ hydride complexes via the decarboxylation process. Furthermore, mass selection of the produced liganded mettalic hydride and its reaction with formic acid regenerated initial formate complex in the experimental series, thus completing catalytic cycle. From the activation times and measured concentrations of formic acid rate constants have been determined. Experimentally observed reactivity follows the following order: $[\text{dppmAu}_2(\text{H})]^+ > [\text{dppmCu}_2(\text{H})]^+ > [\text{dppmCuAu}(\text{H})]^+ > [\text{dppmCuAg}(\text{H})]^+ > [\text{dppmAgAu}(\text{H})]^+ > [\text{dppmAg}_2(\text{H})]^+$, with with approximately two order of magnitude difference in reactivity between most and least reactive complexes. These findings are largely in consistence with the DFT calculated energy diagrams of the reaction profiles.

Extensive theoretical (and experimental) investigation giving insight into the catalytic reaction shows that both metal centers have a role in both steps of the catalytic cycle. One metal atom is always favorable for the binding of the formic acid while the other one serves for the protonation or abstraction of the hydride. Concerning all these results and the price of coinage metals it can be concluded that the optimal catalyst in the reaction of the selective decarboxylation of the formic acid to H_2 and CO_2 is the ligated copper hydride $[\text{dppmCu}_2(\text{H})]^+$.

Altogether, successful extrusion of carbon dioxide from formic acid by coinage metal hydrides and light induced release of hydrogen from ligand protected silver hydride nanoclusters represent an important processes for application in hydrogen storage in the future.

Bibliography

- [1] William Robert Grove. *Philosophical Magazine and Journal of Science*, XIV:127–130, 1839. 5
- [2] William Robert Grove. *Philosophical Magazine and Journal of Science*, XXI:417–420, 1842. 5
- [3] Linda Carrette, K. Andreas Friedrich, and Ulrich Stimming. *ChemPhysChem*, 1(4): 162–193, 2000. ISSN 1439-7641. 5
- [4] Supramaniam Srinivasan, Renaut Mosdale, Philippe Stevens, and Christopher Yang. *Annual Review of Energy and the Environment*, 24(1):281–328, 1999. 5
- [5] Alexis T. Bell. *Science*, 299(5613):1688–1691, 2003. 6
- [6] David L. Trimm and Z. Ilsen Önsan. *Catalysis Reviews*, 43(1-2):31–84, 2001. 7, 11
- [7] D.L. Trimm. *Applied Catalysis A: General*, 296(1):1 – 11, 2005. 7, 11
- [8] Puru Jena. *The Journal of Physical Chemistry Letters*, 2(3):206–211, 2011. 7
- [9] Mildred S. Dresselhaus George W. Crabtree and Michelle V. Buchanan. *Physics Today*, page 39, 2004. 7
- [10] Louis Schlapbach and Andreas Züttel. *Nature*, 6861:353–358, 2001. 7
- [11] F. Schüth. *The European Physical Journal Special Topics*, 176(1):155–166, 2009. 7
- [12] Gadi Rothenberg. *Catalysis Concepts and Green Applications*. Wiley VCH Verlag GmbH Co. KGaA, 2008. 8
- [13] Roger Arthur Sheldon and Herman van Bekkum. *Fine Chemicals through Heterogeneous Catalysis*. Wiley VCH Verlag GmbH, 2007. 8
- [14] Paolo P. Pescarmona, Jan C. van der Waal, Ian E. Maxwell, and Thomas Maschmeyer. *Catalysis Letters*, 63(1):1, 1999. 8
- [15] Oliver Trapp. *Journal of Chromatography A*, 1184(1):160, 2008. 50 Years Journal of Chromatography. 8
- [16] Shik Chi Tsang, Nick Cailuo, William Oduro, Adam T. S. Kong, L. Clifton, K. M. Kerry Yu, Benedicte Thiebaut, James Cookson, and Peter Bishop. *ACS Nano*, 2(12):2547–2553, 2008. 8

- [17] G.A. Somorjai. *Introduction to Surface Chemistry and Catalysis*. John Wiley and Sons, 1994. 8
- [18] E. L. Muetterties. *Science*, 196(4292):839–848, 1977. doi: 10.1126/science.196.4292.839. 8
- [19] Diethard K. Boehme and Helmut Schwarz. *Angewandte Chemie International Edition*, 44(16):2336–2354, 2005. 8, 9
- [20] K. A. Zemski, D. R. Justes, and A. W. Jr. Castleman. *The Journal of Physical Chemistry B*, 106(24):6136–6148, 2002. 8
- [21] A. W. Castleman and K.H. Bowen. *The Journal of Physical Chemistry*, 100(31):12911, 1996. 8
- [22] A. W Castleman and R. G. Keesee. *Science*, 241(4861):36–42, 1988. 8
- [23] Bokwon Yoon, Hannu Häkkinen, Uzi Landman, Anke S. Wörz, Jean-Marie Antonietti, Stéphane Abbet, Ken Judai, and Ueli Heiz. *Science*, 307(5708):403–407, 2005. 8, 10
- [24] Grant E. Johnson, Roland Mitrić, Vlasta Bonačić-Koutecký, and A.W. Castleman Jr. *Chemical Physics Letters*, 475(1-3):1 – 9, 2009. 8
- [25] Yimin Li and Gabor A. Somorjai. *Nano Letters*, 10(7):2289–2295, 2010. 8
- [26] Helmut Schwarz. *Angewandte Chemie International Edition*, 50(43):10096–10115, 2011. 9
- [27] Sandra M. Lang, Thorsten M. Bernhardt, Marjan Krstić, and Vlasta Bonačić-Koutecký. *Angewandte Chemie International Edition*, 53(21):5467–5471, 2014. 9
- [28] Dina R. Justes, Roland Mitric, Nelly A. Moore, Vlasta Bonacic-Koutecky, and A. Welford Castleman. *Journal of the American Chemical Society*, 125(20):6289–6299, 2003. 9
- [29] Nelly A. Moore, Roland Mitric, Dina R. Justes, Vlasta Bonacic-Koutecky, and A. W. Castleman. *The Journal of Physical Chemistry B*, 110(7):3015–3022, 2006. 9
- [30] Knut R. Asmis, Gerard Meijer, Mathias Bruemmer, Cristina Kaposta, Gabriele Santambrogio, Ludger Woeste, and Joachim Sauer. *The Journal of Chemical Physics*, 120(14):6461–6470, 2004. 9
- [31] Eric C. Tyo, Melanie Nossler, Christopher L. Harmon, Roland Mitric, Vlasta Bonacic-Koutecky, and A. W. Castleman. *The Journal of Physical Chemistry C*, 115(44):21559–21566, 2011. 9
- [32] Eric C. Tyo, Melanie Noessler, Sabine Rabe, Christopher L. Harmon, Roland Mitric, Vlasta Bonacic-Koutecky, and A. W. Castleman. *Phys. Chem. Chem. Phys.*, 14:1846–1849, 2012. 9
- [33] Grant E. Johnson, Roland Mitric, Eric C. Tyo, Vlasta Bonacic-Koutecky, and A. W. Castleman. *Journal of the American Chemical Society*, 130(42):13912–13920, 2008. 9

- [34] Melanie Noessler, Roland Mitric, Vlasta Bonacic-Koutecky, Grant E. Johnson, Eric C. Tyo, and A. Welford Castleman. *Angewandte Chemie International Edition*, 49(13): 2272, 2010. 9
- [35] Abdessamad Grirrane, Avelino Corma, and Hermenegildo García. *Science*, 322(5908): 1661–1664, 2008. 9
- [36] Harikrishna Tumma, N. Nagaraju, and K. Vijayakumar Reddy. *Applied Catalysis A: General*, 353(1):54 – 60, 2009. 9
- [37] Eric C. Tyo, Melanie Noessler, Roland Mitric, Vlasta Bonacic-Koutecky, and A. W. Castleman Jr. *Phys. Chem. Chem. Phys.*, 13:4243–4249, 2011. 9
- [38] M. Haruta, N. Yamada, T. Kobayashi, and S. Iijima. *Journal of Catalysis*, 115(2):301 – 309, 1989. 10
- [39] Masatake Haruta. *Catalysis Today*, 36(1):153 – 166, 1997. 10
- [40] A. Sanchez, S. Abbet, U. Heiz, W.D. Schneider, H. Häkkinen, R. N. Barnett, and Uzi Landman. *The Journal of Physical Chemistry A*, 103(48):9573–9578, 1999. 10
- [41] Uzi Landman, Bokwon Yoon, Chun Zhang, Ueli Heiz, and Matthias Arenz. *Topics in Catalysis*, 44(1):145–158, 2007. 10
- [42] Sandra M. Lang, Thorsten M. Bernhardt, Robert N. Barnett, Bokwon Yoon, and Uzi Landman. *Journal of the American Chemical Society*, 131(25):8939–8951, 2009. 10
- [43] Davide Ricci, Angelo Bongiorno, Gianfranco Pacchioni, and Uzi Landman. *Phys. Rev. Lett.*, 97:036106, 2006. 10
- [44] Chun Zhang, Bokwon Yoon, and Uzi Landman. *Journal of the American Chemical Society*, 129(8):2228–2229, 2007. 10
- [45] Chris Harding, Vahideh Habibpour, Sebastian Kunz, Adrian Nam-Su Farnbacher, Ueli Heiz, Bokwon Yoon, and Uzi Landman. *Journal of the American Chemical Society*, 131(2):538–548, 2009. 10
- [46] Vlasta Bonacic-Koutecky, Alexander Kulesza, Lars Gell, Roland Mitric, Rodolphe Antoine, Franck Bertorelle, Ramzi Hamouda, Driss Rayane, Michel Broyer, Thibault Tabarin, and Philippe Dugourd. *Phys. Chem. Chem. Phys.*, 14:9282–9290, 2012. 10
- [47] Yizhong Lu and Wei Chen. *Chem. Soc. Rev.*, 41:3594–3623, 2012. 10
- [48] Daibin Kuang, Seigo Ito, Bernard Wenger, Cedric Klein, Jacques-E Moser, Robin Humphry-Baker, Shaik M. Zakeeruddin, and Michael Graetzel. *Journal of the American Chemical Society*, 128(12):4146–4154, 2006. 10
- [49] Hans Schulz. *Applied Catalysis A: General*, 186(1–2):3 – 12, 1999. 10
- [50] A. Mishra and R. Prasad. *Bulletin of Chemical Reaction Engineering and Catalysis*, 6(1), 2011. 11

- [51] A. H. Webster and J. Halpern. *The Journal of Physical Chemistry*, 60(3):280–285, 1956. 12
- [52] C. W. Liu, Hao-Wei Chang, Bijay Sarkar, Jean-Yves Saillard, Samia Kahlal, and Ying-Yann Wu. *Inorganic Chemistry*, 49(2):468–475, 2010. 12
- [53] George N. Khairallah and Richard A. J. O’Hair. *Dalton Trans.*, pages 2702–2712, 2005. 12
- [54] George N. Khairallah and Richard A. J. O’Hair. *Dalton Trans.*, pages 2956–2965, 2008. 12
- [55] Ken-ichi Shimizu, Kenji Sugino, Kyoichi Sawabe, and Atsushi Satsuma. *Chemistry - A European Journal*, 15(10):2341–2351, 2009. 12
- [56] Anton A. Gabrienko, Sergei S. Arzumanov, Ilya B. Moroz, Alexander V. Toktarev, Wei Wang, and Alexander G. Stepanov. *The Journal of Physical Chemistry C*, 117(15):7690–7702, 2013. 12
- [57] Athanasios Zavras, George N. Khairallah, Timothy U. Connell, Jonathan M. White, Alison J. Edwards, Paul S. Donnelly, and Richard A. J. O’Hair. *Angewandte Chemie International Edition*, 52(32):8391–8394, 2013. 12
- [58] Emily Y. Tsui, Peter Mueller, and Joseph P. Sadighi. *Angewandte Chemie International Edition*, 47(46):8937–8940, 2008. 12
- [59] Danila Gasperini, Alba Collado, Adrian Gomez-Suarez, David B. Cordes, Alexandra M. Z. Slawin, and Steven P. Nolan. *Chemistry - A European Journal*, 21(14):5403–5412, 2015. 12
- [60] Aurelie Escalle, Guilhem Mora, Fabien Gagosz, Nicolas Mezailles, Xavier F. Le Goff, Yves Jean, and Pascal Le Floch. *Inorganic Chemistry*, 48(17):8415–8422, 2009. 12
- [61] Dragos-Adrian Rosca, Dan A. Smith, David L. Hughes, and Manfred Bochmann. *Angewandte Chemie International Edition*, 51(42):10643–10646, 2012. 12
- [62] Stephanie Labouille, Aurelie Escalle-Lewis, Yves Jean, Nicolas Mezailles, and Pascal Le Floch. *Chemistry - A European Journal*, 17(7):2256–2265, 2011. 13
- [63] Hajime Ito, Tomohisa Saito, Takahiro Miyahara, Chongmin Zhong, and Masaya Sawamura. *Organometallics*, 28(16):4829–4840, 2009. 13
- [64] A Wurtz. *C. R. Hebd. Seances Acad. Sci.*, 18:702–704, 1844. 13
- [65] Berthelot. *C. R. Hebd. Seances Acad. Sci.*, 89:1005–1011, 1879. 13
- [66] A Wurtz. *C. R. Hebd. Seances Acad. Sci.*, 89:1066–1068, 1879. 13
- [67] Berthelot. *C. R. Hebd. Seances Acad. Sci.*, 89:1097–1099, 1879. 13
- [68] A Wurtz. *C. R. Hebd. Seances Acad. Sci.*, 90:22–24, 1880. 13

- [69] Heinz Muller and Albert James Bradley. *J. Chem. Soc.*, 129:1669–1673, 1926. 13
- [70] J. A. Goedkoop and A. F. Andresen. *Acta Crystallographica*, 8(2):118–119, 1955. 13
- [71] B. Nowak, R. Burtovyy, and M. Tkacz. *Journal of Alloys and Compounds*, 384(1–2): 71 – 75, 2004. 13
- [72] Nuala P. Fitzsimons, William Jones, and Patrick J. Herley. *J. Chem. Soc. Faraday Trans.*, 91:713–718, 1995. 13
- [73] Athanassios C. Tsipis and Constantinos A. Tsipis. *Journal of the American Chemical Society*, 125(5):1136–1137, 2003. 13
- [74] Afshan Mohajeri, Imaneh Baresh, and Mojtaba Alipour. *Structural Chemistry*, 24(1): 339–348, 2013. 13
- [75] Christoph. Koelmel and Reinhart. Ahlrichs. *The Journal of Physical Chemistry*, 94 (14):5536–5542, 1990. 13
- [76] J. A. Dilts and Duward F. Shriver. *Journal of the American Chemical Society*, 91(15): 4088–4091, 1969. 13
- [77] Zhong Mao, Jie-Sheng Huang, Chi-Ming Che, Nianyong Zhu, Sarana Ka-Yan Leung, and Zhong-Yuan Zhou. *Journal of the American Chemical Society*, 127(13):4562–4563, 2005. 13
- [78] Susan A. Bezman, Melvyn R. Churchill, John A. Osborn, and John Wormald. *Journal of the American Chemical Society*, 93(8):2063–2065, 1971. 13
- [79] Melvyn Rowen. Churchill, Susan A. Bezman, John A. Osborn, and John. Wormald. *Inorganic Chemistry*, 11(8):1818–1825, 1972. 13
- [80] A. Bondi. *The Journal of Physical Chemistry*, 68(3):441–451, 1964. 13
- [81] A. J. Arduengo, R. Krafczyk, R. Schmutzler, H. A. Craig, J. R. Goerlich, W. J. Marshall, and M. Unverzagt. *Tetrahedron*, 55:14523–14534, 1999. 13
- [82] Valdas Jurkauskas, Joseph P. Sadighi, and Stephen L. Buchwald. *Organic Letters*, 5 (14):2417–2420, 2003. 13
- [83] Camille Latouche, Samia Kahlal, Eric Furet, Ping-Kuei Liao, Yan-Ru Lin, Ching-Shiang Fang, Jerome Cuny, C. W. Liu, and Jean-Yves Saillard. *Inorganic Chemistry*, 52(13):7752–7765, 2013. 13
- [84] Ping-Kuei Liao, Bijay Sarkar, Hao-Wei Chang, Ju-Chun Wang, and C. W. Liu. *Inorganic Chemistry*, 48(9):4089–4097, 2009. 13
- [85] Rajendra S. Dhayal, Jian-Hong Liao, Yan-Ru Lin, Ping-Kuei Liao, Samia Kahlal, Jean-Yves Saillard, and C. W. Liu. *Journal of the American Chemical Society*, 135 (12):4704–4707, 2013. 13

- [86] Alison J. Edwards, Rajendra S. Dhayal, Ping-Kuei Liao, Jian-Hong Liao, Ming-Hsi Chiang, Ross O. Piltz, Samia Kahlal, Jean-Yves Saillard, and C. W. Liu. *Angewandte Chemie International Edition*, 53(28):7214–7218, 2014. 13
- [87] Rajendra S. Dhayal, Jian-Hong Liao, samia Kahlal, Xiaoping Wang, Yu-Chiao Liu, Ming-Hsi Chiang, Werner E. van Zyl, Jean-Yves Saillard, and C. W. Liu. *Chemistry - A European Journal*, 21(23):8369–8374, 2015. 13
- [88] Gary V. Goeden and Kenneth G. Caulton. *Journal of the American Chemical Society*, 103(24):7354–7355, 1981. 13
- [89] Bruce H. Lipshutz. *Synlett*, 4:509–524, 2009. 13
- [90] Benjamin A. Baker, Zarko V. Boskovic, and Bruce H. Lipshutz. *Organic Letters*, 10(2):289–292, 2008. 13
- [91] Alison M. Suess, Mycah R. Uehling, Werner Kaminsky, and Gojko Lalic. *Journal of the American Chemical Society*, 137(24):7747–7753, 2015. 13
- [92] P Hohenberg and W. Kohn. *Phys. Rev.*, 136(3B):B864–B871, 1964. 14
- [93] W. Kohn and L. J. Sham. *Phys. Rev.*, 140:A1133–A1138, 1965. 14
- [94] A. D. Becke. *Phys. Rev. A*, 38:3098–3100, 1988. 14
- [95] Axel D. Becke. *The Journal of Chemical Physics*, 98(7):5648–5652, 1993. 14
- [96] Chengteh Lee, Weitao Yang, and Robert G. Parr. *Phys. Rev. B*, 37:785–789, 1988. 14
- [97] John P. Perdew, Kieron Burke, and Matthias Ernzerhof. *Phys. Rev. Lett.*, 77:3865–3868, 1996. 14
- [98] Takeshi Yanai, David P Tew, and Nicholas C Handy. *Chemical Physics Letters*, 393(1–3):51 – 57, 2004. 14, 15
- [99] Ansgar Schäfer, Christian Huber, and Reinhart Ahlrichs. *The Journal of Chemical Physics*, 100(8):5829–5835, 1994. 14
- [100] K Eichkorn, O Treutler, H Öhm, M Häser, and R Ahlrichs. *Chemical Physics Letters*, 242(6):652 – 660, 1995. 14
- [101] D. Andrae, U. Häußermann, M. Dolg, H. Stoll, and H. Preuß. *Theoretica chimica acta*, 77(2):123–141, 1990. 14
- [102] Erich Runge and E. K. U. Gross. *Phys. Rev. Lett.*, 52:997–1000, 1984. 15
- [103] B. J. Alder and T. E. Wainwright. *The Journal of Chemical Physics*, 31(2):459–466, 1959. 16
- [104] A. Rahman. *Phys. Rev.*, 136:A405–A411, 1964. 16
- [105] John C. Tully. *The Journal of Chemical Physics*, 93(2):1061–1071, 1990. 17

- [106] Roland Mitric, Jens Petersen, and Vlasta Bonacic-Koutecky. *Multistate Nonadiabatic Dynamics "on the Fly" in Complex Systems and Its Control by Laser Fields*, chapter 13, pages 497–568. WORLD SCIENTIFIC, 2012. 17
- [107] Merle I. S. Rohr, Roland Mitric, and Jens Petersen. *Phys. Chem. Chem. Phys.*, 18: 8701–8709, 2016. 17
- [108] S. Kirkpatrick, C. D. Gelatt, and M. P. Vecchi. *Science*, 220(4598):671–680, 1983. doi: 10.1126/science.220.4598.671. 17
- [109] Peter Atkins and Julio de Paula. *Elements of Physical Chemistry*, page 459. W. H. Freeman, 2009. 17
- [110] Richard M. Badger. *The Journal of Chemical Physics*, 2(3):128–131, 1934. 18
- [111] Douglas A. Skoog, F. James Holler, and Stanley R. Crouch. *Principles of Instrumental Analysis*, pages 169–173. Belmont, CA: Thomson Brooks/Cole, 2007. 18
- [112] Željka Sanader, Claire Brunet, Michel Broyer, Rodolphe Antoine, Philippe Dugourd, Roland Mitrić, and Vlasta Bonačić-Koutecký. *Chemical Physics Letters*, 570:22 – 25, 2013. 18
- [113] Vincenzo Barone, Alessandro Ferretti, and Ilaria Pino. *Phys. Chem. Chem. Phys.*, 14: 16130–16137, 2012. 18
- [114] Thorsten M. Bernhardt. *International Journal of Mass Spectrometry*, 243(1):1 – 29, 2005. 18
- [115] Armando Colorado and Jennifer Brodbelt. *Journal of the American Society for Mass Spectrometry*, 7(11):1116 – 1125, 1996. 19

III. RUTHENIUM NANOCLUSTERS AND THEIR ROLE IN FUEL CELL FEED GAS PURIFICATION

1 Gas-Phase Synthesis and Structure of Wade-Type Ruthenium Carbonyl and Hydrido Carbonyl Clusters

Gas-Phase Synthesis and Structure of Wade-Type Ruthenium Carbonyl and Hydrido Carbonyl Clusters

Sandra M. Lang,[†] Sandra U. Förtig,[†] Thorsten M. Bernhardt,^{*,†} Marjan Krstić,[‡]
and Vlasta Bonačić-Koutecký^{*,‡,§}

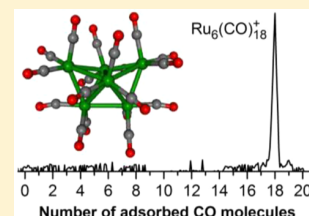
[†]Institute of Surface Chemistry and Catalysis, University of Ulm, Albert-Einstein-Allee 47, 89069 Ulm, Germany

[‡]Interdisciplinary Center for Advanced Sciences and Technology (ICAST), University of Split, Meštrovićevo šetalište 45, 21000 Split, Croatia

[§]Chemistry Department, Humboldt University of Berlin, Brook-Taylor-Straße 2, 12489 Berlin, Germany

Supporting Information

ABSTRACT: The gas-phase reaction of size-selected Ru_n^+ ($n = 4-6$) clusters with CO in an ion trap yields only one specific ruthenium carbonyl complex for each cluster size, $\text{Ru}_4(\text{CO})_{14}^+$, $\text{Ru}_5(\text{CO})_{16}^+$, and $\text{Ru}_6(\text{CO})_{18}^+$. First-principles density functional theory calculations reveal structures for these hitherto unknown carbonyl compounds that are in perfect agreement with the geometries predicted by Wade's electron counting rules. Furthermore, reactions with D_2 show that for Ru_4^+ and Ru_6^+ , CO molecules can be partially replaced by D_2 to form hydrido carbonyl complexes while preserving the total ligand count corresponding to the Wade cluster sizes.



1. INTRODUCTION

The chemical interaction of carbon monoxide with transition metals is a fundamental topic in organometallic chemistry and of utmost importance to applications like, for example, catalysis.¹ Already in 1923, Sidgwick introduced the effective atomic number (EAN) rule, which predicts and explains the pronounced stabilities of mono- and multinuclear transition-metal carbonyl clusters with distinct numbers of carbonyl ligands.^{2,3} Later, Wade and Mingos postulated rules that related the electronic structure of the carbonyl clusters to particular geometric structures.^{4,5} Many of these Wade-type carbonyl clusters have been selectively synthesized in the condensed phase and successfully utilized as homogeneous and heterogeneous catalysts.⁶

In contrast, gas-phase reactions of free mass-selected transition-metal clusters with carbon monoxide yielded distributions of carbonyl complex sizes with the CO saturation limit indicating the Wade-type complexes in some cases (see, e.g., refs 7–11).

In this contribution, we report on the gas-phase reaction of size-selected Ru_n^+ ($n = 4-6$) clusters with CO in an ion trap under multicollision conditions. Most notably, this approach results in the exclusive synthesis of only one specific ruthenium carbonyl complex for each cluster size. The particular stability of all of these selectively formed gas-phase Ru carbonyl clusters can be inferred from their “closed-shell” electronic structure, which is obtained by applying the EAN rule for each apex atom in the cluster. Complementary first-principles density functional theory (DFT) calculations provide detailed structural characterization in accordance with the geometries predicted by Wade's electron counting rules.

In the case of Ru_4^+ and Ru_6^+ , CO molecules can be partially replaced by D_2 when CO and D_2 are both present in the ion trap. The resulting hydrido carbonyl complexes always exhibit the same total ligand count, corresponding to the Wade cluster sizes.

2. EXPERIMENTAL AND COMPUTATIONAL METHODS

A. Experimental Method. Gas-phase ruthenium clusters are prepared by sputtering of Ru metal targets with high-energy Xe ion beams. The produced clusters are mass-selected in a first quadrupole mass filter and are subsequently guided into a home-built radio frequency octopole ion trap, which is prefilled with 2 Pa of helium buffer gas and a small fraction of reactant gases CO and CO/D_2 . The pressure conditions ensure temperature equilibration of the clusters within a few milliseconds prior to the reaction, which occurs on a considerably longer time scale of 0.1 s to several seconds.¹² During the experiments, the ion trap is held at room temperature, and after a chosen reaction time, that is, storage time inside of the ion trap, all ions, products, and intermediates are extracted and mass-analyzed by a second quadrupole mass filter and finally detected with a channeltron electron amplifier. Throughout the presented experiments, deuterium instead of hydrogen was employed to facilitate the mass assignment.

B. Theoretical Method. The structural properties of the ruthenium cluster cations were studied using DFT with the PBE functional¹³ and RI approximation.¹⁴ For the Ru atoms

Special Issue: A. W. Castleman, Jr. Festschrift

Received: February 4, 2014

Revised: February 7, 2014

Published: February 26, 2014

the triple- ζ -valence-plus-polarization (TZVP) atomic basis sets combined with the Stuttgart group relativistic effective core potentials (ECPs) were employed.¹⁵ For the C, O, and H atoms, the TZVP basis sets were used.¹⁶ Our previous studies of the reactivity of transition-metal clusters and oxide clusters have shown that such a combination of hybrid density functionals with triple- ζ -quality basis sets allows the accurate prediction of the reaction energetics and mechanisms.^{17–19} All structures presented were fully optimized using gradient minimization techniques, and stationary points were characterized as minima or transition states by calculating the vibrational frequencies.

3. RESULTS AND DISCUSSION

Figure 1 displays ion mass distributions obtained after the reaction of Ru_4^+ , Ru_5^+ , and Ru_6^+ with CO. All three cluster sizes

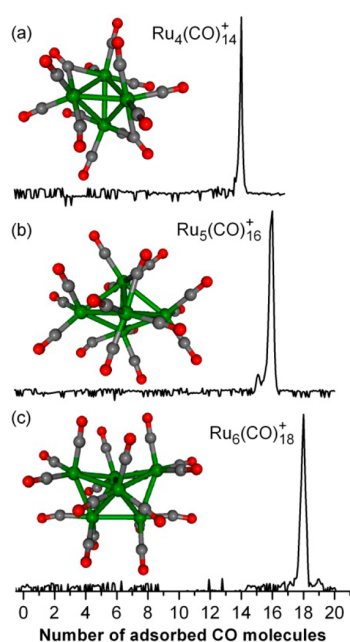


Figure 1. Product mass spectra obtained after the gas-phase reaction of (a) Ru_4^+ , (b) Ru_5^+ , and (c) Ru_6^+ with CO for 0.1 s. Ru_4^+ : $p(\text{CO}) = 0.002$ Pa; $p(\text{He}) = 1.96$ Pa. Ru_5^+ : $p(\text{CO}) = 0.007$ Pa; $p(\text{He}) = 1.98$ Pa. Ru_6^+ : $p(\text{CO}) = 0.002$ Pa; $p(\text{He}) = 1.96$ Pa. The small peak corresponding to $\text{Ru}_5(\text{CO})_{15}^+$ in (b) disappears at slightly longer reaction times. To enhance the comparability for the different metal cluster sizes, the mass spectra show the linear ion intensity as a function of the number of CO molecules adsorbed on the respective metal cluster. The corresponding calculated structures of the products are shown as insets (Ru, C, and O atoms are indicated by green, gray, and red spheres, respectively).

react very fast with CO in our ion trap (faster than the time resolution of our setup) and form exclusively one single product each ($\text{Ru}_4(\text{CO})_{14}^+$, $\text{Ru}_5(\text{CO})_{16}^+$, and $\text{Ru}_6(\text{CO})_{18}^+$). No other products have been detected at longer reaction times or different partial pressure conditions in the ion trap. This observation strongly suggests the particular stability of these carbonyl complexes, which can be explained by the fact that each of these clusters has a “closed-shell” valence electron (VE) count of 18 for each metal atom center, in accordance with the EAN rule.^{2,3} For $\text{Ru}_4(\text{CO})_{14}^+$, for example, each Ru atom contributes eight VEs, each of the six metal cluster single bonds

in a tetrahedral structure two VEs, and each CO molecule bond two VEs. This yields 72 VEs in total, 18 VEs for every Ru atom center. Please note that the positive charge of the complexes is neglected in this simple electron counting procedure. Hence, due to the positive charge, the ruthenium cluster carbonyls never exactly obey the EAN rule but are always one electron deficient. This interesting observation will be discussed further below in the context of hydrido carbonyl clusters.

Wade’s rules⁴ can now be applied to deduce the geometries of all of these (almost) electronically closed-shell cluster ions. For this purpose, the metal VEs and the respective number of CO ligands are counted followed by a reduction to the corresponding boron hydride fragments via the isolobal analogy (i.e., a $\text{Ru}(\text{CO})_3$ unit corresponds to BH).^{6,20} According to Wade’s original rules,⁴ $\text{Ru}_4(\text{CO})_{14}^+$ thus exhibits a nido-type (tetrahedral) cluster geometry, $\text{Ru}_5(\text{CO})_{16}^+$ exhibits closo-type (trigonal bipyramidal) structure, and $\text{Ru}_6(\text{CO})_{18}^+$ represents a hypercloso-Wade-type (bicapped tetrahedral) cluster. These predicted skeletal Wade structures are in perfect agreement with the results of our DFT calculations depicted in Figure 1 (for higher-energy isomers, see Figure S1 of the Supporting Information).

The optimized structures show furthermore that in $\text{Ru}_4(\text{CO})_{14}^+$, each Ru atom of the tetrahedral Ru_4^+ metal core has three CO ligands bound via the carbon atom in a μ_1 -atop geometry. In addition, two CO molecules are arranged each in a μ_2 -bridging position on opposite edges of the Ru_4^+ tetrahedron. Similarly, three CO molecules are bound in a μ_1 -atop geometry to each of the five Ru atoms of the Ru_5^+ core, while one additional CO molecule bridges two of the four-fold-coordinated Ru atoms. In $\text{Ru}_6(\text{CO})_{18}^+$, each Ru atom interacts with three atop-bound CO molecules, and no bridging by CO molecules occur. The calculated average CO binding energies in these three Ru carbonyl cluster amount to 1.89, 1.83, and 1.79 eV, respectively. The CO bonds are extended in average when bound to the Ru clusters (1.151 Å in $\text{Ru}_4\text{CO}_{14}^+$; 1.151 Å in $\text{Ru}_5\text{CO}_{16}^+$; 1.149 Å in $\text{Ru}_6\text{CO}_{18}^+$) compared to free CO (1.136 Å). Structural data and vibrational frequencies are provided in the Supporting Information.

Interestingly, the condensed-phase synthesis of the corresponding neutral tetra- and pentanuclear ruthenium carbonyl clusters $\text{Ru}_4(\text{CO})_{14}$ and $\text{Ru}_5(\text{CO})_{16}$ with an electronically closed-shell structure has not been reported yet, but the isoelectronic $\text{Os}_4(\text{CO})_{14}$ ²¹ and $\text{Os}_5(\text{CO})_{16}$ ²² have been prepared. Similarly, neutral $\text{Ru}_6(\text{CO})_{18}$ has not been synthesized; however, the dianion²³ $\text{Ru}_6(\text{CO})_{18}^{2-}$ represents a well-characterized ruthenium carbonyl complex that has even been functionalized as catalytic material via anchoring in zeolites²⁴ and on oxide supports.^{25,26} It should be noted that $\text{Ru}_6(\text{CO})_{18}^{2-}$ has an octahedral structure due to the additional two electrons.²³

Exposing the ruthenium tetramer Ru_4^+ to a 1:11 CO/ D_2 mixture changes the product distribution completely, as is apparent from the mass spectrum shown in Figure 2. At these partial pressure conditions, up to three CO ligands of the carbonyl complex $\text{Ru}_4(\text{CO})_{14}^+$ can be replaced by deuterium, yielding the hydrido carbonyl clusters $\text{D}_7\text{Ru}_4(\text{CO})_{11}^+$ and $\text{D}_5\text{Ru}_4(\text{CO})_{12}^+$. The relative stability of $\text{D}_7\text{Ru}_4(\text{CO})_{11}^+ + \text{CO}$ and $\text{D}_5\text{Ru}_4(\text{CO})_{12}^+ + \text{H}_2$ amounts to 0.5 eV in favor of the latter. This gives a direct explanation for the relative intensity of these two products. At lower D_2 partial pressures, the ligand exchange is less pronounced. Most notably, the observed product stoichiometries reveal an odd number of D atoms in

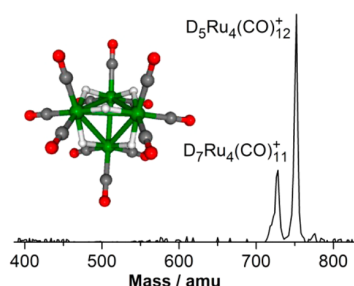


Figure 2. Product mass spectrum (intensity in arbitrary units) obtained after the gas-phase reaction of Ru_4^+ with CO and D_2 for 0.1 s ($p(\text{CO}) = 0.008$ Pa; $p(\text{D}_2) = 0.090$ Pa; $p(\text{He}) = 1.88$ Pa). The corresponding calculated DFT structure of $\text{H}_3\text{Ru}_4(\text{CO})_{12}^+$ is shown as an inset (Ru, C, O, and H atoms are indicated by green, gray, red, and white spheres, respectively).

these product complexes, which indicates that not only CO molecules have been exchanged by D_2 but that also one additional D atom is adsorbed on the cluster. As discussed above, the $\text{Ru}_4(\text{CO})_{14}^+$ has a one-electron deficiency in order to fully obey the EAN rule. On the basis of the assumption that each D atom donates one electron to the complex,⁶ this additional D atom now balances the positive charge, which leads to a perfect closed electronic shell configuration.

Figure 2 also shows the calculated structure corresponding to the experimentally observed hydrido carbonyl cluster $\text{H}_3\text{Ru}_4(\text{CO})_{12}^+$, which reveals that the hydrogen (D_2 in the experiment) molecules are adsorbed dissociatively with each of the altogether five hydrogen atoms μ_2 -bridging two neighboring Ru atoms resulting in a C_{2v} symmetry for $\text{H}_3\text{Ru}_4(\text{CO})_{12}^+$. Due to the fact that two hydrogen atoms provide as many electrons as one CO molecule, the tetrahedral geometry of the Ru_4 cluster core is maintained upon CO substitution by H_2 . Isomers containing also terminal or interstitial hydrogen atoms are found to be considerably higher in energy (cf. Figure S2 of the Supporting Information).

In the condensed phase, the tetranuclear hydrido carbonyl clusters $\text{H}_2\text{Ru}_4(\text{CO})_{13}$,^{27,28} $\text{H}_3\text{Ru}_4(\text{CO})_{12}^-$,^{29,30} and $\text{H}_4\text{Ru}_4(\text{CO})_{12}$ ^{28,31,32} have been synthesized and structurally characterized. Also, the gas-phase reactivity of $\text{H}_3\text{Ru}_4(\text{CO})_{12}^-$ has been investigated recently.³³ All of these complexes are isoelectronic to $\text{H}_3\text{Ru}_4(\text{CO})_{12}^+$. The difference in the number of hydrogen atoms of these condensed-phase complexes and our gas-phase analogue is caused by the positive charge of the Ru_4^+ metal core, which is balanced by an additional fifth deuterium atom. However, in agreement with our optimized DFT structures, the metal cores of all of these complexes exhibit a tetrahedral structure, and hydrogen has also been found to be adsorbed dissociatively on the edges of the Ru_4 tetrahedrons of these complexes in μ_2 -bridging positions.^{28,31,32}

Interestingly, in our experiments, no pentanuclear ruthenium hydrido carbonyl clusters were detected. However, the reaction of Ru_6^+ with a CO/ D_2 mixture also results in an exchange of carbon monoxide ligands by an equal number of D_2 units to yield hexanuclear hydrido carbonyl clusters $\text{D}_{2m}\text{Ru}_6(\text{CO})_{18-m}^+$ ($m = 1, 2$). Yet, no additional single D atom adsorption onto the Ru_6^+ complexes could be identified so far.

In the condensed phase, the hydrido carbonyl cluster $\text{HRu}_6(\text{CO})_{18}$ has been synthesized, and X-ray diffraction as well as infrared spectroscopic experiments revealed an octahedral metal core structure with an interstitial H

atom.^{34–37} As discussed above, the positive charge of $\text{Ru}_6(\text{CO})_{18}^+$ leads to a VE count that corresponds to a bicapped tetrahedral Wade motif of the cluster core geometry instead of an octahedral. The bicapped tetrahedral Wade structure is preserved upon CO to D_2 exchange because the number of electrons does not change. Thus, the reason why no $\text{D}_{2m+1}\text{Ru}_6(\text{CO})_{18-m}^+$ complexes have been observed may be attributed to the bicapped tetrahedral geometry of Ru_6^+ , which hampers interstitial H ligation and stabilization of the closed electronic shell configuration.

4. CONCLUSION

In summary, Wade-type ruthenium carbonyl and ruthenium hydrido carbonyl clusters were for the first time selectively synthesized in the gas phase. The exclusive formation of distinct cluster carbonyl sizes is in agreement with the stabilities predicted by simple electron counting rules, and the geometric structure of the metal cores can be determined on the basis of Wade's rules. However, full insight into the structure of the ruthenium carbonyl complexes as well as the hydrido carbonyl clusters is provided by detailed ab initio calculations.

Condensed-phase analogues $\text{H}_4\text{Ru}_4(\text{CO})_{12}$ and $\text{Ru}_6(\text{CO})_{18}^{2-}$ have been previously shown to be catalytically active in several basic chemical transformations like, for example, the hydrogenation of carbon monoxide²⁵ or of olefins³⁸ and the homologation of methane.²⁴ Work is in progress in our laboratories to elucidate whether such reactions might also be mediated by the analogous gas-phase complexes.

■ ASSOCIATED CONTENT

Supporting Information

DFT structures of higher-energy isomers as well as vibrational frequencies of the shown complexes. This material is available free of charge via the Internet at <http://pubs.acs.org>.

■ AUTHOR INFORMATION

Corresponding Authors

*E-mail: thorsten.bernhardt@uni-ulm.de (T.M.B.).

*E-mail: vbk@chemie.hu-berlin.de (V.B.-K.).

Notes

The authors declare no competing financial interest.

■ ACKNOWLEDGMENTS

This research was supported by the DAAD and the FCI. S.M.L. is grateful to the ESF Baden-Württemberg for a Margarete von Wrangell fellowship.

■ REFERENCES

- (1) Elschenbroich, C.; Salzer, A. *Organometallics*, 3rd. ed. ed.; Wiley-VCH: Wiesbaden, 2005.
- (2) Sidgwick, N. V. The Nature of the Non-Polar Link. *Trans. Faraday Soc.* **1923**, *19*, 469–475.
- (3) Sidgwick, N. V.; Bailey, R. M. Structures of the Metallic Carbonyls and Nitrosyls. *Proc. R. Soc. London, Ser. A* **1934**, *144*, 521–537.
- (4) Wade, K. The Structural Significance of the Number of Skeletal Bonding Electron-Pairs in the Carboranes, the Higher Boranes and Borane Anions, and Various Transition-Metal Carbonyl Cluster Compounds. *Chem. Commun.* **1971**, 792–793.
- (5) Mingos, D. M. P. A General Theory for Cluster and Ring Compounds of the Main Group and Transition Elements. *Nat. Phys. Sci.* **1972**, *236*, 99–102.

- (6) Dyson, P. J.; McIndoe, J. S. *Transition Metal Carbonyl Cluster Chemistry*; Gordon and Breach Science Publishers: Amsterdam, The Netherlands, 2000.
- (7) Guo, B. C.; Kerns, K. P.; Castleman, A. W., Jr. Chemistry and Kinetics of Size Selected Cobalt Cluster Cations at Thermal Energies. I. Reactions with CO. *J. Chem. Phys.* **1992**, *96*, 8177–8186.
- (8) Ervin, K. M. Metal–Ligand Interactions: Gas-Phase Transition Metal Cluster Carbonyls. *Int. Rev. Phys. Chem.* **2001**, *20*, 127–164.
- (9) Fayet, P.; McClinchey, M. J.; Wöste, L. H. Bonding Capabilities of Nickel Cluster Ions: Synthetic Chemistry in a Molecular Beam. *J. Am. Chem. Soc.* **1987**, *109*, 1733–1738.
- (10) Popolan, D. M.; Nößler, M.; Mitrić, R.; Bernhardt, T. M.; Bonačić-Koutecký, V. Composition Dependent Adsorption of Multiple CO Molecules on Binary Silver–Gold Clusters Ag_nAu_m^+ ($n + m = 5$): Theory and Experiment. *Phys. Chem. Chem. Phys.* **2010**, *12*, 7865–7873.
- (11) Lang, S. M.; Schnabel, T.; Bernhardt, T. M. Reactions of Carbon Monoxide with Free Palladium Oxide Clusters: Strongly Size Dependent Competition between Adsorption and Combustion. *Phys. Chem. Chem. Phys.* **2012**, *14*, 9364–9370.
- (12) Bernhardt, T. M. Gas-Phase Kinetics and Catalytic Reactions of Small Silver and Gold Clusters. *Int. J. Mass Spectrom.* **2005**, *243*, 1–29.
- (13) Perdew, J. P.; Burke, K.; Ernzerhof, M. Generalized Gradient Approximation Made Simple. *Phys. Rev. Lett.* **1996**, *77*, 3865–3868.
- (14) Eichkorn, K.; Treutler, O.; Öhm, H.; Häser, M.; Ahlrichs, R. Auxiliary Basis Sets to Approximate Coulomb Potentials. *Chem. Phys. Lett.* **1995**, *242*, 652–660.
- (15) Andrea, D.; Haeussermann, U.; Dolg, M.; Stoll, H.; Preuss, H. Energy-Adjusted Ab Initio Pseudopotentials for the Second and Third Row Transition Elements. *Theor. Chim. Acta* **1990**, *77*, 123–141.
- (16) Schäfer, A.; Huber, H.; Ahlrichs, R. Fully Optimized Contracted Gaussian Basis Sets of Triple Zeta Valence Quality for Atoms Li to Kr. *J. Chem. Phys.* **1994**, *100*, 5829–5835.
- (17) Johnson, G. E.; Mitrić, R.; Bonačić-Koutecký, V.; Castleman, A. W., Jr. Clusters as Model Systems for Investigating Nanoscale Oxidation Catalysis. *Chem. Phys. Lett.* **2009**, *475*, 1–9.
- (18) Justes, D. R.; Mitrić, R.; Moore, N. A.; Bonačić-Koutecký, V.; Castleman, A. W., Jr. Theoretical and Experimental Consideration of the Reactions between V_xO_y^+ and Ethylene. *J. Am. Chem. Soc.* **2003**, *125*, 6289–6299.
- (19) Johnson, G. E.; Mitrić, R.; Nössler, M.; Tyo, E. C.; Bonačić-Koutecký, V.; Castleman, A. W., Jr. Influence of Charge State on Catalytic Oxidation Reactions at Metal Oxide Clusters Containing Radical Oxygen Centers. *J. Am. Chem. Soc.* **2009**, *131*, 5460–5470.
- (20) Hoffmann, R. Nobelvortrag. *Angew. Chem., Int. Ed.* **1982**, *21*, 711–724.
- (21) Johnston, V. J.; Einstein, F. W. B.; Pomeroy, R. K. The New Binary Carbonyl $\text{Os}_4(\text{CO})_{14}$: An Example of Carbonyl Exchange on the Infrared Time Scale? *Organometallics* **1988**, *7*, 1867–1869.
- (22) Eady, C. R.; Johnson, B. F. G.; Lewis, J. Products from the Pyrolysis of $\text{Ru}_3(\text{CO})_{12}$ and $\text{Os}_3(\text{CO})_{12}$. *J. Organomet. Chem.* **1972**, *37*, C39–C40.
- (23) Jackson, P. F.; Johnson, B. F. G.; Lewis, J.; McPartlin, M.; Nelson, W. J. H. $\text{H}_2\text{Ru}_6(\text{CO})_{18}$, $[\text{HRu}_6(\text{CO})_{18}]^-$, and $[\text{Ru}_6(\text{CO})_{18}]^{2-}$: A Simple High Yield Route to These Clusters and the X-ray Structure of $[\text{Ph}_3\text{MeP}]_2[\text{Ru}_6(\text{CO})_{18}]$. *J. Chem. Soc., Chem. Commun.* **1979**, 735–736.
- (24) Shen, J. G. C.; Liu, A. M.; Tanaka, T.; Ichikawa, M. Intrazeolite Anchoring of Ruthenium Carbonyl Clusters: Synthesis, Characterization, and Their Catalytic Performance. *J. Phys. Chem. B* **1998**, *102*, 7782–7792.
- (25) Izumi, Y.; Chihara, T.; Yamazaki, H.; Iwasawa, Y. Selective Synthesis of Oxygenates in the CO– H_2 Reaction on Supported Ruthenium Carbido-Cluster Catalysts. *J. Chem. Soc., Chem. Commun.* **1992**, 1395–1396.
- (26) Minato, T.; Izumi, Y.; Aika, K.-I.; Ishiguro, A.; Nakajima, T.; Wakatsuki, Y. Nitric Oxide Reduction by Carbon Monoxide over Supported Hexaruthenium Cluster Catalysts. I. The Active Site Structure That Depends on Supporting Metal Oxide and Catalytic Reaction Conditions. *J. Phys. Chem. B* **2003**, *107*, 9022–9028.
- (27) Yawney, D. B. W.; Doedens, R. J. The Crystal and Molecular Structure of the Tetranuclear Ruthenium Carbonyl Hydride $\alpha\text{-H}_2\text{Ru}_4(\text{CO})_{13}$. *Inorg. Chem.* **1972**, *11*, 838–844.
- (28) Johnson, B. F. G.; Johnston, R. D.; Lewis, J.; Robinson, B. H.; Wilkinson, G. Chemistry of Polynuclear Compounds. Part XII. Polynuclear Hydrido-Carbonyls of Ruthenium. *J. Chem. Soc. A* **1968**, 2856–2859.
- (29) Koepke, J. W.; Johnson, J. R.; Knox, S. A. R.; Kaesz, H. D. Synthesis and Characterization of Tetrphenylarsonium Tri- μ -hydrido-dodecacarbonyltetraruthene. Observation of Structural Isomers and Their Rapid Interconversion in a Hydrido–Metal Cluster Anion. *J. Am. Chem. Soc.* **1975**, *97*, 3947–3952.
- (30) Jackson, P. F.; Johnson, B. F. G.; Lewis, J. $[\text{H}_3\text{Ru}_4(\text{CO})_{12}]^-$: The X-ray Crystallographic Determination of Two Structural Isomers. *J. Chem. Soc., Chem. Commun.* **1978**, 920–921.
- (31) Knox, S. A. R.; Kaesz, H. D. Intramolecular Tautomerism of Hydrogen in Hydrido Carbonylmetal Clusters. *J. Am. Chem. Soc.* **1971**, *93*, 4594–4596.
- (32) Wilson, R. D.; Wu, S. M.; Love, R. A.; Bau, R. Molecular Structures of $\text{H}_4\text{Ru}_4(\text{CO})_{12}$ and $\text{H}_4\text{Ru}_4(\text{CO})_{10}(\text{PPh}_3)_2$. *Inorg. Chem.* **1978**, *17*, 1271–1280.
- (33) Henderson, M. A.; Kwok, S.; McIndoe, J. S. Gas-Phase Reactivity of Ruthenium Carbonyl Cluster Anions. *J. Am. Soc. Mass Spectrom.* **2009**, *20*, 658–666.
- (34) Oxtun, I. A.; Kettle, S. F. A. Metal–Hydrogen Stretching Frequencies in Metal Cluster Complexes. The First Reported ν_{MH} for an Interstitial Hydrogen Ligand. *J. Chem. Soc., Chem. Commun.* **1979**, 687–688.
- (35) Eady, C. R.; Johnson, B. F. G.; Lewis, J.; Malatesta, M. C.; Machin, P.; McPartlin, M. $[\text{HRu}_6(\text{CO})_{18}]^-$: A Ruthenium Anion Having an Interstitial H-Ligand. X-ray Crystal Structures of Two Modifications. *J. Chem. Soc., Chem. Commun.* **1976**, 945–946.
- (36) Eady, C. R.; Jackson, P. F.; Johnson, B. F. G.; Lewis, J.; Malatesta, M. C.; McPartlin, M.; Nelson, W. J. H. Improved Syntheses of the Hexanuclear Clusters $[\text{Ru}_6(\text{CO})_{18}]^{2-}$, $[\text{HRu}_6(\text{CO})_{18}]^-$, and $\text{H}_2\text{Ru}_6(\text{CO})_{18}$. The X-ray Analysis of $[\text{HRu}_6(\text{CO})_{18}]^-$, a Polynuclear Carbonyl Containing an Interstitial Hydrogen Ligand. *J. Chem. Soc., Dalton Trans.* **1980**, 383–392.
- (37) Jackson, P. F.; Johnson, B. F. G.; Lewis, J.; Raithby, P. R.; McPartlin, M.; Nelson, W. J. H.; Rouse, K. D.; Allibon, J.; Mason, S. A. Direct Location of the Interstitial Hydride Ligand in $[\text{HRu}_6(\text{CO})_{18}]^-$ by Both X-ray and Neutron Analyses of $[\text{Ph}_4\text{As}][\text{HRu}_6(\text{CO})_{18}]$. *J. Chem. Soc., Chem. Commun.* **1980**, 295–297.
- (38) Doi, Y.; Koshizuka, K.; Keii, T. Metal Cluster Catalysis. Kinetics and Mechanism of the Catalytic Hydrogenation of Ethylene by the Ruthenium Cluster Complex $\text{H}_4\text{Ru}_4(\text{CO})_{12}$. *Inorg. Chem.* **1982**, *21*, 2732–2736.

2 The Origin of the Selectivity and Activity of Ruthenium-Cluster Catalysts for Fuel-Cell Feed-Gas Purification: A Gas-Phase Approach

The Origin of the Selectivity and Activity of Ruthenium-Cluster Catalysts for Fuel-Cell Feed-Gas Purification: A Gas-Phase Approach**

Sandra M. Lang, Thorsten M. Bernhardt,* Marjan Krstić, and Vlasta Bonačić-Koutecký*

Abstract: Gas-phase ruthenium clusters Ru_n^+ ($n=2-6$) are employed as model systems to discover the origin of the outstanding performance of supported sub-nanometer ruthenium particles in the catalytic CO methanation reaction with relevance to the hydrogen feed-gas purification for advanced fuel-cell applications. Using ion-trap mass spectrometry in conjunction with first-principles density functional theory calculations three fundamental properties of these clusters are identified which determine the selectivity and catalytic activity: high reactivity toward CO in contrast to inertness in the reaction with CO_2 ; promotion of cooperatively enhanced H_2 coadsorption and dissociation on pre-formed ruthenium carbonyl clusters, that is, no CO poisoning occurs; and the presence of Ru-atom sites with a low number of metal-metal bonds, which are particularly active for H_2 coadsorption and activation. Furthermore, comprehensive theoretical investigations provide mechanistic insight into the CO methanation reaction and discover a reaction route involving the formation of a formyl-type intermediate.

The electrochemical energy conversion is one of the key technologies for the 21st century. In particular the direct conversion of chemical into electrical energy has received utmost attention because of its potential for a “green” environmentally compatible technology. This conversion is realized in fuel cells, in which the energy released by the reaction of hydrogen and oxygen through an electrocatalytic process is directly converted into electricity.^[1,2]

With respect to applications in transportation and decentralized small-scale appliances in particular the low-temperature proton-exchange membrane fuel cell (PEMFC) has gained increasing importance.^[2] Often, the hydrogen feed gas for PEMFCs is generated by reformation of fossil fuels^[3] (e.g.,

methane) which, however, results in the formation of CO as an undesired byproduct. Subsequent energy conversion in the PEMFC is catalyzed by metal particles (often platinum or platinum alloys) which are poisoned by even small amounts of CO. Thus, the development of cost-efficient techniques to improve the feed-gas quality (minimization of the CO fraction) represents an important research field.

One promising procedure for CO removal is the catalytic reaction with hydrogen to form CH_4 and water (methanation). However, feed gases usually also contain about 10 %^[4] of CO_2 which can react catalytically with H_2 to form CH_4 (methanation) or CO (reverse water-gas shift reaction). This process either leads to a non-tolerable loss of hydrogen or to the production of additional CO. Thus, selective CO methanation to minimize CO poisoning of the fuel cell anode is essential for the future viability of the PEMFCs.^[5] For this purpose oxide-supported ruthenium particle catalysts have been shown to be very promising materials.^[6] The high activity and selectivity of these catalysts was traced in particular to the presence of very small Ru clusters (<1 nm).^[7] However, the reason why small ruthenium clusters are active and selective for fuel-cell feed-gas purification remains an open question.

Herein, gas-phase ruthenium clusters Ru_n^+ ($n=2-6$) are employed as model systems to discover the origin of the outstanding performance of supported sub-nanometer ruthenium particles in the catalytic CO methanation reaction. Positively charged clusters have been chosen because previous experiments with supported clusters could show a partial positive charging of Ru particles on oxide supports.^[6,8] Using ion-trap mass spectrometry in conjunction with first-principles density functional theory (DFT) calculations three fundamental properties of these clusters are identified which determine the selectivity and catalytic activity: a) high reactivity toward CO in contrast to inertness in the reaction with CO_2 ; b) promotion of cooperatively enhanced H_2 coadsorption and dissociation on pre-formed ruthenium carbonyl clusters, that is, no CO poisoning occurs; and c) the presence of Ru-atom sites forming a low number of metal-metal bonds, which are particularly active for H_2 coadsorption and activation. Furthermore, comprehensive theoretical investigations provide mechanistic insight into the CO methanation reaction and discover a reaction route involving the formation of a formyl-type intermediate.

In the following we will first address the origin of the CO/ CO_2 selectivity: In a first series of experiments the reaction of Ru_n^+ ($n=2-6$) with several typical components of a fuel-cell feed gas,^[4,9] such as CO_2 , CO, H_2 , CH_4 , and N_2 have been investigated independently. The clusters were found to

[*] Dr. S. M. Lang, Prof. Dr. T. M. Bernhardt
Institute of Surface Chemistry and Catalysis, University of Ulm
Albert-Einstein-Allee 47, 89069 Ulm (Germany)
E-mail: thorsten.bernhardt@uni-ulm.de

M. Krstić, Prof. Dr. V. Bonačić-Koutecký
Interdisciplinary Center for Advanced Sciences and Technology
(ICAST), University of Split
Meštrovićevo Šetalište 45, 21000 Split (Croatia)

Prof. Dr. V. Bonačić-Koutecký
Chemistry Department, Humboldt University of Berlin
Brook-Taylor-Strasse 2, 12489 Berlin (Germany)
E-mail: vbk@chemie.hu-berlin.de

[**] This work was supported by the DAAD and the FCI. S.M.L. is grateful to the ESF Baden-Württemberg for a Margarete von Wrangell fellowship. We thank Sandra Förtig for experimental assistance and Prof. R. Jürgen Behm for stimulating discussions.

strongly react with CO, while being completely non-reactive toward CO₂ in agreement with the calculated CO and CO₂ binding energies (e.g., $E_b(\text{Ru}_4^+-\text{CO}) = 1.76$ eV vs. $E_b(\text{Ru}_4^+-\text{CO}_2) = 0.45$ eV). This already explains why small ruthenium clusters are highly selective in catalyzing the methanation of CO whilst preventing concurrent unwanted hydrogen consuming CO₂ conversion.

In fact, the strong binding of CO to ruthenium results in the formation of ruthenium carbonyl complexes as apparent from the product mass spectra obtained after the reaction of Ru_4^+ and Ru_6^+ with CO shown in Figure 1 a,b. These reactions

count for each metal atom center.^[10,12] The geometries of these closed-shell configurations were revealed by first principles DFT calculations and are depicted in Figure 1 a,b.^[10]

All the ruthenium clusters were non-reactive with nitrogen and methane, which are both present at high abundance in the fuel-cell feed gas (only Ru_2^+ yielded Ru_2CD_2^+). Furthermore, in the presence of hydrogen (D_2) Ru_4^+ and Ru_6^+ were the only clusters found to yield reaction products (Ru_4D_4^+ and Ru_6D_2^+ , respectively). Overall, the exceptional reactive behavior of the small Ru clusters toward CO (in contrast to CO₂, which was found not to react under any reaction conditions) and the formation of the stable carbonyl complexes provide the basis for the understanding of the observed CO methanation selectivity and the pertinent size effect.

Now we will turn to the origin of the activity of the small Ru clusters focusing on cooperative coadsorption effects and adsorption site dependent hydrogen dissociation: In a second series of gas-phase experiments the coadsorption of CO and D₂ has been investigated. If a mixture of CO and D₂ is introduced into the ion trap, Ru_4^+ and Ru_6^+ form complexes containing both molecules as can be seen from the mass spectra in Figure 1 c,d. This finding is particularly important since it demonstrates that in spite of the high calculated CO binding energies ($E_b(\text{Ru}_4^+-\text{CO}) = 1.76$ eV vs. $E_b(\text{Ru}_4^+-\text{H}_2) = 0.66$ eV and $E_b(\text{Ru}_6^+-\text{CO}) = 1.69$ eV vs. $E_b(\text{Ru}_6^+-\text{H}_2) = 0.59$ eV) the coadsorption of hydrogen is possible and CO poisoning does not occur.

On the contrary, CO even actively promotes the hydrogen coadsorption because the observed complex $\text{Ru}_4(\text{CO})_{11}\text{D}_7^+$ (Figure 1 c) contains seven hydrogen (deuterium) atoms while with only hydrogen present in the ion trap at most four D ligands are adsorbed. This cooperative coadsorption is even more pronounced for Ru_6^+ which coadsorbs up to eight D atoms ($\text{Ru}_6(\text{CO})_{14}\text{D}_8^+$ in Figure 1 d). In contrast, the adsorption of only two D atoms is observed in the presence of exclusively hydrogen in the ion trap.

Even more insight into the origin of this cooperative effect of CO pre-adsorption on the subsequent D₂ coadsorption is provided by our theoretical results. From the calculated structures shown in Figure 1 c,d it is clear that hydrogen is dissociatively bound in the hydrido carbonyl complexes. In addition, the dissociation of a single hydrogen molecule has been calculated to be 0.2 eV more exothermic in the presence of a CO molecule adsorbed on the same Ru center than without pre-adsorbed CO. This result illustrates that the presence of the pre-adsorbed CO supports the hydrogen dissociation which is the essential prerequisite for the subsequent methanation reaction via formyl formation.

Figure 1 e illustrates that these cooperative effects prevail at high CO partial pressures. This graph displays the detected hydrido carbonyl complex compositions as a function of the CO to D₂ partial-pressure ratio. Even at the highest investigated CO contents (28 %) the coadsorption of hydrogen is still observed (technically employed fuel-cell feed gases contain only up to about 8 mol % of CO^[4]). All the observed hydrido carbonyl complexes exhibit the stoichiometries $\text{Ru}_4(\text{CO})_{14-m}\text{D}_{2m+1}^+$ and $\text{Ru}_6(\text{CO})_{18-m}\text{D}_{2m}^+$, respectively, in

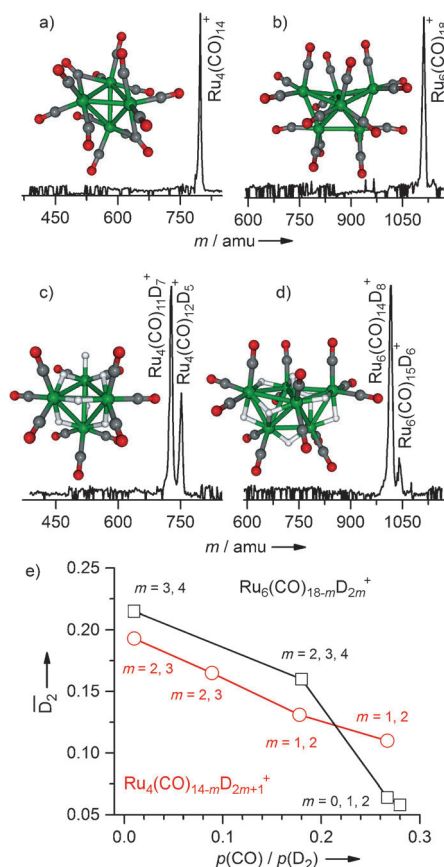


Figure 1. Product mass spectra obtained after reaction of a) Ru_4^+ and b) Ru_6^+ with CO as well of c) Ru_4^+ and d) Ru_6^+ with a 1:100 mixture of CO and D₂ for $t_R = 0.1$ s. Also displayed are the corresponding DFT structures of the most abundant products. Ru green, C gray, O red and H white spheres. e) D₂ ligand fraction \bar{D}_2 (average number of D₂ molecules normalized to the total number of ligands in all observed complexes $\text{Ru}_4(\text{CO})_{14-m}\text{D}_{2m+1}^+$ and $\text{Ru}_6(\text{CO})_{18-m}\text{D}_{2m}^+$, respectively) as a function of the CO/D₂ partial pressure ratio. Next to each data point the numbers m of the observed coadsorption products are given. The solid lines are to guide the eye.

are very fast (faster than the time resolution of the experiment which amounts to about 0.1 s) and yield only one single reaction product each.^[10] The exclusive appearance of $\text{Ru}_4(\text{CO})_{14}^+$ and $\text{Ru}_6(\text{CO})_{18}^+$ (and $\text{Ru}_5(\text{CO})_{16}^+$, not shown)^[11] in the ion-trap reaction mass spectra under all reaction conditions points toward their pronounced stability, which can be explained by a closed-shell-type 18 valence electron

which the total number of ligands remains unchanged, while the number m of coadsorbed hydrogen molecules varies with the applied CO/D₂ pressure ratio. Hence, the 18 valence electron count for each Ru atom is preserved.^[10] The odd number of D atoms in Ru₄(CO)_{14-m}D_{2m+1}⁺ can be explained by the fact that the additional D atom in this case now balances the positive charge which had been neglected above in the original valence electron count.^[10]

To further elucidate the high activity of the small ruthenium clusters, the preferred adsorption site of H₂ in the carbonyl cluster complexes was analyzed. In the tetrahedral Ru₄⁺ all the Ru atoms are equivalent and each forms three Ru–Ru bonds and our DFT studies reveal that H₂ adsorbs dissociatively on the Ru₄⁺ carbonyl cluster (Figure 1c). In contrast, the bicapped tetrahedral Ru₆⁺ cluster also contains Ru atoms involved in four or five Ru–Ru bonds as well as those bound to three other ruthenium centers. Figure 2 shows that in the energetically lowest structure of Ru₆(CO)₁₇H₂⁺ (Figure 2a) the hydrogen is bound dissociatively to a Ru atom bound to three other Ru centers. The binding of hydrogen to Ru atoms with more metal–metal bonds is considerably less favorable (Figure 2b and c).

Hence, Ru atoms with a low number of metal–metal bonds present the centers of highest activity in the first step of the methanation reaction. In terms of numbers of metal–metal bonds such a coordination environment resembles that of low-coordinate metal atoms on bulk metal surfaces. Such sites are most abundant in very small particles, thus, representing in addition to the cooperative effects the origin of the high activity of small ruthenium clusters.

Finally, we employ first-principles DFT calculations to reveal the CO methanation reaction mechanism. We first focus on the reaction of Ru₆⁺. This bare cluster exhibits a trigonal prismatic structure comprising only equivalent atoms bound to three other metal centers (cf. structure A in Figure 3), which we found to be particularly reactive above. Therefore, it serves as a good model for the reaction study in which CO and H₂ are coadsorbed at the same Ru atom of this cluster (structure B in Figure 3). Starting from this species two fundamentally different reaction pathways can be envisaged: 1) The hydration of the carbon atom and 2) the hydration of the oxygen atom of CO. The first pathway involves the formation of a formyl-type reaction intermediate and is identified herein to be the energetically most favorable mechanism (black line in Figure 3). In contrast, the second pathway proceeds by C–O bond breaking and is unfeasible because the energy barrier involved considerably exceeds the binding energies of CO and H₂, respectively (dashed line in Figure 3). Therefore only pathway (1) is considered in the following.

The dissociation of H₂ involves only a small barrier (as discussed above) and leads to structure D. The subsequent formyl (HCO) formation (structure F) proceeds across an activation barrier of 1.36 eV, which is associated with the transfer of hydrogen to the carbon atom (D→E→F), and

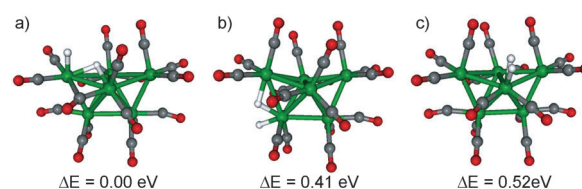


Figure 2. Optimized structures of Ru₆(CO)₁₇H₂⁺ comprising H₂ adsorbed at a Ru atom bound to a) three, b) four, and c) five other Ru atoms.

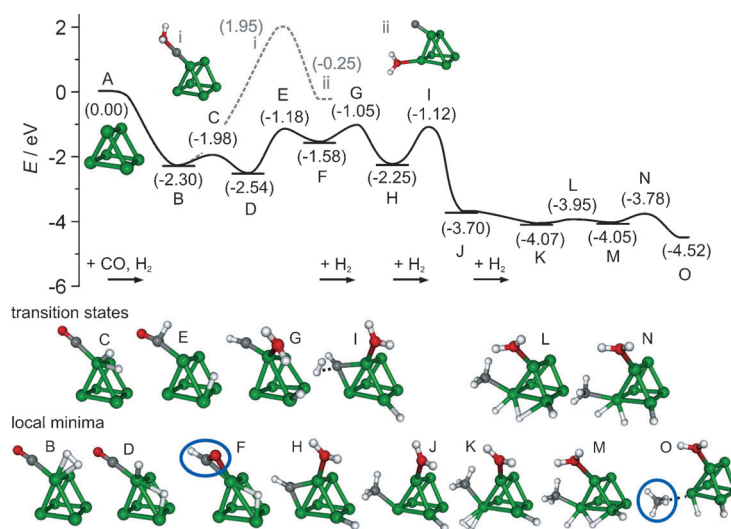


Figure 3. Calculated energy profile and corresponding structures for CO methanation by reaction of one CO with four sequentially adsorbed H₂ molecules mediated by Ru₆⁺ (doublet ground state). The solid black line labels the pathway involving the formyl-type intermediate, whereas the gray dashed line labels the first step of the alternative CO bond breaking pathway. The blue circles highlight the formyl-type intermediate in structure F and the final methane product in structure O. The numbers denote the relative energies of the local minima and transition states in eV.

overall is exothermic by 1.58 eV. Notice that for the reaction with neutral clusters the corresponding activation barrier is only slightly higher (by 0.2 eV) which illustrates that the charge of the complexes is not decisive for the formyl formation. However the slightly more favorable path with charged clusters is in very good agreement with the partial positive charge observed for the highly active Ru particles on oxide supports.^[6,8]

By adding a second hydrogen molecule, the formation of a water molecule and a methyne (CH) ligand at the same Ru atom (structure G) occurs (F→G→H). The adsorption of two more H₂ molecules is required to accomplish the formation of CH₄ which is finally liberated to yield structure O in Figure 3. The overall methanation reaction is exothermic by 4.52 eV and the calculated barriers are substantially lower than the initial energy. Furthermore, the discovery of a reaction mechanism proceeding via formation of a formyl-type intermediate is in favorable agreement with in situ IR spectroscopic studies which unambiguously identified

HCO_{ad} as the intermediate in the CO methanation mediated by Ru/ Al_2O_3 catalysts.^[13]

To build the link from the simplified model system (Ru_6^+ with one CO and four sequentially adsorbed H_2 , Figure 3) to the experimentally observed CO-rich complexes, the energy profile for the methanation reaction starting from the hydrido carbonyl complex $\text{Ru}_4(\text{CO})_{13}\text{H}_2^+$ has been calculated as shown in Figure 4. The reaction proceeds along a mechanis-

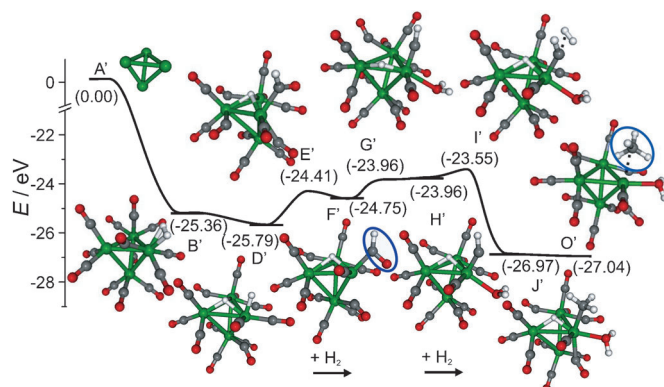


Figure 4. Calculated energy profile for CO methanation by reaction of the hydrido carbonyl $\text{Ru}_4(\text{CO})_{13}\text{H}_2^+$ (doublet ground state) with two sequentially adsorbed H_2 molecules shown together with the corresponding structures. The numbers indicate the relative energies in eV. The blue circles highlight the formyl-type intermediate in structure F' and the final methane product in structure O'.

tically and energetically very similar pathway involving a formyl-type intermediate. In particular, the main activation barrier associated with the formation of the formyl-type intermediate F' (1.38 eV) is identical to the barrier in case of Ru_6^+ (1.36 eV). In contrast, the subsequent barrier for water formation is slightly increased while, however, the barrier for methyne hydrogenation is considerably decreased in the presence of multiple CO molecules. Furthermore it is interesting to note that the increased number of CO molecules leads to the disappearance of the activation barrier for the dissociation of the first H_2 molecule and to the stabilization of the dissociated hydrogen. This observation is in agreement with the discussion above.

All of the calculated activation barriers are smaller than 1.4 eV and thus can be easily surmounted at room temperature under the reaction conditions of our ion-trap experiment as previously shown.^[14] Indeed, all the reaction products are in equilibrium in the ion-trap experiment (the intensities in Figure 1c,d do not change with increasing reaction time) which supports the occurrence of the catalytic CO methanation reaction cycle. The neutral reaction products of the catalytic cycle (CH_4 and H_2O , see Figure 3 and Figure 4) have been shown theoretically and experimentally to only very weakly bind to the Ru clusters. Thus, once formed they will be immediately released and instantly CO and H_2 adsorption will occur again closing the reaction cycle and leading to the observed equilibrium reaction products.

It is important to emphasize that the reactions in the ion trap proceed in thermal equilibrium, thus, the formyl-type

intermediate mechanism is operative. In contrast, in additional, separate non-thermal collision-induced activation experiments the C–O bond cleavage could be observed at high impact energies thus confirming the considerably higher calculated activation barrier for this mechanism as shown in Figure 3.

Herein we have presented a joint experimental and theoretical gas-phase investigation that aims at elucidating the origin of the outstanding catalytic selectivity and activity of small ruthenium clusters in the CO methanation reaction. These model studies can be considered as an important step toward a conceptual mechanistic understanding of the recently discovered excellent performance of oxide-supported Ru particle catalysts employed for fuel-cell feed-gas purification. Moreover, these conceptual insights also open a new avenue for transferring model system results to guide the design strategies for catalytic materials for fuel-cell feed-gas purification. Hence, improved supported methanation catalysts should have the following properties: a) high reactivity toward CO (precondition for CO/ CO_2 selectivity), b) yet, promoting hydrogen coadsorption, and c) clusters with Ru atom sites with few metal–metal bonds, which facilitate the methanation reaction via formyl intermediate formation. Apparently, only catalysts containing very small Ru clusters will satisfy all three of these conditions. Therefore, we wish to propose to employ intrazeolite anchored Ru carbonyl and hydridocarbonyl complexes, in particular $\text{Ru}_6(\text{CO})_{18}$ as well as $\text{H}_4\text{Ru}_4(\text{CO})_{12}$, which have been synthesized in the condensed phase previously,^[15] as a new catalytic system for fuel-cell feed-gas purification by methanation of CO. Work is in progress in our laboratories in this direction.

Experimental Section

Experimental Method: Gas-phase ruthenium clusters are prepared by sputtering of Ru metal targets with high energy Xe ion beams. The produced clusters are mass selected in a first quadrupole mass filter and are subsequently guided into the home-built radio frequency octopole ion trap, which is pre-filled with 1–2 Pa of helium buffer gas and 0.002–0.1 Pa partial pressures of the reactant molecules.^[16] During the experiments the ion trap is held at room temperature and after a chosen reaction time, that is, storage time inside the ion trap, all ions, products, and intermediates, are extracted and mass analyzed by a second quadrupole mass filter. Throughout these experiments deuterium and deuterated methane was employed to facilitate the mass assignment.

Theoretical Method: The structural properties of the ruthenium cluster cations and their reactivity were studied using DFT with the hybrid B3LYP functional.^[17] For the Ru atoms the Stuttgart group relativistic effective core potentials (ECPs)^[18] were employed together with the triple- ζ -valence-plus-polarization basis sets which was also used for the C, O, and H atoms.^[19] Our previous studies of the reactivity of transition-metal clusters and oxide clusters have shown that such a combination of hybrid density functionals with triple- ζ quality basis sets allows the accurate prediction of the reaction energetics and mechanisms.^[20] All structures presented were fully optimized using gradient minimization techniques and stationary points were characterized as minima or transition states by calculating the vibrational frequencies. Moreover, from the energy profiles based on energies obtained from DFT calculations the reaction mechanisms were deduced. To improve efficiency for the larger carbonyl complexes and their reactivity, the resolution of identity (RI)-DFT

procedure^[21] has been employed using the Perdew-Burke-Ernzerhof functional with the same ECPs and basis sets.^[22] The accuracy of this functional has been checked through comparison with the results obtained by the B3LYP functional for the $\text{Ru}_4(\text{CO})_{14}^+$ complex.

Received: November 21, 2013

Revised: February 4, 2014

Published online: May 5, 2014

Keywords: ab initio calculations · heterogeneous catalysis · CO methanation · mass spectrometry · ruthenium clusters

- [1] S. Srinivasan, R. Mosdale, P. Stevens, C. Yang, *Ann. Rev. Energy Environ.* **1999**, *24*, 281–328.
- [2] L. Carrette, K. A. Friedrich, U. Stimmig, *ChemPhysChem* **2000**, *1*, 162–193.
- [3] D. L. Trimm, Z. I. Önsan, *Catal. Rev.* **2001**, *43*, 31–84.
- [4] D. L. Trimm, *Appl. Catal. A* **2005**, *296*, 1–11.
- [5] A. Mishra, R. Prasad, *Bull. Chem. React. Eng. Catal.* **2011**, *6*, 1–14.
- [6] S. Eckle, Y. Denkwitz, R. J. Behm, *J. Catal.* **2010**, *269*, 255–268.
- [7] a) S. Tada, R. Kikuchi, K. Urasaki, S. Satokawa, *Appl. Catal. A* **2011**, *404*, 149–154; b) S. Eckle, M. Augustin, H.-G. Anfang, R. J. Behm, *Catal. Today* **2012**, *181*, 40–51.
- [8] S. Scirè, C. Crisafulli, R. Maggiore, S. Minicò, S. Galvagno, *Catal. Lett.* **1998**, *51*, 41–45.
- [9] W. Ruettinger, O. Ilinich, R. J. Farrauto, *J. Power Sources* **2003**, *118*, 61–65.
- [10] S. M. Lang, S. U. Förtig, T. M. Bernhardt, M. Krstić, V. Bonačić-Koutecký, *J. Phys. Chem. A* **2014**, DOI: 10.1021/jp501242c.
- [11] In the case of Ru_2^+ and Ru_3^+ the reaction with CO leads to fragmentation of these species (to yield Ru^+) because the Ru–Ru binding energy is smaller than the CO adsorption energy.
- [12] a) N. Sidgwick V, *Trans. Faraday Soc.* **1923**, *19*, 469–475; b) N. Sidgwick V, R. W. Bailey, *Proc. R. Soc. London Ser. A* **1934**, *144*, 521–537.
- [13] S. Eckle, H.-G. Anfang, R. J. Behm, *J. Phys. Chem. C* **2011**, *115*, 1361–1367.
- [14] S. M. Lang, T. M. Bernhardt, R. N. Barnett, U. Landman, *Angew. Chem.* **2010**, *122*, 993–996; *Angew. Chem. Int. Ed.* **2010**, *49*, 980–983.
- [15] J. G. C. Shen, A. M. Liu, T. Tanaka, M. Ichikawa, *J. Phys. Chem. B* **1998**, *102*, 7782–7792.
- [16] T. M. Bernhardt, *Int. J. Mass Spectrom.* **2005**, *243*, 1–29.
- [17] a) A. D. Becke, *Phys. Rev.* **1988**, *38*, 3098–3100; b) A. D. Becke, *J. Chem. Phys.* **1993**, *98*, 5648–5652; c) C. Lee, W. Yang, R. G. Parr, *Phys. Rev. B* **1988**, *37*, 785–789.
- [18] D. Andrae, U. Haeussermann, M. Dolg, H. Stoll, H. Preuss, *Theor. Chim. Acta* **1990**, *77*, 123–141.
- [19] A. Schäfer, H. Huber, R. Ahlrichs, *J. Chem. Phys.* **1994**, *100*, 5829–5835.
- [20] a) G. E. Johnson, R. Mitric, V. Bonacic-Koutecký, A. W. Castleman, Jr., *Chem. Phys. Lett.* **2009**, *475*, 1–9; b) D. R. Justes, R. Mitric, N. A. Moore, V. Bonačić-Koutecký, A. W. Castleman, Jr., *J. Am. Chem. Soc.* **2003**, *125*, 6289–6299; c) G. E. Johnson, R. Mitric, M. Nössler, E. C. Tyo, V. Bonacic-Koutecký, A. W. Castleman, Jr., *J. Am. Chem. Soc.* **2009**, *131*, 5460–5470.
- [21] K. Eichkorn, O. Treutler, H. Öhm, M. Häser, R. Ahlrichs, *Chem. Phys. Lett.* **1995**, *240*, 283–290.
- [22] J. P. Perdew, K. Burke, M. Ernzerhof, *Phys. Rev. Lett.* **1996**, *77*, 3865–3868.

IV. SILVER, GOLD AND COPPER HYDRIDES AND THEIR ROLE IN HYDROGEN STORAGE

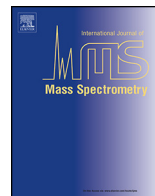
- 1 ESI/MS investigation of routes to the formation of silver hydride nanocluster dications $[\text{Ag}_x\text{H}_{x-2}\text{L}_y]^{2+}$ and gas-phase unimolecular chemistry of $[\text{Ag}_{10}\text{H}_8\text{L}_6]^{2+}$



Contents lists available at ScienceDirect

International Journal of Mass Spectrometry

journal homepage: www.elsevier.com/locate/ijms



ESI/MS investigation of routes to the formation of silver hydride nanocluster dications $[\text{Ag}_x\text{H}_{x-2}\text{L}_y]^{2+}$ and gas-phase unimolecular chemistry of $[\text{Ag}_{10}\text{H}_8\text{L}_6]^{2+}$ *

Marjan Krstić^{a,1}, Athanasios Zavras^{b,1}, George N. Khairallah^b, Philippe Dugourd^c,
Vlasta Bonačić-Koutecký^{a,d}, Richard A.J. O'Hair^{b,*}

^a Center of Excellence for Science and Technology—Integration of Mediterranean region (STIM) at Interdisciplinary Center for Advanced Science and Technology (ICAST), University of Split, Meštrovićevo šetalište 45, Split 21000, Croatia

^b School of Chemistry and Bio21 Molecular Science and Biotechnology Institute, The University of Melbourne, 30 Flemington Rd, Parkville, Victoria 3010, Australia

^c Institut Lumière Matière, Université Lyon 1-CNRS, Université de Lyon, 69622 Villeurbanne cedex, France

^d Humboldt-Universität Berlin, Institut für Chemie, Berlin 12489, Germany

ARTICLE INFO

Article history:

Received 30 April 2016

Accepted 27 May 2016

Available online xxx

Keywords:

Electrospray

Mass spectrometry

Gas-phase

Ligated silver hydride nanoclusters

ABSTRACT

When the bis(diphenylphosphino)methane (dppm) ligated silver hydride nanocluster salt $[\text{Ag}_3(\text{L})_3(\mu_3\text{-H})](\text{BF}_4)_2$ is allowed to react with NaBH_4 in a methanol/chloroform solution for 5 mins., and then diluted with acetonitrile and subjected to electrospray ionization mass spectrometry (ESI/MS), a range of silver hydride nanocluster dications are observed including: $[\text{Ag}_8\text{H}_6\text{L}_5]^{2+}$ and $[\text{Ag}_x\text{H}_{x-2}\text{L}_6]^{2+}$, where $x = 9\text{--}15$ and $\text{L} = \text{dppm}$. All of these clusters are no longer present in the ESI mass spectrum at 40 mins after mixing. Multistage mass spectrometry (MS^n) experiments were carried out to determine the fragmentation chemistry of $[\text{Ag}_{10}\text{H}_8\text{L}_6]^{2+}$ under conditions of collision-induced dissociation (CID). The initial CID reactions involve sequential loss of two ligands (L) to produce $[\text{Ag}_{10}\text{H}_8\text{L}_4]^{2+}$. Further isolation and CID of $[\text{Ag}_{10}\text{H}_8\text{L}_4]^{2+}$ resulted in a rich series of product ions which arise from three classes of fragmentation reactions: (i) cluster fission to yield complementary ion pairs $[\text{Ag}_{10-x}\text{H}_{8-(x-1)}\text{L}_{4-y}]^+$ and $[\text{Ag}_x\text{H}_{x-1}\text{L}_y]^+$ ($x = 1, 2$ and 4); (ii) ligand loss associated with cluster fission to yield pairs of singly charged clusters $[\text{Ag}_{10-x}\text{H}_{8-(x-1)}\text{L}_{4-y}]^+$ and $[\text{Ag}_x\text{H}_{x-1}\text{L}_{y-1}]^+$ ($x = 1\text{--}4$); (iii) ligand loss with concomitant loss of all the hydrides, presumably as four molecules of hydrogen to give the ligated silver cluster, $[\text{Ag}_{10}\text{L}_3]^{2+}$. The subsequent fragmentation reactions of the product ions were also examined. Most of the singly charged ligated silver hydride clusters fragment to form $[\text{Ag}_x\text{H}_{x-1}\text{L}_y]^+$. The exceptions are $[\text{Ag}_9\text{H}_8\text{L}_2]^+$ and $[\text{Ag}_7\text{H}_6\text{L}_2]^+$ which, upon ligand loss also release all of the hydrides to form the ligated silver clusters, $[\text{Ag}_9\text{L}]^+$ and $[\text{Ag}_7\text{L}]^+$ respectively. DFT calculations were carried out to examine how the cluster geometry changes for the following processes: $[\text{Ag}_{10}\text{H}_8\text{L}_6]^{2+} \rightarrow [\text{Ag}_{10}\text{H}_8\text{L}_4]^{2+} + 2\text{L} \rightarrow [\text{Ag}_{10}\text{H}_8\text{L}_3]^{2+} + \text{L} \rightarrow [\text{Ag}_{10}\text{L}_3]^{2+} + 4\text{H}_2$. Losses of 2L from $[\text{Ag}_{10}\text{H}_8\text{L}_6]^{2+}$ and L from $[\text{Ag}_{10}\text{H}_8\text{L}_4]^{2+}$ were calculated to be endothermic by 2.9 and 1.9 eV respectively, but the subsequent loss of 4H_2 from $[\text{Ag}_{10}\text{H}_8\text{L}_3]^{2+}$ is exothermic by 0.2 eV .

© 2016 Elsevier B.V. All rights reserved.

1. Introduction

The chemistry of alkali metal borohydrides reacting with coinage metal salts in the presence of ligands or other additives

has been studied for over 6 decades [1]. A rich series of products are formed including metal borohydrides [2–4], metal hydrides [5–7], mixed metal hydride-borohydrides [8] and reduced metal species [9–14]. These products can span multiple length scales ranging from discrete mononuclear compounds [2–4] through to ligand capped nanoclusters [5–11], nanoparticles, and colloids capped with various species [12–14]. There is growing evidence that ligand capped nanoclusters can act as precursors to nanoparticles and colloids [5,15]. In many instances electrospray ionization (ESI) and matrix assisted laser desorption ionization (MALDI) have been used to establish the molecular formulas and polydispersity of these

* Dedicated to the memory of Prof. Nico Nibbering, a true friend of International Mass Spectrometry, whose seminal contributions to the physical organic chemistry of gas phase ions inspired a generation of scientists.

* Corresponding author.

E-mail address: rohair@unimelb.edu.au (R.A.J. O'Hair).

¹ These authors contributed equally to the work.

products [16,17]. In the case of bisphosphine capped gold nanoclusters, mechanisms for the condensed-phase growth of these clusters have been proposed by Hudgens et al. using a combination of ESI/MS and UV/vis spectroscopy [18]. Tandem mass spectrometry approaches have been used to examine the fundamental gas-phase chemistry of these coinage metal nanoclusters [19,20].

The nature of the product(s) formed and their polydispersity are influenced by a range of factors including the nature of coinage metal salt, borohydride and ligand(s) used, the solvent, the temperature and the reaction time. For example, ESI/MS monitoring of the reaction of NaBH_4 of gold salts in the presence of the bis(diphenylphosphino)methane (dppm) ligand, L, gave rise to gold nanoclusters with the stoichiometry: $[\text{Au}_5\text{L}_3(\text{L-H})]^{2+}$, $[\text{Au}_9\text{L}_5]^{3+}$, $[\text{Au}_9\text{L}_5]^{3+}$, $[\text{Au}_{10}\text{L}_4]^{2+}$, $[\text{Au}_{11}\text{L}_5]^{3+}$, $[\text{Au}_{11}\text{L}_6]^{3+}$, $[\text{Au}_{13}\text{L}_6]^{3+}$ and $[\text{Au}_{14}\text{L}_6(\text{L-H})]^{3+}$ [20c]. In contrast, ESI/MS of solutions of NaBH_4 of silver salts in the presence of the dppm ligand reveals the formation of silver hydride nanoclusters with the stoichiometry: $[\text{Ag}_3(\text{H})(\text{Cl})\text{L}_3]^+$ [6e]; $[\text{Ag}_3(\text{H})(\text{BH}_4)\text{L}_3]^+$ [8]; $[\text{Ag}_3(\text{H})\text{L}_3]^{2+}$ [6f] and $[\text{Ag}_{10}\text{H}_8\text{L}_6]^{2+}$ [6e]. Clusters with the same stoichiometries were formed when the bis(dimethylphosphino)methane (dmpm) ligand was used instead, except for $[\text{Ag}_{10}\text{H}_8\text{L}_6]^{2+}$ which was not observed [19b]. In the case of the dppm ligand, variations in the solution phase conditions allowed the isolation and structural characterization via X-ray crystallography of the following salts: $[\text{Ag}_3(\text{L})_3(\mu_3\text{-H})(\mu_3\text{-Cl})]\text{BF}_4$ [6e]; $[\text{Ag}_3(\text{L})_3(\mu_3\text{-H})](\text{BF}_4)_2$ [6f] and $[\text{Ag}_3(\text{L})_3(\mu_3\text{-H})(\mu_3\text{-BH}_4)]\text{BF}_4$ [8]. Although we have not successfully isolated salts of $[\text{Ag}_{10}\text{H}_8\text{L}_6]^{2+}$ for structure determination using X-ray crystallography, we recently reported on experiments and DFT calculations of its gas-phase ionization energy, which allowed us to suggest a likely structure [19c].

Here we use: (i) ESI experiments to examine the types of cluster ions formed from when NaBH_4 is added to the $[\text{Ag}_3(\text{L})_3(\mu_3\text{-BH}_4)](\text{BF}_4)_2$ salt; (ii) MS^n experiments to probe the gas phase fragmentation chemistry of ligated silver hydride cluster cations, particularly $[\text{Ag}_{10}\text{H}_8\text{L}_6]^{2+}$ (where $\text{L}=\text{dppm}$) and its subsequent fragment ions to establish whether the coordinated hydride ligands remain bound to the silver clusters or whether they are lost as molecular hydrogen. DFT calculations were used to examine the energetics and structural changes associated with the formation of $[\text{Ag}_{10}\text{L}_3]^{2+}$ from $[\text{Ag}_{10}\text{H}_8\text{L}_6]^{2+}$.

2. Methods

2.1. Experimental

The following suppliers were used to purchase chemicals, which were used without further purification: (i) Aldrich: bis(diphenylphosphino)methane (dppm, L) (97%), sodium borodeuteride (98%), silver tetrafluoroborate (98%), (ii) Chemsupply: silver nitrate (99%), (iii) Ajax Finechem: sodium borohydride (97%), (iv) Merck: chloroform and methanol (AR grade for synthesis and HPLC grade for ESI/MSⁿ experiments), (v) Burdick & Jackson: acetonitrile (HPLC grade).

2.1.1. Cluster synthesis

Silver hydride nanoclusters were synthesized by dissolving 16.5 mg (10 μmol) of the silver hydride nanocluster $[\text{Ag}_3(\mu_3\text{-H})(\text{dppm})_3](\text{BF}_4)_2$ in 20 mL of solvent (acetonitrile or a 1:1 methanol:chloroform mixture), followed by addition of NaBH_4 (3.6 mg, 100 μmol). The solution was then stirred for ca. 5 min and the sample was diluted in acetonitrile or a 1:1 methanol:chloroform mixture to 50 μM prior to analysis by ESI/MS. Upon addition of sodium borohydride the solution changed from colourless to light orange over 40 min. In order to determine the source of hydride in the clusters, the same procedure was followed,

but by replacing sodium borohydride with sodium borodeuteride (4.2 mg, 100 μmol).

2.1.2. Mass spectrometry

Solutions containing silver hydride nanoclusters were injected at a sample flow rate of 5 $\mu\text{L min}^{-1}$ into the Finnigan ESI source of a LTQ FT Hybrid Linear Ion Trap (LIT) Mass Spectrometer (Thermo, Bremen, Germany) described in detail elsewhere [21]. Typical electrospray source conditions involved needle potentials of 3.6–4.8 kV with the capillary temperature set at ca. 250 °C. The tube lens voltage was set to 20.0 V, and the capillary voltage was set to 10.0 V. For the unimolecular reactions, the silver cluster cation of interest were mass selected with a window of 15 m/z units and then subjected to CID under multi collision conditions using the helium bath gas as the collision gas, and where a normalized collision energy was selected to deplete the parent ion to a relative abundance generally less than 20% for an activation Q of 0.25 and activation time of 30 ms. The scan mass range set between the low m/z cut-off for an ion trap and m/z 2000. For high-resolution mass analysis, the silver cluster cations were transferred to the FT-ICR cell ($<1.5 \times 10^{-9}$ Torr) via the ion optics transfer region ($\sim 2 \times 10^{-7}$ Torr). Since all isotopologues are isolated during the mass selection process, confirmation of the assignment of the products ions formed during the CID steps was carried out by an analysis of both their isotope envelopes and exact masses, as carried using the Thermo Scientific™ Xcalibur™ software.

2.2. Computational

The Turbomole [22] program was used with the Perdew–Burke–Ernzerhof (PBE) RI functional [23,24] and 19-electron relativistic effective core potential (19e-RECP) basis set for silver atoms [25] in combination with the split-valence-plus-polarization (SVP) atomic basis set for all other atoms [26] to fully optimize structures of silver hydride nanocluster dications $[\text{Ag}_{10}\text{H}_8\text{L}_y]^{2+}$ ($y=3, 4$ and 6) and the silver nanocluster dication $[\text{Ag}_{10}\text{L}_3]^{2+}$ to determine relative energies for removal of ligands and hydrogen atoms. All structures presented were fully optimized using gradient minimization techniques and stationary points were characterized as minima by calculating the vibrational frequencies. The structural search has been carried out taking advantage of structural properties obtained for fully ligand protected complex $[\text{Ag}_{10}\text{H}_8\text{L}_6]^{2+}$ [19c] by removing subsequently ligands which induced changes in the structures of the silver cores. Consequently, an extensive search for structural changes within the cores of ligated complexes has been carried out. Similar procedures have been employed for the search of the structures after removal of hydrogen atoms.

3. Results & discussion

3.1. The crucial role of the silver precursor in forming silver hydride nanocluster dications $[\text{Ag}_x\text{H}_{x-2}\text{L}_y]^{2+}$

As noted in the introduction, we have previously observed that ESI/MS of solutions of NaBH_4 of silver salts in the presence of the dppm ligand results in the formation of silver hydride nanoclusters with the stoichiometry: $[\text{Ag}_3(\text{H})(\text{Cl})\text{L}_3]^+$ [6e]; $[\text{Ag}_3(\text{H})(\text{BH}_4)\text{L}_3]^+$ [8]; $[\text{Ag}_3(\text{H})\text{L}_3]^{2+}$ [6f] and $[\text{Ag}_{10}\text{H}_8\text{L}_6]^{2+}$ [6e]. The relative abundances of these ions depend on a number of factors including the solvent system, and the relative stoichiometries of the silver salt, ligand and NaBH_4 . Fig. 1a shows optimal solution phase conditions to maximize the signal of $[\text{Ag}_{10}\text{H}_8\text{L}_6]^{2+}$. In order to find the optimal solution phase conditions to isolate the $[\text{Ag}_3(\text{L})_3(\mu_3\text{-BH}_4)](\text{BF}_4)_2$ salt, we previously tried several other solvents systems and discovered that by switching from methanol:chloroform (1:1 v/v) to pure acetonitrile, we were able to generate bulk $[\text{Ag}_3(\text{L})_3(\mu_3\text{-BH}_4)](\text{BF}_4)_2$

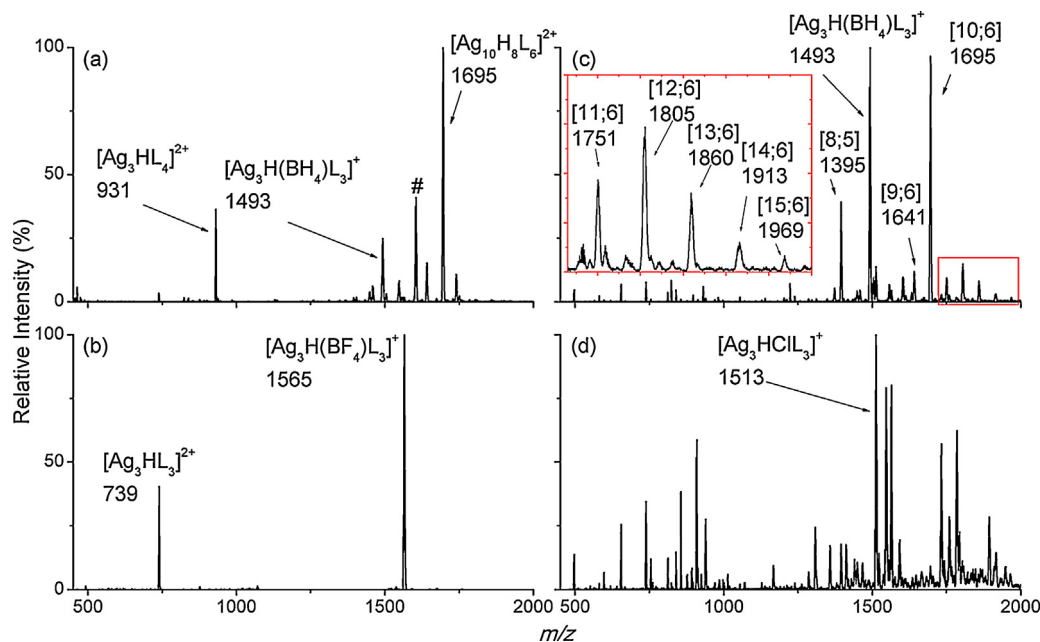


Fig. 1. Full ESI/MS in the positive ion mode showing the crucial role of the silver precursor in generating silver hydride nanocluster dications $[\text{Ag}_x\text{H}_{x-2}\text{Ly}]^{2+}$ via reaction with sodium borohydride: (a) $\text{dppm}:\text{AgBF}_4:\text{NaBH}_4$ (1:1:5) in methanol:chloroform (1:1 v/v); (b) spectrum for optimal conditions to form $[\text{Ag}_3(\text{L})_3(\mu_3-\text{H})]^{2+}$ by substituting to acetonitrile as the solvent; (c) $[\text{Ag}_3(\text{L})_3(\mu_3-\text{H})](\text{BF}_4)_2$ and NaBH_4 (1:10 molar ratio) in methanol:chloroform (1:1 v/v), then diluted to $50\ \mu\text{mol}$ in acetonitrile and subject to ESI/MS at around 5 min after mixing reagents together; (d) same solution as per (c), but now 40 mins after mixing. The m/z values of the labelled peaks represent the most abundant peak of isotope cluster. The # represents an impurity identified as $[\text{Ag}_3(\text{H})(\text{I})\text{L}_3]^+$ (m/z 1605) due to residual iodine in the ESI transfer tubing from a previous experiment.

material. Fig. 1b shows optimal solution phase conditions to maximize the signal of $[\text{Ag}_3(\text{H})\text{L}_3]^{2+}$. An important question is how are the larger silver hydride clusters formed? In particular, are smaller trinuclear hydride cluster ions such as $[\text{Ag}_3(\text{H})\text{L}_3]^{2+}$ precursors for growth via reactions with NaBH_4 and other silver “building blocks”? To address this question, we redissolved the $[\text{Ag}_3(\text{L})_3(\mu_3-\text{H})](\text{BF}_4)_2$ bulk material in methanol:chloroform (1:1 v/v) and added 10 equivalents of NaBH_4 and then examined the cations formed via ESI/MS after 5 min of mixing. Fig. 1c shows that not only is $[\text{Ag}_{10}\text{H}_8\text{L}_6]^{2+}$ formed, but that several other new silver hydride nanocluster dications $[\text{Ag}_x\text{H}_{x-2}\text{Ly}]^{2+}$ are formed—their assignments were confirmed by high resolution measurements (Supporting information Fig. S1). The reason that we did not previously observe these clusters is that we have used a higher concentration of NaBH_4 and that they are both short lived, and appear to transform into other species, as evident from a comparison of Fig. 1c and d, the latter where the identical solution was subject to ESI/MS after reacting for 40 min. It is noteworthy that the total ion count decreases by ca. two orders of magnitude from Fig. 1c to d, which may arise from silver hydride nanocluster dications $[\text{Ag}_x\text{H}_{x-2}\text{Ly}]^{2+}$ transforming into even larger clusters that are outside of the m/z range used, or into nanoparticles. This change in the mass spectrum is also associated with a change in colour of the solution from colourless to a light orange colour.

3.2. Multistage mass spectrometry experiments on $[\text{Ag}_{10}\text{H}_8\text{L}_6]^{2+}$

Multistage (MS^n) CID of $[\text{Ag}_{10}\text{H}_8\text{L}_6]^{2+}$ (m/z 1695) resulted in sequential ligand loss, Eq. (1) (MS^2 , $y=6$; MS^3 , $y=5$, for $[\text{Ag}_{10}\text{H}_8\text{Ly}]^{2+}$ (data not shown)). Isolation of $[\text{Ag}_{10}\text{H}_8\text{L}_4]^{2+}$ (m/z 1312) followed by another stage of CID, leads amongst others, to a series of even-electron, singly charged ligated silver hydride fragment ions arising from fission of the silver cluster core (Fig. 2). The assignment of the structural formulae of all ions was confirmed by HRMS measurements (Supporting information Fig. S1)

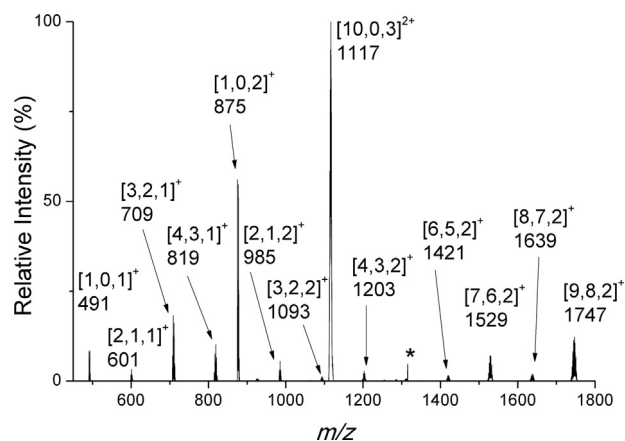
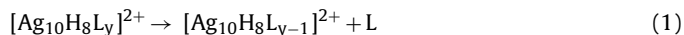


Fig. 2. LTQ MS^4 CID of $[\text{Ag}_{10}\text{H}_8\text{L}_4]^{2+}$ (m/z 1312). A * represents the mass selected precursor ion. The m/z values of the labelled peaks represent the most abundant peak of isotope cluster. Normalized collision energy: 18%; activation time: 30 ms. The numbers in the square brackets represent the stoichiometry of silver atoms, hydrogen atoms and ligands, e.g. $[4,3,1]^+ = [\text{Ag}_4\text{H}_3\text{L}_1]^+$.

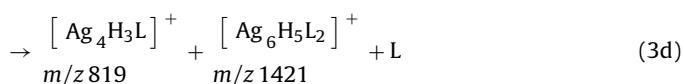
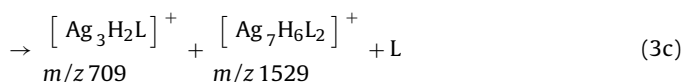
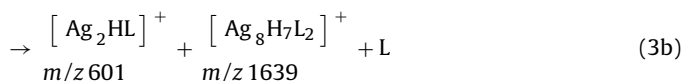
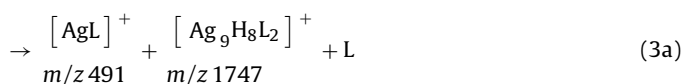
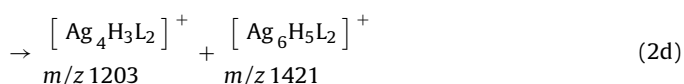
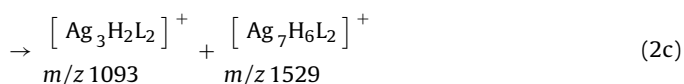
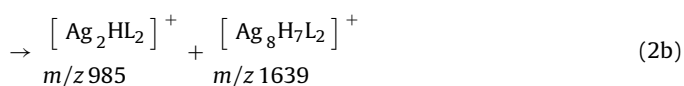
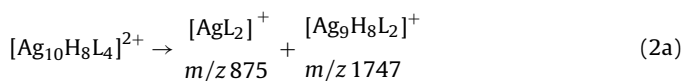
and deuterium labelling studies by examining the CID reaction of $[\text{Ag}_{10}\text{D}_8\text{L}_6]^{2+}$ (Supporting information Fig. S2).



There are four sets of complementary fragment ions arising from direct core fission (Eqs. (2a)–(2d)). We cannot tell whether completely symmetrical core fission of $[\text{Ag}_{10}\text{H}_8\text{L}_4]^{2+}$ occurs, as the resultant $[\text{Ag}_5\text{H}_4\text{Ly}]^+$ products are isobaric with the precursor ion and so will be on resonance with the applied RF of the mass-selected precursor ion and thus be subjected to further fragmentation. Since the relative peak heights do not take into account the total isotope distribution associated with each of these complementary ions, we have integrated the area under each peak and then normalized to the smallest area to give the following ratios for each of complimen-

tary ions: $[\text{AgL}_2]^+$ and $[\text{Ag}_9\text{H}_8\text{L}_2]^+$ are 1.6:1 (Eq. (2a)); $[\text{Ag}_2\text{HL}_2]^+$ and $[\text{Ag}_8\text{H}_7\text{L}_2]^+$ are 1.2:1 (Eq. (2b)); $[\text{Ag}_3\text{H}_2\text{L}_2]^+$ and $[\text{Ag}_7\text{H}_6\text{L}_2]^+$ are 1:8.9 (Eq. (2c)); $[\text{Ag}_4\text{H}_3\text{L}_2]^+$ and $[\text{Ag}_6\text{H}_5\text{L}_2]^+$ are 1.2:1 (Eq. (2d)). The fact that the two fragments are not equal may be due to either of the following factors: mass discrimination [27]; one of the complementary fragment ions might be more susceptible to further fragmentation (e.g. ligand loss). The latter appears to be the case for $[\text{Ag}_3\text{H}_2\text{L}_2]^+$, which is both significantly less abundant than and for which the abundant potential fragment ion $[\text{Ag}_3\text{H}_2\text{L}]^+$ is observed.

Since there are no complementary ions for $[\text{Ag}_4\text{H}_3\text{L}]^+$, $[\text{Ag}_3\text{H}_2\text{L}]^+$, $[\text{Ag}_2\text{HL}]^+$ and $[\text{AgL}]^+$, they must be secondary fragment ions arising from either ligand loss followed by core fission (Eqs. (3a)–(3d)) and/or by loss of a ligand (Eq. (4)) from the one of the complementary ions formed in Eqs. (2a)–(2d). While we cannot rule out the former, the latter reaction seems likely as each of the mass selected $[\text{Ag}_4\text{H}_3\text{L}_2]^+$, $[\text{Ag}_3\text{H}_2\text{L}_2]^+$, $[\text{Ag}_2\text{HL}_2]^+$ and $[\text{AgL}_2]^+$ fragments via ligand loss upon CID, as discussed further below.



Finally, the base peak in the spectrum is the all silver dication $[\text{Ag}_{10}\text{L}_3]^{2+}$ formed by loss of a ligand and all of the hydrides. Supplementary Information Fig. S3a shows the expanded isotope region of $[\text{Ag}_{10}\text{L}_3]^{2+}$ formed in the CID spectra of $[\text{Ag}_{10}\text{H}_8\text{L}_4]^{2+}$ and $[\text{Ag}_{10}\text{D}_8\text{L}_4]^{2+}$ (Supplementary Information Fig. S3c), which highlights that not only is $[\text{Ag}_{10}\text{L}_3]^{2+}$ formed, but a small amount of $[\text{Ag}_{10}\text{H}_8\text{L}_4]^{2+}$ (Supplementary Information Fig. S3b) and $[\text{Ag}_{10}\text{D}_8\text{L}_4]^{2+}$ (Supplementary Information Fig. S3d) are formed. We have been unable to isolate and carry out CID on $[\text{Ag}_{10}\text{H}_8\text{L}_3]^{2+}$ or $[\text{Ag}_{10}\text{D}_8\text{L}_3]^{2+}$, suggesting they are fragile and prone to fragmentation. Based on our study of reductive elimination of H_2 from the smaller cluster $[\text{Ag}_3\text{H}_2\text{L}]^+$ [19a], we suggest that $[\text{Ag}_{10}\text{L}_3]^{2+}$ arises from ligand loss to form $[\text{Ag}_{10}\text{H}_8\text{L}_3]^{2+}$ (Eq. (5)) which then triggers reductive elimination of four hydrogen molecules Eq. (6). DFT calculations aimed at examining the structures of $[\text{Ag}_{10}\text{H}_8\text{L}_4]^{2+}$, $[\text{Ag}_{10}\text{H}_8\text{L}_3]^{2+}$, and $[\text{Ag}_{10}\text{L}_3]^{2+}$ are discussed in Section 3.5 below.

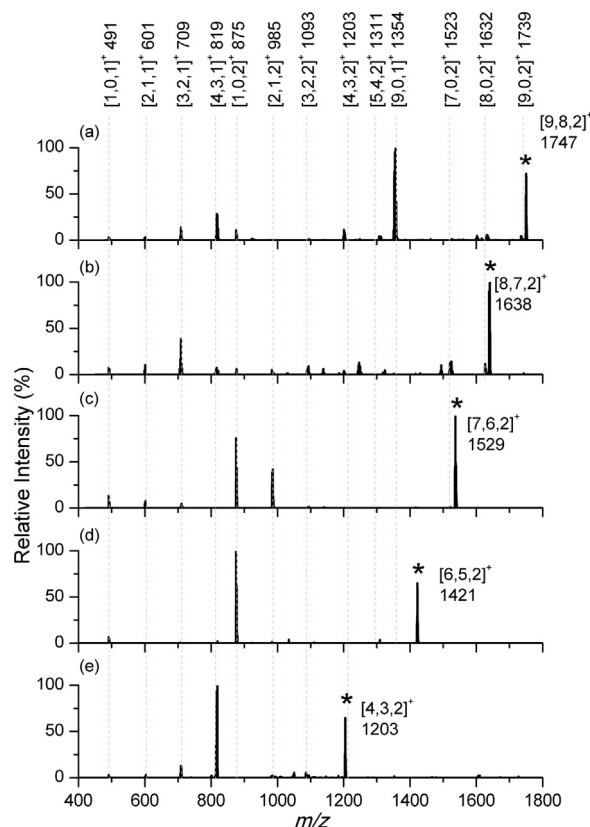
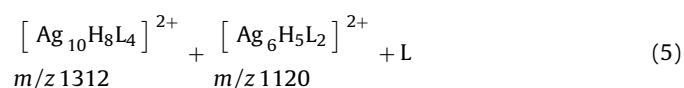
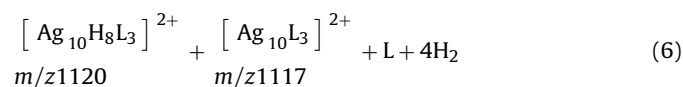
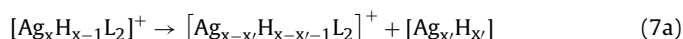


Fig. 3. LTQ MS⁵ CID of (a) $[\text{Ag}_9\text{H}_8\text{L}_2]^+$ (m/z 1747) (b) $[\text{Ag}_8\text{H}_7\text{L}_2]^+$ (m/z 1638) (c) $[\text{Ag}_7\text{H}_6\text{L}_2]^+$ (m/z 1529) (d) $[\text{Ag}_6\text{H}_5\text{L}_2]^+$ (m/z 1421) and, (e) $[\text{Ag}_4\text{H}_3\text{L}_2]^+$ (m/z 1203). A * represents the mass selected precursor ion. Normalized collision energy: 15%; activation time: 30 ms. The numbers in the square brackets represent the stoichiometry of silver atoms, hydrogen atoms and ligands, e.g. $[4,3,2]^+ = [\text{Ag}_4\text{H}_3\text{L}_2]^+$. The m/z values of the labelled peaks and next to the numbers in square brackets represent the most abundant peak of isotope cluster.



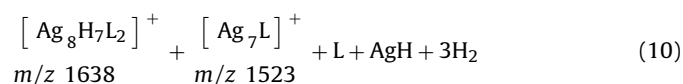
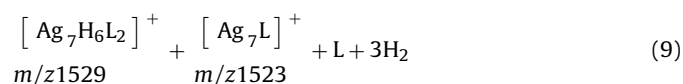
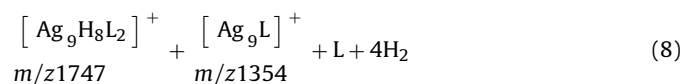
3.3. CID experiments on the silver hydride cluster cations $[\text{Ag}_x\text{H}_{x-1}\text{L}_2]^+$ and $[\text{Ag}_x\text{H}_{x-1}\text{L}]^+$

The CID spectra of silver hydride cluster cations $[\text{Ag}_x\text{H}_{x-1}\text{L}_2]^+$ for $x=9-4$ are shown in Fig. 3, while those for $x=3$ and 2 are given in Supporting information Fig. S4. An examination of these stacked spectra reveals that while there are some common fragment ions, there are no “magic number” clusters that are formed. A common fragmentation channel of $[\text{Ag}_x\text{H}_{x-1}\text{L}_2]^+$ involves the loss of neutral silver hydride units, to form smaller silver hydride clusters $[\text{Ag}_{x'}\text{H}_{x'-1}\text{L}_2]^+$, where $x' < x$, or ligated silver cation, $[\text{AgL}_2]^+$. These neutral silver hydride units could be lost as either neutral silver hydride clusters (Eq. (7a)) or as individual silver hydrides (Eq. (7b)). The former channel is favoured by enthalpy due to the formation of stable silver hydride clusters [28]. Related AgX losses have been observed in the bare Ag_xH^+ and $\text{Ag}_x\text{Br}_{x-1}^+$ clusters [29]. Related silver hydride clusters, $[\text{Ag}_{x-x'}\text{H}_{x-x'-1}\text{L}_2]^+$ or silver cation, $[\text{AgL}]^+$, which have lost a ligand are also observed.



The silver cluster cation $[\text{Ag}_9\text{L}]^+$ is formed by ligand loss in conjunction with losses of hydrogen in the CID spectrum of $[\text{Ag}_9\text{H}_8\text{L}_2]^+$

(Eq. (8)). $[\text{Ag}_7\text{L}]^+$ can be formed by ligand loss in conjunction with losses of hydrogen in the CID spectrum of $[\text{Ag}_7\text{H}_6\text{L}_2]^+$ (Eq. (9)) or via the combined ligand, AgH and hydrogen losses in the case of $[\text{Ag}_8\text{H}_7\text{L}_2]^+$ (Eq. (10)). Supporting information Fig. S5 shows the expanded isotope region of $[\text{Ag}_9\text{L}]^+$ and $[\text{Ag}_7\text{L}]^+$, which clearly highlights that all of the hydrides have been lost.



The $[\text{Ag}_x\text{H}_{x-1}\text{L}]^+$ clusters solely fragment via loss of silver hydrides (Supporting information Fig. S6), which could be lost as either neutral silver hydride clusters (cf. Eq. (7a)) or as individual silver hydrides (cf. Eq. (7b)).

3.4. CID experiments on the silver cluster cations $[\text{Ag}_{10}\text{L}_3]^{2+}$ and $[\text{Ag}_9\text{L}]^+$

The ligand induced loss triggered reductive elimination of the 8 coordinated hydrides as four molecules of hydrogen in the CID spectra of $[\text{Ag}_{10}\text{H}_8\text{L}_4]^{2+}$ (Fig. 2) and $[\text{Ag}_9\text{H}_8\text{L}_2]^+$ (Fig. 3a) gave rise to the formation of all silver cluster cations $[\text{Ag}_{10}\text{L}_3]^{2+}$ (Eqs. (5) and (6)) and $[\text{Ag}_9\text{L}]^+$ (Eq. (8)). Since we have examined the formation and gas-phase chemistry of bare silver cluster cations Ag_x^+ , ($x = 3, 5, 7$) [29i], it was of interest to examine the gas-phase unimolecular chemistry of these ligated silver cluster cations. Given that the smallest bare silver dication that has been isolated for subsequent CID studies in the gas-phase is Ag_9^{2+} [30,31], key questions are: (1) what is the smallest ligated silver dication that can be formed in our experiments; (2) how does ligation influence the fragmentation chemistry compared to the bare dication?

CID of $[\text{Ag}_{10}\text{L}_3]^{2+}$ (Fig. 4a) gives rise to four products ions. Ligand loss gives the dication $[\text{Ag}_{10}\text{L}_2]^{2+}$ (Eq. (11)) while cluster fission can occur to give the complementary ions $[\text{AgL}_2]^+$ and $[\text{Ag}_9\text{L}]^+$ (Eq. (12)). $[\text{AgL}]^+$ could be formed by cluster fission triggered by ligand loss (Eq. (13)) or as a secondary product of ligand loss from $[\text{AgL}_2]^+$ (Eq. (14)). It is worth noting that asymmetric cluster fission has also been observed in the photoionization and photofragmentation of the silver deuteride dication, $[\text{Ag}_{10}\text{D}_8\text{L}_4]^{2+}$, [19c] and well as for multiply charged bare metal silver and gold cluster cations [28,31]. CID of $[\text{Ag}_{10}\text{L}_2]^{2+}$ (Fig. 4b) only fragments via cluster fission to give two sets of complementary ions: the dominant pair $[\text{AgL}]^+$ and $[\text{Ag}_9\text{L}]^+$ (Eq. (15)); and a minor amount of $[\text{Ag}_3\text{L}]^+$ and $[\text{Ag}_7\text{L}]^+$ (Eq. (16)).

So to answer the first question, the smallest stable silver dication that we are able to observe is Ag_{10}^{2+} ligated by two dpmm ligands. With regards to the second question, Kruckeberg et al. have shown that bare Ag_{10}^{2+} also fragments via asymmetric cluster fission, but in this case Ag_3^+ and Ag_7^+ are formed (Eq. (17)) [25b]. Thus ligation changes the types of clusters that are formed.

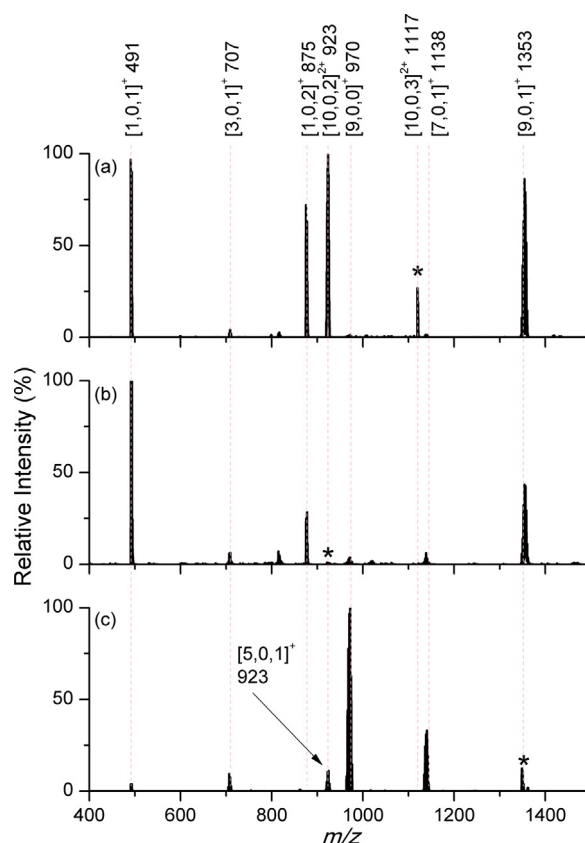
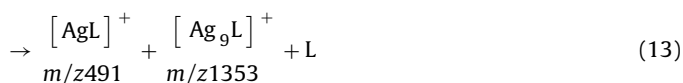
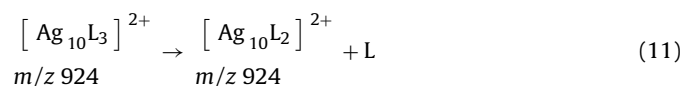
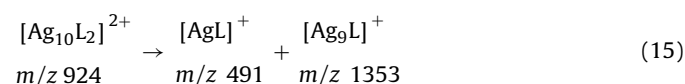
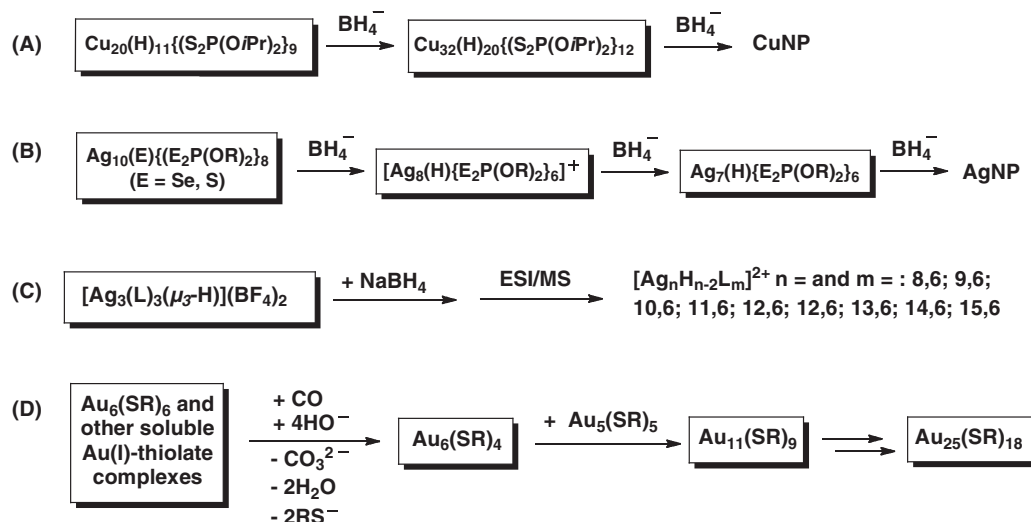


Fig. 4. (a) MS^5 CID of $[\text{Ag}_{10}\text{L}_3]^{2+}$ (m/z 1117); (b) MS^6 CID of $[\text{Ag}_{10}\text{L}_2]^{2+}$ (m/z 923); (c) MS^6 CID of $[\text{Ag}_9\text{L}]^+$ (m/z 1353). A * represents the mass selected precursor ion. Normalized collision energy: 15%; activation time: 30 ms. The numbers in the square brackets represent the stoichiometry of silver atoms, hydrogen atoms and ligands, e.g. $[5,0,1]^+ = [\text{Ag}_5\text{L}]^+$. The m/z values of the labelled peaks and next to the numbers in square brackets represent the most abundant peak of isotope cluster.



We also examined the unimolecular chemistry of the largest singly charged clusters that we have been able to form. $[\text{Ag}_9\text{L}]^+$ fragments via loss of a ligand (Eq. (18), Fig. 4c) as well as via a series of cluster fission reactions in which bare even electron neutral silver clusters are lost and the ligand remains on cation (Eq. (19), where $x = 2, 4, 6$ and 8).



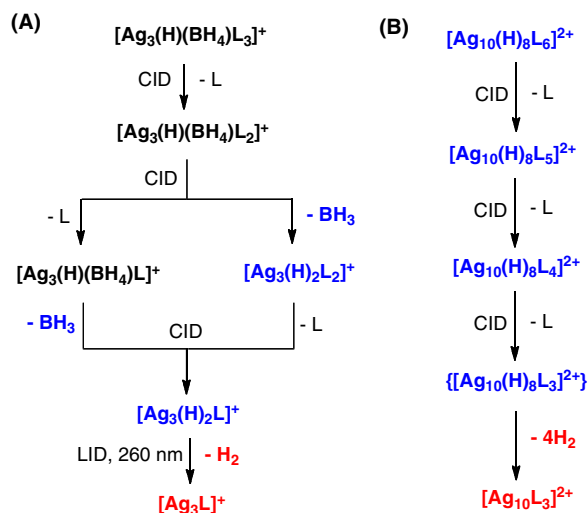


Scheme 1. Examples showing the link between smaller ligated nanoclusters, larger clusters and nanoparticles: (A) excess BH_4^- induced growth to copper nanoparticles (CuNPs) [5e]; (B) excess BH_4^- induced growth to AgNPs [15]; (C) excess BH_4^- induced formation of larger silver hydride cluster cations (this work); (D) Au nanocluster formation via CO induced reduction of Au thiolate complexes [32].

3.5. DFT calculations on structural changes to the silver cluster core upon the sequence of ligand loss reactions: $[\text{Ag}_{10}\text{H}_8\text{L}_6]^{2+} \rightarrow [\text{Ag}_{10}\text{H}_8\text{L}_4]^{2+} + 2\text{L} \rightarrow [\text{Ag}_{10}\text{H}_8\text{L}_3]^{2+} + \text{L} \rightarrow [\text{Ag}_{10}\text{L}_3]^{2+} + 4\text{H}_2$

The ligand induced loss triggered reductive elimination of the 8 coordinated hydrides is interesting since it represents a change from the ionic silver hydride cluster $[\text{Ag}_{10}\text{H}_8\text{L}_6]^{2+}$ to the metallic silver cluster $[\text{Ag}_{10}\text{L}_3]^{2+}$. In order to investigate the energetics and structural consequences of this transformation, DFT calculations were carried out. The previously DFT optimized structure of $[\text{Ag}_{10}\text{H}_8\text{L}_6]^{2+}$ [19][19c] served as a starting geometry. Removal of two ligands L from this cluster followed by re-optimization gave the fully optimized $[\text{Ag}_{10}\text{H}_8\text{L}_4]^{2+}$ structure (Fig. 5). In turn, this structure was used as a starting geometry for optimization of the $[\text{Ag}_{10}\text{H}_8\text{L}_3]^{2+}$ and $[\text{Ag}_{10}\text{L}_3]^{2+}$ complexes via removal of a ligand or a ligand together with all 8 hydrogen atoms derived from the coordinated hydrides. Other geometric isomers in the case of the $[\text{Ag}_{10}\text{H}_8\text{L}_3]^{2+}$ and $[\text{Ag}_{10}\text{L}_3]^{2+}$ complexes are given in Supporting information Figs. S7 and S8. They differ mainly in the structure of the silver core. Isomeric structures of $[\text{Ag}_{10}\text{H}_8\text{L}_3]^{2+}$ (Supporting information Fig. S7) are built either from pentagons mutually connected accordingly. Removal of hydrogen atoms gave rise to $[\text{Ag}_{10}\text{L}_3]^{2+}$ (Supplementary Information Fig. S8) also causing changes in the structures of the Ag_{10} core. Therefore, isomeric structures of these complexes contain cores built up from hexagon units decorated differently with 4 Ag atoms. Three ligands are bound via phosphine sites symmetrically to the core. The most stable structures were used to determine the energies for loss of ligands as well as loss of four dihydrogen molecules.

DFT calculations show that loss of two dppm ligands from $[\text{Ag}_{10}\text{H}_8\text{L}_6]^{2+}$ requires 2.9 eV and the loss of next ligand to produce $[\text{Ag}_{10}\text{H}_8\text{L}_3]^{2+}$ requires an additional 1.9 eV. In contrast, the loss of all hydrogen atoms from $[\text{Ag}_{10}\text{H}_8\text{L}_3]^{2+}$ to yield $[\text{Ag}_{10}\text{L}_3]^{2+}$ is slightly exothermic by 0.2 eV as shown in Fig. 5. These results fully support the experimental finding that CID of $[\text{Ag}_{10}\text{H}_8\text{L}_6]^{2+}$ produces $[\text{Ag}_{10}\text{L}_3]^{2+}$ (Figs. 2 and 3). Finally, it is noteworthy that removal of the two dppm and hydride ligands strongly influences the structure of the silver core of the clusters for the sequence of reactions: $[\text{Ag}_{10}\text{H}_8\text{L}_6]^{2+} \rightarrow [\text{Ag}_{10}\text{H}_8\text{L}_4]^{2+} + 2\text{L}$ and $[\text{Ag}_{10}\text{H}_8\text{L}_3]^{2+} + \text{L} \rightarrow [\text{Ag}_{10}\text{L}_3]^{2+} + 4\text{H}_2$, as depicted in Fig. 5. Thus, the lowest energy structure of $[\text{Ag}_{10}\text{H}_8\text{L}_6]^{2+}$ contains a symmet-



Scheme 2. Results of multistage mass spectrometry experiments highlighting how ligand loss can trigger fragmentation reactions involving coordinated anionic ligands to transform the clusters: (A) Direct link established between mixed hydride/borohydride clusters (black), dihydride clusters (blue) and “all metal” clusters (red) in Refs. [8] and [19a], where LID=laser induced dissociation; (B) Direct link established between hydride clusters (blue) and “all metal” clusters (red) in this work. (For interpretation of the references to colour in this figure legend, the reader is referred to the web version of this article.)

ric bicapped square antiprism structure as the silver core, where the hydrides take up two different coordination modes: $4\mu_2$ hydride ligands and $4\mu_3$ hydride ligands. Upon removal of the two dppm ligands that bind via only 1 phosphine site, the silver core of $[\text{Ag}_{10}\text{H}_8\text{L}_4]^{2+}$ rearranges to two rotated mutually connected pentagonal rings, with the hydrides taking up the following coordination modes: $4\mu_2$ hydride ligands and $4\mu_3$ hydride ligands. Removal of a further ligand gives $[\text{Ag}_{10}\text{H}_8\text{L}_3]^{2+}$ structure with the same silver core as in the case of $[\text{Ag}_{10}\text{H}_8\text{L}_4]^{2+}$, with 4 hydrides located at edges exhibiting μ_2 binding modes and 4 hydrides located at faces exhibiting μ_3 binding modes. Removal of the hydride ligands from the silver core gives rise to the $[\text{Ag}_{10}\text{L}_3]^{2+}$ structure with the core formed by trigonal bipyramid capped with 5 silver atoms, altogether containing also hexagonal subunit to which ligands are bound.

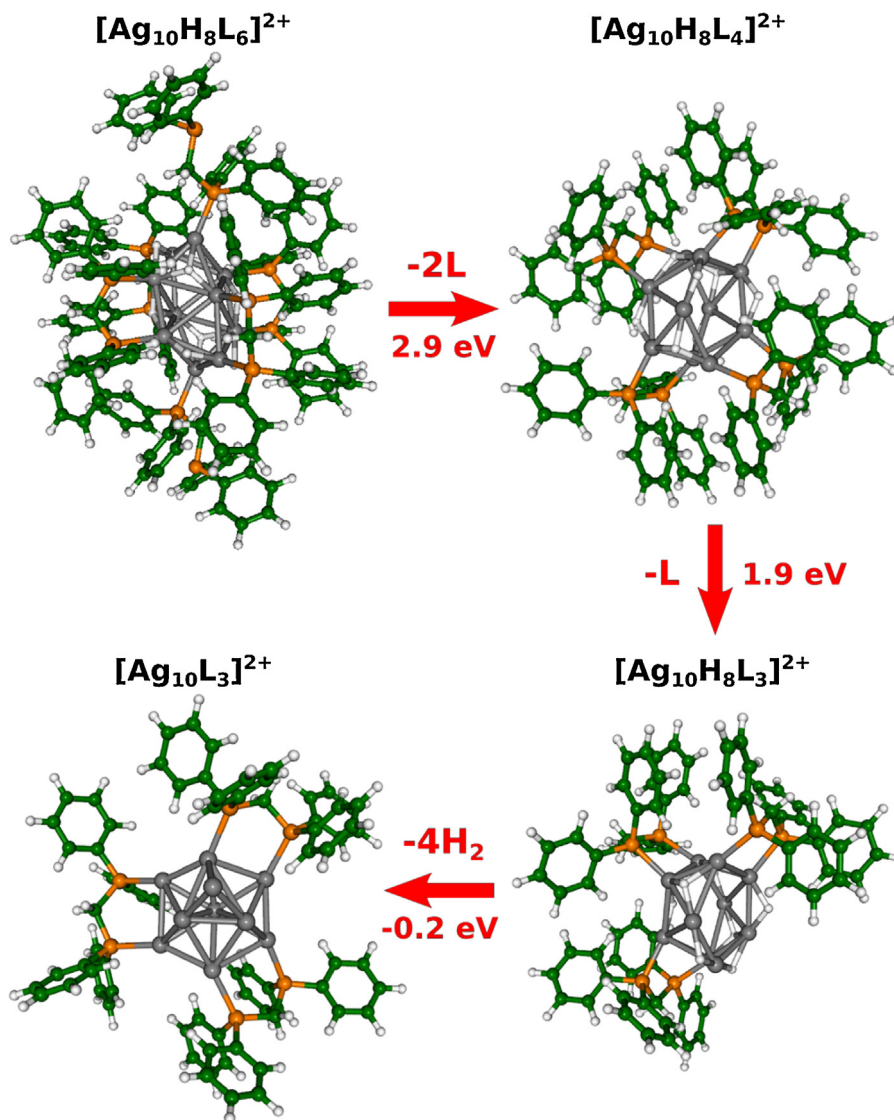


Fig. 5. RI-PBE/RECP-def2-SVP optimized lowest energy structures and relative energies of $[Ag_{10}H_8L_6]^{2+}$, $[Ag_{10}H_8L_4]^{2+}$, $[Ag_{10}H_8L_3]^{2+}$ and $[Ag_{10}L_3]^{2+}$ for removal of dppm ligands and hydrogen atoms. Grey, orange, white and green colours label silver, phosphorus, hydrogen and carbon atoms respectively. (For interpretation of the references to colour in this figure legend, the reader is referred to the web version of this article.)

4. Conclusions

There is growing evidence that small ligand protected coinage metal nanoclusters detected by ESI/MS, and in some cases isolated and fully structurally characterized, can transform to larger clusters and nanoparticles when allowed to undergo further reactions in solution (Scheme 1). Examples include further reaction of copper and silver hydride clusters with borohydride to form nanoparticles (Scheme 1(A) and (B)); reduction of gold thiolate complexes followed by growth reactions to form the gold nanocluster $Au_{25}(SR)_{18}$ (Scheme 1(D)). We have found that the combined reactants $[Ag_3(L)_3(\mu_3-H)](BF_4)_2$ and $NaBH_4$ act as precursors to a range of larger silver hydride nanocluster dications $[Ag_xH_{x-2}L_y]^{2+}$ that are observed using ESI/MS. The ESI/MS sampling of this solution over time reveals that these dications disappear at longer reaction times, suggesting that complex solution phase processes are at play.

Multistage mass spectrometry experiments on coinage metal nanoclusters highlight how fragmentation reactions involving coordinated anionic ligands can transform the clusters core structure. For example, previous gas-phase experiments and DFT

calculations on $[Ag_3(H)_{2-x}(BH_4)_xL_y]^+$ clusters provide a direct link between mixed hydride/borohydride silver clusters ($x=1$), dihydride silver clusters ($x=0$) and silver clusters via discrete unimolecular reactions occurring for isolated clusters (Scheme 2(A)) [8,19a]. Thus CID triggers loss of the ligand, L resulting in a change of the binding mode(s) of the H and BH_4 ligands. In the larger cluster, $[Ag_{10}H_8L_6]^{2+}$ sequential ligand losses ultimately drive the loss of all hydrides to form the all metal cluster, $[Ag_{10}L_3]^{2+}$ (Scheme 2(B)). This suggests that related reactions could occur at the surfaces of silver nanoparticles. There is convincing evidence that reduction of silver salts with an excess of borohydride produces silver nanoparticles protected at their surfaces by borohydride [33]. The role of surface hydrides, has however been largely neglected. An exception is the work of Hinks and Pullman, who used online mass spectrometry to carefully examining the evolution of HD and D_2 from the reduction of silver salts with $NaBD_4$. They were able to suggest that these reduction reactions produce silver nanoparticles with surface bound deuterides, which are then able to undergo reductive elimination of D_2 or acid base reactions with solution species reaction at the surface of the nanoparticle to produce HD [34].

Acknowledgements

We thank the Australian Research Council for financial support (DP150101388). AZ acknowledges the award of an Australian Postgraduate PhD Scholarship. The research leading to these results has received funding from the European Research Council under the European Union's Seventh Framework Programme (FP7/2007–2013 Grant agreement No. 320659). VBK and MK acknowledge Prof. Miroslav Radman at MedILS and Split-Dalmatia County for kind support. We thank Prof. David Pullman for discussions of his work on the evolution of hydrogen gas during the preparation of silver nanoparticles.

Appendix A. Supplementary data

Supplementary data associated with this article can be found, in the online version, at <http://dx.doi.org/10.1016/j.ijms.2016.05.022>.

References

- [1] E. Wiberg, W. Henle, Silver borohydride, *AgBH₄*, *Z. Naturforsch.* 7b (1952) 575–576.
- [2] (a) J.C. Bommer, K.W. Morse, Single hydrogen–boron bridged species: tris(methyldiphenylphosphine) complexes of silver(I) and copper(I) containing tetrahydroborate and (ethoxycarbonyl) trihydroborate, *Inorg. Chem.* 19 (1980) 587–593; (b) M. Besora, A. Lledos, Coordination modes and hydride exchange dynamics in transition metal tetrahydroborate complexes, *Struct. Bond.* 130 (2008) 149–202.
- [3] (a) F. Cariati, L. Naldini, Complexes of Group IB metals. II. Complexes of Ag(I) with triphenylphosphine and their reaction products with sodium tetrahydroborate, *Gazz. Chim. Ital.* 95 (1965) 201–205; (b) E.B. Lobkovskii, M.Y. Antipin, A.P. Borisov, V.D. Makhaev, K.N. Semenenko, Y.T. Struchkov, Crystal and molecular structure of tetrahydroborato–tris(methyldiphenylphosphino)silver(I), *Koord. Khim.* 7 (1981) 307–310.
- [4] D.G. Musaev, K. Morokuma, Does the tetrahydroborate species AuBH_4 exist? Ab initio MO study of the structure and stability of CuBH_4 , AgBH_4 , and AuBH_4 , *Organometallics* 14 (1995) 3327–3334.
- [5] (a) R.S. Dhayal, J.-H. Liao, Y.-R. Lin, P.-K. Liao, S. Kahlal, J.-Y. Saillard, C.W. Liu, A nanospheric polyhydrido copper cluster of elongated triangular orthobicupola array: liberation of H₂ from solar energy, *J. Am. Chem. Soc.* 135 (2013) 4704–4707; (b) A.J. Edwards, R.S. Dhayal, P.-K. Liao, J.-H. Liao, M.-H. Chiang, R.O. Piltz, S. Kahlal, J.-Y. Saillard, C.W. Liu, Chinese puzzle molecule: a 15 hydride, 28 copper atom nanoball, *Angew. Chem., Int. Ed.* 53 (2014) 7214–7218; (c) M.A. Huertos, I. Cano, N.A.G. Bandeira, J. Benet-Buchholz, C. Bo, P.W.N.M. van Leeuwen, Phosphinothiolates as ligands for polyhydrido copper nanoclusters, *Chem. Eur. J.* 20 (2014) 16121–16127; (d) R.S. Dhayal, J.-H. Liao, X. Wang, Y.-C. Liu, M.-H. Chiang, S. Kahlal, J.-Y. Saillard, C.W. Liu, Diselenophosphate–induced conversion of an achiral $[\text{Cu}_{20}\text{H}_{11}\{\text{S}_2\text{P}(\text{O}i\text{Pr})_2\}_9]$ into a chiral $[\text{Cu}_{20}\text{H}_{11}\{\text{Se}_2\text{P}(\text{O}i\text{Pr})_2\}_9]$ polyhydrido nanocluster, *Angew. Chem., Int. Ed.* 54 (2015) 13604–13608; (e) R.S. Dhayal, J.-H. Liao, S. Kahlal, X. Wang, Y.-C. Liu, M.-H. Chiang, W.E. van Zyl, J.-Y. Saillard, C.W. Liu, $[\text{Cu}_{32}(\text{H})_{20}\{\text{S}_2\text{P}(\text{O}i\text{Pr})_2\}_{12}]$: the largest number of hydrides recorded in a molecular nanocluster by neutron diffraction, *Chem. Eur. J.* 21 (2015) 8369–8374; (f) R.S. Dhayal, W.E. van Zyl, C.W. Liu, Polyhydrido copper clusters: synthetic advances, structural diversity, and nanocluster-to-nanoparticle conversion, *Acc. Chem. Res.* 49 (2016) 86–95.
- [6] (a) C.W. Liu, H.-W. Chang, C.-S. Fang, B. Sarkar, J.-C. Wang, Anion-templated syntheses of octanuclear silver clusters from a silver dithiophosphate chain, *Chem. Comm.* 46 (2010) 4571–4573; (b) C.W. Liu, H.-W. Chang, B. Sarkar, J.-Y. Saillard, S. Kahlal, Y.-Y. Wu, Stable silver(I) hydride complexes supported by diselenophosphate ligands, *Inorg. Chem.* 49 (2010) 468–475; (c) C.W. Liu, P.-K. Liao, C.-S. Fang, J.-Y. Saillard, S. Kahlal, J.-C. Wang, An eleven-vertex deltahedron with hexacapped trigonal bipyramidal geometry, *Chem. Comm.* 47 (2011) 5831–5833; (d) B.K. Tate, C.M. Wyss, J. Bacsa, K. Kluge, L. Gelbaum, J.P. Sadighi, A dinuclear silver hydride and an umpolung reaction of CO₂, *Chem. Sci.* 4 (2013) 3068–3074; (e) A. Zavras, G.N. Khairallah, T.U. Connell, J.M. White, A.J. Edwards, P.S. Donnelly, R.A.J. O'Hair, Synthesis, structure and gas-phase reactivity of a silver hydride complex $[\text{Ag}_3\{(\text{PPh}_2)_2\text{CH}_2\}_3(\mu_3\text{-H})(\mu_3\text{-Cl})]\text{BF}_4$, *Angew. Chem., Int. Ed.* 52 (2013) 8391–8394; (f) A. Zavras, G.N. Khairallah, T.U. Connell, J.M. White, A.J. Edwards, R.J. Mulder, P.S. Donnelly, R.A.J. O'Hair, Synthesis, structural characterization, and gas-phase unimolecular reactivity of the silver hydride nanocluster $[\text{Ag}_3\{(\text{PPh}_2)_2\text{CH}_2\}_3(\mu_3\text{-H})](\text{BF}_4)_2$, *Inorg. Chem.* 53 (2014) 7429–7437.
- [7] (a) E.Y. Tsui, P. Miller, J.P. Sadighi, Gold hydrides: reactions of a stable monomeric gold(I) hydride complex, *Angew. Chem., Int. Ed.* 47 (2008) 8937–8940; (b) H. Schmidbaur, H.G. Raubenheimer, L. Dobrzańska, The gold–hydrogen bond, Au–H, and the hydrogen bond to gold $\text{Au}\cdots\text{H-X}$, *Chem. Soc. Rev.* 43 (2014) 345–380.
- [8] A. Zavras, A. Ariafard, G.N. Khairallah, J.M. White, R.J. Mulder, A.J. Canty, R.A.J. O'Hair, Synthesis, structure and gas-phase reactivity of the mixed silver hydride borohydride nanocluster $[\text{Ag}_3(\mu_3\text{-H})(\mu_3\text{-BH}_4)(\text{L}^{\text{Ph}})_3]\text{BF}_4$ ($\text{L}^{\text{Ph}} = \text{bis}(\text{diphenylphosphino})\text{methane}$), *Nanoscale* 7 (2015) 18129–18137.
- [9] C. Vazquez-Vazquez, M. Banobre-Lopez, A. Mitra, M.A. Lopez-Quintela, J. Rivas, Synthesis of small atomic copper clusters in microemulsions, *Langmuir* 25 (2009) 8208–8216.
- [10] (a) A. Desireddy, B.E. Conn, J. Guo, B. Yoon, R.N. Barnett, B.M. Monahan, K. Kirschbaum, W.P. Griffith, R.L. Whetten, U. Landman, T.P. Bigioni, Ultrastable silver nanoparticles, *Nature* 501 (2013) 399–402; (b) H. Yang, J. Lei, B. Wu, Y. Wang, M. Zhou, A. Xia, L. Zheng, N. Zheng, Crystal structure of a luminescent thiolated Ag nanocluster with an octahedral Ag_6Ag^+ core, *Chem. Commun.* 49 (2013) 300–302; (c) H. Yang, Y. Wang, H. Huang, L. Gell, L. Lehtovaara, S. Malola, H. Hakkinen, N. Zheng, All-thiol-stabilized Ag_{44} and $\text{Au}_{12}\text{Ag}_{32}$ nanoparticles with single-crystal structures, *Nat. Comm.* 4 (2013) 2422; (d) H. Yang, Y. Wang, N. Zheng, Stabilizing subnanometer Ag(0) nanoclusters by thiolate and diphosphine ligands and their crystal structures, *Nanoscale* 5 (2013) 2674–2677; (e) R.S. Dhayal, J.-H. Liao, Y.-C. Liu, M.-H. Chiang, S. Kahlal, J.-Y. Saillard, C.W. Liu, An $[\text{Ag}_{21}\{\text{S}_2\text{P}(\text{O}i\text{Pr})_2\}_{12}]^{+}$: eight-electron superatom, *Angew. Chem., Int. Ed.* 54 (2015) 3702–3706; (f) L.G. AbdulHalim, M.S. Bootharaju, Q. Tang, S. del Gobbo, R.G. AbdulHalim, M. Eddoudi, D. -e. Jiang, O.M. Bakr, A $\text{Ag}_{29}(\text{BDT})_{12}(\text{TPP})_4$: tetravalent nanocluster, *J. Am. Chem. Soc.* 137 (2015) 11970–11975; (g) C.P. Joshi, M.S. Bootharaju, M.J. Alhilaly, O.M. Bakr, $[\text{Ag}_{25}(\text{SR})_{18}]^{-}$: the “golden” silver nanoparticle, *J. Am. Chem. Soc.* 137 (2015) 11578–11581.
- [11] Historical introduction to gold colloids, clusters and nanoparticles, in: D.M.P. Mingos (Ed.), “Gold Clusters, Colloids and Nanoparticles I”, Structure and Bonding, 161, Springer, New York, USA, 2014, ISBN 978-3-319-07847-2, pp. 1–47.
- [12] M.B. Gawande, A. Goswami, F.-X. Felpin, T. Asefa, X. Huang, R. Silva, X. Zou, R. Zboril, R.S. Varma, Cu and Cu-based nanoparticles: synthesis and applications in catalysis, *Chem. Rev.* 116 (2016) 3722–3811.
- [13] (a) J. Polte, X. Tuae, M. Wuitschick, A. Fischer, A.F. Thuenemann, K. Rademann, R. Kraehnert, F. Emmerling, Formation mechanism of colloidal silver nanoparticles: analogies and differences to the growth of gold nanoparticles, *ACS Nano* 6 (2012) 5791–5802; (b) M. Wuitschick, B. Paul, R. Bienert, A. Sarfraz, U. Vainio, M. Sztucki, R. Kraehnert, P. Strasser, K. Rademann, F. Emmerling, J. Polte, Size-controlled synthesis of colloidal silver nanoparticles based on mechanistic understanding, *Chem. Mater.* 25 (2013) 4679–4689; (c) D.L. Van Hynning, C.F. Zukowski, Formation mechanisms and aggregation behavior of borohydride reduced silver particles, *Langmuir* 14 (1998) 7034–7046; (d) J.-S. Seo, D.-M. Son, H. Lee, J. Kim, Y. Kim, The characterization of borohydride-stabilized nanosilvers in laponite sol using ¹H NMR: its ligand exchange reactions with MUA and TOP, *Bull. Korean Chem. Soc.* 30 (2009) 2651–2654.
- [14] (a) J. Perez-Juste, I. Pastoriza-Santos, L.M. Liz-Marzan, P. Mulvaney, Gold nanorods: synthesis, characterization and applications, *Coord. Chem. Rev.* 249 (2005) 1870–1901; (b) M. Grzelczak, J. Perez-Juste, P. Paul Mulvaney, L.M. Liz-Marzan, Shape control in gold nanoparticle synthesis, *Chem. Soc. Rev.* 37 (2008) 1783–1791; (c) R. Sardar, A.M. Funston, P. Mulvaney, R.W. Murray, Gold nanoparticles: past, present, and future, *Langmuir* 25 (2009) 13840–13851.
- [15] C.W. Liu, Y.-R. Lin, C.-S. Fang, C. Latouche, S. Kahlal, J.-Y. Saillard, $[\text{Ag}_7(\text{H})\{\text{E}_2\text{P}(\text{OR})_2\}_6]$ (E = Se, S): precursors for the fabrication of silver nanoparticles, *Inorg. Chem.* 52 (2013) 2070–2077.
- [16] (a) A. Zavras, G.N. Khairallah, R.A.J. O'Hair, Gas phase formation, structure and reactivity of gold cluster ions, in: D.M.P. Mingos (Ed.), “Gold Clusters, Colloids and Nanoparticles II”, Structure and Bonding, 162, Springer, New York, USA, 2014, ISBN 978-3-319-07844-1, pp. 139–230, <http://dx.doi.org/10.1007/430-2014-140>; (b) Y. Lu, W. Chen, Application of mass spectrometry in the synthesis and characterization of metal nanoclusters, *Anal. Chem.* 87 (2015) 10659–10667.
- [17] (a) M.F. Bertino, Z.-M. Sun, R. Zhang, L.-S. Wang, Facile syntheses of monodisperse ultra-small Au clusters, *J. Phys. Chem. B* 110 (2006) 21416–21418; (b) D.E. Bergeron, J.W. Hudgens, Ligand dissociation and core fission from diphosphine-protected gold clusters, *J. Phys. Chem. C* 111 (2007) 8195–8201; (c) J.S. Golightly, L. Gao, A.W. Castleman Jr., D.E. Bergeron, J.W. Hudgens, R.J. Magyar, C.A. Gonzalez, Impact of swapping ethyl for phenyl groups on diphosphine-protected undecagold, *J. Phys. Chem. C* 111 (2007) 14625–14627; (d) D.E. Bergeron, O. Coskuner, J.W. Hudgens, C.A. Gonzalez, Ligand exchange reactions in the formation of diphosphine-protected gold clusters, *J. Phys. Chem. C* 112 (2008) 12808–12814; (e) J.M. Pettibone, J.W. Hudgens, Synthetic approach for tunable, size-selective formation of monodisperse, diphosphine-protected gold

- nanoclusters, *J. Phys. Chem. Lett.* 1 (2010) 2536–2540;
(f) A. Olivares, J. Laskin, G.E. Johnson, Investigating the synthesis of ligated metal clusters in solution using a flow reactor and electrospray ionization mass spectrometry, *J. Phys. Chem. A* 118 (2014) 8464–8470.
- [18] (a) J.W. Hudgens, J.M. Pettibone, T.P. Senftle, R.N. Bratton, Reaction mechanism governing formation of 1,3-bis(diphenylphosphino)propane-protected gold nanoclusters, *Inorg. Chem.* 50 (2011) 10178–10189;
(b) J.M. Pettibone, J.W. Hudgens, Reaction network governing diphosphine-protected gold nanocluster formation from nascent cationic platforms, *Phys. Chem. Chem. Phys.* 14 (2012) 4142–4154;
(c) J.M. Pettibone, J.W. Hudgens, Predictive gold nanocluster formation controlled by metal–ligand complexes, *Small* 8 (2012) 715–725.
- [19] (a) M. Girod, M. Krstić, R. Antoine, L. MacAleese, J. Lemoine, A. Zavras, G.N. Khairallah, V. Bonačić-Koutecký, P. Dugourd, R.A.J. O'Hair, Formation and characterisation of the silver hydride nanocluster cation $[\text{Ag}_3\text{H}_2((\text{Ph}_2\text{P})_2\text{CH}_2)]^+$ and its release of hydrogen, *Chem. Eur. J.* 20 (2014) 16626–16633;
(b) A.J. Clark, A. Zavras, G.N. Khairallah, R.A.J. O'Hair, Bis(dimethylphosphino)methane-ligated silver chloride, cyanide and hydride cluster cations: synthesis and gas-phase unimolecular reactivity, *Int. J. Mass Spectrom.* 378 (2015) 86–94;
(c) A. Daly, M. Krstić, A. Giuliani, R. Antoine, L. Nahon, A. Zavras, G.N. Khairallah, V. Bonačić-Koutecký, P. Dugourd, R.A.J. O'Hair, Gas-phase VUV photoionization and photofragmentation of the silver deuteride nanocluster $[\text{Ag}_{10}\text{D}_8\text{L}_6]^{2+}$ ($\text{L} = \text{bis}(\text{diphenylphosphino})\text{methane}$). A joint experimental and theoretical study, *Phys. Chem. Chem. Phys.* 17 (2015) 25772–25777.
- [20] (a) P.S.D. Robinson, G.N. Khairallah, G. da Silva, H. Lioe, R.A.J. O'Hair, Gold mediated C–I bond activation of iodobenzene, *Angew. Chem. Int. Ed.* 51 (2012) 3812–3817;
(b) P.S.D. Robinson, T.-L. Nguyen, H. Lioe, R.A.J. O'Hair, G.N. Khairallah, Synthesis and gas-phase uni- and bi- molecular reactivity of bisphosphine ligated gold clusters, $[\text{Au}_x\text{L}_y]^{n+}$, *Int. J. Mass Spectrom.* 330–332 (2012) 109–117;
(c) A. Zavras, G.N. Khairallah, R.A.J. O'Hair, Bis(diphenylphosphino)methane ligated gold cluster cations: synthesis and gas phase unimolecular reactivity, *Int. J. Mass Spectrom.* 354–355 (2013) 242–248;
(d) G.E. Johnson, T. Priest, J. Laskin, Size-dependent stability toward dissociation and ligand binding energies of phosphine ligated gold cluster ions, *Chem. Sci.* 5 (2014) 3275–3286;
(e) G.E. Johnson, A. Olivares, D. Hill, J. Laskin, Cationic gold clusters ligated with differently substituted phosphines: effect of substitution on ligand reactivity and binding, *Phys. Chem. Chem. Phys.* 17 (2015) 14636–14646.
- [21] L. Feketeová, G.N. Khairallah, R.A.J. O'Hair, Intercluster chemistry of protonated and sodiated betaine dimers upon collision induced dissociation and electron induced dissociation, *Eur. J. Mass Spectrom.* 14 (2008) 107–110.
- [22] TURBOMOLE V7.0, A Development of University of Karlsruhe and Forschungszentrum Karlsruhe GmbH, 1989–2007, TURBOMOLE GmbH, Since 2007, 2015, Available from <http://www.turbomole.com>.
- [23] J.P. Perdew, K. Burke, M. Ernzerhof, Generalized gradient approximation made simple, *Phys. Rev. Lett.* 77 (1996) 3865–3868.
- [24] K. Eichkorn, O. Treutler, H. Öhm, M. Häser, R. Ahlrichs, Auxiliary basis sets to approximate Coulomb potentials, *Chem. Phys. Lett.* 242 (1995) 652–660.
- [25] D. Andrae, U. Haeussermann, M. Dolg, H. Stoll, H. Preuss, Energy-adjusted ab initio pseudopotentials for the second and third row transition elements, *Theor. Chim. Acta* 77 (1990) 123.
- [26] F. Weigend, R. Ahlrichs, Balanced basis sets of split valence, triple zeta valence and quadruple zeta valence quality for H to Rn: design and assessment of accuracy, *Phys. Chem. Chem. Phys.* 7 (2005) 3297–3305.
- [27] D.J. Douglas, A.J. Frank, D. Mao, Linear ion traps in mass spectrometry, *Mass Spectrom. Rev.* 24 (2005) 1–29.
- [28] C.A. Tsipis, E.E. Karagiannis, P.F. Kladou, A.C. Tsipis, Aromatic gold and silver 'rings': hydrosilver(I) and hydrogold(I) analogues of aromatic hydrocarbons, *J. Am. Chem. Soc.* 126 (2004) 12916–12929.
- [29] (a) I. Rabin, W. Schulze, G. Ertl, Mass spectrometric investigation of nonstoichiometric silver-fluorine cluster compounds Ag_nF_m ($0 \leq m \leq n$), *Zeitschr. Phys. Chem.* 169 (1990) 85;
(b) I. Rabin, C. Jackschath, W. Schulze, F.W. Froben, Silver-halogen cluster compounds Ag_nX_m ($n \geq 2$; $0 \leq m \leq n$; $\text{X} = \text{F}, \text{Br}$), *Zeitschr. Phys. D: At. Mol. Cl.* 19 (1991) 401;
(c) J.-M. L'Hermite, F. Rabilloud, P. Labastie, F. Spiegelman, Evidence for trimers in the evaporation in silver bromide clusters, *Eur. Phys. J. D16* (2001) 77;
(d) J.-M. L'Hermite, F. Rabilloud, L. Marcou, P. Labastie, Metastable fragmentation of silver bromide clusters, *Eur. Phys. J. D14* (2001) 323;
(e) C.K. Fagerquist, D.K. Sensharma, M.A. El-Sayed, "Mixed" metallic-ionic clusters of silver/silver iodide, *J. Phys. Chem.* 95 (1991) 9169;
(f) C.K. Fagerquist, D.K. Sensharma, T.S. Ahmadi, M.A. El-Sayed, Adhesion of silver iodide molecules to gaseous metallic silver cluster cations, *J. Phys. Chem.* 97 (1993) 6598;
(g) C.K. Fagerquist, D.K. Sensharma, M.A. El-Sayed, A. Rubio, M.L. Cohen, Enhancement of metallic silver monomer evaporation by the adhesion of polar molecules to silver nanocluster ions, *J. Phys. Chem.* 99 (1995) 7723;
(h) T. Jerger, D. Kreisler, E. Recknagel, A novel desorption mechanism of $(\text{Ag}_n\text{I}_{n-1})^+$ cluster ions, *Zeitschr. Phys. D* 26 (1993) 181;
(i) G.N. Khairallah, R.A.J. O'Hair, Gas phase synthesis and reactivity of Ag_n^+ and $\text{Ag}(n-1)^+$ cluster cations, *Dalton Trans.* (2005) 2702–2712;
(j) G.N. Khairallah, R.A.J. O'Hair, 'Gas phase synthesis, structure and unimolecular reactivity of silver iodide cluster cations, Ag_nI_m^+ ($n = 2-5$, $0 < m < n$), *Dalton Trans.* (2008) 2956–2965.
- [30] (a) I. Rabin, W. Schulze, Second ionization potentials of selected silver and gold clusters, *Chem. Phys. Lett.* 201 (1993) 265;
(b) A. Halder, A. Liang, C. Yin, V.V. Kresin, Double and triple ionization of silver clusters by electron impact, *J. Phys. Condens. Matter* 24 (2012) 104009.
- [31] (a) S. Krückeberg, G. Dietrich, K. Lützenkirchen, L. Schweikhard, C. Walther, J. Ziegler, Time resolved photofragmentation of Au_n^+ and Ag_n^+ clusters ($n = 9, 21$), *Hyperfine Interact.* 108 (1997) 107;
(b) J. Ziegler, G. Dietrich, S. Krückeberg, K. Lützenkirchen, L. Schweikhard, C. Walther, Dissociation pathways of doubly and triply charged gold clusters, *Hyperfine Interact.* 115 (1998) 171;
(c) S. Krückeberg, G. Dietrich, K. Lützenkirchen, L. Schweikhard, C. Walther, J. Ziegler, Low-energy decay pathways of doubly charged silver clusters (Ag_n^{2+} ($N = 9-24$)), *Z. Phys. D* 40 (1997) 341;
(d) S. Krückeberg, L. Schweikhard, G. Dietrich, K. Lützenkirchen, C. Walther, J. Ziegler, Decay pathway determination of even- size dicationic silver clusters: Ag_{162}^{2+} and Ag_{182}^{2+} revisited by pre- precursor selection and sequential decay, *Chem. Phys.* 262 (2000) 105;
(e) S. Krückeberg, G. Dietrich, K. Lützenkirchen, L. Schweikhard, J. Ziegler, Experimental dissociation energies of metal cluster dications and their interpretation in a liquid- drop model with empirical corrections, *Phys. Rev. A* 60 (1999) 1251–1257.
- [32] Z. Luo, V. Nachammai, B. Zhang, N. Yan, D.T. Leong, D.-E. Jiang, J. Xie, Toward understanding the growth mechanism: tracing all stable intermediate species from reduction of $\text{Au}(\text{I})$ -thiolate complexes to evolution of Au_{25} nanoclusters, *J. Am. Chem. Soc.* 136 (2014) 10577–10580.
- [33] (a) L. Mulfinger, S.D. Solomon, M. Bahadory, A.V. Jeyarajasingam, S.A. Rutkowsky, C. Boritz, Synthesis and study of silver nanoparticles, *J. Chem. Educ.* 84 (2007) 322;
(b) K.C. Song, S.M. Lee, T.S. Park, B.S. Lee, Preparation of colloidal silver nanoparticles by chemical reduction method, *Kor. J. Chem. Eng.* 26 (2009) 153–155.
- [34] (a) M.L. Hinks, D. Pullman, Mechanistic study of the production of silver nanoparticles, in: 241st ACS National Meeting, Anaheim, CA, 2011, presentation 285;
(c) M.L. Hinks, Mechanistic Study of the Production of Silver Nanoparticles, MSc Thesis, State University, San Diego, 2011, pp. 50–51.

2 Formation and Characterisation of the Silver Hydride Nanocluster Cation $[\text{Ag}_3\text{H}_2((\text{Ph}_2\text{P})_2\text{CH}_2)]^+$ and Its Release of Hydrogen

Photochemistry

Formation and Characterisation of the Silver Hydride Nanocluster Cation $[\text{Ag}_3\text{H}_2((\text{Ph}_2\text{P})_2\text{CH}_2)]^+$ and Its Release of Hydrogen

Marion Girod,^[a, b] Marjan Krstić,^[c] Rodolphe Antoine,^[a, d] Luke MacAleese,^[a, d] Jérôme Lemoine,^[a, b] Athanasios Zavras,^[e] George N. Khairallah,^[e] Vlasta Bonačić-Koutecký,^{*, [c, f]} Philippe Dugourd,^{*, [a, d]} and Richard A. J. O'Hair^{*, [e]}

Dedicated to the memory of Professor Oliver Hampe

Abstract: Multistage mass spectrometry and density functional theory (DFT) were used to characterise the small silver hydride nanocluster, $[\text{Ag}_3\text{H}_2\text{L}]^+$ (where $\text{L}=(\text{Ph}_2\text{P})_2\text{CH}_2$) and its gas-phase unimolecular chemistry. Collision-induced dissociation (CID) yields $[\text{Ag}_2\text{HL}]^+$ as the major product while laser-induced dissociation (LID) proceeds via H_2 formation and subsequent release from $[\text{Ag}_3\text{H}_2\text{L}]^+$, giving rise to $[\text{Ag}_3\text{L}]^+$ as the major product. Deuterium labelling studies on $[\text{Ag}_3\text{D}_2\text{L}]^+$ prove that the source of H_2 is from the hydrides and not from the ligand. Comparison of TD-DFT absorption patterns obtained for the optimised structures with action spectroscopy

results, allows assignment of the measured features to structures of precursors and products. Molecular dynamics "on the fly" reveal that AgH loss is favoured in the ground state, but H_2 formation and loss is preferred in the first excited state S_1 , in agreement with CID and LID experimental findings. This indicates favourable photo-induced formation of H_2 and subsequent release from $[\text{Ag}_3\text{H}_2\text{L}]^+$, an important finding in context of metal hydrides as a hydrogen storage medium, which can subsequently be released by heating or irradiation with light.

Introduction

Hydrogen continues to be an attractive source of clean, renewable energy, since combustion produces water as a sole by-product, thereby overcoming challenges associated with CO_2 emissions from traditional hydrocarbon sources.^[1] The widespread use of hydrogen is hampered due to the challenge of safely storing and transporting it in its natural gaseous state.^[1, 2] Notwithstanding the issue of H% weight content,^[3]

metal hydrides have long attracted attention as a storage medium for hydrogen, which can subsequently be released by heating or via irradiation with light.^[4]

Silver hydrides are key intermediates in a number of reactions involving organic substrates^[5] and several silver hydrides have been recently isolated and structurally characterised by X-ray crystallography.^[6] In one such study, hydrogen evolution from $[(\text{LAg})_2\text{H}]^+$ (where $\text{L}=\text{N}$ -heterocyclic carbene ligand 1,3-bis(2,6-diisopropylphenyl)imidazolin-2-ylidene) was observed, but the precise mechanism for H_2 formation is unknown.^[6e] Gas-phase studies on mass selected silver hydride clusters allow their structure^[7] and reactivity^[8] to be directly probed. Here we present one of the first examples of the use of multistage mass spectrometry experiments to probe the formation of hydrogen from a small silver hydride nanocluster, $[\text{Ag}_3\text{H}_2\text{L}]^+$ (where $\text{L}=\text{bis}(\text{diphenylphosphino})\text{methane}$, $(\text{Ph}_2\text{P})_2\text{CH}_2$, DPPM) in the gas-phase.^[9, 10] Collision-induced dissociation (CID) and laser-induced dissociation (LID) were used to activate the cluster in order to examine its fragmentation reactions.^[11] Structures of precursor and product ions were identified by the combination of action spectroscopy and density functional theory (DFT), while molecular dynamics (MD) was used to identify H_2 formation mechanisms both in ground and excited states.

[a] Dr. M. Girod, Dr. R. Antoine, Dr. L. MacAleese, Prof. J. Lemoine, Prof. P. Dugourd
Université of Lyon, 69622 (France)
E-mail: philippe.dugourd@univ-lyon1.fr

[b] Dr. M. Girod, Prof. J. Lemoine
Institut des Sciences Analytiques, Université Lyon 1
CNRS UMR 5280 Lyon (France)

[c] M. Krstić, Prof. V. Bonačić-Koutecký
Interdisciplinary Center for Advanced Science and Technology (ICAST)
University of Split, Split (Croatia)

[d] Dr. R. Antoine, Dr. L. MacAleese, Prof. P. Dugourd
Institut Lumière Matière, Université Lyon 1
CNRS UMR 5306, Lyon (France)

[e] A. Zavras, Dr. G. N. Khairallah, Prof. R. A. J. O'Hair
School of Chemistry, University of Melbourne, Victoria (Australia)
E-mail: rohair@unimelb.edu.au

[f] Prof. V. Bonačić-Koutecký
Humboldt-Universität Berlin, Institut für Chemie, Berlin (Germany)
E-mail: vbk@cms.hu-berlin.de

Supporting information for this article is available on the WWW under <http://dx.doi.org/10.1002/chem.201404110>.

Results and Discussion

Gas-phase “synthesis” of $[\text{Ag}_3\text{H}_2\text{L}]^+$

The ESI mass spectrum of silver hydride clusters synthesised in solution is displayed in Figure 1 a.

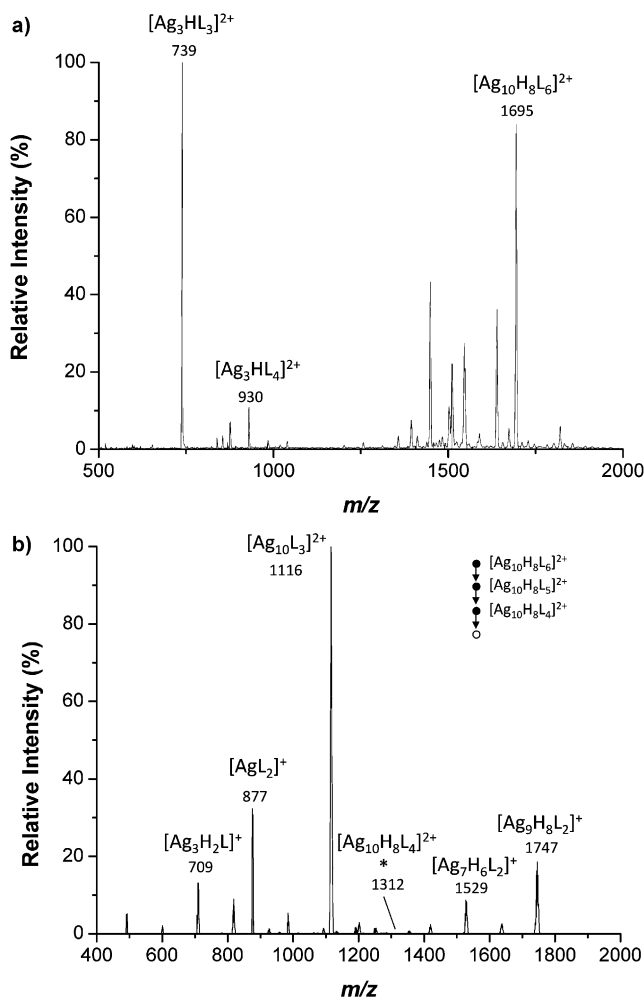
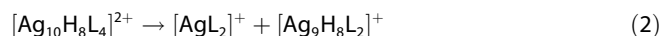
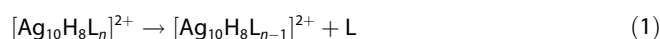


Figure 1. a) Full ESI/MS of silver hydride nanocluster ions synthesized from reaction of AgNO_3 with NaBH_4 . b) MS^5 CID spectrum of $[\text{Ag}_{10}\text{H}_8\text{L}_4]^{2+}$ ion (m/z 1312), which was mass selected with a window of 20 Th to allow isolation of the full distribution of ^{107}Ag and ^{109}Ag isotopes. A NCE of 10% was used to dissociate the cluster and the m/z values of the products ions indicate the most intense peak in the cluster as a result the various combination of the silver(I) isotopes; *: the mass selected precursor ion.

Multistage (MS^n) CID of $[\text{Ag}_{10}\text{H}_8\text{L}_6]^{2+}$ (m/z 1695) resulted in sequential ligand loss [Eq. (1); MS^2 , $n=6$; MS^3 , $n=5$, data not shown]. Isolation of $[\text{Ag}_{10}\text{H}_8\text{L}_4]^{2+}$ (m/z 1312) followed by another stage of CID, leads amongst others, to a series of even-electron, singly charged ligated silver hydride fragment ions arising from fission of the cluster core (Figure 1 b). Some of these are complementary fragment ions arising from direct core fission [e.g., $[\text{AgL}_2]^+$ and $[\text{Ag}_9\text{H}_8\text{L}_2]^+$, Eq. (2)] while others arise from the initial loss of a ligand [e.g., $[\text{Ag}_3\text{H}_2\text{L}]^+$ and $[\text{Ag}_7\text{H}_6\text{L}_2]^+$, Eq. (3)]:



Gas-phase fragmentation of $[\text{Ag}_3\text{H}_2\text{L}]^+$ under CID and LID conditions

$[\text{Ag}_3\text{H}_2\text{L}]^+$ is the smallest DPPM ligated silver hydride cluster with the Ag_3 subunit and was selected for further experiments. Under CID conditions, the dominant product ion observed is $[\text{Ag}_2\text{HL}]^+$, formed via the loss of AgH [Eq. (4)] (Figure 2 a).

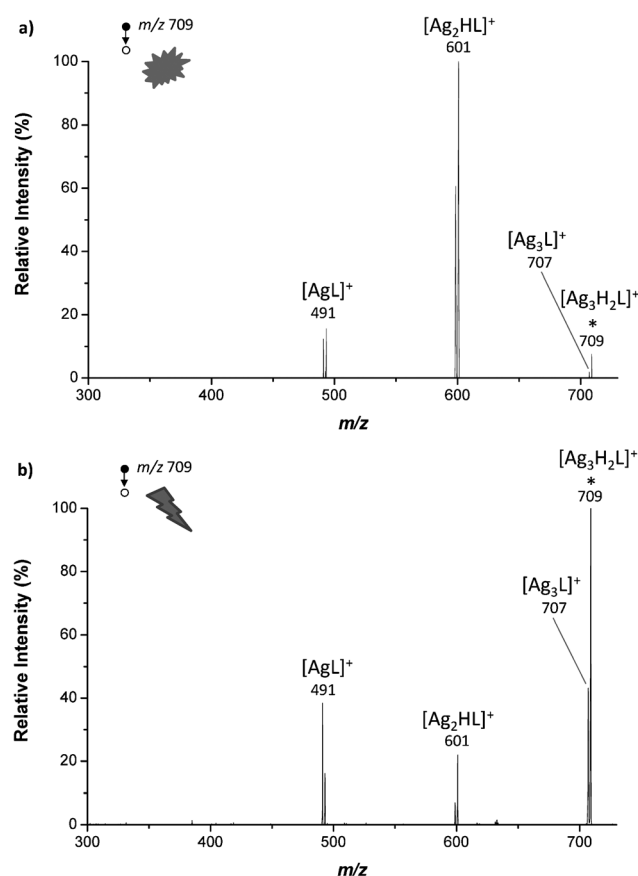
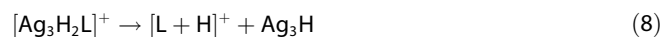


Figure 2. MS^5 spectra showing the fragmentation of the $[\text{Ag}_3\text{H}_2\text{L}]^+$ ion (m/z 709) under conditions of: a) CID with a NCE of 25%, b) laser-induced dissociation (LID) at 260 nm with five laser shots; *: the mass selected precursor ions. A window of 1.3 Th was used to isolate a single peak from the isotope cluster, corresponding to $^{107}\text{Ag}_2^{109}\text{AgH}_2\text{L}^+$.

The next most abundant ion is $[\text{AgL}]^+$, which could arise from the loss of two AgH [Eq. (5)] or the dimer [Eq. (6)]. Minor channels due to the formation of H_2 [Eq. (7)] and Ag_3H [Eq. (8)] are also observed. In contrast, the major product of LID arises from dehydrogenation [Eq. (7)] (Figure 2 b), with minor products $[\text{Ag}_2\text{HL}]^+$, $[\text{Ag}_2\text{L}]^+$ and $[\text{AgL}]^+$ also occurring. All fragmentation channels were confirmed by substituting NaBH_4 for NaBD_4 during the synthesis and using the $[\text{Ag}_3\text{D}_2\text{L}]^+$ deuterium labelled cluster (Supporting Information Figure S1). These ex-

periments highlight that DPPM is not the source of the H for either the AgH losses under CID conditions (Figure S1a) or H₂ formation and release under LID (Figure S1b):



Gas-phase reaction of [Ag₃L]⁺ with hydrogen

We also examined the reaction of [Ag₃L]⁺ with hydrogen, to establish whether [Ag₃H₂L]⁺ could be regenerated [Eq. (9)]. No reaction was observed under a range of conditions including near thermal reaction conditions (reaction times of up to 10 s), as well as activation of [Ag₃L]⁺ by collisions of the mass selected precursor with the neutral bath gas (reaction time of 100 ms) or laser irradiation at either 265 or 310 nm (reaction times of 500 ms) in the ion trap (Supporting Information Figure S2). The lack of reactivity under “near thermal” conditions^[12] for the given concentration of H₂ and the reaction times examined establishes an upper limit for the rate of about $2 \times 10^{-16} \text{ cm}^3 \text{ molecule}^{-1} \text{ s}^{-1}$, which corresponds to a reaction efficiency of $10^{-5} \%$.^[13] This is consistent with DFT calculations, which reveal that while Equation (9) is exothermic by 0.37 eV, it has a barrier of 0.61 eV (Supporting Information Figure S3).



Structural and optical properties of [Ag₃H₂L]⁺

Comparison of the action spectrum and calculated TD-DFT spectrum for the lowest energy structure, shown in Figure 3a, confirms the structural properties of [Ag₃H₂L]⁺, which possesses an Ag₃H₂ planar subunit that is attached to the DPPM ligand via both phosphorous atoms. It is worth noting that the equilibrium structure of S₁ differs from the ground state structure (see Supporting Information Figure S4), with the two hydrogen atoms being inserted into two Ag–Ag bonds. The absorption features are characterised by two bands centred at 250 nm with a shoulder at 270 nm. Corresponding TD-DFT transitions to S₁ and S₈ excited states, which are dominant in the wavelength region, are characterised mainly by the transitions within Ag₃H₂-P₂ subunits, as shown in Figure 3b.

To confirm structural assignment for [Ag₃L]⁺, the main product after photoexcitation of [Ag₃H₂L]⁺ [Eq. (7)], action spectroscopy as well as complementary calculations were performed. The main fragmentation channel after collision and excitation of [Ag₃L]⁺ is the loss of Ag₂ [Eq. (10)] (Supporting Information Figure S5). The absorption features are characterised by two bands between 200 and 300 nm (Figure 4a).

The calculated lowest energy transition at 380 nm is not accessible experimentally. The main features are reproduced experimentally while the exact positions are slightly red-shifted

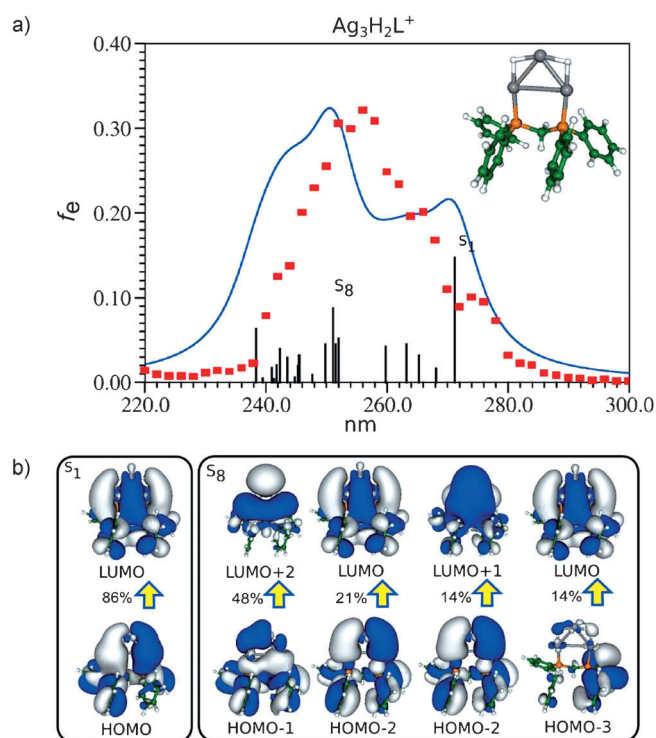


Figure 3. a) Photo-fragmentation spectrum (red dotted line) and calculated TD-DFT spectrum (the blue full line corresponds to Lorentzian broadening with half width of 10 nm, the black vertical lines correspond to values of oscillator strength f_o) for the lowest energy structure of [Ag₃H₂L]⁺; b) analysis of leading excitations contributing to the most intense transitions (to S₁ and S₈ states); cut-off for MOs is 0.04, minus and plus are labelled by blue and grey colours, respectively.

(Figure 4a). This might be caused by the conformational structure of the DPPM ligand in which the relative position of the phenyl rings substantially influences the spectroscopic pattern (vide infra). Analysis of the dominant transitions (Figure 4b) shows significant participation of excitations within the metal-ligand subunit.^[14]



Structural and optical properties of the protonated ligand

The experimental and calculated absorption properties of [L + H]⁺ were examined as a reference point (Figure 4c). The structure shown in the inset of Figure 4c, which matches the conformation of the neutral ligand determined by X-ray crystallography,^[15] is comparable to the theoretically found lowest-energy structure. However, the relative position of the phenyl rings substantially influences the absorption features (Supporting Information Figure S6). The spectrum of [L + H]⁺ (Figure 4c) is characterised by a dominant transition at 260 nm with smaller shoulders at around 240 and 300 nm. The analysis of leading excitations for intense transition (Figure 4d) illustrates that excitations occur either between left and right phenyl rings or bottom and up phenyl rings. The main fragmentation channel for this ion after UV excitation is the cleavage of the C–P bond [Eq. (11)] (Supporting Information Fig-

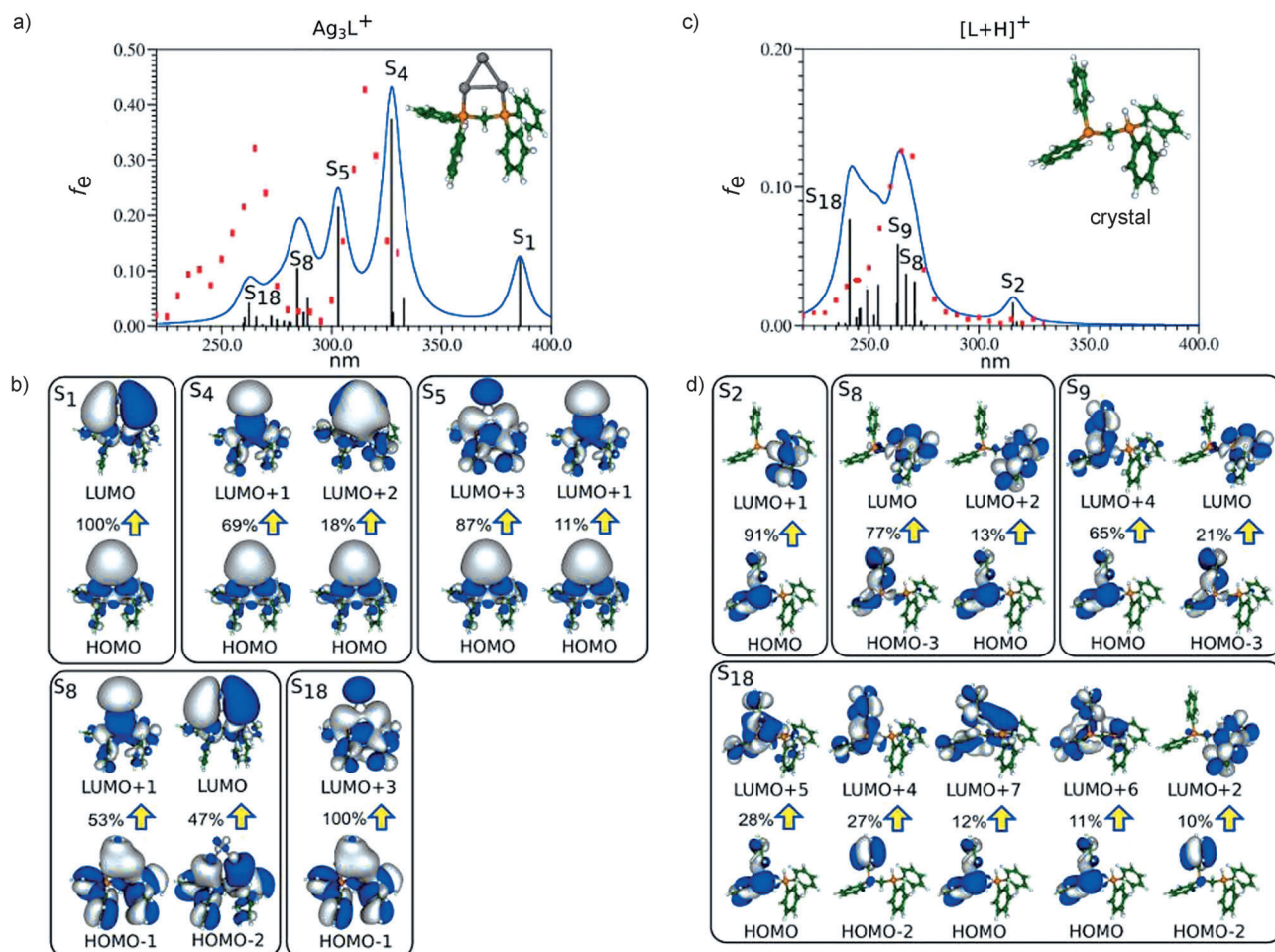
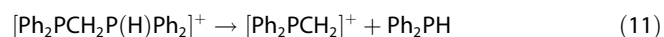


Figure 4. a) Photo-fragmentation spectrum (red dotted line) and calculated TD-DFT spectrum (the blue full line corresponds to Lorentzian broadening with half width of 10 nm, the black vertical lines correspond to values of oscillator strength f_e) for the lowest energy structure of $[Ag_3L]^+$; b) analysis of leading excitations contributing to the most intense transitions; c) spectra for the conformation of $[L+H]^+$ that matches the crystal structure of the neutral ligand (for labelling see a); and d) analysis of excitations contributing to the most intense transitions; cut-off for MOs is 0.04, minus and plus are labelled by blue and grey colours, respectively.

ure S7), which is not observed when it is complexed with silver:



Molecular dynamics for the fragmentation of $[Ag_3H_2L]^+$ in the ground state

The experimental findings described above were confirmed by MD simulations, which show that in the ground state (S_0) loss of AgH occurs [Eq. (4)] (Figure 5a) and that the experimentally observed product $[AgL]^+$ is likely to be formed by loss of 2AgH [Eq. (5)] (Figure 5b) as well as Ag_2H_2 [Eq. (6)] (Figure 5c). The fragmentation channel leading to H_2 formation and release was also found [Eq. (7)] (Figure 5d). The MD simulations were carried out at 2400 K, confirming the high stability of the precursor ion. At this high temperature, the observed fragmentation channels are initiated by Ag–Ag bond breaking that can be qualitatively explained by the nature of HOMO, which contains a node between the Ag–Ag bond, as shown in Figure 3. Note that fragmentation of the bound DPPM ligand was not

observed experimentally but that the MD simulation at high temperature indicates that fragmentation of the DPPM ligand occurs via C–P bond activation (Figure 5e). The MD simulations suggest that loss of the Ag_3H_2 subunit (Figure 5f) might occur, and this may be related to the experimentally observed formation of $[L+H]^+$ [Eq. (8)].

Molecular dynamics for the fragmentation of $[Ag_3H_2L]^+$ in the first excited state

The MD “on the fly” was also carried out in the first excited state (S_1) and compared with LID experimental results. The leading excitation for the S_1 state (cf. Figure 3) is HOMO → LUMO where LUMO contains two nodes separating each H from Ag_3 indicating qualitatively that formation of H_2 in the first excited state might occur. Indeed, in the S_1 state, two fragmentation channels involving dissociation by the formation of H_2 (cf. Figure 6a) and AgH (cf. Figure 6b) have been found by MD simulations and LID measurements (cf. Figure 2). In the latter, H_2 dissociation is dominant as expected due to the

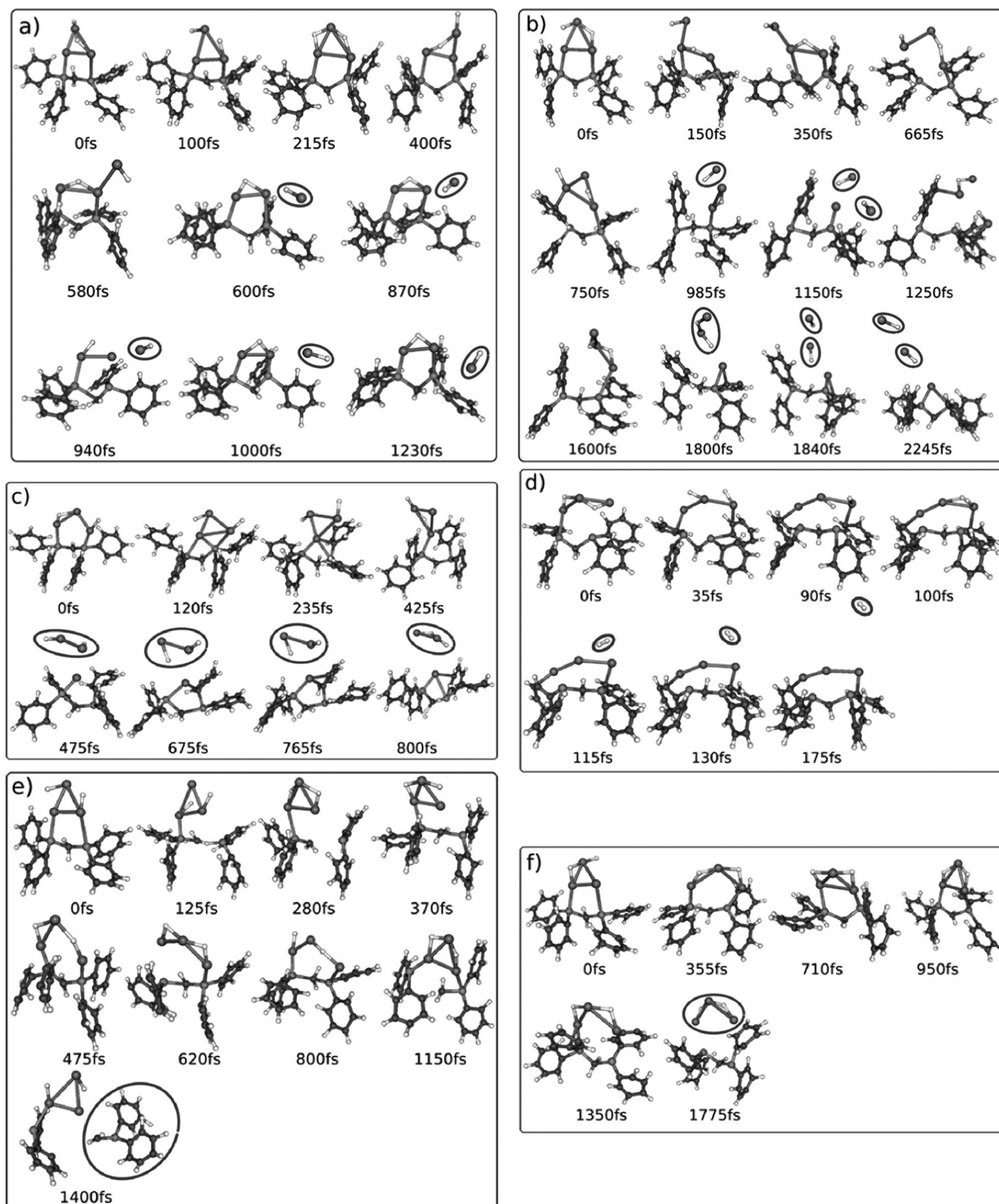


Figure 5. Snapshots of the MD "on the fly" using the DFT method with PBE functional and TZVP AO basis set in the electronic ground state S_0 from selected trajectory at high temperature (2400 K) yielding the following fragmentation channels of $[Ag_3H_2L]^+$: a) $Ag_3H_2L^+ \rightarrow Ag_2HL^+ + AgH$, b) $Ag_3H_2L^+ \rightarrow AgL^+ + 2AgH$, c) $Ag_3H_2L^+ \rightarrow AgL^+ + Ag_2H_2$, d) $Ag_3H_2L^+ \rightarrow Ag_3L^+ + H_2$, e) $Ag_3H_2L^+ \rightarrow Ag_3H_2(PPh_2)^+ + \cdot CH_2PPh_2$, f) $Ag_3H_2L^+ \rightarrow L + Ag_3H_2^+$.

nature of S_1 state. The mechanism for H_2 formation involves weakening of Ag–Ag bonds at the beginning of dynamics, which corresponds to a motion towards the equilibrium structure in S_1 state. This induces formation and subsequent release

of H_2 and deformation of Ag_3 subunit. This is not the case for the fragmentation of H_2 in the ground state (cf. Figures 5 and 6). In contrast, the mechanism for fragmentation via AgH loss in the ground and excited state are less distinguishable (cf. Fig-

ures 5a and 6b). The structure and nature of S_1 favours hydrogen formation and subsequent release, which explains why hydrogen loss is the most abundant relaxation channel after photo-excitation.

Conclusion

While transition metal hydrides are unlikely to be used as hydrogen storage materials due to their low H% weight content, there is continued interest in the use of transition metal compounds to catalyse the decomposition of other compounds with higher H% weight content.^[3,16] Since these latter process-

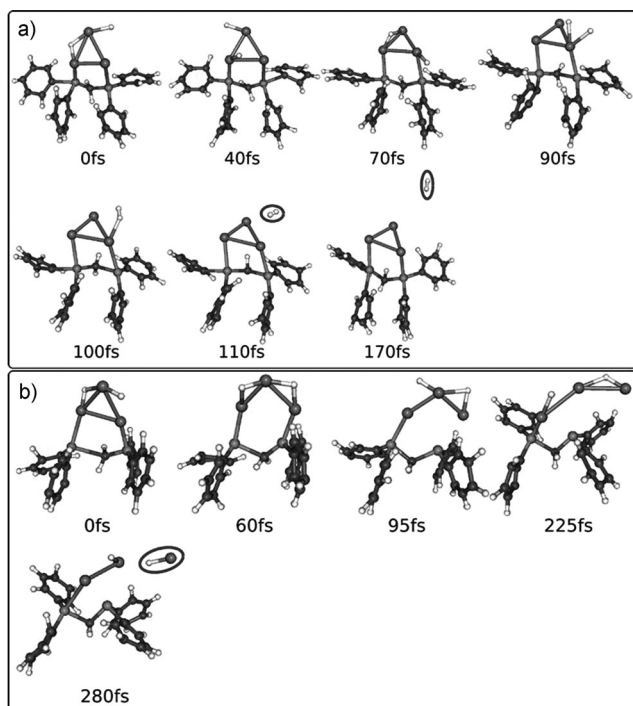


Figure 6. Snapshots of the MD “on the fly” using DFT with PBE functional and TZVP AO basis set in the first electronic excited state S_1 from selected trajectory at high temperature (2400 K) of $[Ag_3H_2L]^+$ yielding the following fragmentation channels: a) $[Ag_3H_2L]^+ \rightarrow [Ag_3L]^+ + H_2$, b) $[Ag_3H_2L]^+ \rightarrow [Ag_2HL]^+ + AgH$.

es are likely to involve the formation of transition metal hydrides, our findings are important as they reveal a key difference in the ground versus excited state dissociation of a hydride containing nanocluster. Photo-activation leads to excitation within the Ag_3H_2 core involving a geometry change, which weakens the silver–hydrogen bonds. This is a consequence of the difference between the geometry in ground and excited states of the complex. This finding may be a general route for the photo-release of hydrogen in ligated metallic hydrides. Stabilization of the metal cluster by the ligands may favour hydrogen release, which was not observed for example after UV photo-excitation of $[Li_3H_2]^+$.^[17] Current work is underway to examine the decomposition of the promising hydrogen storage material formic acid catalysed by ligated silver nanoclusters.^[18]

Finally, the observation of photo-induced hydrogen formation from an ionic silver hydride nanocluster is also important as it: 1) is a model for a photo-induced reductive elimination, which is likely to be a key step in bond formation from reactive intermediates involved in photo-catalysis by metal clusters;^[19] 2) provides a direct link between ionic silver clusters and metallic silver clusters. The reactions of sodium borohydride with silver salts in the presence of ligands is widely used to generate silver nanoclusters and silver nanoparticles.^[20] The vast majority of these studies fail to consider the possibility of forming silver hydride containing species, and while evolution of hydrogen is formulated as a key reaction during the reduction of silver salts by sodium borohydride,^[21] no-one appears to have considered light- or thermal-induced reductive elimination of hydrogen from silver hydride nanoclusters or nanoparticles.

Experimental Section

Chemicals

Silver(I) trifluoroacetate, bis(diphenylphosphino)methane (DPPM), sodium borohydride and sodium borodeuteride were purchased from Sigma–Aldrich (Saint Quentin Fallavier, France). Chloroform and methanol were HPLC grade sourced from Sigma–Aldrich. Helium seeded with 1% hydrogen gas used for the ion-molecule reactions was purchased from Air Liquide (Pierre-Bénite, France). All chemicals were used as received. $[Ag_{10}H_8L_6]^{2+}$ and $[Ag_{10}D_8L_6]^{2+}$ were synthesized in solution by the reaction of a mixture of silver(I) trifluoroacetate (2.2 mg, 0.010 mmol) and bis(diphenylphosphino)methane (3.8 mg, 0.010 mmol) with sodium borohydride (2.0 mg, 0.050 mmol) and sodium borodeuteride (2.1 mg, 0.050 mmol), respectively, in 20 mL MeOH/ $CHCl_3$ (1:1) as described previously.^[6d]

Mass spectrometry

Solutions of $[Ag_{10}H_8L_6]^{2+}$ or $[Ag_{10}D_8L_6]^{2+}$ prepared as outlined above were further diluted with methanol to a concentration of around $75 \mu M$ and introduced into a modified quadrupole linear ion trap mass spectrometer (LTQ, Thermo Fisher Scientific, San Jose, CA, USA) via electrospray ionization (ESI) using a syringe pump set to a flow rate of $5 \mu L min^{-1}$. The typical ESI conditions used were: spray voltage, 4.2–5.0 kV, capillary temperature, $250^\circ C$, nitrogen sheath gas pressure, 5 (arbitrary units), capillary voltage 15 V. The modification to the mass spectrometer consists of the installation of a quartz window fitted on the rear of the MS chamber to allow the introduction of a laser beam.^[22] The laser is a nanosecond frequency-doubled tuneable Panther™ EX OPO (Optical Parametric Oscillator) laser pumped by a Surelite™ II Nd:YAG laser (both from Continuum, Santa Clara, CA, USA). The repetition rate of the laser was 10 Hz. The laser beam passes through two diaphragms (1 mm diameter), lenses and a mechanical shutter electronically synchronized with the mass spectrometer, after which it is injected on the axis of the linear trap. The laser power was monitored with a power meter located just before the injection in the ion trap. The mechanical shutter is used to synchronize the laser irradiation with the trapping of the ions. To perform laser irradiation for a given number of laser pulses, we add in the ion trap radio frequency (RF) sequence an MS^n step with an activation amplitude of 0% and a reaction time of 500 ms, during which the shutter located on the laser beam is opened. The activation q value was set to 0.25. An m/z window of 1.3 Th was applied for ion precursor iso-

lation which contained the 2×10^7 Ag and 1×10^9 Ag isotopes. For CID experiments the normalized collision energy was set to 15% and the activation time to 100 ms.

For action spectroscopy, mass spectra were recorded after laser irradiation as a function of the laser wavelength. At each laser wavelength from 220 to 330 nm (with a 2 nm step), a laser-normalized yield of photo-fragmentation is deduced from the mass spectrum through:

$$\sigma = \ln((\text{parent} + \text{daughter})/\text{parent})/\Phi \quad (12)$$

where Φ is the laser fluence, parent is the intensity of the precursor ion, and daughter represents the intensity of the product ion peaks. Optical action spectra were obtained by plotting the normalized yield of photo-fragmentation as a function of the laser wavelength.

To assess the optical properties of $[\text{Ag}_3\text{L}]^+$ ion, we combined a BrilliantB Nd:YAG laser (from Quantel, Les Ulis, France) to the OPO laser in a two colour scheme.^[23] The 4th harmonic at $\lambda = 266$ nm was used with a repetition rate of 20 Hz and 20 mJ per pulse. The two photon beams were spatially combined via a 266 nm dichroic mirror located approximately 30 cm upstream of the ion trap entrance. The 266 nm laser beam was reflected at 90° by the dichroic mirror and injected collinearly to the axis of the ion trap. The UV laser light was injected along the same ion trap axis passing through the dichroic mirror. Two electromechanical shutters, electronically synchronized with the mass spectrometer, were placed along the 266 nm laser and UV beam from the OPO and allowed to inject the two colour lights according to a given time sequence. For UV irradiation of $[\text{Ag}_3\text{L}]^+$ ion, we used the deuterated species, $[\text{Ag}_3\text{D}_2\text{L}]^+$ precursor ions which were first selected in MS^0 , irradiated by the 266 nm UV laser for 500 ms, then the produced ion was isolated during the $\text{MS}^{(n+1)}$ stage and activated by UV from the OPO during 500 ms. Mass spectra were recorded after OPO irradiation as a function of the OPO wavelength.

For the ion-molecule reactions of $[\text{Ag}_3\text{L}]^+$ with hydrogen, the normal high purity helium bath gas was replaced with a helium cylinder seeded with 1% hydrogen. $[\text{Ag}_3\text{L}]^+$ was formed by multistage mass spectrometry experiments using CID to induce fragmentation of precursor ions, and then mass selected and stored in the ion trap with reaction times of up to 10 s.

Theory

DFT was used to determine the structural properties of the $[\text{Ag}_3\text{L}]^+$ and $[\text{Ag}_3\text{H}_2\text{L}]^+$. For this purpose the hybrid B3LYP functional^[24] with TZVP atomic basis set was used for all atoms.^[25] Silver atoms were treated by Stuttgart relativistic effective core potential (RECP) with corresponding AO basis set.^[26] Although the extensive search for lowest energy structures were performed, the crystal structure of the bis(diphenylphosphino)methane ligand, $(\text{Ph}_2\text{P})_2\text{CH}_2$, was used as a starting reference for the relative orientation of the phenyl rings, which seem to have a large influence on optical properties of their complexes with Ag_3 and H_2 . For optimized structures the stationary points were characterised by calculating the harmonic vibrational frequencies. For calculations of the absorption spectra time dependent density functional method (TD-DFT) with B3LYP functional and TZVP AO basis set was employed. The fragmentation channels in the ground and excited states were determined using molecular dynamics (MD) "on the fly" based on DFT approach with Perdew–Burke–Ernzerhof (PBE) functional^[27] and resolution of identity (RI) approximation^[28] due to considerably smaller computational demand. The initial conditions for the MD "on the fly" in the ground and first excited state were obtained by sam-

pling coordinates and momenta at regular time intervals along a ground-state trajectory at constant temperature in the framework of DFT method.

Acknowledgements

R.A.J.O. thanks the Australian Research Council for financial support through the CoE program; The Université de Lyon for a visiting Professorship and the School of Chemistry at the University of Melbourne for a short term study leave. V.B.-K. and P.D. thank the CNRS NCBA international laboratory. V.B.-K. acknowledges support by the Deutsche Forschungsgemeinschaft (DFG, FOR1282) and by Split–Dalmatia County.

Keywords: fragmentation channels • hydrogen formation • molecular dynamics • multistage mass spectrometry • photochemistry

- [1] a) *The Hydrogen Economy: Opportunities, Costs, Barriers, and R&D Needs*, National Academy, **2004**; b) G. W. Crabtree, M. S. Dresselhaus, M. V. Buchanan, *Physics Today* **2004**, 57, 39–44; c) P. Jena, *J. Phys. Chem. Lett.* **2011**, 2, 206–211.
- [2] a) L. Schlapbach, A. Züttel, *Nature* **2001**, 414, 353–358; b) F. Schüth, *Eur. Phys. J. Special Topics* **2009**, 176, 155–166; c) M. T. Kelly, *Struct. Bonding (Berlin)* **2011**, 141, 169–201.
- [3] For an excellent review on hydrogen storage materials, including a discussion on the "5 commandments" for the ideal hydrogen storage material, see: W. Grochala, P. P. Edwards, *Chem. Rev.* **2004**, 104, 1283–1315.
- [4] A. S. Weller, J. S. McIndoe, *Eur. J. Inorg. Chem.* **2007**, 4411–4423.
- [5] a) K. Shimizu, R. Sato, A. Satsuma, *Angew. Chem. Int. Ed.* **2009**, 48, 3982–3986; *Angew. Chem.* **2009**, 121, 4042–4046; b) K. Shimizu, K. Sugino, K. Sawabe, A. Satsuma, *Chem. Eur. J.* **2009**, 15, 2341–2351; c) K. Shimizu, A. Satsuma, *J. Jpn. Pet. Inst.* **2011**, 54, 347–360.
- [6] a) C. W. Liu, H.-W. Chang, C.-S. Fang, B. Sarkar, J.-C. Wang, *Chem. Commun.* **2010**, 46, 4571–4573; b) C. W. Liu, H.-W. Chang, B. Sarkar, J.-Y. Saillard, S. Kahal, Y.-Y. Wu, *Inorg. Chem.* **2010**, 49, 468–475; c) C. W. Liu, P.-K. Liao, C.-S. Fang, J.-Y. Saillard, S. Kahal, J.-C. Wang, *Chem. Commun.* **2011**, 47, 5831–5833; d) A. Zavras, G. N. Khairallah, T. U. Connell, J. M. White, A. J. Edwards, P. S. Donnelly, R. A. J. O'Hair, *Angew. Chem. Int. Ed.* **2013**, 52, 8474–8474; *Angew. Chem.* **2013**, 125, 8632–8632; e) B. K. Tate, C. M. Wyss, J. Bacsa, K. Kluge, L. Gelbaum, J. P. Sadighi, *Chem. Sci.* **2013**, 4, 3068–3074; f) A. Zavras, G. N. Khairallah, T. U. Connell, J. M. White, A. J. Edwards, R. J. Mulder, P. S. Donnelly, R. A. J. O'Hair, *Inorg. Chem.* **2014**, 53, 7429–7437.
- [7] R. Mitrić, J. Petersen, A. Kulesza, M. Röhr, V. Bonačić-Koutecký, C. Brunet, R. Antoine, P. Dugourd, M. Broyer, R. A. J. O'Hair, *J. Phys. Chem. Lett.* **2011**, 2, 548–552.
- [8] a) G. N. Khairallah, R. A. J. O'Hair, *Angew. Chem. Int. Ed.* **2005**, 44, 728–731; *Angew. Chem.* **2005**, 117, 738–741; b) G. N. Khairallah, R. A. J. O'Hair, *Dalton Trans.* **2005**, 2702–2712; c) G. N. Khairallah, R. A. J. O'Hair, *Dalton Trans.* **2007**, 3149–3157; d) G. N. Khairallah, R. A. J. O'Hair, *Dalton Trans.* **2008**, 2956–2965; e) F. Q. Wang, G. N. Khairallah, R. A. J. O'Hair, *Int. J. Mass Spectrom.* **2009**, 283, 17–25; f) A. J. Clark, A. Zavras, G. N. Khairallah, R. A. J. O'Hair, *Int. J. Mass Spectrom.* **2014**; DOI: 10.1016/j.ijms.2014.07.015.
- [9] For an example of the gas-phase collision-induced formation and loss of H_2 from the metal hydride cluster ion Nb_7H_8^+ see: A. B. Vakhtin, E. M. Markin, K.-I. Sugawara, *Chem. Phys.* **2000**, 262, 93–104.
- [10] The gas-phase reactions of transition metal atomic cations with H_2 have been widely studied: a) P. B. Armentrout, *Int. Rev. Phys. Chem.* **1990**, 9, 115–148. For examples of the gas-phase reactions of metal cluster ions with H_2 see: b) A. B. Vakhtin, K.-I. Sugawara, *J. Chem. Phys.* **2001**, 115, 3629–3639; c) F. Liu, P. B. Armentrout, *J. Chem. Phys.* **2005**, 122, 194320/1–194320/12.
- [11] The gas-phase IR spectrum of the $\text{Ag}(\text{H}_2)^+$ complex has been recently reported: V. Dryza, E. J. Bieske, *J. Phys. Chem. Lett.* **2011**, 2, 719–724.

- [12] W. A. Donald, G. N. Khairallah, R. A. J. O'Hair, *J. Am. Soc. Mass Spectrom.* **2013**, *24*, 811–815.
- [13] Activation of the H–H bond by Ag^+ is endothermic and produces AgH^+ : Y.-M. Chen, J. L. Elkind, P. B. Armentrout, *J. Phys. Chem.* **1995**, *99*, 10438–10445.
- [14] T. Tabarin, A. Kulesza, R. Antoine, R. Mitrić, M. Broyer, P. Dugourd, V. Bonačić-Koutecký, *Phys. Rev. Lett.* **2008**, *101*, 213001.
- [15] R. A. Burrow, F. C. Wouters, L. Borgen de Castro, C. Peppe, *Acta Crystallogr. E* **2007**, *63*, o2559.
- [16] For reviews of the metal catalysed decomposition of formic acid for applications in hydrogen storage, see: a) S. Enthaler, J. Langermann, T. Schmidt, *Energy Environ. Sci.* **2010**, *3*, 1207–1217; b) M. Grasemann, G. Laurenczy, *Energy Environ. Sci.* **2012**, *5*, 8171–8181.
- [17] R. Antoine, P. Dugourd, D. Rayane, E. Benichou, M. Broyer, *J. Chem. Phys.* **1997**, *107*, 2664–2672.
- [18] For a report on the gas-phase decomposition of formic acid catalyzed by magnesium hydrides see: G. N. Khairallah, R. A. J. O'Hair, *Int. J. Mass Spectrom.* **2006**, *254*, 145–151.
- [19] a) R. J. Wang, T. Fujimoto, T. Shido, M. Ichikawa, *J. Chem. Soc. Chem. Commun.* **1992**, 962–963; b) Y. Negishi, *Bull. Chem. Soc. Jpn.* **2014**, *87*, 375–389.
- [20] M. Wuthschick, B. Paul, R. Bienert, A. Sarfraz, U. Vainio, M. Sztucki, R. Kraehnert, P. Strasser, K. Rademann, F. Emmerling, *J. Polym. Mater.* **2013**, *25*, 4679–4689, and references cited therein.
- [21] S. D. Solomon, M. Bahadory, A. V. Jeyarajasingam, S. A. Rutkowsky, C. Boritz, L. Mulfinger, *J. Chem. Educ.* **2007**, *84*, 322–325.
- [22] a) V. Larraillet, R. Antoine, P. Dugourd, J. Lemoine, *Anal. Chem.* **2009**, *81*, 8410–8416; b) R. Antoine, P. Dugourd, *Phys. Chem. Chem. Phys.* **2011**, *13*, 16494–16509.
- [23] L. Joly, R. Antoine, A. R. Allouche, P. Dugourd, *J. Am. Chem. Soc.* **2008**, *130*, 13832–13833.
- [24] a) A. D. Becke, *J. Chem. Phys.* **1988**, *38*, 3098; b) A. D. Becke, *J. Chem. Phys.* **1993**, *98*, 5648; c) C. Lee, W. Yang, R. G. Parr, *Phys. Rev. B* **1988**, *37*, 785.
- [25] A. Schäfer, H. Huber, R. Ahlrichs, *J. Chem. Phys.* **1994**, *100*, 5829–5835.
- [26] D. Andrae, U. Haeussermann, M. Dolg, H. Stoll, H. Preuss, *Theor. Chim. Acta* **1990**, *77*, 123.
- [27] J. P. Perdew, K. Burke, M. Ernzerhof, *Phys. Rev. Lett.* **1996**, *77*, 3865–3868.
- [28] K. Eichkorn, O. Treutler, H. Öhm, M. Häser, R. Ahlrichs, *Chem. Phys. Lett.* **1995**, *242*, 652–660.

Received: June 24, 2014

Published online on October 16, 2014

3 Ligand-induced substrate steering and reshaping of $[\text{Ag}_2(\text{H})]^+$ scaffold for selective CO_2 extrusion from formic acid

ARTICLE

Received 14 Dec 2015 | Accepted 26 Apr 2016 | Published 6 Jun 2016

DOI: 10.1038/ncomms11746

OPEN

Ligand-induced substrate steering and reshaping of $[\text{Ag}_2(\text{H})]^+$ scaffold for selective CO_2 extrusion from formic acid

Athanasios Zavras^{1,2}, George N. Khairallah^{1,2}, Marjan Krstić³, Marion Girod⁴, Steven Daly⁵, Rodolphe Antoine⁵, Philippe Maitre⁶, Roger J. Mulder⁷, Stefanie-Ann Alexander^{1,2}, Vlasta Bonačić-Koutecký^{3,8}, Philippe Dugourd⁵ & Richard A.J. O'Hair^{1,2}

Metalloenzymes preorganize the reaction environment to steer substrate(s) along the required reaction coordinate. Here, we show that phosphine ligands selectively facilitate protonation of binuclear silver hydride cations, $[\text{LAg}_2(\text{H})]^+$ by optimizing the geometry of the active site. This is a key step in the selective, catalysed extrusion of carbon dioxide from formic acid, HO_2CH , with important applications (for example, hydrogen storage). Gas-phase ion-molecule reactions, collision-induced dissociation (CID), infrared and ultraviolet action spectroscopy and computational chemistry link structure to reactivity and mechanism. $[\text{Ag}_2(\text{H})]^+$ and $[\text{Ph}_3\text{PAg}_2(\text{H})]^+$ react with formic acid yielding Lewis adducts, while $[(\text{Ph}_3\text{P})_2\text{Ag}_2(\text{H})]^+$ is unreactive. Using bis(diphenylphosphino)methane (dppm) reshapes the geometry of the binuclear $\text{Ag}_2(\text{H})^+$ scaffold, triggering reactivity towards formic acid, to produce $[\text{dppmAg}_2(\text{O}_2\text{CH})]^+$ and H_2 . Decarboxylation of $[\text{dppmAg}_2(\text{O}_2\text{CH})]^+$ via CID regenerates $[\text{dppmAg}_2(\text{H})]^+$. These gas-phase insights inspired variable temperature NMR studies that show CO_2 and H_2 production at 70 °C from solutions containing dppm, AgBF_4 , NaO_2CH and HO_2CH .

¹School of Chemistry and Bio21 Molecular Science and Biotechnology Institute, The University of Melbourne, 30 Flemington Road, Parkville, Victoria 3010, Australia. ²ARC Centre of Excellence for Free Radical Chemistry and Biotechnology, 30 Flemington Road, Parkville, Victoria 3010, Australia. ³Center of Excellence for Science and Technology – Integration of Mediterranean region (STIM) at Interdisciplinary Center for Advanced Science and Technology (ICAST), University of Split, Meštrovićevo šetalište 45, 21000 Split, Croatia. ⁴Institut des Sciences Analytiques, Université de Lyon, Université Lyon 1-CNRS-ENS Lyon, 69100 Villeurbanne, France. ⁵Institut Lumière Matière, Université Lyon 1-CNRS, Université de Lyon 69622 Villeurbanne Cedex, France. ⁶Laboratoire de Chimie Physique, Bâtiment 349, Université Paris-Sud, CNRS, Université Paris-Saclay, F-91405 Orsay, France. ⁷CSIRO Manufacturing, Bayview Avenue, Clayton, Victoria 3168, Australia. ⁸Humboldt-Universität Berlin, Institut für Chemie, 12489 Berlin, Germany. Correspondence and requests for materials should be addressed to V.B.-K. (email: vbk@chemie.hu-berlin.de) or to P.D. (email: philippe.dugourd@univ-lyon1.fr) or to R.A.J.O. (email: rohair@unimelb.edu.au).

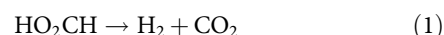
Nature uses a number of design principles to create different classes of enzyme catalysts capable of a wide range of chemical transformations of substrates¹. A metal ion or metal cluster often has a critical role as a co-factor². A key concept in enzyme catalysis is the preorganization of the reaction environment by the enzyme, directing the substrate to the reaction site, which provides a favourable geometry for the transition state required for bond activation. In essence, the enzyme steers the substrate along the required reaction coordinate to allow the desired transformation to product(s)³.

The concept of changing the environment at a metal centre to switch on reactivity has also been recently exploited in gold chemistry. Au(I) complexes prefer to be linear, which is why they are unreactive toward oxidative addition of iodobenzene (Fig. 1a). To promote reactivity, ligand-induced preorganization of the metal centre has been shown to accommodate the geometry of the ensuing oxidative addition of aryl halides (Fig. 1b)⁴. Embedding the metal centre within a ligated nanocluster also facilitates reactivity, which can be further tuned by the choice of ligand (Fig. 1c)⁵.

Here, we use gas-phase experiments and density functional theory (DFT) calculations to examine how the binuclear silver hydride cation, $[\text{Ag}_2(\text{H})]^+$ (Fig. 1d,f), can be structurally manipulated by the appropriate choice of phosphine ligands to switch on the protonation of the hydride by formic acid to liberate hydrogen, which is a key step in the selective, catalysed decomposition of formic acid that does not occur in absence of ligands. We chose $[\text{Ag}_2(\text{H})]^+$ since it has been spectroscopically

characterized⁷ and ligated variants can readily be formed^{8–10}. Formic acid was chosen as a substrate since its decomposition is one of the most widely studied topics in chemistry, with a rich history spanning more than a century^{11–14}. Apart from the academic interest in establishing the mechanism(s) of decomposition, the selective, catalysed decomposition of formic acid has potentially important applications in areas ranging from hydrogen storage^{15–17} through to the generation of *in situ* hydrogenation sources for reduction of organic substrates^{18,19}.

In the absence of a catalyst, pyrolysis of formic acid proceeds via two primary pathways: decarboxylation (equation (1)) and dehydration (equation (2)). These reactions are coupled by the water–gas shift reaction (Equation (3))^{20,21} and have been widely studied experimentally²² and theoretically²³. In the gas-phase, the dehydration channel (Equation (2)) is the dominant reaction²², consistent with a lower activation energy, as predicted by DFT calculations²³.



The concept of using metal catalysts to selectively decompose formic acid dates back over 100 years to Sabatier's work on the role of metal and metal oxide catalysts¹¹, and the substantial early literature has been reviewed^{12–14}. Over the past century, a wide range of metal catalysts have been surveyed for their potential to

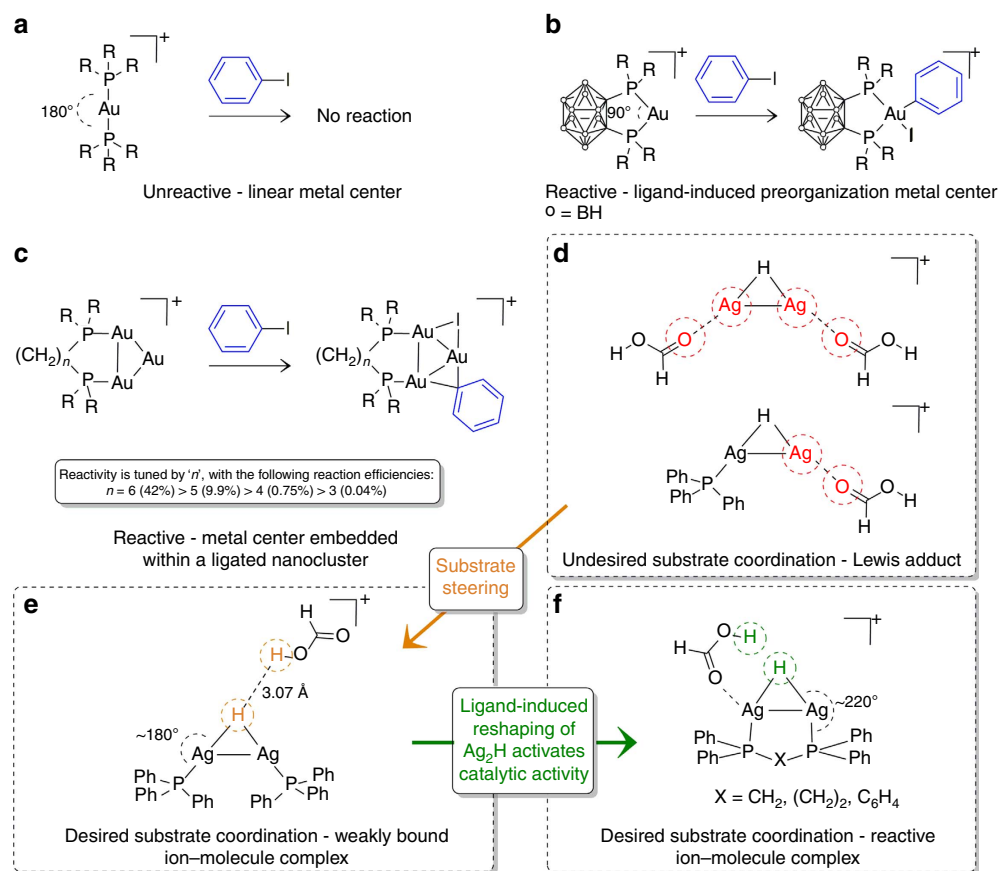


Figure 1 | Key concepts for switching on reactivity at coinage metal centres. (a) Linear diphosphine Au(I) complexes do not undergo oxidative addition of iodobenzene. Oxidative addition of iodobenzene does occur for: (b) bisphosphine Au(I) complexes with P–Au–P bond angles of $\approx 90^\circ$; and (c) bisphosphine ligated gold cluster. Switching on desired protonation of binuclear silver hydride cations, $[\text{LAg}_2(\text{H})]^+$ by formic acid: (d) undesired Lewis adduct formation occurs when silver centres have vacant coordination sites; (e) formic acid is steered to active site by phosphine ligands; (f) bisphosphine ligands reshape geometry of active site to switch on desired protonation reaction.

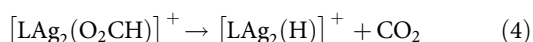
selectively decarboxylate formic acid (Equation (1)). The types of metal catalysts examined include metal and metal oxide surfaces¹⁴, mononuclear metal complexes²⁴, metal clusters²⁵ and metal nanoparticles²⁶.

The powerful combination of gas-phase ion–molecule reactions (IMRs), collision-induced dissociation (CID), infrared and ultraviolet action spectroscopy and computational chemistry allows us to examine the role of the ligand (L) in promoting decomposition of formic acid catalysed by the binuclear silver hydride cations, $[\text{LAg}_2(\text{H})]^+$. Guided by the right choice of ligand, we have translated our gas-phase results to achieve the selective condensed-phase decarboxylation of formic acid.

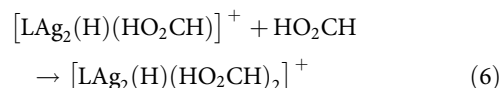
Results

Catalyst systems. The six systems that we have studied to examine the catalytic cycle (Fig. 2a) for decomposition of formic acid are designated by the letters, which identify the ligands as: **1a** = no ligand; **1b** L = PPh_3 ; **1c** L = $2 \times \text{PPh}_3$; **1d** L = bis(diphenylphosphino)methane (dppm); **1e** L = 1,2-bis(diphenylphosphino)benzene (dppbz); and **1f** L = bis(diphenylphosphino)ethane (dppe). DFT calculations reveal that the ligand(s) can induce changes to the geometry of the $\text{Ag}_2(\text{H})^+$ scaffold (Fig. 2b).

Reactions of 1a–1f with formic acid. $[\text{Ag}_2(\text{H})]^+$ and its ligated variants, $[\text{LAg}_2(\text{H})]^+$, were prepared in the gas-phase via well-established ligand fragmentation reactions (Supplementary Figs 1–6; Supplementary equations 1 and 2), including decarboxylation of coordinated formates, equation (4) (refs 27,28). The precursor ions were formed via electrospray ionization (ESI).



1a m/z 215, reacts via sequential addition of formic acid (Supplementary Fig. 7a,b; equations (5) and (6); Fig. 2a (iii) and (v)), as confirmed via mass selection of $[\text{Ag}_2(\text{H})(\text{HCOH})]^+$ m/z 261, and subsequent reaction with formic acid, which yields $[\text{Ag}_2(\text{H})(\text{HO}_2\text{CH})_2]^+$ m/z 307. CID of $[\text{Ag}_2(\text{H})(\text{HCOH})]^+$ regenerates **1a** via loss of formic acid (Fig. 2b and Supplementary Fig. 7c). These results confirm the concept that formic acid is trapped down the wrong reaction pathway (Fig. 2a (iii)).



We next tested whether ligation could steer the substrate away from coordination to form a Lewis adduct and toward the hydride site. Blocking one Ag site in **1b** results in the formation of a mono adduct (equation (5), L = Ph_3P , Supplementary Fig. 8b). Kinetic modelling of the temporal profiles of $[(\text{Ph}_3\text{P})_n\text{Ag}_2(\text{H})]^+$ and $[(\text{Ph}_3\text{P})_n\text{Ag}_2(\text{H})(\text{HO}_2\text{CH})_{2-n}]^+$ (Supplementary Table 1) reveals that: (i) the addition of formic acid for $n=0$ and 1 is at $\approx 1\%$ of the collision rate; (ii) in the case of $n=0$, addition of formic acid is reversible. Blocking both Ag sites makes **1c** unreactive toward formic acid (Supplementary Fig. 8a). By replacing both Ph_3P ligands with the dppm ligand, the $\text{Ag}_2(\text{H})^+$ scaffold of **1e** is compressed, with the P–Ag–H angle deviating substantially away from linearity. As a consequence $[\text{dppmAg}_2(\text{H})]^+$ **1d** (m/z 601) reacts with formic acid to form $[\text{dppmAg}_2(\text{O}_2\text{CH})]^+$ and H_2 (equation (7), Fig. 3a), a reaction that proceeds at $\approx 1\%$ of the collision rate (Supplementary Table 1). When $[\text{dppmAg}_2(\text{D})]^+$ m/z 602, formed via

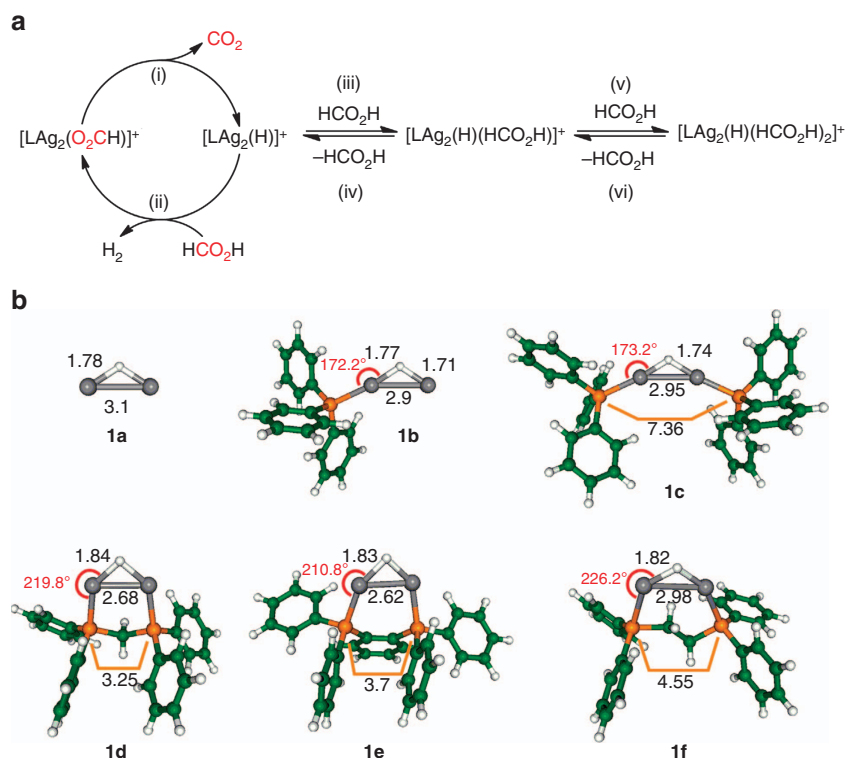


Figure 2 | Role of the ligand in the selective decarboxylation of formic acid catalysed by $[\text{LAg}_2(\text{H})]^+$. (a) catalytic cycle, with following steps: (i), decarboxylation of $[\text{LAg}_2(\text{O}_2\text{CH})]^+$ via CID to generate $[\text{LAg}_2(\text{H})]^+$. (ii), IMR of $[\text{LAg}_2(\text{H})]^+$ to regenerate $[\text{LAg}_2(\text{O}_2\text{CH})]^+$. (iii), IMR of $[\text{LAg}_2(\text{H})]^+$. (iv), CID of $[\text{LAg}_2(\text{H})(\text{HO}_2\text{CH})]^+$ to regenerate $[\text{LAg}_2(\text{H})]^+$. (v), IMR of $[\text{LAg}_2(\text{H})(\text{HO}_2\text{CH})]^+$ with HO_2CH to yield $[\text{LAg}_2(\text{H})(\text{HO}_2\text{CH})_2]^+$. (vi), CID of $[\text{LAg}_2(\text{H})(\text{HO}_2\text{CH})_2]^+$ to regenerate $[\text{LAg}_2(\text{H})(\text{HO}_2\text{CH})]^+$. Most stable DFT-calculated structures of systems examined: (b) **1a**, **1b**, **1c**, **1d**, **1e** and **1f**. DFT calculations used the hybrid functional B3LYP⁵³ with def2-TZVP AO basis set⁵⁴ for all atoms and corresponding relativistic effective core potential for Ag atoms⁵⁵. Bond distances are given in Å (black) and P–Ag–H bond angles in degrees (red).

fragmentation of the cluster cation $[\text{Ag}_3(\mu_3\text{-D})\text{dppm}_3]^{2+}$,⁸ was allowed to react with formic acid, the unlabelled formate $[\text{dppmAg}_2(\text{O}_2\text{CH})]^+$ and HD are formed (equation (8) and Supplementary Fig. 9b), which is consistent with a mechanism in which the hydride is protonated by formic acid to release H_2 . The reactions given by equations (4) and (7) represent those associated with the catalytic cycle (Fig. 2a) for the selective decarboxylation of formic acid (equation (1)). Indeed, sequential reactions of CID of $[\text{dppmAg}_2(\text{O}_2\text{CH})]^+$ to form $[\text{dppmAg}_2(\text{H})]^+$ followed by ion-molecule reaction (IMR) with formic acid, allows completion of the cycle multiple times with no significant loss of signal (Supplementary Fig. 9). The other binuclear silver hydride cations, $[\text{LAg}_2(\text{H})]^+$, containing bisphosphine ligands also reacted with formic acid to reform the $[\text{LAg}_2(\text{O}_2\text{CH})]^+$ and H_2 (equation (7) and Fig. 3b,c), although the nature of the ligand influences the reaction efficiencies, which follow the order $1\text{d} \approx 1\text{e} \gg 1\text{f}$ (Supplementary Table 1).



IR and UV spectroscopy of reactive intermediates. In order to relate the structure of the proposed reactive intermediates **1d** and $[\text{dppmAg}_2(\text{O}_2\text{CH})]^+$ to their observed reactivity (Fig. 2a), we next turned our attention to their gas-phase characterization²⁹ using infrared multiple photon dissociation (IRMPD) spectroscopy (Fig. 4a,b)³⁰ and ultraviolet action-spectroscopy (Fig. 4c,d)³¹. For each complex, the experimental IRMPD spectrum is compared against the theoretically predicted infrared absorption spectrum of the lowest energy isomer. In the case of $[\text{dppmAg}_2(\text{H})]^+$ (m/z 601), infrared features could only be observed if mass-selected ions were irradiated on resonance with the infrared free electron laser (FEL) and in conjunction with an auxiliary CO_2 laser³². The enhancement of the spectroscopic resolution was such that relatively weak IRMPD features could be observed (Fig. 4a). In the case of $[\text{dppmAg}_2(\text{O}_2\text{CH})]^+$ (m/z 645), however, infrared-induced

fragmentation was more easily achieved using the infrared FEL only, and the auxiliary CO_2 laser was thus not used.

For both $[\text{dppmAg}_2(\text{H})]^+$ and $[\text{dppmAg}_2(\text{O}_2\text{CH})]^+$, a good match was observed between the experimental and theoretically predicted infrared spectrum for the lowest energy structure. A detailed assignment of the main observed infrared features is provided (Supplementary Table 2). As expected, infrared bands associated with the auxiliary dppm ligand are observed. This is particularly true in the case of the $[\text{dppmAg}_2(\text{H})]^+$ spectrum where four bands can be assigned to phenyl in plane ring deformation (998 cm^{-1}), CH_2 twist and $\text{P-C}_6\text{H}_5$ stretch ($1,097\text{ cm}^{-1}$), phenyl in plane CH bending ($1,438\text{ cm}^{-1}$), and phenyl CH bending and ring deformation ($1,478\text{ cm}^{-1}$).

More importantly, diagnostic bands of the coordination mode of the hydride and formate ligands are also observed. In the case of $[\text{dppmAg}_2(\text{H})]^+$ (Fig. 4a), the μ^2 bridging coordination mode of the hydride is well characterized by two bands associated with the asymmetric and symmetric Ag-H stretching bands observed at 900 and $1,250\text{ cm}^{-1}$, respectively, in excellent agreement with the theoretical prediction (916 and $1,236\text{ cm}^{-1}$, respectively). In the case of $[\text{dppmAg}_2(\text{O}_2\text{CH})]^+$ (Fig. 4b), it was expected that the positions of the asymmetric and symmetric formate CO stretching bands were sensitive to the formate coordination modes. These two bands are strongly infrared active, and could thus be revealed through IRMPD without the use of the auxiliary CO_2 laser. As can be seen in Supplementary Table 2, the observed position of these two bands ($1,360$ and $1,547\text{ cm}^{-1}$, respectively) is in excellent agreement with their predicted positions ($1,345$ and $1,564\text{ cm}^{-1}$, respectively) for the lowest energy structure of the $[\text{dppmAg}_2(\text{O}_2\text{CH})]^+$ complex. It can thus be concluded that IRMPD spectroscopy of $[\text{dppmAg}_2(\text{H})]^+$ and $[\text{dppmAg}_2(\text{O}_2\text{CH})]^+$, in conjunction with electronic structure calculations, provide clear structural diagnostic of the coordination mode within the Ag_2H^+ or $\text{Ag}_2(\text{O}_2\text{CH})^+$ scaffolds.

Comparison of the ultraviolet action spectra and calculated time dependent density functional method (TDDFT) spectra using dispersion correction D3 (ref. 33) for the lowest energy structures for $[\text{dppmAg}_2(\text{H})]^+$ and $[\text{dppmAg}_2(\text{O}_2\text{CH})]^+$ are shown in Fig. 4c,d. Introduction of dispersion correction into TDDFT reduces the distance between two parallel aromatic rings, thus preventing their mobility. In the case of $[\text{dppmAg}_2(\text{H})]^+$, the experimental spectrum shows an increase in fragmentation yield as the wavelength decreases, with two superimposed bands at 270 and 235 nm (Fig. 4c). The corresponding TDDFT transitions with dominant oscillator strengths are due to leading excitations from HOMO-1 and HOMO to LUMO+2 (Supplementary Fig. 10), respectively. They involve the Ag_2H subunit as well as the ligand. In contrast, the S_1 and S_2 states located close to 300 nm are characterized by HOMO to LUMO and HOMO-1 to LUMO excitations, respectively, in which Ag_2 or Ag_2HP_2 are more involved than ring subunits of the ligand.

In the case of $[\text{dppmAg}_2(\text{O}_2\text{CH})]^+$, a similar action spectrum was obtained. The main difference is a pronounced shoulder at 250 nm resulting from an intense S_1 transition involving mainly the Ag_2HP_2 subunit (Supplementary Fig. 10). The formate has little role in the excitations leading to absorption in this spectral region, which explains the similarity between the two optical spectra. Absorption spectra obtained with TDDFT-D3 are in good agreement with the experimental ultraviolet photodissociation (UVPD) spectra, thus confirming the calculated structural properties. Altogether, on the basis of UVPD and IRMPD spectra, the structural assignments of $[\text{dppmAg}_2(\text{H})]^+$ and $[\text{dppmAg}_2(\text{O}_2\text{CH})]^+$ are unambiguous.

DFT-calculated mechanism of steps associated with the catalytic cycle. The catalytic cycle for the selective decomposition

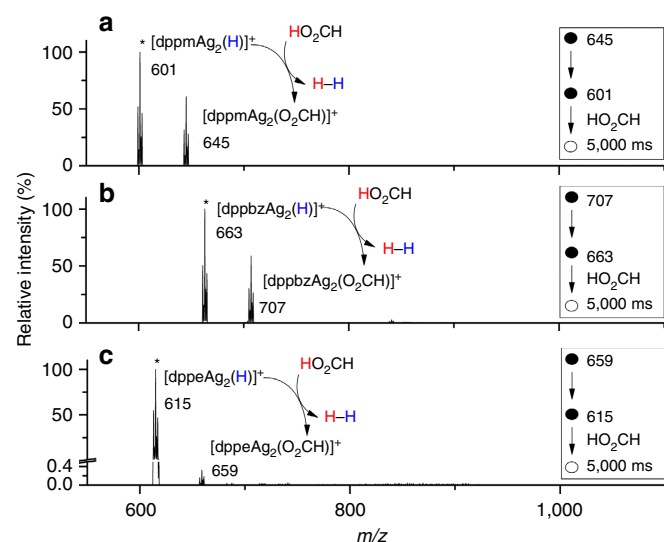


Figure 3 | Ion-molecule reaction of formic acid with mass-selected hydrides, $[\text{LAg}_2(\text{H})]^+$. (a) $\text{L} = \text{dppm}$, **1d**, $[\text{HO}_2\text{CH}]_{\text{ion trap}} = 7.19 \times 10^9$ molecules cm^{-3} . (b) $\text{L} = \text{dppbz}$, **1e**, $[\text{HO}_2\text{CH}]_{\text{ion trap}} = 7.30 \times 10^9$ molecules cm^{-3} . (c) $\text{L} = \text{dppe}$, **1f**, $[\text{HO}_2\text{CH}]_{\text{ion trap}} = 7.09 \times 10^9$ molecules cm^{-3} . The most intense peak of the isotope cluster is represented by the m/z value. * Represents the mass selected precursor ion.

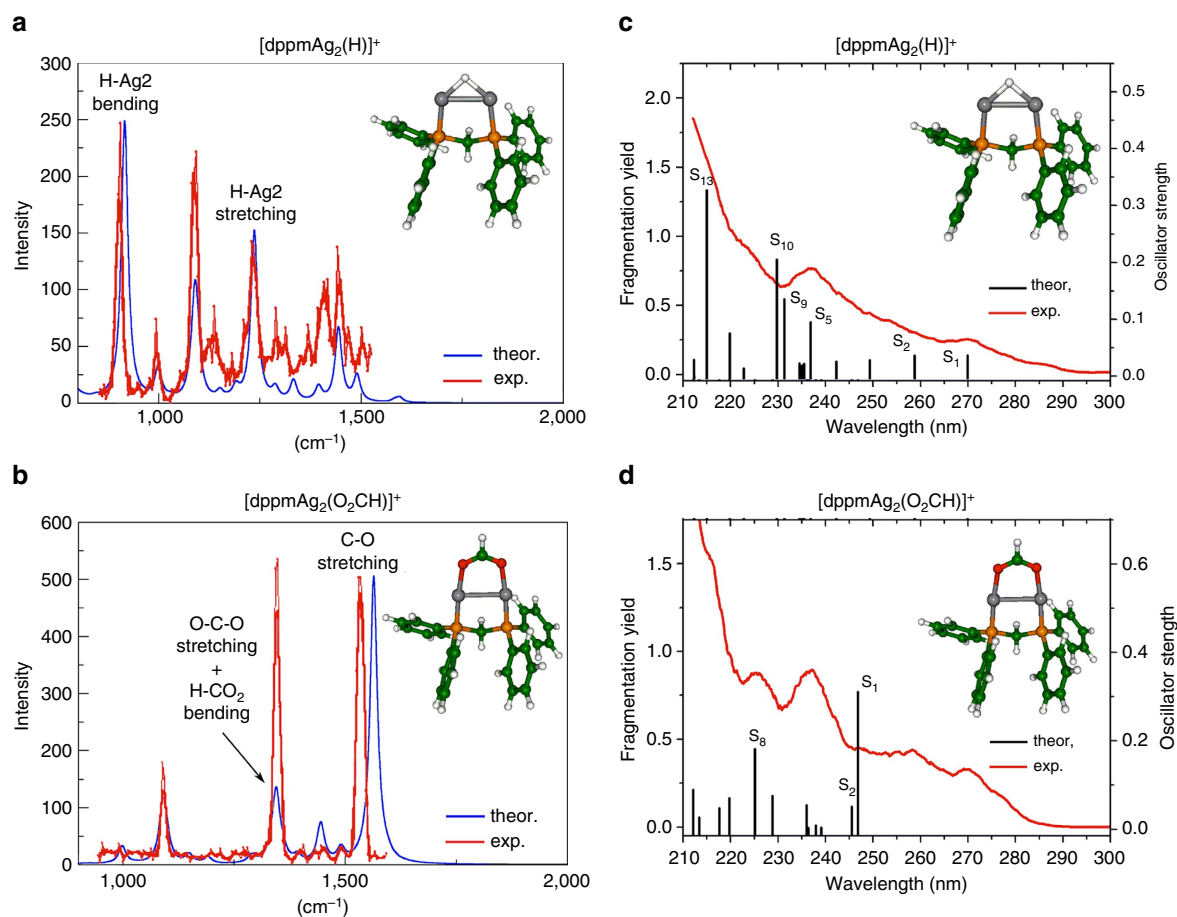


Figure 4. | Experimental (red line) and DFT-calculated (blue line) IRMPD and UV spectra (hybrid functional B3LYP with Stuttgart relativistic effective core potential for Ag atoms with corresponding def2-TZVP AO basis set, same AO basis set for all other atoms) of (a) $[\text{dppmAg}_2(\text{H})]^+$, **1d**. (b) $[\text{dppmAg}_2(\text{O}_2\text{CH})]^+$. A scaling factor of 0.98 was applied to the calculated harmonic frequencies. UV action spectrum (red line) and calculated TDDFT spectrum with dispersion correction D3 (using CAM-B3LYP functional with Stuttgart relativistic effective core potential for Ag atoms with corresponding def2-TZVP AO basis set for all atoms, the black vertical lines correspond to values of oscillator strength frequency f_e) for the lowest energy structure of: (c) $[\text{dppmAg}_2(\text{H})]^+$. (d) $[\text{dppmAg}_2(\text{O}_2\text{CH})]^+$. The analysis of leading excitations is in Supplementary Fig. 10.

of formic acid involves two distinct types of reactions (Fig. 2a for **1d**, Supplementary Fig. 11 for **1e** and **1f**, Supplementary Table 3 for all systems). The ion–molecule reaction of formic acid with $[\text{LAG}_2(\text{H})]^+$ to produce $[\text{LAG}_2(\text{O}_2\text{CH})]^+$, and H_2 must be an exothermic process with barriers that lie below the separated reactants in order for it to occur under the near thermal conditions of the ion-trap³⁴. Indeed, DFT calculations reveal this to be the case, for **1d** (Fig. 5 and Supplementary Table 3). The binding energy of cis-formic acid to $[\text{dppmAg}_2(\text{H})]^+$ is 0.24 eV, and subsequent reaction via H_2 formation proceeds via a transition state with barrier of 0.18 eV leading to the formation of $[\text{dppmAg}_2(\text{O}_2\text{CH})]^+$, which is exothermic by 0.95 eV. Throughout this reaction, the dppm ligand keeps the Ag_2 subunit intact, while allowing the Ag–Ag bond length to relax. The overall exothermicities for this first reaction (step 1) for the other $[\text{LAG}_2(\text{H})]^+$ complexes examined follow the order $\text{L} = \text{dppm}$, (0.95 eV) > $\text{L} = \text{dppe}$ (0.76 eV) > $\text{L} = \text{dppbz}$ (0.71 eV) > $\text{L} = 2 \times \text{Ph}_3\text{P}$ (0.68 eV) > $\text{L} = \text{Ph}_3\text{P}$ (0.51 eV), which is in qualitative agreement with experimental findings that dihydrogen release (equation (7)) occurs for $\text{L} = \text{dppm}$, dppbz and dppe , but not for the other ligands. The corresponding heights of barriers are **1d** (0.18 eV) < **1f** (0.25 eV) < **1e** (0.36 eV) indicate that all three barriers can overcome under experimental conditions, although the efficiency of the reaction will depend on the height of the barrier. Only in these three cases do the Ag_2HP_2 subunits remain

intact as can be seen from Fig. 1. Analysis of the charge distributions in these $[\text{LAG}_2(\text{H})]^+$ complexes reveals delocalization of positive charge in this subunit (Supplementary Fig. 12).

In contrast, decarboxylation of $[\text{LAG}_2(\text{O}_2\text{CH})]^+$ is endothermic as it requires energization through multiple collisions with the helium bath gas during the CID process in order to occur. The mechanism for CO_2 release involves two steps. First, the formate needs to change from an O,O-bridging ligand to an O-bound ligand. This involves breaking one of the Ag–O bonds via a barrier of 1.7 eV. The next step involves decarboxylation²⁸, which proceeds over a barrier of 1.86 eV to release of CO_2 . Altogether, a catalytic cycle involving the selective decomposition of formic acid via the release of H_2 and CO_2 (Equation (1)) can occur according to calculated energy profile for $[\text{dppmAg}_2(\text{H})]^+$ (Fig. 5), under experimental conditions involving IMR for the spontaneous release of H_2 and activation via CID for the release of CO_2 . It is to be expected that this is also the case for $[\text{dppbzAg}_2(\text{H})]^+$ and $[\text{dppeAg}_2(\text{H})]^+$ since that $\text{Ag}_2\text{H}(\text{X})\text{P}_2$ subunit remains intact, although the energetics are slightly less favourable than in the case of $[\text{dppmAg}_2(\text{H})]^+$ (Supplementary Table 3).

Solution-phase selective decarboxylation of formic acid. The fact that $[\text{dppmAg}_2(\text{O}_2\text{CH})]^+$ is both readily decarboxylated in the gas-phase and reformed via the reaction of $[\text{dppmAg}_2(\text{H})]^+$

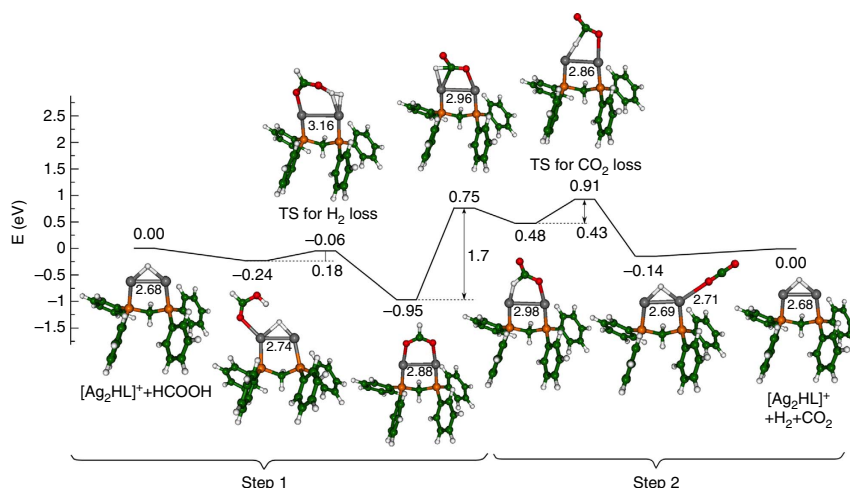


Figure 5 | DFT-calculated energy profile for the two reaction steps in the catalytic cycle of Fig. 1a. (Step 1) ion-molecule reaction of formic acid with $[\text{dppmAg}_2(\text{H})]^+$; (step 2) CID decarboxylation of $[\text{dppmAg}_2(\text{O}_2\text{CH})]^+$. Relative energies are in eV.

with formic acid prompted us to prepare stoichiometrically well-defined solutions in order to use variable temperature ^1H and ^{13}C NMR spectroscopy to examine the evolution of the two gaseous products formed in the selective decarboxylation of formic acid (equation (1)). No H_2 evolution was observed by ^1H NMR when a solution of AgBF_4 , ^{13}C -labelled formic acid and dppm was heated from 25 to 70°C (Supplementary Fig. 13). When the experiment was repeated with the addition of sodium formate, no evolution of H_2 was observed from 25 to 55°C (Supplementary Fig. 14). When the temperature was raised to 70°C , H_2 evolution was observed almost instantly (Supplementary Fig. 15). The evolution of both H_2 and CO_2 were observed to increase over time at 70°C , and both H_2 and CO_2 reached a steady-state concentration after ~ 11.5 min (Supplementary Figs 15 and 16).

Discussion

While concepts of steric and electronic effects are well established in guiding the choice of ligand to modulate the reactivity of mononuclear catalysts in homogenous catalysis^{35,36}, related concepts for choosing ligands to modulate the reactivity of binuclear and cluster catalysts are yet to be fully developed⁵. The value of gas-phase studies employing mass spectrometry (MS)-based methods^{37,38} is that they allow a systematic exploration of the factors that control reactivity for all steps in a catalytic cycle^{39,40}. When used in conjunction with DFT calculations, where mechanistic pathways can be explored, different types of catalysts that vary in the metal, ligand and/or nuclearity that catalyse the same transformation⁴¹ or which transform the same substrate in different ways⁴² can be directly compared⁴³.

Here, we have shown that ligand choice is a crucial factor in designing a binuclear silver hydride cluster that catalyses the selective decarboxylation of formic acid. Ligation of the $\text{Ag}_2(\text{H})^+$ scaffold clearly has an influence on its geometry by shortening the Ag–Ag distance and increasing the Ag–H distance (Fig. 1). In the absence of bidentate bridging ligands, the reactivity pattern of **1a**, **1b** and **1c** towards formic acid is consistent with simple Lewis acid/base interactions in which the number of vacant coordination sites in $[(\text{Ph}_3\text{P})_n\text{Ag}_2(\text{H})]^+$ dictates how many formic acid molecules can coordinate via the O atom of the C=O to form the adducts $[(\text{Ph}_3\text{P})_n\text{Ag}_2(\text{H})(\text{HO}_2\text{CH})_{2-n}]^+$. Indeed DFT calculations reveal that this coordination mode yields the most stable adducts for $n=0$ and 1, while in the case of $n=2$ only a weakly bound ion–molecule complex is formed (Supplementary Fig. 17) and this is likely to simply dissociate back to separated reactants, which is why no adduct is observed experimentally. In contrast,

the tight-bite angles of the bidentate bridging ligands dppm, dppbz and dppe switch on the protonation of the silver hydride in step 1 (Fig. 5) by providing an appropriate geometry to weaken the Ag–H bonds and bend the P–Ag–H away from linearity, thereby allowing coordination of formic acid and subsequent reaction between the coordinated moieties $\text{Ag}(\text{OCH}(\text{OH}))$ and $\text{Ag}(\text{H})$. The ligand further tunes the reactivity as highlighted by both the experimentally determined reaction efficiencies, which follow the order $\mathbf{1d} \approx \mathbf{1e} \gg \mathbf{1f}$ and the DFT-calculated barrier heights for reaction with cis-formic acid (Supplementary Fig. 18) to release H_2 , which follow the order $\mathbf{1d}$ (0.18 eV) < $\mathbf{1f}$ (0.25 eV) < $\mathbf{1e}$ (0.36 eV). The ligand also exerts an effect in step 2, with energy resolved CID experiments (Supplementary Fig. 5) providing reactivity orders for the ease of decarboxylation that are in agreement with the DFT-calculated barrier heights: $[\text{dppeAg}_2(\text{O}_2\text{CH})]^+$ (1.64 eV) \approx $[\text{dppbzAg}_2(\text{O}_2\text{CH})]^+$ (1.65 eV) < $[\text{dppmAg}_2(\text{O}_2\text{CH})]^+$ (1.86 eV).

Finally, the gas-phase results encouraged us to examine related selective decarboxylation reactions in solution^{44,45}. We found that both H_2 and $^{13}\text{CO}_2$ are evolved when a stoichiometrically well-defined solution containing dppm, AgBF_4 , ^{13}C -labelled formic acid and sodium formate was warmed to 70°C . While the precise nature of the reactive species in solution is unknown, previous studies have shown that: (i) related dppm complexes of silver carboxylates exist as dimers in solution^{46,47}; (ii) the related silver hydride $[(\text{NHC})_2\text{Ag}_2(\text{H})]^+$ (where, NHC = 1,3-bis(2,6-diisopropylphenyl)imidazolin-2-ylidene) exists in solution and reacts with CO_2 to form $[(\text{NHC})_2\text{Ag}_2(\text{O}_2\text{CH})]^+$, a reaction that is the reverse of decarboxylation of a coordinated formate ligand (equation (4)) studied here⁴⁸.

Two key concepts have emerged from this work: (i) that ligands can have a vital role in reshaping the scaffold of a metal cluster to activate its reactivity towards a substrate; and (ii) that fundamental gas-phase studies can be used to direct the search for new types of metal complexes that promote related reactivity in solution⁴⁹. Together these concepts have allowed us to achieve the selective extrusion of carbon dioxide from formic acid, an important process for applications in hydrogen storage^{15–17}.

Methods

Materials. Chemicals listed in the Supplementary information were used as received.

Preparation of silver complexes for MS analysis. *In situ* silver precursor complexes for ESI/MS were typically generated by adding 20 mmol AgX

($X = \text{NO}_3^-$ or BF_4^-) followed by 10 mmol of phosphine ligand, L ($L = \text{PPh}_3$, dpmm, dpbbz or dppe), to 20 ml of freshly prepared solvent mixtures in a 50 ml Quickfit round-bottom flask covered in foil and equipped with a glass stopper and magnetic stir bar. The solution was stirred for at least 5 min and 10 mmol of sodium formate was added. MS experiments were conducted immediately after the addition of sodium formate.

Gas-phase studies using CID and IMR. Gas-phase experiments on phosphine ligated silver formate clusters were carried out using a Finnigan hybrid linear quadrupole Fourier transform ion-cyclotron resonance mass spectrometer. The silver complexes prepared above were typically diluted in methanol or acetonitrile to a final silver(I) concentration of 50 μM and at least 1.0 ml. The diluted solution was drawn into a 500 μl gas tight borosilicate glass syringe with polytetrafluoroethylene (PTFE) plunger tips and injected into the Finnigan ESI source at a flow rate of 3–5 $\mu\text{l min}^{-1}$. ESI source conditions to yield a stable current of 0.5 μA were: needle potential (3.5–5.0 kV); nitrogen sheath gas pressure (5–10 a.u.). The ion transfer capillary temperature was set to 250 $^\circ\text{C}$. Voltages were: tube lens (≈ 20.0 V) and capillary voltage (10.0 V). The unimolecular fragmentation/dissociation of mass-selected precursor silver complexes occurred via CID using a normalized collision energy typically between 20 and 25%, and an activation time of 30 ms. IMR were carried by injecting formic acid into the helium bath gas⁵. The stoichiometry of all ions was confirmed by high-resolution MS experiments (Supplementary Table 4).

Energy-resolved CID experiments. Energy-resolved CID experiments were carried out using a Finnigan 3D ion trap (LCQ) mass spectrometer. The method of Brodbelt was adapted and details are given in the Supplementary methods (see text associated with Supplementary Fig. 4)⁵⁰. The activation voltage was determined by Supplementary equation 3.

MS for IR action spectroscopy. Infrared spectroscopy of mass-selected ions in the 800–1,600 cm^{-1} range was performed using a 7 Tesla Fourier transform ion cyclotron resonance tandem mass spectrometer (Bruker Apex IV Qe)⁵¹ equipped with an ESI source and coupled to the infrared FEL beam line of CLIO⁵². This IR FEL delivers ~ 10 μs long trains of picosecond pulses at 25 Hz. Ions of interest were accumulated and trapped in a ~ 5 cm long hexapole ion-trap pressurized with argon. The trapping delay (~ 500 ms) allows for an efficient collisional cooling of the ions. Ions are then pulse extracted to the ICR cell where they are mass-selected, and then irradiated for 1 s. Upon resonant vibrational excitation, dissociation of the selected ion can be monitored via its fragment peaks.

A significant enhancement of the photofragmentation yield can be observed using an auxiliary CO_2 laser (10 W continuous wave, BFi OPTiLAS, France)³². For this purpose, a train of CO_2 pulses at 25 Hz is generated and synchronized with the IR FEL laser with a retarding delay being on the order of ~ 1 μs . This auxiliary CO_2 laser was used in the case of $[\text{dpmmAg}_2(\text{H})]^+$ (m/z 601), and the CO_2 laser pulse length (25 ms) was adjusted to avoid CO_2 induced dissociation.

The experimental IRMPD bandwidth (fwhm) for both $[\text{dpmmAg}_2(\text{H})]^+$ and $[\text{dpmmAg}_2(\text{O}_2\text{CH})]^+$ is on the order of 20 cm^{-1} , as generally observed for IRMPD spectra of other systems obtained using the CLIO FEL.

MS for ultraviolet action spectroscopy. For ultraviolet action spectroscopy, a dual linear ion trap (LTQ-VELOS, ThermoScientific) was used to generate, mass select and trap ions in a first, high-pressure ion trap, for a controlled duration. During ion trapping, ions can be activated and fragmented by photons or CID. Fragment ions are transmitted to a second ion trap, with low pressure, where they are mass analyzed. A fused-silica window is positioned at the back end of the instrument allowing for the introduction of laser beams in the ultraviolet-visible range along the ion trap axis. Ultraviolet light was generated by doubling the output of an optical parametric oscillator (Horizon optical parametric oscillator pumped by the third harmonic of a Surelite II Nd:YAG laser, Continuum). A mechanical shutter, synchronized with the mass spectrometer, is used to stop the beam at all times except the ‘ion activation window’—that is the time after ion accumulation and before the mass analysis. A single laser pulse was used for the irradiation of the trapped ions and when irradiating ions the normalized collision energy is kept at zero. The fragmentation yield (FY) is given by equation (9).

$$\text{FY} = -\log\left(\frac{P}{P+F}\right)/\lambda \cdot Pw \quad (9)$$

P and F are the intensities on the mass spectrum for respectively the parent ion and the ensemble of photo-fragment ions. λ and Pw are respectively the wavelength and measured average power of the incoming ultraviolet laser beam.

DFT calculations. The extensive search for lowest energy structures and transitions states were performed by the hybrid B3LYP⁵³ functional with def2-TZVP atomic basis set⁵⁴, which has been used for all atoms. Silver atoms have been treated by Stuttgart relativistic effective core potential with corresponding atomic orbital (AO) basis set⁵⁵. The same combination of functional and basis set was used for calculation of the infrared spectra, which were scaled by 0.98 to match

experimental data. The IR spectrum for neutral monomeric cis-formic acid calculated at this level of DFT theory is also in good agreement with experimental data (Supplementary Fig. 19). For calculations of the absorption spectra TDDFT with the long-range corrected version of the hybrid B3LYP functional, the Coulomb-attenuated CAM-B3LYP functional and TZVP AO basis set has been employed.

Potential interactions between the aromatic rings of dpmm, raises the question of whether the dispersion correction within DFT are required. We have tested the influence of dispersion correction on the structural and spectroscopic properties of $[\text{dpmmAg}_2\text{H}]^+$ and $[\text{dpmmAg}_2(\text{O}_2\text{CH})]^+$ complexes by introducing D3 into DFT and TDDFT⁵³. Comparison of the measured and calculated infrared spectra suggest that dispersion corrections has no influence. In contrast, the absorption transitions calculated using the D3 correction in which aromatic rings are involved are only slightly blue shifted, thus improving agreement with the experimental UVPD spectra. Finally, the energy profile shown in Fig. 5 is almost unchanged when single point B3LYP-D3 energy calculations are carried out for each reaction step of the catalytic cycle (Supplementary Table 3).

NMR spectroscopy experiments. The NMR experiments were performed on a Bruker Avance Av500 NMR spectrometer (500.13 MHz ^1H frequency) equipped with a 5 mm triple resonance CryoProbe Prodigy probe ($^1\text{H}/^{19}\text{F}$ – $^2\text{H}/^{13}\text{C}/^{15}\text{N}$). Solutions for analysis by NMR were prepared by dissolving: (1) solution A: AgBF_4 (195 mg, 1 mmol), dpmm (192 mg, 0.5 mmol), ^{13}C formic acid (24 mg, 0.5 mmol) and sodium formate (34 mg, 0.5 mmol) in 1 ml of deuteroacetonitrile; (2) solution B: same as solution A, but without sodium formate added. NMR experiments were performed with the sample held at temperatures between +25 $^\circ\text{C}$ and +70 $^\circ\text{C}$ (± 0.1 $^\circ\text{C}$). Chemical shifts for ^1H experiments are referenced to the residual protonated solvent signal (CD_2HCN , δ 1.94 ppm); ^{13}C referenced to the solvent signal (CD_3CN , δ 1.39 ppm). One-dimensional NMR experiments were acquired using standard Bruker library pulse sequences.

Data availability. The data that support the findings of this study are available from the corresponding author upon request.

References

- Menger, F. M. An alternative view of enzyme catalysis. *Pure Appl. Chem.* **77**, 1873–1886 (2005).
- Valdez, C. E., Smith, Q. A., Nechay, M. R. & Alexandrova, A. N. Mysteries of metals in metalloenzymes. *Acc. Chem. Res.* **47**, 3110–3117 (2014).
- Cannon, W. R., Singleton, S. F. & Benkovic, S. J. A perspective on biological catalysis. *Nat. Struct. Biol.* **3**, 821–833 (1996).
- Joost, M. *et al.* Facile Oxidative addition of aryl iodides to gold(I) by ligand design: bending turns on reactivity. *J. Am. Chem. Soc.* **136**, 14654–14657 (2014).
- Robinson, P. S. D., Khairallah, G. N., da Silva, G., Lioe, H. & O’Hair, R. A. J. Gold mediated C–I bond activation of iodobenzene. *Angew Chem. Int. Ed.* **51**, 3812–3817 (2012).
- Meijboom, R., Bowen, R. J. & Berners-Price, S. J. Coordination complexes of silver(I) with tertiary phosphine and related ligands. *Coord. Chem. Rev.* **253**, 325–342 (2009).
- Mitric, R. *et al.* Gas-phase synthesis and vibronic action spectroscopy of Ag_2H^+ . *J. Phys. Chem. Lett.* **2**, 548–552 (2011).
- Zavras, A. *et al.* Synthesis, Structural characterisation and gas-phase unimolecular reactivity of the silver hydride nanocluster $[\text{Ag}_3((\text{PPh}_2)_2\text{CH}_2)_3(\mu_3\text{-H})](\text{BF}_4)_2$. *Inorg. Chem.* **53**, 7429–7437 (2014).
- Girod, M. *et al.* Formation and characterisation of the silver hydride nanocluster cation $[\text{Ag}_3\text{H}_2((\text{Ph}_2\text{P})_2\text{CH}_2)]^+$ and its release of hydrogen. *Chem. Eur. J.* **20**, 16626–16633 (2014).
- Khairallah, G. N., O’Hair, R. A. J. & Bruce, M. I. Gas-phase synthesis and reactivity studies of binuclear gold hydride cations, $(\text{R}_3\text{PAu})_2\text{H}^+$ ($\text{R} = \text{Me}$ and Ph). *Dalton Trans.* **30**, 3699–3707 (2006).
- Sabatier, P. & Mailhe, A. Catalytic decomposition of formic acid. *Compt. Rend.* **152**, 1212–1215 (1912).
- Sabatier, P. *Catalysis in Organic Chemistry* 538–539 (Library Press, 1923).
- Mars, P., Scholten, J. J. F. & Zwietering, P. The catalytic decomposition of formic acid. *Adv. Catal.* **14**, 35–113 (1963).
- Trillo, J. M., Munuera, G. & Criado, J. M. Catalytic decomposition of formic acid on metal oxides. *Catal. Rev.* **7**, 51 (1972).
- Grasemann, M. & Laurenczy, G. Formic acid as a hydrogen source—recent developments and future trends. *Energy Environ. Sci.* **5**, 8171–8181 (2012).
- Boddien, A. *et al.* CO_2 –‘Neutral’ hydrogen storage based on bicarbonates and formates. *Angew Chem. Int. Ed.* **50**, 6411–6414 (2011).
- Enthaler, S., von Langermann, J. & Schmidt, T. Carbon dioxide and formic acid—the couple for environmental-friendly hydrogen storage? *Energy Environ. Sci.* **3**, 1207–1217 (2010).
- Wiñhöfer, G. *et al.* General and selective iron-catalyzed transfer hydrogenation of nitroarenes without base. *J. Am. Chem. Soc.* **133**, 12875–12879 (2011).

19. Braden, D. J., Henao, C. A., Heltzel, J., Maravelias, C. T. & Dumesic, J. A. Production of liquid hydrocarbon fuels by catalytic conversion of biomass-derived levulinic acid. *Green Chem.* **13**, 1755–1765 (2011).
20. Herrmann, W. A. & Muehlhofer, M. in *Applied Homogeneous Catalysis with Organometallic Compounds*, 2nd edn, Vol. 3 (eds Cornils, B. and Herrmann, W. A.), 1086 (Wiley-VCH, 2002).
21. Odabasi, C., Gunay, M. E. & Yildirim, R. Knowledge extraction for water gas shift reaction over noble metal catalysts from publications in the literature between 2002 and 2012. *Int. J. Hydrogen Energy* **39**, 5733–5746 (2014).
22. Saito, K. *et al.* Unimolecular decomposition of formic acid in the gas phases on the ratio of the competing reaction channels. *J. Phys. Chem. A* **109**, 5352–5357 (2005).
23. Chang, J.-G., Chen, H.-T., Xu, S. & Lin, M. C. Computational study on the kinetics and mechanisms for the unimolecular decomposition of formic and oxalic acids. *J. Phys. Chem. A* **111**, 6789–6797 (2007).
24. Loges, B., Boddien, A., Gärtner, F., Junge, H. & Beller, M. Catalytic generation of hydrogen from formic acid and its derivatives: useful hydrogen storage materials. *Topics Catal.* **53**, 902–914 (2010).
25. Bi, Q.-Y. *et al.* Efficient subnanometric gold-catalyzed hydrogen generation via formic acid decomposition under ambient conditions. *J. Am. Chem. Soc.* **134**, 8926–8933 (2012).
26. Tedsree, K. *et al.* Hydrogen production from formic acid decomposition at room temperature using a Ag–Pd core–shell nanocatalyst. *Nat. Nanotechnol.* **6**, 302–307 (2011).
27. O'Hair, R. A. J. in *Reactive Intermediates. MS Investigations in Solution* (ed Santos, L.S.) Ch. 6, 199–227 (Wiley-VCH, 2010).
28. O'Hair, R. A. J. & Rijs, N. J. Gas phase studies of the Pesci decarboxylation reaction: synthesis, structure, and unimolecular and bimolecular reactivity of organometallic ions. *Acc. Chem. Res.* **48**, 329–340 (2015).
29. Duncan, M. A. Spectroscopy of metal ion complexes: gas-phase models for solvation. *Ann. Rev. Phys. Chem.* **48**, 69–93 (1997).
30. MacAleese, L. & Maitre, P. Infrared spectroscopy of organometallic ions in the gas phase: from model to real world complexes. *Mass Spectrom. Rev.* **26**, 583–605 (2007).
31. Antoine, R. & Dugourd, P. Visible and ultraviolet spectroscopy of gas phase protein ions. *Phys. Chem. Chem. Phys.* **13**, 16494–16509 (2011).
32. Lanucara, F. *et al.* Naked five-coordinate Fe(III)(NO) porphyrin complexes: vibrational and reactivity features. *Inorg. Chem.* **50**, 4445–4452 (2011).
33. Grimme, S., Antony, J., Ehrlich, S. & Krieg, H. A consistent and accurate *ab initio* parameterization of density functional dispersion correction (DFT-D) for the 94 elements H–Pu. *J. Chem. Phys.* **132**, 154104 (2010).
34. Donald, W. A., Khairallah, G. N. & O'Hair, R. A. J. The effective temperature of ions stored in a linear quadrupole ion trap mass spectrometer. *J. Am. Soc. Mass Spectrom.* **24**, 811–815 (2013).
35. Kamer, P. & van Leeuwen, P. W. N. M. *Phosphorus(III) Ligands in Homogeneous Catalysis: Design and Synthesis* (Wiley, 2012).
36. Gorin, D. J., Sherry, B. D. & Toste, F. D. Ligand effects in homogeneous Au catalysis. *Chem. Rev.* **108**, 3351–3378 (2008).
37. Eller, K. & Schwarz, H. Organometallic chemistry in the gas phase. *Chem. Rev.* **91**, 1121–1177 (1991).
38. Jena, P. & Castleman, Jr A. W. Cluster chemistry and dynamics special feature introductory perspective clusters: a bridge across the disciplines of physics and chemistry. *Proc. Natl Acad. Sci. USA* **103**, 10560–10569 (2006).
39. Waters, T., O'Hair, R. A. J. & Wedd, A. G. Catalytic gas phase oxidation of methanol to formaldehyde. *J. Am. Chem. Soc.* **125**, 3384–3396 (2003).
40. O'Hair, R. A. J. The 3D quadrupole ion trap mass spectrometer as a complete chemical laboratory for fundamental gas phase studies of metal mediated chemistry. *Chem. Commun.* **14**, 1469–1481 (2006).
41. O'Hair, R. A. J. Gas-phase studies of metal catalyzed decarboxylative cross-coupling reactions of esters. *Pure. Appl. Chem.* **87**, 391–404 (2015).
42. Schwarz, H. Chemistry with methane: concepts rather than recipes. *Angew Chem. Int. Ed.* **50**, 10096–10115 (2011).
43. Schwarz, H. How and why do cluster size, charge state, and ligands affect the course of metal-mediated gas-phase activation of methane? *Isr. J. Chem.* **54**, 1413–1431 (2014).
44. Agrawal, D. & Schröder, D. Insight into solution chemistry from gas-phase experiments. *Organometallics* **30**, 32–35 (2011).
45. Schröder, D. Applications of electrospray ionization mass spectrometry in mechanistic studies and catalysis research. *Acc. Chem. Res.* **45**, 1521–1532 (2012).
46. Neo, S. P., Zhou, Z. Y., Mak, T. C. W. & Hor, T. S. A. Solid-state tetramer vs. solution-state dimer reinvestigation of $[\text{Ag}_2(\text{OAc})_2(\text{dppm})]_2$ and its dppm addition product $[\text{Ag}(\text{OAc})(\text{dppm})]_2$ (dppm = $\text{Ph}_2\text{PCH}_2\text{PPh}_2$). *Inorg. Chem.* **34**, 520–523 (1995).
47. Szlyk, E. *et al.* X-ray crystal structure of $[\text{Ag}_4(\mu\text{-dppm})_2(\mu\text{-C}_2\text{F}_5\text{COO})_4]$. Synthesis and spectroscopy of silver(I) perfluorinated carboxylate complexes with bis(diphenylphosphino)methane. *Dalton Trans.* **17**, 3404–3410 (2003).
48. Tate, B. K. *et al.* A dinuclear silver hydride and an umpolung reaction of CO_2 . *Chem. Sci.* **4**, 3068–3074 (2013).
49. Chen, P. Electrospray ionization tandem mass spectrometry in high-throughput screening of homogeneous catalysts. *Angew Chem. Int. Ed.* **42**, 2832–2847 (2003).
50. Colorado, A. & Brodbelt, J. An empirical approach to estimation of critical energies by using a quadrupole ion trap. *J. Am. Soc. Mass Spectrom.* **7**, 1116–1125 (1996).
51. Bakker, J. M., Besson, T., Lemaire, J., Scuderi, D. & Maitre, P. Gas-phase structure of a π -allyl-palladium complex: efficient infrared spectroscopy in a 7 T Fourier transform mass spectrometer. *J. Phys. Chem. A* **111**, 13415–13424 (2007).
52. Prazeres, R., Glotin, F., Insa, C., Jaroszynski, D. A. & Ortega, J. M. Two-colour operation of a free-electron laser and applications in the mid-infrared. *Eur. Phys. J. D* **3**, 87–93 (1998).
53. Becke, A. D. Density functional thermochemistry. III. The role of exact exchange. *J. Chem. Phys.* **98**, 5648–5652 (1993).
54. Schäfer, A., Huber, H. & Ahlrichs, R. Fully optimized contracted Gaussian basis sets of triple zeta valence quality for atoms Li to Kr. *J. Chem. Phys.* **100**, 5829–5835 (1994).
55. Andrae, D., Haeussermann, U., Dolg, M., Stoll, H. & Preuss, H. Energy-adjusted *ab initio* pseudopotentials for the second and third row transition elements. *Theor. Chim. Acta* **77**, 123–141 (1990).

Acknowledgements

We thank the ARC for financial support via grant DP150101388 (to R.A.J.O. and P.D.). A.Z. acknowledges the award of an Australian Postgraduate PhD Scholarship. The research leading to these results has received funding from the European Research Council under the European Union's Seventh Framework Programme (FP7/2007–2013 Grant Agreement No. 320659). Financial support from the French FT-ICR network (FR 3624 CNRS) for conducting the research is gratefully acknowledged. V.B.-K. and M.K. acknowledge Prof. Miroslav Radman at MedILS and Split-Dalmatia County for kind support.

Author contributions

A.Z. identified and optimized routes to the gas-phase formation of the silver hydride and silver formate complexes, carried out the CID, IMR and UVPD experiments and contributed to manuscript preparation. G.N.K. carried out the IRMPD experiments and contributed to manuscript preparation. M.K. carried out all the DFT calculations and contributed to manuscript preparation; M.G., S.D., R.A., P.M., R.J.M., S.-A.A. performed experiments and/or analyzed data and/or provided intellectual input; V.B.-K. and P.D. contributed to the project design, interpretation of data and writing of the manuscript; R.A.J.O. devised the project, contributed to the design of experiments and interpretation of data, project management and writing of the manuscript.

Additional information

Supplementary Information accompanies this paper at <http://www.nature.com/naturecommunications>

Competing financial interests: The authors declare no competing financial interests.

Reprints and permission information is available online at <http://npg.nature.com/reprintsandpermissions/>

How to cite this article: Zavras, A. *et al.* Ligand-induced substrate steering and reshaping of $[\text{Ag}_2(\text{H})]^+$ scaffold for selective CO_2 extrusion from formic acid. *Nat. Commun.* **7**:11746 doi: 10.1038/ncomms11746 (2016).



This work is licensed under a Creative Commons Attribution 4.0 International License. The images or other third party material in this article are included in the article's Creative Commons license, unless indicated otherwise in the credit line; if the material is not included under the Creative Commons license, users will need to obtain permission from the license holder to reproduce the material. To view a copy of this license, visit <http://creativecommons.org/licenses/by/4.0/>

- 4 **Selectivity Effects in Bimetallic Catalysis: Role of the Metal Sites in the Decomposition of Formic Acid into H₂ and CO₂ by the Coinage Metal Binuclear Complexes [dppmMM'(H)]⁺ (submitted)**

Selectivity Effects in Bimetallic Catalysis: Role of the Metal Sites in the Decomposition of Formic Acid into H₂ and CO₂ by the Coinage Metal Binuclear Complexes [dppmMM'(H)]⁺

Athanasios Zavras,^[a] Marjan Krstić,^[b] Philippe Dugourd,^[c] Vlasta Bonačić-Koutecký*^[b,d] and Richard A. J. O'Hair*^[a]

Abstract: Design of new bimetallic catalysts requires an understanding of how cooperative effects of the metal sites influences reactivity. Here we show how switching one or both of the silver atoms in binuclear silver hydride cations, [dppmAg₂(H)]⁺, with all combinations of copper and/or gold maintains selective protonation by formic acid while enhancing reactivity by up to 2 orders of magnitude. This is a key step in the selective, catalyzed extrusion of carbon dioxide from formic acid, HO₂CH, with important applications in hydrogen storage and in situ generation of H₂. Decarboxylation of [dppmMM'(O₂CH)]⁺ via collision induced dissociation (CID) regenerates [dppmMM'(H)]⁺. DFT calculations provide insights into these cooperative effects. The copper homobinuclear catalyst performs best overall.

Catalytic cooperative effects are ubiquitous in nature and in synthetic systems.^[1] The requirement for two metals, either of the same element or of two different elements, to complete a catalytic cycle represents an important synergistic effect in both heterogeneous^[2] and homogenous catalysis^[3,4] and has been termed **bimetallic catalysis**.^[2-4] While single site homogenous catalysis represents an attractive way of "bottom-up" design of catalysts, the design principles for bimetallic catalysis are still not well understood. In cases where reactivity is catalytic in one metal and stoichiometric in the other metal, transmetalation can be the crucial step for a successful catalytic cycle.^[3] Catalysts that contain two metal sites are attractive candidates for developing a deeper understanding of bimetallic catalysis since they allow the role of the ligand and each of the metal centres to be examined.^[4] By using multistage mass spectrometry techniques^[5] to study these systems in the gas-phase^[6] it is possible to examine the role of each metal centre on the elementary steps of a catalytic cycle involving homo- and heteronuclear clusters.^[7]

We recently showed that the choice of ligand is crucial to developing a two-step catalytic cycle for the selective extrusion of carbon dioxide from formic acid by [dppmAg₂(H)]⁺ (Figure 1).^[8] The bis(diphenylphosphino)methane (dppm) ligand was found to reshape the geometry of the binuclear Ag₂(H)⁺ scaffold, thereby switching on protonation of the hydride to produce [dppmAg₂(O₂CH)]⁺ and H₂ (Figure 1a, Step 1). Decarboxylation of [dppmAg₂(O₂CH)]⁺ via collision induced dissociation (CID) regenerates [dppmAg₂(H)]⁺ (Figure 1a, Step 2). Both silver sites are involved in the crucial transition states for protonation (Figure 1b) and decarboxylation (Figure 1c). Here we use MS experiments and DFT calculations to examine the chemistry of all of the related homo- and heterobinuclear complexes [dppmMM'(H)]⁺ of the d¹⁰ coinage metals where M or M' = Cu, Ag and Au. This allows an evaluation of how cooperative effects between the metal centers influence both steps of the catalytic cycle.

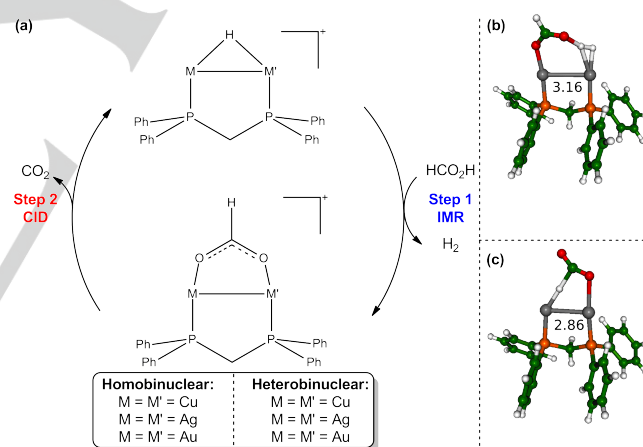


Figure 1. Selective decarboxylation of formic acid. (a) Two step catalytic cycle involving bimetallic catalysis. DFT calculations highlight the role of both metal centers for: (b) Transition state (TS) for protonation of formic acid for [dppmAg₂H]⁺.^[8] (c) TS for decarboxylation for [dppmAg₂(O₂CH)]⁺.^[8]

Our entry into the catalytic cycle was via the coordinated formates, [dppmMM'(O₂CH)]⁺, which were transferred to the gas-phase via electrospray ionization (ESI) of a 50 μM acetonitrile solution containing a mixture of Cu₂O:Ag₂O:AuClPPh₃ (1:1:2) to which 10 equivalents of formic acid was added (Supporting information Figure S1a and related discussion). All homo and hetero binuclear formates were formed from this solution, as confirmed via their isotope patterns (Figure S1b) and high-resolution mass spectrometry (HRMS) experiments (Figure S2). The HRMS experiments also identified the presence of isobaric impurities for [dppmAu₂(O₂CH)]⁺ (*m/z* 823, Figure S2b), [dppmCuAu(O₂CH)]⁺ (*m/z* 689, Figure S2d),

[a] Mr. A. Zavras, Prof. R. A. J. O'Hair, School of Chemistry and Bio21 Molecular Science and Biotechnology Institute, University of Melbourne, 30 Flemington Rd, Parkville, Victoria 3010 (Australia) E-mail: rohair@unimelb.edu.au

[b] Mr. M. Krstić, Prof. V. Bonačić-Koutecký, Interdisciplinary Center for Advanced Sciences and Technology (ICAST), University of Split, Meštrovićevo Šetalište 45, 21000 Split (Croatia)

[c] Prof. P. Dugourd, Université Claude Bernard Lyon 1, CNRS, Institut Lumière Matière, F-69622, LYON, France.

[d] Prof. V. Bonačić-Koutecký, Chemistry Department, Humboldt University of Berlin, Brook-Taylor-Strasse 2, 12489 Berlin (Germany)

Supporting information for this article is given via a link at the end of the document.

and $[\text{dppmAgAu}(\text{O}_2\text{CH})]^+$ (m/z 733, Figure S2e). CID (MS^2) of the mass selected formate complexes, $[\text{dppmMM}'(\text{O}_2\text{CH})]^+$ (Figure S3), generated abundant hydride complexes $[\text{dppmMM}'(\text{H})]^+$ via decarboxylation with the exception of $[\text{dppmAu}_2(\text{H})]^+$ (m/z 779, Figure S3b) and $[\text{dppmAgAu}(\text{H})]^+$ (m/z 689, Figure S3e). The elemental composition of each of the hydride complexes generated via the decarboxylation of the coordinated formates (Figure 1a, Step 2) was confirmed by HRMS (Figure S4). Subsequent mass selection provided hydride complexes devoid of any isobaric impurities for ion-molecule reactions with formic acid in a series of MS^3 experiments. All hetero- and homobimetallic hydride complexes react with formic acid to regenerate the formate complex $[\text{dppmMM}'(\text{O}_2\text{CH})]^+$ (Figure 1a, Step 1 and Figure 2).

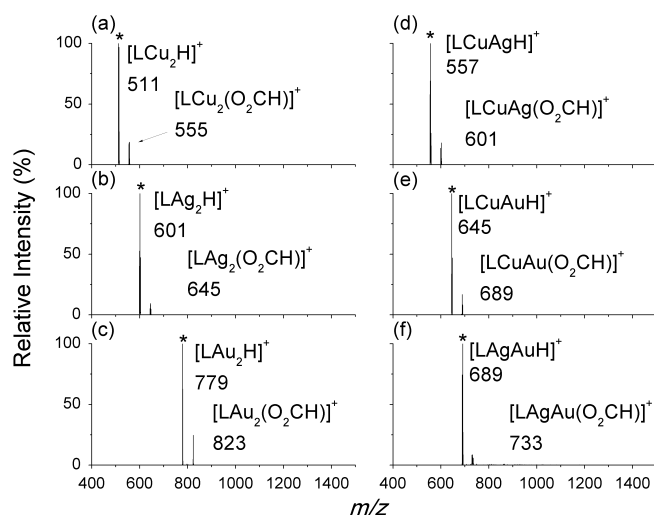


Figure 2. MS^3 LTQ spectra obtained in a 2D linear-ion trap at 298 K showing the ion-molecule reaction of formic acid with mass selected hydrides, $[\text{LMM}'\text{H}]^+$ ($\text{L}=\text{dppm}$) for: **a**, $\text{M}=\text{M}'=\text{Cu}$, Activation time = 60 ms, $[\text{HO}_2\text{CH}]_{\text{ion trap}} = 2.24 \times 10^9 \text{ molecules.cm}^{-3}$, **b**, $\text{M}=\text{M}'=\text{Ag}$, Activation time = 1000 ms, $[\text{HO}_2\text{CH}]_{\text{ion trap}} = 4.75 \times 10^9 \text{ molecules.cm}^{-3}$, **c**, $\text{M}=\text{M}'=\text{Au}$, Activation time 20 ms = , $[\text{HO}_2\text{CH}]_{\text{ion trap}} = 2.24 \times 10^9 \text{ molecules.cm}^{-3}$, **d**, $\text{M}=\text{Cu}; \text{M}'=\text{Ag}$, Activation time = 30 ms, $[\text{HO}_2\text{CH}]_{\text{ion trap}} = 3.72 \times 10^9 \text{ molecules.cm}^{-3}$, **e**, $\text{M}=\text{Cu}; \text{M}'=\text{Ag}$ Activation time = 50 ms, $[\text{HO}_2\text{CH}]_{\text{ion trap}} = 8.19 \times 10^9 \text{ molecules.cm}^{-3}$, and **f**, $\text{M}=\text{Ag}; \text{M}'=\text{Au}$ Activation time = 1000 ms, $[\text{HO}_2\text{CH}]_{\text{ion trap}} = 8.96 \times 10^8 \text{ molecules.cm}^{-3}$. A * represents the mass-selected precursor ion. The most intense peak in the cluster is represented by the m/z value.

To evaluate the roles of the metal centers on reactivity, the temporal decay of the reactant ion, $[\text{dppmMM}'(\text{H})]^+$, was monitored over a range of activation times and concentrations of formic acid (Figure S5) to yield rate constants, which when compared to the predicted collision rates gave the reaction efficiencies listed Table 1. The experimentally observed

reactivity order follows: $[\text{dppmAu}_2(\text{H})]^+ \approx [\text{dppmCu}_2(\text{H})]^+ > [\text{dppmCuAu}(\text{H})]^+ \approx [\text{dppmCuAg}(\text{H})]^+ \gg [\text{dppmAgAu}(\text{H})]^+ \approx [\text{dppmAg}_2(\text{H})]^+$ with a ca. 2 orders of magnitude difference in reactivity between the most and least reactive complexes.

Table 1. Rates of ion-molecule reactions between $[\text{dppmMM}'(\text{H})]^+$ and formic acid.

Reactant ion	$k_{\text{expt}}^{[a,b,c]}$	Reaction efficiency ^[d]	DFT calculated E_{act} (eV) ^[f]
$[\text{dppmCu}_2(\text{H})]^+$ m/z 511	$1.20 \pm 0.01 \times 10^{-9}$	113.6 ± 6.1	-0.66 (0.07)
$[\text{dppmAg}_2(\text{H})]^+$ m/z 601	$1.53 \pm 0.03 \times 10^{-11}$	1.4 ± 0.1	-0.06 (0.18)
$[\text{dppmAu}_2(\text{H})]^+$ ^[e] m/z 779	$1.47 \pm 0.09 \times 10^{-9}$	141.0 ± 9.2	-1.02 (0.06)
$[\text{dppmCuAg}(\text{H})]^+$ m/z 557	$3.31 \pm 0.2 \times 10^{-10}$	31.5 ± 2.1	-0.25 (0.47)
$[\text{dppmCuAu}(\text{H})]^+$ m/z 645	$4.51 \pm 0.4 \times 10^{-10}$	43.1 ± 4.1	-0.3 (0.74)
$[\text{dppmAgAu}(\text{H})]^+$ m/z 689	$3.33 \pm 0.3 \times 10^{-11}$	3.2 ± 0.3	-0.08 (0.18)

[a] Mean \pm standard deviation ($n=3$) [b] In units of $\text{cm}^3 \cdot \text{molecules}^{-1} \cdot \text{s}^{-1}$. [c] Rates for the reaction with formic acid with $[\text{LMM}'\text{H}]^+$ to regenerate $[\text{LMM}'(\text{O}_2\text{CH})]^+$ as the product. Rates were determined by monitoring the decay of the reactant ion with a known concentration of formic acid over time. [d] Reaction efficiency = $(k_{\text{expt}}/k_{\text{ADO}}) \times 100$. The k_{ADO} is the theoretical ion-molecule collision rate constant obtained from the average-dipole orientation (ADO) theory,^[10] which was calculated using the Colrate program^[11] [e] data from [8]. [f] E_{act} relative to separated reactants (or relative to initial complex).

We next examined the ease of decarboxylation (Step 2, Figure 1). Due to the presence of isobaric impurities from ESI/MS as discussed previously, the formate complexes, formed via ion-molecule reactions between the hydrides and formic acid (Step 1), were mass selected and allowed to undergo CID in a MS^4 experiment (Figure S6). This precluded energy resolved CID measurements of thresholds for decarboxylation. In all cases decarboxylation was the major fragmentation pathway (Scheme S1), with competing formation of $[\text{dppmM}]^+$ and/or $[\text{dppmM}']^+$ being minor channels. At a normalized collision energy of 15% and an activation time of 10 msec, the amount of hydride formed (relative to all ions present in the CID spectrum) via decarboxylation follows the order of: $[\text{dppmAg}_2(\text{O}_2\text{CH})]^+$ (88.6%) \approx $[\text{dppmCu}_2(\text{O}_2\text{CH})]^+$ (85%) $>$ $[\text{dppmCuAu}(\text{O}_2\text{CH})]^+$ (76.6%) \approx $[\text{dppmCuAg}(\text{O}_2\text{CH})]^+$ (76.5%) $>$ $[\text{dppmAgAu}(\text{O}_2\text{CH})]^+$ (45%) $>$ $[\text{dppmAu}_2(\text{O}_2\text{CH})]^+$ (28.1%).

The DFT calculated energy diagrams are largely consistent with the experiments and provide insights into how reactivity is modulated by the nature of the metal centers (Figure 3 and Supporting Information Figures S8-S11).

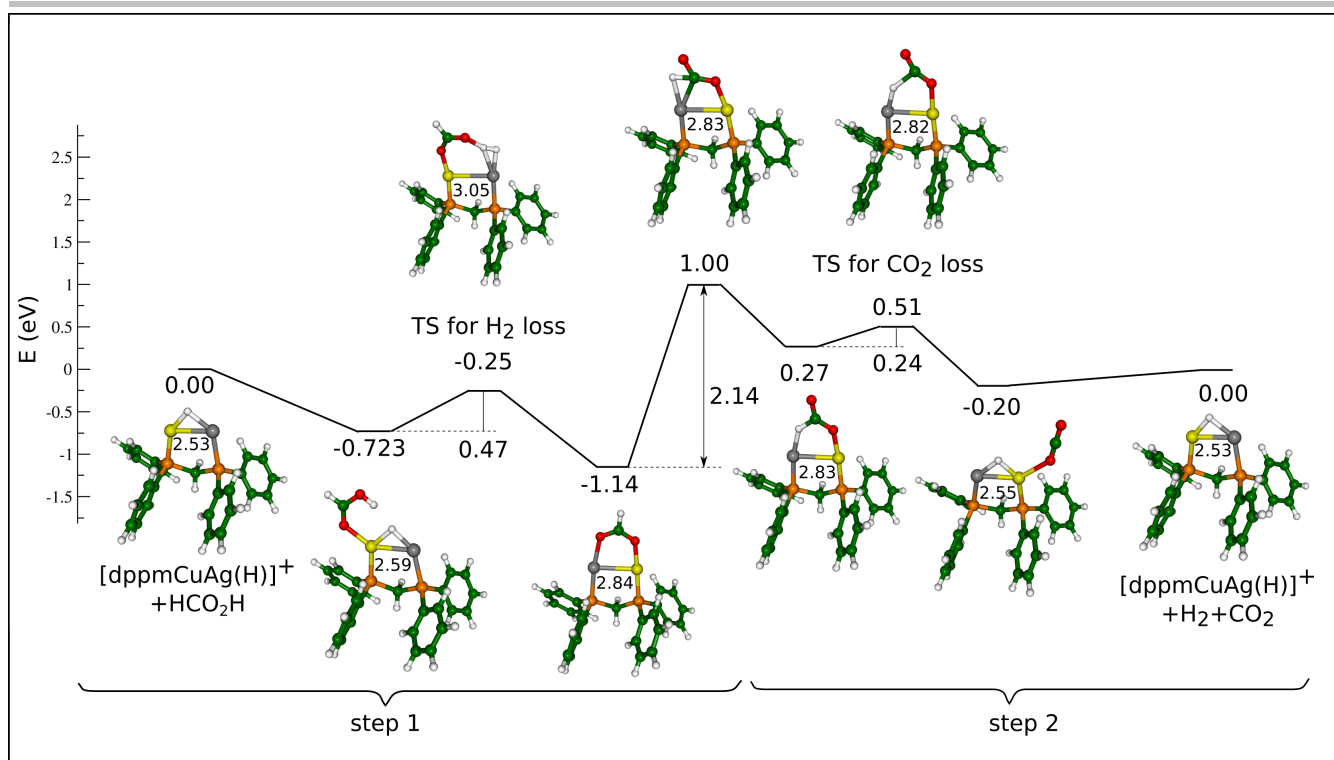


Figure 3. DFT-calculated energy profile for the preferred site of reactivity of the heterobinuclear complex for the two reaction steps in the catalytic cycle of Fig. 1a. Step 1: ion-molecule reaction of formic acid with $[\text{dppmCuAg}(\text{H})]^+$ at the copper site; step 2: CID decarboxylation of $[\text{dppmCuAg}(\text{O}_2\text{CH})]^+$ with hydride transfer to the silver site. Relative energies are in eV. All structures were fully optimized using DFT method with the hybrid B3LYP functional and def2-TZVP atomic basis set which has been used for all atoms. Silver atoms have been treated by Stuttgart relativistic effective core potential (RECP) with corresponding AO basis set. Silver = Ag, Yellow = Cu.

Step 1 of the catalytic cycle must be an exothermic process with barriers that lie below the separated reactants in order for it to occur under the near thermal conditions of the ion-trap.^[12] Indeed this is the case, with the most exothermic reaction occurring for $[\text{dppmCu}_2(\text{H})]^+$ (Table S2). In all cases an initial complex between the hydride, $[\text{dppmMM}'(\text{H})]^+$, and formic acid is formed, which then proceeds via a single transition state to produce H_2 and the thermodynamically favoured O,O-bridged formate complex, $[\text{dppmMM}'(\text{O}_2\text{CH})]^+$. In all cases this critical TS has a structure where one metal site acts as an "anchor" for the oxygen of the formic acid while the other metal site contains the hydride that is being protonated. In the case of the homobinuclear complexes, the well depth associated with the formation of the initial complex follows the order $[\text{dppmAu}_2(\text{H})]^+$ (-1.08 eV) > $[\text{dppmCu}_2(\text{H})]^+$ (-0.73 eV) > $[\text{dppmAg}_2(\text{H})]^+$ (-0.24 eV) and thus dictates the observed reactivity.^[13] For the heterobinuclear complexes, formic acid can approach either of the two different metal centres. A detailed examination of all possible reactant complexes and transition states for attack at both copper and silver was carried out for $[\text{dppmCuAg}(\text{H})]^+$ (Supporting Information Table S2). The most favoured site of attack is at copper (Figure 3), consistent with the relative reactivity order for the homobinuclear complexes. For $[\text{dppmCuAu}(\text{H})]^+$ the preferred site of reactivity is Cu (Figures S10), while for $[\text{dppmAgAu}(\text{H})]^+$ it is Au (Figures S11). Overall, there is good agreement between theory and experiment, with the DFT predicted activation energies for step 1 being inversely

related to the measured reaction efficiencies (compare columns 4 and 3 of Table 1).

In contrast, decarboxylation is endothermic as it requires energization of $[\text{dppmMM}'(\text{O}_2\text{CH})]^+$ through multiple collisions with the helium bath gas during the CID process. The DFT calculations reveal that both metal centers play a role in the mechanism for CO_2 release, which involves two steps (Figure 3 and Figures S8-10), except for $[\text{dppmAgAu}(\text{O}_2\text{CH})]^+$, which only requires a single transition state (Figures S11). The first step involves breaking one of the M-O bonds to isomerize the O,O-bridged formate to its O-bound form, and is the rate determining step except for $[\text{dppmAg}_2(\text{O}_2\text{CH})]^+$ and $[\text{dppmCuAu}(\text{O}_2\text{CH})]^+$. The next step involves decarboxylation, to give the O bound $[\text{dppmMM}'(\text{H})(\text{OCO})]^+$ complex, which then loses CO_2 . For the heterobinuclear complexes, hydride transfer from the coordinated formate can occur to either metal centre. A detailed examination of all possible transition states and intermediates associated with hydride transfer to either copper or silver sites was carried out for $[\text{dppmCuAg}(\text{H})]^+$ (Supporting Information Table S2). In step 2, the most favoured site of attack is at silver (Figure 3), consistent with both the experimentally determined relative reactivity order and DFT calculated energetics for the homobinuclear complexes.

In conclusion, the DFT calculations show that both metal centers play a role in both steps of the catalytic cycle. One metal site acts as an "anchor" for the oxygen of formic acid (step 1) or

formate (step 2) while the other site facilitates protonation of the hydride (step 1) or abstraction of the hydride (step 2). Since each metal center may influence each step of a catalytic cycle in a different way, the overall preferred bimetallic catalyst is that which represents a compromise in reactivity for all steps as well as the cost of the metal. This is the case here, where the cheaper, earth abundant copper catalyst $[\text{dppmCu}_2(\text{H})]^+$ is the second most reactive complex and is regenerated from $[\text{dppmCu}_2(\text{O}_2\text{CH})]^+$ slightly less efficiently than the hydride from CID of $[\text{dppmAg}_2(\text{O}_2\text{CH})]^+$.

Experimental Section

Gas-phase studies using CID and IMR

Gas-phase experiments on phosphine ligated bimetallic formate clusters, formed as discussed in the Supporting Information, were carried out using a Finnigan hybrid linear quadrupole Fourier transform ion-cyclotron resonance (LTQ FTICR) mass spectrometer modified to allow the study of IMR.^[14] The unimolecular fragmentation/dissociation of mass-selected phosphine ligated bimetallic clusters occurred via CID using a normalized collision energy between 20 – 25% and an activation time of 30 ms. The CID isolation width was 5 – 8 m/z from the centre of the ion cluster distribution. IMRs were carried by delivering a measured concentration of formic acid into the helium bath gas.

DFT calculations

The extensive search for lowest energy structures and transition states were performed by the hybrid B3LYP^[15] functional with def2-TZVP atomic basis set,^[16] which has been used for all atoms. Silver/Gold atoms have been treated by Stuttgart relativistic effective core potential (RECP) with corresponding AO basis set.^[17]

Potential interactions between the aromatic rings of dppm, raises the question of whether the dispersion correction within DFT are required. We have tested the influence of dispersion correction on the structural properties of $[\text{dppmAg}_2\text{H}]^+$ and $[\text{dppmAg}_2(\text{O}_2\text{CH})]^+$ complexes by introducing D3 into the DFT.^[18] Since the energy profile remained almost unchanged when single point B3LYP-D3 energy calculations were carried out for each reaction step of the catalytic cycle we have not used it for all profiles.

Acknowledgements

We thank the ARC for financial support via grant DP150101388 (to RAJO and PD). AZ acknowledges the award of an Australian Postgraduate PhD Scholarship. The research leading to these results has received funding from the European Research Council under the European Union's Seventh Framework Programme (FP7/2007-2013 Grant agreement N°320659). VBK and MK acknowledge computational facilities of the supercomputer "Bura" at the University of Rijeka and SRCE at University of Zagreb as well as Prof. Miroslav Radman at MedILS and Split-Dalmatia County for kind support.

Keywords: Bimetallic catalysis • Selective Decomposition • Formic acid • Gas phase • Coinage Metal Hydrides

- [1] J. I. van der Vlugt, *Eur. J. Inorg. Chem.* **2012**, 363 – 375.
- [2] W. Yu, M. D. Porosoff, J. G. Chen, *Chem. Rev.* **2012**, 112, 5780–5817.
- [3] M. H., Pérez-Temprano, J. A. Casares, P. Espinet, *Chem. Eur. J.* **2012**, 18, 1864 – 1884.
- [4] N. P. Mankad, *Chem. Eur. J.* **2016**, 22, 5822 – 5829.

- [5] a) R. A. J. O'Hair, *Chem. Comm.* **2006**, 1469 – 1481. b) R. A. J. O'Hair, N. J. Rijs, *Acc. Chem. Res.* **2015**, 48, 329 – 340. c) R. A. J. O'Hair, *Pure. Appl. Chem.* **2015**, 87, 391 – 404.
- [6] For reviews on the use of MS to examine catalysis in the gas phase see: a) D. K. Böhme, H. Schwarz, *Angew. Chem. Int. Ed.*, **2005**, 44, 2336–2354; b) D. Schröder, *Acc. Chem. Res.*, **2012**, 45, 1521–1532; c) H. Schwarz, *Isr. J. Chem.* **2014**, 54, 1413–1431; d) R. A. J. O'Hair, *Int. J. Mass Spectrom.* **2015**, 377, 121 – 129.
- [7] For examples of bimetallic reactivity in the gas-phase, see: a) K. Koszinowski, D. Schröder, H. Schwarz, *J. Am. Chem. Soc.* **2003**, 125, 3676–3677; b) K. Koszinowski, D. Schröder, H. Schwarz, *ChemPhysChem* **2003**, 4, 1233–1237; c) K. Koszinowski, D. Schröder, H. Schwarz, *Organometallics* **2004**, 23, 1132–1139; d) H. Al Sharif, K. L. Vikse, G. N. Khairallah, R. A. J. O'Hair, *Organometallics*, **2013**, 32, 5416 – 5427; e) G. N. Khairallah, G. R. da Silva, R. A. J. O'Hair, *Angew. Chem. Int. Ed.*, **2014**, 53, 10979–10983; f) K. L. Vikse, A. Zavras, T. H. Thomas, A. Ariafard, G. N. Khairallah, A. J. Canty, B. F. Yates, R. A. J. O'Hair, *Organometallics*, **2015**, 34, 3255–3263.
- [8] A. Zavras, G. N. Khairallah, M. Krstić, M. Girod, S. Daly, R. Antoine, P. Maitre, R. J. Mulder, S.-A. Alexander, V. Bonačić-Koutecký, P. Dugourd, R. A. J. O'Hair, *Nature Communications*, **2016**, 7, 11746.
- [9] For a comprehensive review on the formation and reactions of coinage metal hydrides see: A. J. Jordan, G. Lalic, J. P. Sadighi, *Chem. Rev.*, **2016**, 116, 8318–8372.
- [10] T. Su, M. T. Bowers, *Gas-Phase Ion Chemistry* **1949**.
- [11] K. F. Lim, *Quantum Chemistry Program Exchange* **1994** 14, 3. The program Colrate is available for download from the author's website at Deakin University, Geelong, Victoria, Australia: <http://www.deakin.edu.au/~lim/programs/COLRATE.html>.
- [12] a) S. Gronert, *J. Am. Soc. Mass Spectrom.*, **1998**, 9, 845–848; b) W. A. Donald, G. N. Khairallah, R. A. J. O'Hair, *J. Am. Soc. Mass Spectrom.*, **2013**, 24, 811–815.
- [13] Although there is a dearth of experimental thermochemical data for these systems, the DFT calculated binding energy orders are consistent with the relative atomic metal cation water binding energy orders: $\text{D}(\text{H}_2\text{O}-\text{Au}^+) > \text{D}(\text{H}_2\text{O}-\text{Cu}^+) > \text{D}(\text{H}_2\text{O}-\text{Ag}^+)$ (J. Roithová, D. Schröder, *Coord. Chem. Rev.* **2009**, 253, 666).
- [14] W. A. Donald, C. J. McKenzie, R. A. J. O'Hair, *Angew. Chem. Int. Ed.*, **2011**, 50, 8379–8383.
- [15] A. D., Becke, *J. Chem. Phys.* **1993** 98, 5648.
- [16] A. Schäfer, H. Huber, R. Ahlrichs, *J. Chem. Phys.* **1994**, 100, 5829 – 5835.
- [17] D. Andrae, U. Haeussermann, M. Dolg, H. Stoll, H. Preuss, *Theor. Chim. Acta.* **1990**, 77, 123 – 141.
- [18] S. Grimme, J. Antony, S. Ehrlich, H. Krieg, *J. Chem. Phys.* **2010**, 132, 154104.

CONCLUSIONS AND OUTLOOK

In this thesis the contributions to major challenges that hinders worldwide application of the hydrogen fuel cells have been accomplished. (1) The first one is low quality of the hydrogen fuel cell feed gas which contains minor amounts of CO which acts as a poison to the platinum nanoparticle catalyst within the fuel cell. (2) The second challenge is related to safe storage and release of hydrogen.

Issue of the insufficient quality of the fuel cell feed gas containing minor percentage of the carbon monoxide has been investigated on the model systems of the gas-phase ruthenium nanoclusters which has been shown to actively and selectively promote catalytic carbon monoxide methanation reaction. Full insight into the structural properties of these ruthenium carbonyl clusters is provided by extensive *ab initio* calculations. These results are in accordance with experimental findings. namely, the exclusive formation of only one complex for each cluster size in mass spectrometry ion-trap shows particular stability of these ruthenium nanoclusters in accordance with structures predicted by theoretical results and Wade's counting rules. Moreover, synthesized ruthenium carbonyl and hydrido carbonyl clusters in the gas phase are analogues to condensed-phase findings which have showed that $\text{H}_4\text{Ru}_4\text{CO}_{12}$ and $\text{Ru}_6\text{CO}_{18}^{2-}$ mediate several important chemical reactions like the hydrogenation of CO and olefins or to promote methanation reaction. This proves that the gas phase investigation has particular value because it allows for complementary theoretical study of structural and reactivity properties. In fact, these structures of carbonyl and hydrido carbonyl clusters obtained in this part of theses were used as input structures to study methanation reaction.

Second, a calculation of step by step reaction profile of the methanation reaction on the simple model system of Ru_6^+ binding one CO molecule and sequential binding of 4 H_2 molecules allowed to elucidate the origin of the remarkable catalytic selectivity and activity of oxide supported ruthenium particles in sub-nanometer regime. Reaction profile demonstrated that reaction proceeds over the formyl-type intermediate. All calculated transition states for methanation reaction to occur are lower than the energy of the initial reactants and overall reaction is exothermic by 4.52 eV. Following simple model, more complex model of experimentally observed CO-rich $\text{Ru}_4\text{CO}_{13}\text{H}_2^+$ has been theoretically studied in context of catalytic CO methanation reaction. It has been shown that the reaction proceeds along mechanistically similar pathway. All theoretical findings are fully supported by the experimental results.

It is worth to emphasize that conceptual mechanistic insight gained through these investigations are an important step towards understanding of supported Ru particle catalysts. Unraveling fundamental processes taking place in the CO methanation reaction mediated by the gas-phase ruthenium nanoclusters opens new possibility for transferring model system results to guide an intelligent design of superior catalytic materials for fuel cell feed gas purification. Improved methanation catalysts based on ruthenium nanoclusters should

exhibit following properties: 1) 100% CO/CO₂ selectivity; 2) promote hydrogen and carbon monoxide co-adsorption on the same active center; and 3) contain catalytically active centers forming low number of metal-metal bonds. Only very small ruthenium nanoclusters containing up to 10 atoms satisfy all preconditions. Therefore, as outlook we propose to employ zeolites as support to anchor Ru carbonyl and hydrido carbonyl clusters as a new catalytic systems. This will allow to prevent poisoning of platinum nanoparticles by CO inside the hydrogen fuel cells and extend its durability.

The second part of this thesis is focused on the fuel cell challenge concerning hydrogen release in context of improving hydrogen storage technology. Combination of extensive density functional investigations and multistage mass spectrometry under collision and light induced dissociation conditions have been used to probe:

- 1) fragmentation chemistry of ligated silver hydride nanoclusters and
- 2) catalytic reactivity towards selective decomposition of formic acid to H₂ and CO₂ promoted by homo- and heterobinuclear coinage metal hydrides.

1) Concerning first issue, theoretical study of the series of decanuclear ligand protected silver hydride clusters gave insight into fragmentation processes leading eventually to simultaneous release of all hydrogen atoms from the silver core. Step by step analysis of energetics and structural consequences of this transformation showed the changes in the structure of the silver core upon sequential loss of two and one dppm ligands, respectively, which triggered loss of 8 hydrogen atoms. First two steps are calculated to be exothermic while hydrogen loss is slightly exothermic which is in perfect agreement with collision induced dissociation experiments. This process is of particular interest since it represents a change from the ionic silver hydride [Ag₁₀H₈L₆]²⁺ to the metallic silver cluster [Ag₁₀L₆]²⁺.

Further understanding of the fragmentation chemistry concerning hydrogen release has been gained by comprehensive theoretical molecular dynamics simulations of the smaller ligand protected silver hydrides, namely [Ag₃H₂L]⁺. MD simulations have been performed in the ground and first excited state showing that hydrogen formation and release can occur when the hydride cluster is irradiated by light. Experiments in the gas-phase under CID and LID conditions are in excellent agreement with the theoretically predicted fragmentation during MD simulations, showing AgH and H₂ as a major fragmentation channels in the ground state S₀ and excited state S₁, respectively. This finding might be a general pathway for the photo-release of hydrogen from metallic clusters in which the ligand plays the key role. All together, these investigations provide detailed insight into fragmentation chemistry of ligand protected silver hydrides with potential for application in the hydrogen storage and release technology.

2) Concerning second issue catalytic activity of noble metal hydrides in context of hydrogen release stimulated us to pursue investigation of selective extrusion of hydrogen and carbon dioxide from formic acid. DFT calculations have been employed to systematically study the role of different ligands to modulate the activation and reactivity of binuclear silver hydride. Catalytic cycle is divided in two steps: (1) formation of hydrogen molecule and its release which is exothermic process and (2) release of carbon dioxide for which additional energy have to be introduced in system to overcome the relatively high barriers. Theoretical approach in conjunction with mass spectrometry based methods allows for systematic exploration of the factors that controls reactivity for both steps in a catalytic cycle. Here we have shown that the proper choice of a ligand is a crucial factor in design of the silver hydride catalyst that mediate the formic acid decomposition reaction. Indeed, we have demonstrated

that dppm ligand (dppbz and dppe also) has an influence on the Ag_2H geometry and overall catalytic activity by shortening the Ag-Ag bond and weakening the Ag-H interaction thus switching on the protonation of the silver hydride in the step 1 of the catalytic cycle. The same dppm ligand also has influence on the step 2 compared to other ligand types studied by lowering the barriers needed for decarboxylation to occur. Furthermore, to gain complete insight into selective decomposition of formic acid to H_2 and CO_2 the role of metallic centers has been investigated. Theoretical calculations enabled us to study the influence of different homo- and heterobinuclear metal hydrides composed from silver, gold and copper atoms on the reaction profiles. The results unambiguously showed that both metal centers play a role in both catalytic steps. One metal site acts as a binding site for the oxygen atom of the formic acid while the other site mediates protonation of the hydride. Concerning the overall reactivity and the cost of coinage metals it is concluded that the optimal bimetallic catalyst is the earth abundant ligand protected copper hydride $[\text{dppmCu}_2(\text{H})]^+$. It is important to emphasize that all theoretical results are in excellent agreement with experimental findings (e.g. multistage energy resolved CID experiments). Moreover, theoretical results stimulated experimentalists to transfer the catalytic reaction from gas-phase to solution-phase where hydrogen and carbon dioxide evolution were observed almost instantly. Finally, two key concepts emerged from this work: (i) the role of ligands and different metal types have a vital role in catalyst activation and its reactivity towards substrate, and (ii) fundamental gas-phase studies can be used to gain insight into crucial steps of the catalytic cycle with possibility to direct design of new metal complexes that promote the desired reaction in the solution. Conceptual issues presented here together with successful extrusion of carbon dioxide from formic acid represent an important process for application in hydrogen storage in the future.

In conclusion, throughout this thesis we demonstrated that powerful combination of density functional theory and experimental investigations can contribute to intelligently developed new materials and procedures to overcome the challenges hampering worldwide application of fuel cells as "green" technology of the future. This has been achieved through: 1) improving quality of the hydrogen fuel cell feed gas by carbon monoxide methanation and 2) knowledge-driven design of small ligated noble metal hydrides which can promote hydrogen release, an important prerequisite for advancing hydrogen storage technology. Results from both directions are promising for future research.

APPENDIX

- 1 **Composition dependent selectivity in the coadsorption of H₂O and CO on pure and binary silver-gold clusters**



Contents lists available at SciVerse ScienceDirect

Chemical Physics Letters

journal homepage: www.elsevier.com/locate/cplettComposition dependent selectivity in the coadsorption of H₂O and CO on pure and binary silver–gold clustersIrene Fleischer^a, Denisia M. Popolan^a, Marjan Krstić^b, Vlasta Bonačić-Koutecký^{b,c,*}, Thorsten M. Bernhardt^{a,*}^a Institute of Surface Chemistry and Catalysis, University of Ulm, Albert-Einstein-Allee 47, 89069 Ulm, Germany^b Interdisciplinary Center for Advanced Sciences and Technology (ICAST), University of Split, Meštrovićevo, Šetalište bb., 2100 Split, Croatia^c Chemistry Department, Humboldt University of Berlin, Brook-Taylor-Strasse 2, 12489 Berlin, Germany

ARTICLE INFO

Article history:

Received 20 August 2012

In final form 7 February 2013

Available online 16 February 2013

ABSTRACT

Small cationic gold clusters exhibit a strong affinity toward carbon monoxide. This prevents the coadsorption of water which would be the first step of a catalytic water gas shift chemistry on these clusters. In a gas phase ion trap experiment with mass selected Ag_nAu_m⁺ it was however possible to demonstrate that the replacement of gold by silver atoms in triatomic cluster ions liberates sites for H₂O adsorption. The resulting observed coadsorption effect occurs at a cross-over in the molecular binding energies of carbon monoxide and water to these clusters determined by reaction kinetics measurements and first principles calculations.

© 2013 Elsevier B.V. All rights reserved.

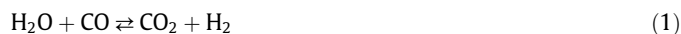
1. Introduction

There is currently a strong interest in the properties of intermetallic compounds with finite nanoscale dimensions which are often conveniently termed ‘nanoalloys’ [1]. With respect to the reactive properties of such small alloy particles in heterogeneous catalysis recent results show surprising activities and in particular product selectivities that clearly deviate from those of the pure constituent metal compounds [2–4].

Gas phase experiments with mass-selected clusters can contribute to gain molecular level insight into the mechanistic origin of such new chemical properties of nanoalloy metal particles [5]. In addition to the exactly defined size also the composition can be varied atom by atom in such small clusters and thus detailed trends in the chemical reactivity can be revealed [6–10].

In this contribution we explore the possibility to tune the reactive properties of triatomic gold cluster cations by ‘alloying’ with silver. Small positively charged gold clusters are known to strongly bind carbon monoxide [9–13] which prevents the coadsorption of

many other ligands. Here, we are interested in the interaction of CO with water in a water gas shift reaction scheme:



This reaction is technically important for the production of hydrogen and the removal of noxious CO impurities in, e.g., fuel cell feed gases. In the water gas shift reaction the coadsorption of CO and H₂O on the catalyst represents the necessary first reaction step, followed by activation of the ligands and the subsequent actual chemical transformation. Previous studies already indicated that the replacement of gold by silver atoms leads to a weaker bonding of CO to the clusters [10,11,13].

In the following we present the first investigation (experimental and theoretical) of the coadsorption of water with carbon monoxide as a function of the composition of binary silver–gold cluster cations. The results reveal that the adsorption of both molecules is indeed possible on Ag₂Au⁺ and that this effect can be related to a cross-over in the binding energies of these molecules to the clusters of different composition.

2. Methods

The reaction between mass-selected cluster ions and neutral reactant gases without the influence of a surface were investigated in a gas phase low energy ion beam setup that includes a radio frequency (rf) octopole ion trap inserted into a system of quadrupoles to guide the ions and a quadrupole mass spectrometer to detect the products. This experimental layout has been described in detail elsewhere [14–16] and will only be described briefly here. In addition to the data acquisition routine a concise summary of the data

* Corresponding authors. Addresses: Chemistry Department, Humboldt University of Berlin, Brook-Taylor-Str. 2, 12489 Berlin, Germany. Fax: +49 (0)30 2093 5573, and Interdisciplinary Center for Advanced Sciences and Technology (ICAST), University of Split, Meštrovićevo, Šetalište bb., 2100 Split, Croatia (V. Bonačić-Koutecký), Institute of Surface Chemistry and Catalysis, University of Ulm, Albert-Einstein-Allee 47, 89069 Ulm, Germany. Fax: +49 (0) 731 50 25452 (T. M. Bernhardt).

E-mail addresses: vbk@chemie.hu-berlin.de (V. Bonačić-Koutecký), thorsten.bernhardt@uni-ulm.de (T.M. Bernhardt).

evaluation methods will be given in the following. Finally, the computational methods will be described.

2.1. Data acquisition

The sputtering of metal-alloy targets (70 wt.% Ag, 30 wt.% Au) with a cold reflex discharge ion source (CORDIS [17]) was employed to generate the metal cluster cations. The cluster ions were thermalized by collisions with helium gas, mass-selected by a first quadrupole filter and subsequently guided to the octopole ion trap which was filled with about 1 Pa helium buffer gas and small partial pressures of reactant gas. The total pressure inside the ion trap was measured by a Baratron gauge (MKS, type 627B). The temperature of the trap could be varied between 20 and 300 K by resistive heating against an attached helium cryostat. Thermal equilibration of the clusters was achieved under these experimental conditions within a few milliseconds [15]. After a defined reaction time, i.e. storage time inside the trap, the products were extracted and analyzed with a further quadrupole mass filter. By recording all the product ion concentrations as a function of the reaction time, the kinetics of the reaction could be measured.

2.2. Data evaluation

To determine the binding energies of the carbonyl ligands to the metal clusters the thermodynamic equilibrium evaluation method was used (see Ref. [10] and references therein). This method is based on temperature dependent measurements of the reactions of interest under thermodynamic equilibrium conditions.

Yet, the reaction experiments with water as reactant gas could be performed reliably only at room temperature because of condensation effects that occurred, if the trap was held at a different temperature than the gas inlet. Therefore, room temperature kinetics measurements were performed in the case of the reaction between the metal clusters and water and statistical reaction rate analysis employing the Rice-Ramsperger-Kassel-Marcus (RRKM) method was applied to determine the water binding energies [18,19]. Details of the statistical kinetics evaluation procedure and of the corresponding error analysis have been described elsewhere [10,16] and thus only a summary of this method to obtain ligand binding energies will be given in the following.

For the analysis of the metal cluster reactions with H₂O simple association reactions according to Eq. (2) were assumed to proceed in the ion trap.

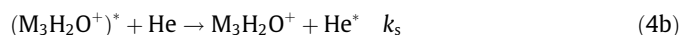
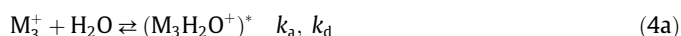


During the reaction the concentration of the reactive gas in the octopole ion trap was orders of magnitude larger than the metal cluster ion concentration and a steady flow of the reactants was ensured. Hence, the concentration of the reactive gas was considered to remain constant in the data evaluation procedure. Consequently, the association reaction (2) was assumed to follow pseudo-first-order kinetics with the rate constant k . The reaction kinetics was evaluated by fitting the integrated rate equations of the mechanism Eq. (2) to the normalized experimental kinetic data [19]. The pseudo-first-order rate constant k contains the termolecular rate constant $k^{(3)}$ as well as the concentrations of the helium buffer gas and the reactive gas (Eq. (3)).

$$k = k^{(3)}[He][H_2O] \quad (3)$$

Thus, the termolecular rate constant can be obtained from the experimentally determined pseudo-first-order rate constant k and the partial pressures of Helium buffer gas and water (after correction for thermal transpiration [16,20–23]). As the total pressure inside the trap was about 1 Pa the reactions were performed in the

kinetic low-pressure regime. Therefore, an energy transfer mechanism has to be considered for the overall association reaction Eq. (2) to occur [19]:



The energy transfer mechanism consists of three elementary steps including the formation of an energized complex $(M_3H_2O^+)^*$ in the first association step with the rate constant k_a . The reverse dissociation reaction with the rate constant k_d describes the potential unimolecular decomposition back to the reactants. In competition with this dissociation step, the stabilization through an energy-transfer collision with a Helium atom is possible. k_s is the rate constant for the stabilization reaction.

If the steady-state approximation is considered [19], the overall third-order rate constant is given by

$$k^{(3)} = k_a k_s / (k_d + k_s[He]) \quad (5)$$

Under the given low pressure conditions the decomposition rate constant can be considered to be much larger than the stabilization rate constant ($k_d \gg k_s[He]$) resulting in a new expression for the third-order rate constant

$$k^{(3)} = k_a k_s / k_d \quad (6)$$

The association rate constant k_a and the stabilization rate constant k_s can be approximated by ion–molecule collision rate constants as specified by Langevin theory [16,19,24]. Both reactions are ion–dipole or ion-induced dipole interactions, respectively, without energy barriers.

In contrast, the unimolecular decomposition reaction with the rate constant k_d exhibits an activation energy barrier, which is associated with the molecular binding energy of the ligand to the metal clusters. k_d can be obtained from statistical reaction rate theory in the framework of the RRKM method [18,25] and thus be used to determine the H₂O binding energies E_b . For this purpose the software package 'MassKinetics' was employed to simulate the decomposition rate constant k_d on the basis of a given binding energy [26]. The vibrational frequencies of the metal clusters required in the RRKM calculations have been taken from the current theoretical results.

In the calculations a 'tight' and a 'loose' transition state (TS) model was assumed [16]. A 'tight' TS model describes bond rearrangement processes and results in a lower limit of E_b [16,28]. In contrast, a 'loose' TS model is usually associated with simple dissociation reactions and thus represents a more realistic model for the cluster-molecule systems investigated here. For a detailed description of the RRKM evaluation procedure please see Ref. [16].

2.3. Computational methods

The structural properties of all binary silver–gold trimer cluster complexes $Ag_nAu_m(H_2O)^+$ ($n + m = 3$) were determined using density functional theory (DFT) with the hybrid B3LYP functional [29–32]. For gold and silver atoms a triple-zeta-valence-plus-polarization (TZVP) atomic basis set combined with a 19-electron relativistic effective core potential (19e-RECP) were employed [33,34]. For the hydrogen and oxygen atoms we used the TZVP atomic basis sets [35]. All structures presented were fully optimized using gradient minimization techniques.

3. Results

The reactions between CO and the free gold, silver and binary silver–gold trimer clusters have been studied in our laboratories

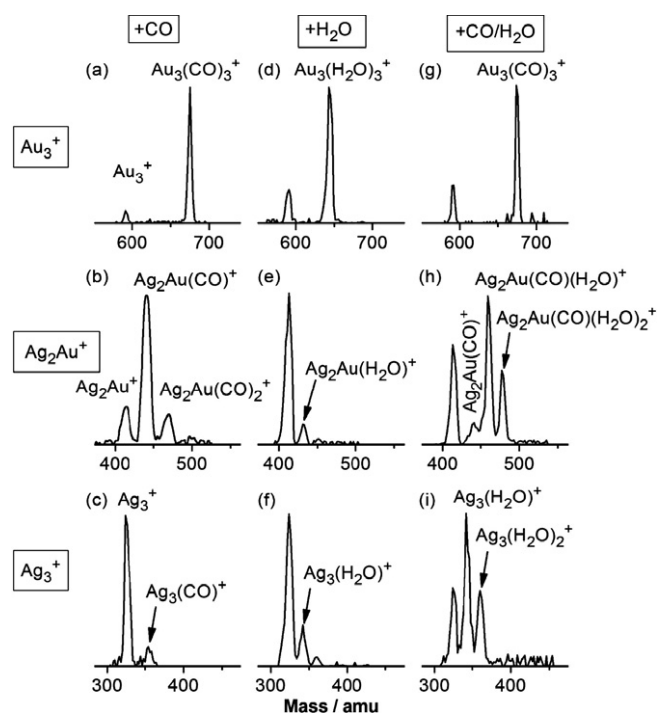


Figure 1. Product ion mass distributions measured after the reaction of Au_3^+ (a, d, g), Ag_2Au^+ (b, e, h), and Ag_3^+ (c, f, i) with CO (a–c) and H_2O (d–f) at 300 K ($p(\text{He}) = 1$ Pa; $p(\text{CO}) = 0.02$ Pa, except in (b) $p(\text{CO}) = 0.22$ Pa; $p(\text{H}_2\text{O}) = 0.003$ Pa). The spectra in the right column display product ion mass distributions obtained when both reactive molecules CO and H_2O were present in the ion trap ($p(\text{CO}) = 0.04$ Pa, $p(\text{H}_2\text{O}) = 0.004$, 300 K) for Au_3^+ (g), Ag_2Au^+ (h) and Ag_3^+ (i). All the spectra were obtained after a reaction time of 500 ms.

previously [10]. Depending on the reaction temperature all investigated trimer clusters adsorb CO in sequential equilibrium reaction steps. Figure 1a–c displays the corresponding product mass spectra obtained at room temperature and a reaction time of 500 ms. The complete kinetics and temperature dependent analysis can be found in Reference [10]. Under these conditions the pure gold cluster Au_3^+ rapidly reacts with three CO, each attached to one gold atom of the cluster, leading to the final product $\text{Au}_3(\text{CO})_3^+$ [10]. Under similar experimental conditions, the pure silver and the binary silver–gold cluster Ag_2Au^+ react with only one CO each. If the CO pressure is increased, further CO adsorption is observed. This is shown for the case of Ag_2Au^+ in Figure 1b. The enhanced reactivity of Au_3^+ toward CO is also reflected in the composition dependent binding energy (displayed in Figure 2), which is considerably higher for Au_3^+ than for the other trimers.

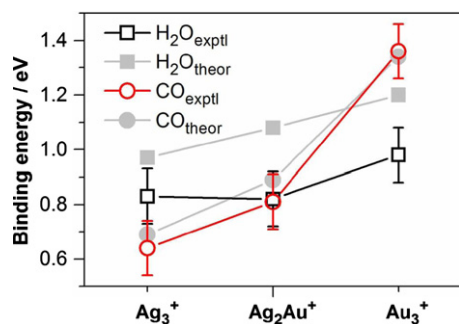


Figure 2. Experimental and theoretical composition dependent binding energies of a first H_2O (squares, experimental values based on the ‘loose’ TS model) and CO (circles) molecule, respectively, to the clusters Ag_3^+ , Ag_2Au^+ and Au_3^+ . Binding energies of CO to the clusters have been taken from Ref. [10]. The lines connecting the data points have been drawn to guide the eye.

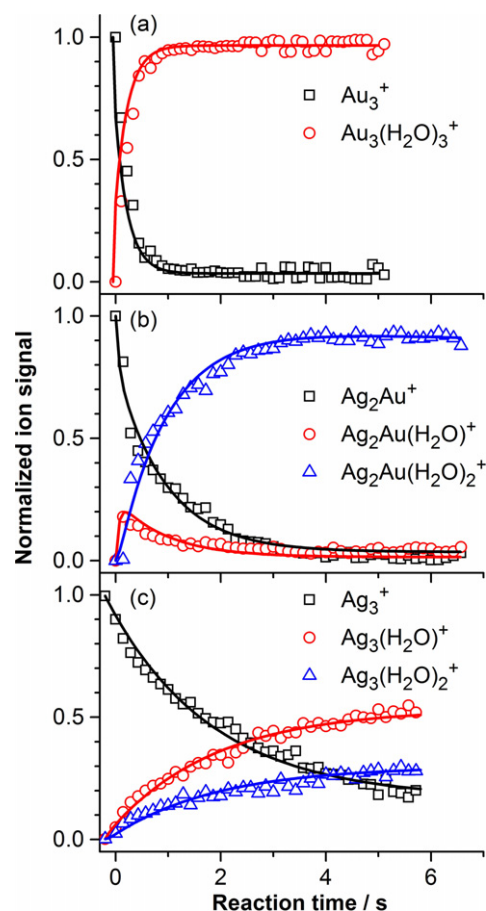
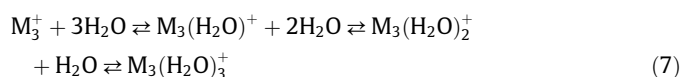


Figure 3. Kinetics of the reactions of Ag_3^+ (a), Ag_2Au^+ (b), and Au_3^+ (c) with H_2O at 300 K. The open symbols represent the experimental data, normalized to the initial metal cluster concentration and to the total ion concentration in the trap. The solid lines have been obtained by fitting the integrated rate equations of the proposed reaction mechanism (Eq. (7)) to the experimental data. The experimental pressure conditions are included in Table 1.

The interaction of H_2O with Au_3^+ has been investigated previously [36]. However, no quantitative binding energies have been determined so far. Also no reaction studies of Ag_3^+ or of Ag_2Au^+ with water have been reported in the literature. Figure 1d–f displays the product mass spectra after reaction of H_2O with these trimer clusters at room temperature. The corresponding kinetic traces are depicted in Figure 3. All clusters have the capability to form adsorption products with H_2O . The pure silver cluster reacts with up to two ligands as does Ag_2Au^+ . Au_3^+ is again the most reactive cluster and leads to the complex $\text{Au}_3(\text{H}_2\text{O})_3^+$ as final product.

Experimental binding energies of the first H_2O molecule to these clusters have been determined via statistical analysis of the kinetic data in Figure 3 as described in the Methods Section. The solid lines in Figure 3 represent the best fit of the integrated rate equations to the experimental data according to the following sequential H_2O association reaction mechanism:



The thus obtained rate constants k for the adsorption of the first water molecule are listed in Table 1 and the resulting binding energies can be found in Table 2 for the different transition state models as detailed in Section 2.2 together with the theoretically obtained values.

From the graphical comparison of the CO and the H_2O binding energies (experimental values are displayed only for the more

Table 1

Measured pseudo first order (k) and termolecular ($k^{(3)}$) rate constants for the investigated reactions of the trimer cluster cations M_3^+ with water, as well as deduced unimolecular decomposition rate constants (k_d) of the energized complexes ($M_3H_2O^+$) * at 300 K. Also included are the experimental pressure conditions (not yet corrected for thermal transpiration [16]) and the Langevin rate constants k_a and k_s .

M_n^+	$p(\text{He})$ (Pa)	$p(\text{H}_2\text{O})$ (Pa)	k (s^{-1})	$k^{(3)}$ ($10^{-28} \text{ cm}^6 \text{ s}^{-1}$)	k_a ($10^{-10} \text{ cm}^3 \text{ s}^{-1}$)	k_s ($10^{-10} \text{ cm}^3 \text{ s}^{-1}$)	k_d (10^9 s^{-1})
Ag_3^+	1.000	0.004	0.41 ± 0.08	19 ± 6	23.27	5.328	67 ± 22
Ag_2Au^+	1.000	0.004	1.17 ± 0.23	53 ± 17	23.13	5.322	23 ± 8
Au_3^+	1.011	0.005	4.0 ± 0.8	178 ± 6	22.98	5.315	0.07 ± 0.02

Table 2

Binding energies E_b of H_2O to all investigated cluster ions M_3^+ as deduced by employing RRKM theory for 'tight' and 'loose' TSs as well as DFT theory.

M_3^+	E_b (eV) exptl. 'tight' TS	E_b (eV) exptl. 'loose' TS	E_b (eV) theoretical
Ag_3^+	0.49 ± 0.1	0.83 ± 0.1	0.97
Ag_2Au^+	0.47 ± 0.1	0.82 ± 0.1	1.08
Au_3^+	0.58 ± 0.1	0.98 ± 0.1	1.20

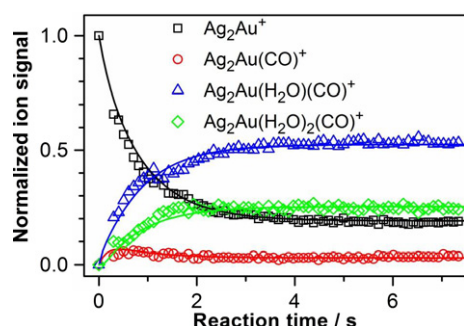


Figure 4. Kinetics of the reaction of Ag_2Au^+ with CO and H_2O at 300 K. The open symbols represent the normalized ion signals, while the solid lines are obtained by fitting the integrated rate equations of the proposed reaction mechanism (Eq. (8)) to the experimental data.

realistic 'loose' transition state model) in Figure 2 it is apparent that a cross over occurs in the affinity of the small clusters toward these molecules as a function of the composition. Whereas CO binds more strongly to Au_3^+ than H_2O the reverse relative bonding behavior is observed for Ag_3^+ . The theoretical data confirm this result as can be seen from Figure 2. The agreement between the theoretical CO binding energies and the experimental data is very favorable. Also the trend in the calculated H_2O binding energies is quite similar to the experiment. Yet, the quantitative theoretical H_2O binding energies are systematically 0.18–0.22 eV higher than the experimental values.

The major goal of this Letter was to investigate the potential coadsorption of CO and H_2O on the chosen noble metal trimers which is the mandatory first step with respect to their prospective activation and subsequent reaction in a water gas shift type chemistry. Figure 1g–i thus shows product mass spectra of the investigated clusters in the case when both reactants H_2O and CO are present in the ion trap.

No difference is detected in the presence of water compared to the result when CO is the sole reactant for Au_3^+ . The complex $\text{Au}_3(\text{CO})_3^+$ is observed as the major product. However, most surprisingly, the replacement of two gold atoms by silver in Ag_2Au^+ apparently liberates sites for the adsorption of H_2O and the coadsorption complexes $\text{Ag}_2\text{Au}(\text{H}_2\text{O})\text{CO}^+$ as well as $\text{Ag}_2\text{Au}(\text{H}_2\text{O})_2\text{CO}^+$ are detected. The corresponding kinetic data shown in Figure 4 will be discussed below. Finally, Ag_3^+ prefers the exclusive adsorption of two water molecules at room temperature (see Figure 1i; obtained at slightly different partial pressure conditions with respect to Figure 1f).

4. Discussion

The interactions of free mass-selected gold, silver, and binary silver–gold clusters with CO have been studied in great detail by numerous groups experimentally as well as theoretically (please see references in [9,10,16]). Our results for the trimer cluster carbonyls presented here are in excellent agreement with the concurrent theoretical calculations reported earlier [10]. The tendency of small gold clusters to strongly bind carbon monoxide is also generally recognized. In particular cationic gold clusters with sizes up to seven atoms exhibit CO binding energies clearly larger than 1 eV [12]. The CO bonding strength then quickly decreases and remains approximately constant around 0.7 eV for clusters with 20–65 atoms [12]. Yet, this value is still considerably above the heat of adsorption of CO on an extended gold surface ($\text{Au}(110)$) which amounts to 0.3 eV [37].

Interestingly, with 0.55 eV the CO adsorption is notably stronger on a silver surface ($\text{Ag}(111)$ [38]) than on the gold surface. However, this relation is reversed for the case of the CO binding to atomic cations ($\text{Au}^+\text{--CO}$ $E_b = 2.08$ eV [39]; $\text{Ag}^+\text{--CO}$ $E_b = 0.93$ eV [40]). A similar stronger interaction of CO with gold compared to silver is also observed for the small trimer clusters as can be seen from Figure 2. This trend generally applies to small Ag_nAu_m^+ in that the CO binding energy to these clusters decreases with increasing silver content [8–10].

With respect to the structures of the trimer carbonyls theoretical simulations show that each CO molecule binds via the carbon atom in a μ_1 -atop position to one metal atom of the small triangular clusters [10,41]. The low temperature CO saturation coverage is three for Ag_3^+ and Ag_2Au^+ , but four for Au_3^+ [10].

Much less is known about the bonding of water to small gas phase noble metal clusters. Small gold cluster anions were reported to adsorb one water molecule at room temperature and several H_2O molecules at lower temperatures [42]. The complex $\text{Au}_3(\text{H}_2\text{O})_3^+$ was detected in our ion trap experiment previously, but no binding energies have been determined so far [36]. Earlier experimental and theoretical studies on the $\text{Au}(\text{H}_2\text{O})^+$ complex revealed binding energies of H_2O to the positively charged gold atom in the range from 1.1 to 1.8 eV [27,39,43,44]. The experimental binding energy of H_2O to Au_3^+ determined in this contribution ($E_b = 0.98$ eV for the 'loose' TS, see Table 2) is slightly below these values.

The theoretical simulations performed in the present study result in a binding energy of 1.20 eV with the water molecule being bound via the more electronegative oxygen atom to a gold atom, in agreement with previous DFT calculations. In the $\text{Au}_3^+\text{--H}_2\text{O}$ complex, the bound water molecule was found not to change its geometry and the O–H bond length of 0.97 Å is not significantly altered. For larger gold clusters the H_2O bonding strength has been found to further decrease: Theoretical simulations of the neutral cluster Au_8 yielded water adsorption energies between 0.3 and 0.6 eV [45]. The calculated $\text{Au}_{10}^+\text{--H}_2\text{O}$ binding energy is 0.54 eV [46].

No data are available so far concerning the interaction of water with silver clusters or binary silver–gold clusters. Our DFT calculations show that also in these cases the water molecule is bound to

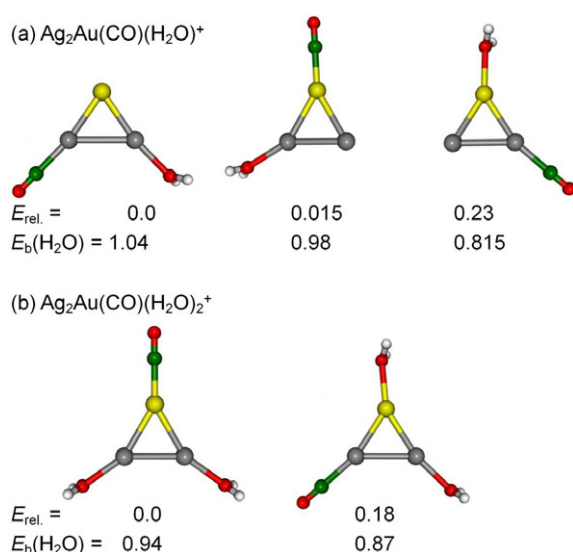


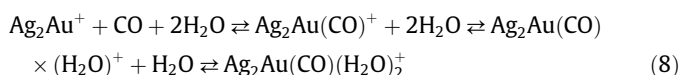
Figure 5. Calculated lowest energy structures of the experimentally detected coadsorption complexes (a) $\text{Ag}_2\text{Au}(\text{CO})(\text{H}_2\text{O})^+$ and (b) $\text{Ag}_2\text{Au}(\text{CO})(\text{H}_2\text{O})_2^+$. Displayed below the structures are also the relative total energies $E_{\text{rel.}}$ of the complexes and the binding energies of H_2O $E_{\text{b}}(\text{H}_2\text{O})$ (the average binding energies of both H_2O in the case of $\text{Ag}_2\text{Au}(\text{CO})(\text{H}_2\text{O})_2^+$, respectively). All energies are given in units of eV.

the clusters via the oxygen atom and that the H_2O geometry remains nearly unperturbed upon adsorption. Interestingly, the most stable $\text{Ag}_2\text{Au}(\text{H}_2\text{O})^+$ complex has the water molecule bound to a silver atom (as listed in Table 2), while the H_2O interaction is weakened by 0.18 eV, if it is attached to the gold atom of the triangular Ag_2Au^+ cluster.

The composition dependent H_2O binding energy trend observed in the present experiments is similar to that of CO (Figure 2) in that E_{b} decreases with increasing silver content. However, this trend is much less pronounced for the H_2O binding energies (which are actually quite similar for Ag_3^+ and Ag_2Au^+) and thus, a cross over occurs as apparent from Figure 2. This results in comparable H_2O and CO binding strength to the binary cluster Ag_2Au^+ , but a stronger interaction of CO with Au_3^+ , in contrast to Ag_3^+ , which binds H_2O more strongly. The experimental observations in this respect are well supported by the results of our first principles calculations (Table 2 and Figure 2).

This cross over in E_{b} with the change in composition is clearly reflected in the results of the coadsorption experiment as shown in Figure 1g–i. The gold trimer reacts to $\text{Au}_3(\text{CO})_3^+$, while the silver trimer yields $\text{Ag}_3(\text{H}_2\text{O})_{1,2}^+$. Apparently, the most strongly bound ligand prevents the coadsorption of the more weakly bound molecule. Similar competitive adsorption effects have been observed also for other ligands on gold clusters previously [47]. In the case of Ag_2Au^+ , however, coadsorption of H_2O and CO is indeed detected leading to the complexes $\text{Ag}_2\text{Au}(\text{H}_2\text{O})\text{CO}^+$ and $\text{Ag}_2\text{Au}(\text{H}_2\text{O})_2\text{CO}^+$ (Figure 1h). The calculated structures of these complexes are depicted in Figure 5. Interestingly, the structures of $\text{Ag}_2\text{Au}(\text{H}_2\text{O})\text{CO}^+$ with the water molecule attached to Ag and the CO bound to Au is almost degenerate with the structure, in which both molecules H_2O and CO are attached to silver atoms. In contrast, the binding of H_2O to Au is clearly energetically unfavorable (Figure 5a).

The mechanism of this coadsorption reaction can be deduced from the kinetic measurements shown in Figure 4. The first reaction step is the adsorption of one CO molecule followed by sequential H_2O adsorption:



Although the CO binding energy to Ag_2Au^+ is comparable to the H_2O binding energy (cf. Figure 2), the order of magnitude larger CO partial pressure apparently determines the pre-adsorption of CO.

A further interesting aspect is the stoichiometry of the largest observed coadsorption complex $\text{Ag}_2\text{Au}(\text{CO})(\text{H}_2\text{O})_2^+$ (Figure 1h). Because the number of H_2O (CO) molecules corresponds to the number of silver (gold) atoms it might be speculated based on the experiment that these ligands are each attached to one of the respective metal atoms. This structural conjecture is nicely confirmed by the results of our quantum chemical calculations, which are depicted in Figure 5b. The lowest energy structure of $\text{Ag}_2\text{Au}(\text{CO})(\text{H}_2\text{O})_2^+$ is indeed clearly the one with the H_2O molecules adsorbed onto the silver atoms.

Yet, nothing can be deduced from the experimental data about the potential activation and/or reaction of the adsorbed molecules because no fragment loss has been detected in the mass spectra. However, considering the above observation that each molecule is attached to one separate metal atom and that the mechanisms Eqs. (7) and (8) reveal equilibrium reaction kinetics, i.e. the adsorbed CO and H_2O may be lost again, a further interaction of CO with H_2O might be rather unlikely without an additional Langmuir–Hinshelwood type reaction step. In this case the future strategy will be to extend the experiments to larger cluster sizes and in particular to higher temperatures which might help to overcome potential activation barriers involved in the perspective water gas shift chemistry on the binary silver–gold clusters.

5. Conclusion

In this contribution the adsorption and coadsorption behavior of H_2O and CO on pure and binary silver–gold cluster cations Ag_nAu_m^+ ($n + m = 3$) was investigated employing gas phase reaction kinetics measurements in an ion trap and first principles DFT simulations. In particular, for the adsorption of water on the investigated clusters binding energies could be determined for the first time via statistical reaction rate analysis. These results are in favorable agreement with the respective calculated data. The comparison to the CO binding energies revealed a cross over in the binding energy values with H_2O being more strongly bound compared to CO on Ag_3^+ , while the reverse was observed for Au_3^+ . For Ag_2Au^+ the bonding strength of H_2O and CO are almost identical and only in this case coadsorption is observed resulting in the complexes $\text{Ag}_2\text{Au}(\text{CO})(\text{H}_2\text{O})^+$ and $\text{Ag}_2\text{Au}(\text{CO})(\text{H}_2\text{O})_2^+$.

Acknowledgment

The authors would like to thank Dr. Sandra Lang for helpful discussions. Financial support by the Deutsche Forschungsgemeinschaft is gratefully acknowledged.

References

- [1] R. Ferrando, J. Jellinek, R.L. Johnston, Chem. Rev. 108 (2008) 845.
- [2] J.K. Edwards, E. Ntainjua, A.F. Carley, A.A. Herzog, C.J. Kiely, G.J. Hutchings, Angew. Chem. Int. Ed. 48 (2009) 8512.
- [3] D.I. Enache et al., Science 311 (2006) 362.
- [4] M. Chen, D. Kumar, C.-W. Yi, D.W. Goodman, Science 310 (2005) 291.
- [5] S.M. Lang, T.M. Bernhardt, Phys. Chem. Chem. Phys. 14 (2012) 9255.
- [6] K. Koszinowski, D. Schröder, H. Schwarz, Chem. Phys. Chem. 4 (2003) 1233.
- [7] M. Neumaier, F. Weigend, O. Hampe, M.M. Kappes, J. Chem. Phys. 125 (2006) 104308.
- [8] M. Neumaier, F. Weigend, O. Hampe, M.M. Kappes, Faraday Discuss. 138 (2008) 393.
- [9] D.M. Popolan, M. Nößler, R. Mitrić, T.M. Bernhardt, V. Bonačić-Koutecký, Phys. Chem. Chem. Phys. 12 (2010) 7865.
- [10] D.M. Popolan, M. Nößler, R. Mitrić, T.M. Bernhardt, V. Bonačić-Koutecký, J. Phys. Chem. A 115 (2011) 951.
- [11] M. Okumura, Y. Kitagawa, M. Haruta, K. Yamaguchi, Appl. Catal. A 291 (2005) 37.

- [12] M. Neumaier, F. Weigend, O. Hampe, M.M. Kappes, J. Chem. Phys. 122 (2005) 104702.
- [13] A. Prestianni, A. Martorana, F. Labat, I. Ciofini, C. Adamo, J. Phys. Chem. B 110 (2006) 12240.
- [14] H. Hess, S. Kwiet, L. Socaciu, S. Wolf, T. Leisner, L. Wöste, Appl. Phys. B 71 (2000) 337.
- [15] T.M. Bernhardt, Int. J. Mass Spectrom. 243 (2005) 1.
- [16] T.M. Bernhardt, J. Hagen, S.M. Lang, D.M. Popolan, L. Socaciu-Siebert, L. Wöste, J. Phys. Chem. A 113 (2009) 2724.
- [17] R. Keller, F. Nöhmeier, P. Spädtke, M.H. Schönenberg, Vacuum 34 (1984) 31.
- [18] K.A. Holbrook, M.J. Pilling, S.H. Robertson, Unimolecular Reactions, John Wiley & Sons Ltd., Chichester, 1996.
- [19] J.I. Steinfeld, J.S. Francisco, W.L. Hase, Chemical Kinetics and Dynamics, Prentice Hall, Upper Saddle River, New Jersey, 1999.
- [20] O. Reynolds, Phil. Trans. Roy. Soc. 10 (1879) 727.
- [21] J.C. Maxwell, Phil. Trans. Roy. Soc. 170 (1879) 231.
- [22] G. Lorient, T. Moran, Rev. Sci. Instrum. 46 (1975) 140.
- [23] R.C. Bell, K.A. Zemski, D.R. Justes, A.W. Castleman Jr., J. Chem. Phys. 114 (2001) 798.
- [24] P.M. Langevin, Ann. Chem. Phys. 5 (1905) 245.
- [25] R. Marcus, J. Chem. Phys. 43 (1965) 2658.
- [26] L. Drahos, K. Vekey, J. Mass Spectrom. 36 (2001) 237.
- [27] D. Feller, E.D. Glendening, W.A. de Jong, J. Chem. Phys. 110 (1999) 1475.
- [28] Y. Shi, V.A. Spasov, K.M. Ervin, J. Chem. Phys. 111 (1999) 938.
- [29] A.D. Becke, J. Chem. Phys. 38 (1988) 3098.
- [30] A.D. Becke, J. Chem. Phys. 98 (1993) 5648.
- [31] C. Lee, W. Yang, R.G. Parr, Phys. Rev. B 37 (1988) 785.
- [32] B. Miehlich, A. Savin, H. Stoll, H. Preuss, Chem. Phys. Lett. 157 (1989) 200.
- [33] K. Eichkorn, F. Weigend, O. Treutler, R. Aldrichs, Theor. Chim. Acta 97 (1997) 119.
- [34] D. Andrea, U. Haeussermann, M. Dolg, H. Stoll, H. Preuss, Theor. Chim. Acta 77 (1990) 123.
- [35] A. Schäfer, H. Huber, R. Ahlrichs, J. Chem. Phys. 100 (1994) 5829.
- [36] S.M. Lang, T.M. Bernhardt, Int. J. Mass Spectrom. 286 (2009) 39.
- [37] J.M. Gottfried, K.J. Schmidt, S.L.M. Schroeder, K. Christmann, Surf. Sci. 536 (2003) 206.
- [38] G. McElhiney, H. Papp, J. Pritchard, Surf. Sci. 54 (1976) 617.
- [39] D. Schröder, H. Schwarz, J. Hrusak, P. Pyykkö, Inorg. Chem. 37 (1998) 624.
- [40] F. Meyer, Y.-M. Chen, P.B. Armentrout, J. Am. Chem. Soc. 117 (1995) 4071.
- [41] A. Fielicke, G. von Helden, G. Meijer, D.B. Pedersen, B. Simard, D.M. Rayner, J. Am. Chem. Soc. 127 (2005) 8416.
- [42] W.T. Wallace, R.B. Wyrwas, A.J. Leavitt, R.L. Whetten, Phys. Chem. Chem. Phys. 7 (2005) 930.
- [43] L. Poisson, P. Pradel, F. Lepetit, F. Réau, J.-M. Mestdagh, J.-P. Visticot, Eur. J. Phys. D 14 (2001) 89.
- [44] L. Poisson, F. Lepetit, J.-M. Mestdagh, J.-P. Visticot, J. Phys. Chem. A 106 (2002) 5455.
- [45] A. Bongiorno, U. Landman, Phys. Rev. Lett. 95 (2005) 106102.
- [46] M. Okumura, M. Haruta, Y. Kitagawa, K. Yamaguchi, Gold Bull. 40 (2007) 40.
- [47] S.M. Lang, T.M. Bernhardt, Eur. J. Phys. D 52 (2009) 139.

2 Water activation by small free ruthenium oxide clusters



Cite this: *Phys. Chem. Chem. Phys.*,
2014, **16**, 26578

Water activation by small free ruthenium oxide clusters†‡

Sandra M. Lang,^a Thorsten M. Bernhardt,^{*a} Marjan Krstić^b and
Vlasta Bonačić-Koutecký^{*bc}

The reactions of ruthenium clusters, Ru_x^+ ($x = 2-5$), and ruthenium oxide clusters, $Ru_xO_y^+$ ($x = 2-5$, $y = 1-2$), with water molecules have been investigated by gas phase ion trap mass spectrometry and first principle density functional calculations. The joint experimental and theoretical study reveals that the reactions of the ruthenium oxide clusters with water are considerably more efficient. This is assigned theoretically to the stronger binding of the water molecules to $Ru_xO_y^+$ and, more importantly, to water activation leading to an efficient hydrogen transfer reaction from the water molecules to the oxygen atoms of the ruthenium oxide clusters. The theoretically predicted hydrogen shift reaction has been confirmed experimentally through $^{16}O/^{18}O$ isotope exchange experiments. Calculated energy profiles for the reactions of selected oxide clusters with water illustrate that the oxygen isotope exchange relies on the facile transfer of hydrogen atoms via [1,3] shift reactions between the oxygen atoms of the complexes due to the relatively low barriers involved. These findings might open perspectives for the future realization of water oxidation driven by ruthenium oxide clusters.

Received 30th May 2014,
Accepted 7th August 2014

DOI: 10.1039/c4cp02366h

www.rsc.org/pccp

1. Introduction

The so-called “blue dimer”, the ruthenium oxide complex $[(bpy)_2(H_2O)Ru(\mu-O)Ru(H_2O)(bpy)_2]^{4+}$ ($bpy = 2,2'$ -bipyridine) comprises a Ru–O–Ru center which effectively oxidizes water to O_2 . Its discovery in the early 1980s by Meyer and coworkers¹ has stimulated a great interest in the Ru based homogenous water oxidation catalysis. Apart from numerous μ -oxo ruthenium dimer derivatives also non-oxo bridge di-ruthenium complexes with robust and rigid bridging ligands as well as various mono-ruthenium complexes have been synthesized and shown to be active molecular water oxidation catalysts.^{2–7} Most interestingly, a highly active complex has recently been reported which contains a larger ruthenium oxide core, namely an adamantane Ru_4O_6 unit.^{8,9} However, despite the numerous investigations in this field, mechanistic aspects of the water oxidation reaction remain still largely elusive and the reaction rates of the synthesized complexes

are several orders of magnitude slower than that of the oxygen evolving complex of the natural photosystem II.³

One of the key features of the di-ruthenium complexes has been found to be the bridging ligand⁶ and in particular the role of μ -oxo bridges in the water oxidation reaction is discussed controversially.¹⁰ Furthermore, the importance of the size of the Ru center is not clear since Ru complexes comprising more than two Ru atoms have been hardly addressed so far. Additionally, all the synthesized Ru-based molecular catalysts have been observed to only be active in the presence of a strong oxidant, in particular $Ce(IV)$, which sets the ruthenium atoms in the oxidation state required for water oxidation.^{3,7}

In this context the fundamental investigation of ligand free ruthenium and ruthenium oxide clusters interacting with water molecules might provide conceptual insights on a molecular level into the water activation capabilities of ruthenium containing complexes and open routes for the future design of molecular water oxidation catalysts.

The reaction of water with transition metal oxide clusters has been an area of intense research since several years and a great number of systems have been studied so far (see, *e.g.*, ref. 11–15 and references therein). However, free ruthenium and ruthenium oxide clusters interacting with water have not been investigated yet, neither experimentally nor theoretically.

In this contribution we present our joint experimental and theoretical study of the reactions of free ruthenium and in particular ruthenium oxide clusters with water, whereby the latter are found to be considerably more reactive with strong cluster size and composition dependencies. The theoretical

^a University of Ulm, Institute of Surface Chemistry and Catalysis,
Albert-Einstein-Allee 47, 89069 Ulm, Germany.
E-mail: thorsten.bernhardt@uni-ulm.de

^b Interdisciplinary Center for Advanced Sciences and Technology (ICAST),
University of Split, Meštrovićevo šetalište 45, 21000 Split, Croatia

^c Chemistry Department, Humboldt University of Berlin, Brook-Taylor-Straße 2,
12489 Berlin, Germany. E-mail: vbk@chemie.hu-berlin.de

† This article is part of the Themed Issue “Size Selected Clusters and Particles: From Physical Chemistry to Catalysis”.

‡ Electronic supplementary information (ESI) available: Fig. S1 to S5 display detailed oxygen binding energies for the presented clusters, higher energy isomers, as well as structures and energy profiles of the hydrogen shift reactions. See DOI: 10.1039/c4cp02366h

simulations predict a facile hydrogen shift from the adsorbed water molecules to the oxygen atom in the Ru_xO_y^+ clusters, which is confirmed by $^{16}\text{O}/^{18}\text{O}$ -isotope exchange experiments. On the basis of this apparent capability of the ruthenium oxide clusters to activate water molecules, their potential for water oxidation (H_2O_2 or O_2 formation) is considered.

2. Methods

2.1 Experimental

The reactions between the mass-selected cluster ions and water were investigated in a gas phase low energy ion beam setup consisting of a radio frequency (rf) octopole ion trap inserted into a tandem quadrupole mass spectrometer. This experimental layout has been described in detail elsewhere^{16,17} and will only be outlined briefly here. The free ruthenium and ruthenium oxide clusters were prepared by sputtering of Ru metal targets with high energy Xe ion beams generated by a cold reflex discharge ion source (CORDIS¹⁸). The produced clusters were mass selected in a first quadrupole mass filter and subsequently guided into the home-built rf ion trap, which was pre-filled with 1 Pa of helium buffer gas and about 0.001 Pa partial pressure of water. During the experiments the ion trap was held at room temperature. After a chosen reaction time, *i.e.* storage time inside the ion trap, all ions, products and intermediates, were extracted and mass analyzed. Deuterated water (D_2O) as well as isotopically labeled water (H_2^{18}O) were employed in the presented experiments.

2.2 Theoretical

The structural properties of the ruthenium and ruthenium oxide cluster cations and their interaction with water were studied using DFT with the hybrid B3LYP functional.^{19–21} For the Ru atoms the Stuttgart group relativistic effective core potentials (ECPs)²² were employed together with the triple- ζ -valence-plus-polarization basis set²³ which was also used for the O and H atoms.²⁴ Our previous studies of the reactivity of transition metal clusters and oxide clusters have shown that such a combination of hybrid density functionals with triple- ζ quality basis sets allows the accurate prediction of the reaction energetics and mechanisms.^{25–27} Moreover, the comparison of results obtained with B3LYP and PBE0 functionals yield equivalent structural and energetic properties of ruthenium oxides. Both functionals were tested and compared with other ones for ruthenium complexes.²⁸ All structures presented were fully optimized using gradient minimization techniques and stationary points were characterized as minima or transition states by calculating the vibrational frequencies. Since we investigated cationic systems the structures were optimized in the doublet and quadruplet ground states. We present results for the structures obtained in the doublet states because they are energetically favorable. For the lowest energy isomers the energy difference between doublet and quadruplet ground states ranges from 0.3 to 0.1 eV for complexes with increasing size. In addition, we have determined energy profiles based on the energies for the minima and transition states obtained from DFT calculations to deduce the reaction mechanisms.

3. Results and discussion

In the following we first present the generation of the free ruthenium and ruthenium oxide clusters and assign their structural properties through first principles calculations. Second, the interaction of the mass selected cluster ions with water is investigated in the ion trap and by theoretical simulations. Subsequently, the water activation *via* hydrogen shift to the Ru_xO_y^+ oxygen atoms predicted theoretically is demonstrated experimentally employing oxygen isotope exchange experiments. Finally, these findings are discussed in the context of the potential water oxidation capabilities of the ruthenium oxides.

3.1 Ruthenium and ruthenium oxide clusters

Fig. 1a displays a typical mass spectrum generated by sputtering ruthenium targets with high energy Xe ion beams. It reveals in addition to bare ruthenium clusters Ru_x^+ ($x = 2–6$) also the production of oxide clusters Ru_xO_y^+ ($x = 2–6$, $y = 1–3$). This is due to the unavoidable oxidation of the ruthenium targets in air prior to their installation in the sputter source.

The broad natural isotope distribution of ruthenium atoms (96 to 104 amu) causes an overlap of the Ru_x^+ and Ru_xO_y^+ signals with increasing cluster size x . However, an unambiguous mass selection can be achieved by eliminating the lightest and heaviest isotope combinations for a selected Ru_x^+ or Ru_xO_y^+ cluster as shown in Fig. 1b–d for the example of $\text{Ru}_4\text{O}_{0–2}^+$.

The calculated lowest energy structures of the ruthenium and ruthenium oxide clusters are displayed in Fig. 2 showing that the structures of the Ru-cluster subunits remain almost unchanged within the ruthenium oxide complexes. Notably, the structures with the oxygen atom in terminal or bridging positions,

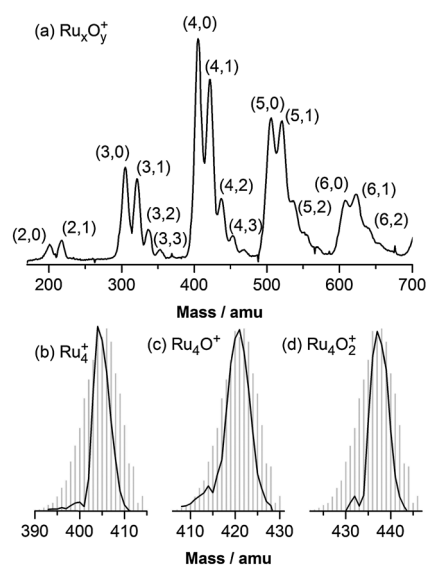


Fig. 1 (a) Cluster ion distribution generated by sputtering air pre-oxidized ruthenium targets with high energy Xe ion beams (the peak labelling (x,y) corresponds to the stoichiometry Ru_xO_y^+). Also shown are the cluster ion signals (black lines) of (b) Ru_4^+ , (c) Ru_4O^+ , and (d) Ru_4O_2^+ after mass selection with the first quadrupole mass spectrometer together with the mass distributions calculated on the basis of the natural occurrence of Ru isotopes (gray bars).

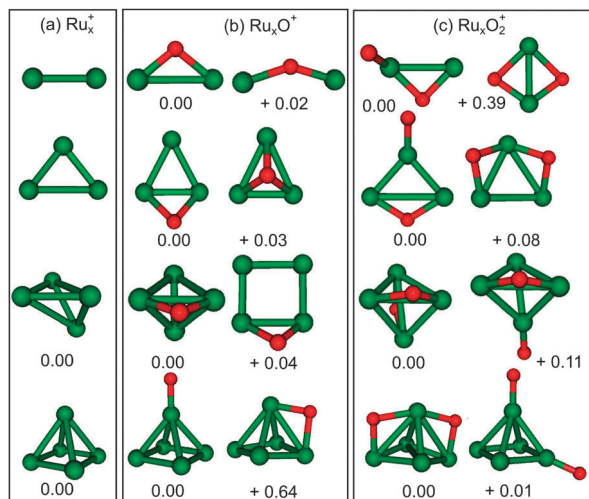


Fig. 2 Optimized structures in the doublet ground states of (a) Ru_x^+ ($x = 2-5$) as well as two lowest isomeric structures of (b) Ru_xO^+ ($x = 2-5$) and (c) Ru_xO_2^+ ($x = 2-5$). The energy differences between the isomers are given in eV. Notice that the isomeric structure of Ru_3O^+ with a terminal oxygen atom is by 0.28 eV higher in energy with respect to the lowest energy structure. The isomer for Ru_5O_2^+ with one terminal and one bridging O atom is by 0.11 eV higher in energy with respect to the lowest energy isomer. Ru and O atoms are indicated by green and red spheres, respectively.

respectively, are very close in energy for the dioxides Ru_3O_2^+ , Ru_4O_2^+ , and Ru_5O_2^+ . In contrast, for the Ru_5O^+ monoxide the energy for the isomer with a terminal oxygen atom is by 0.64 eV lower than for the isomer with the oxygen in a bridging position (*cf.* Fig. 2).

In the lowest energy structures the binding energy of the first oxygen atom ranges between 7.5 and 8.3 eV while the second oxygen atom in Ru_xO_2^+ is bound by 7.1 to 7.7 eV (see Fig. S1 of the ESI†). These oxygen binding energies are considerably higher than the measured binding energy of the Ru–O molecule (5.48 eV, *ref.* 29) and also high compared to the oxygen bond strength of most of the other cationic transition metal atoms³⁰ as well as of, *e.g.*, the cationic palladium clusters Pd_xO^+ ($x = 2-8$)³¹ or Ni_2O^+ .³²

3.2 Size and composition dependent water activation

Fig. 3 displays the average number of adsorbed water (D_2O) molecules measured in the ion trap experiment after the reaction of the bare ruthenium clusters, Ru_x^+ ($x = 2-5$), and their corresponding mono-oxides, Ru_xO^+ ($x = 3-5$), and di-oxides, Ru_xO_2^+ ($x = 3-5$). Strikingly, the water adsorption is considerably enhanced for the ruthenium oxides compared to the bare Ru_x^+ for all investigated cluster sizes. This is also reflected in the generally higher calculated binding energies of water molecules to ruthenium oxide clusters compared to the bare ruthenium clusters as apparent from Table 1.

Furthermore, the ruthenium oxide clusters offer the possibility for water activation *via* a hydrogen shift reaction from adsorbed water molecules to the oxygen atoms of the clusters. Such hydrogen shift reactions have been observed in other metal oxide cluster systems before.³³ Indeed, our theoretical findings reveal that the lowest energy structures in most of the investigated complexes

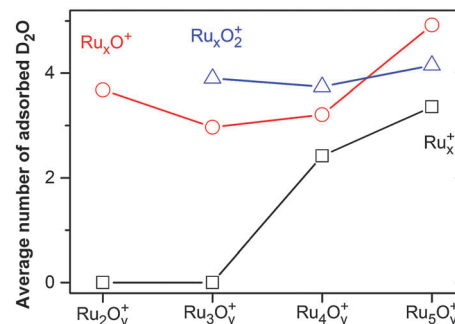


Fig. 3 Cluster size and composition dependent average number of adsorbed D_2O molecules on Ru_x^+ ($x = 2-5$), Ru_xO^+ ($x = 2-5$), and Ru_xO_2^+ ($x = 3-5$). The average number of adsorbed water molecules has been deduced from the reaction product mass spectra depicted in Fig. 4 below.

Table 1 Theoretically obtained cluster size and composition dependent binding energies of z adsorbed water molecules in $\text{Ru}_x\text{O}_y(\text{H}_2\text{O})_z^+$. The energy values are given in eV. The water molecules are always bound to Ru atoms and most of the structures are displayed in Fig. 4 and 6, and the ESI

Cluster	Complex $\text{Ru}_x\text{O}_y(\text{H}_2\text{O})_z^+$			
	$z = 2$	$z = 3$	$z = 4$	$z = 5$
Ru_2^+	2.44		4.18	
Ru_2O^+	2.97		4.55	
Ru_3^+		2.97	3.40	
Ru_3O^+		3.17	3.81	
Ru_3O_2^+			4.60	
Ru_4^+	2.01	2.79	3.54	
Ru_4O^+		3.27	3.65	
Ru_4O_2^+		3.36	3.59	
Ru_5^+		3.14	3.63	4.31
Ru_5O^+			4.03	4.75
Ru_5O_2^+			3.92	

contain hydrogenated oxides. The structures assigned to the most abundant products observed experimentally together with the corresponding mass spectra are shown in Fig. 4. In the following we will discuss the nature of the water complex structures for each cluster size.

While the bare Ru_2^+ does not react with water at all under the given experimental condition (Fig. 4a), the major reaction product of Ru_2O^+ contains four water molecules (Fig. 4b). The lowest energy structure assigned to this product results from a hydrogen shift from a water molecule to the bridging oxygen atom and is 0.26 eV lower in energy than the structure with two water molecules bound to each Ru atom. The calculated barrier for the hydrogen shift reaction amounts to 1.29 eV which is however surmountable under the given experimental conditions³⁴ (see also Fig. S2 of the ESI†).

Ru_3^+ does not react with water, similar to Ru_2^+ (Fig. 4c). In the case of Ru_3O^+ the energy barrier for the hydrogen shift reaction amounts to only 0.88 eV. However, the structures before, $\text{Ru}_3\text{O}(\text{H}_2\text{O})_3^+$, and after hydrogen shift, $\text{Ru}_3(\text{OH})_2(\text{H}_2\text{O})_2^+$, are very similar in energy with the first one (containing only intact water molecules) being more stable by 0.02 eV (see Fig. 4d and Fig. S3 of the ESI†). For Ru_3O_2^+ the reaction barrier for the first

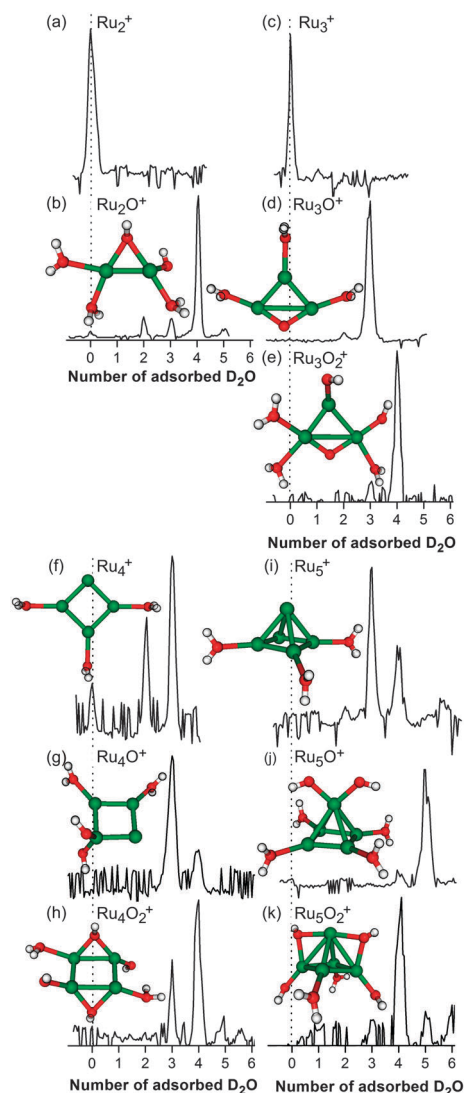


Fig. 4 Product mass spectra measured after the reaction of Ru_x^+ ($x = 2-5$), Ru_xO^+ ($x = 2-5$), and Ru_xO_2^+ ($x = 3-5$) with D_2O for 1.0 s at room temperature. Also shown are the most stable calculated structures with doublet ground states corresponding to the dominating mass signals. Ru, O, and H atoms are indicated by green, red, and white spheres, respectively.

hydrogen shift is further reduced (0.30 eV, *cf.* Fig. 6a). The second hydrogen shift involves a barrier of 1.20 eV (Fig. S4, ESI†). $\text{Ru}_3\text{O}(\text{OH})_2(\text{H}_2\text{O})_3^+$ (Fig. 4e) as well as $\text{Ru}_3(\text{OH})_4(\text{H}_2\text{O})_2^+$ (Fig. S4, ESI†) are both more stable (by 0.27 and 0.16 eV, respectively) than the complex with intact water only, $\text{Ru}_3\text{O}_2(\text{H}_2\text{O})_4^+$ (see also Fig. 6a below and Fig. S4, ESI†).

The most abundant reaction product in the case of the bare tetramer cluster is $\text{Ru}_4(\text{H}_2\text{O})_3^+$ (see structure in Fig. 4f). Note that the geometry of the Ru_4 subunit in this complex is a square and thus different from the tetrahedral structure of bare Ru_4^+ (Fig. 2). The same square geometry of the Ru_4 core occurs in the oxide clusters in which the hydrogen shifted structures are always considerably lower in energy than the structures with intact water molecules only (Fig. 4g and h: $\text{Ru}_4(\text{OH})_2(\text{H}_2\text{O})_2^+$ is 0.66 eV more stable than $\text{Ru}_4\text{O}(\text{H}_2\text{O})_3^+$ (*cf.* Fig. S5, ESI†);

$\text{Ru}_4(\text{OH})_4(\text{H}_2\text{O})_2^+$ is 0.55 eV more stable than $\text{Ru}_4\text{O}(\text{OH})_2(\text{H}_2\text{O})_3^+$ which is 0.38 eV more stable than the structure with non-dissociated water only $\text{Ru}_4\text{O}_2(\text{H}_2\text{O})_4^+$ (*cf.* Fig. 6b below)). For the mono-oxide the barrier for the hydrogen shift amounts to 1.36 eV (see also Fig. S5, ESI†) and for the dioxide the sequential barriers are 0.62 and 0.58 eV, respectively (see also Fig. 6b below). As in the case of $\text{Ru}_3\text{O}_{1-2}^+$, this reaction is more favorable for the dioxide than for the mono-oxide.

In marked contrast to the geometry change of Ru_4^+ in the reaction with water, the three-dimensional square pyramidal structure of Ru_5^+ is retained upon water adsorption (Fig. 4i) and is also present in the oxide cluster complexes. For the mono-oxide complex the hydrogen shifted and non-shifted structures are very close in energy again with the first being more stable by 0.02 eV (Fig. 4j). In contrast, for the dioxide complex the hydrogenated structures are clearly lower in energy than the structures with non-dissociated water only (0.99 eV, see also Fig. 4k).

From these findings it is clear that each cluster shows individual reactive properties toward water. Nevertheless, it appears that the water activation *via* hydrogen shift reaction is most favorable for the dioxide cluster ions.

3.3 $^{16}\text{O}/^{18}\text{O}$ isotope exchange investigations

To confirm the theoretically predicted water activation *via* hydrogen shift to the oxygen atoms of $\text{Ru}_x\text{O}_{1-2}^+$, isotope exchange experiments were performed. The prototype clusters $\text{Ru}_3^{16}\text{O}_2^+$ and $\text{Ru}_4^{16}\text{O}_2^+$ were reacted with isotopically labeled water H_2^{18}O because in these cases unambiguous distinction between the ^{16}O and ^{18}O containing oxide clusters was possible. Moreover, for these clusters the most stable structures predicted theoretically clearly contain hydrogenated oxygen atoms.

Fig. 5 displays mass spectra obtained after the reaction of $\text{Ru}_3^{16}\text{O}_2^+$ and $\text{Ru}_4^{16}\text{O}_2^+$ with D_2^{16}O (grey mass peaks) as well as H_2^{18}O (black lines). Since both D_2^{16}O and H_2^{18}O have the same

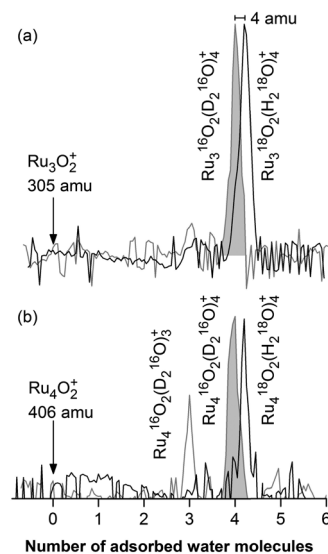


Fig. 5 Product ion mass distributions obtained after the reactions of (a) $\text{Ru}_3^{16}\text{O}_2^+$ and (b) $\text{Ru}_4^{16}\text{O}_2^+$ with D_2^{16}O (grey mass peaks) and H_2^{18}O (black lines), respectively.

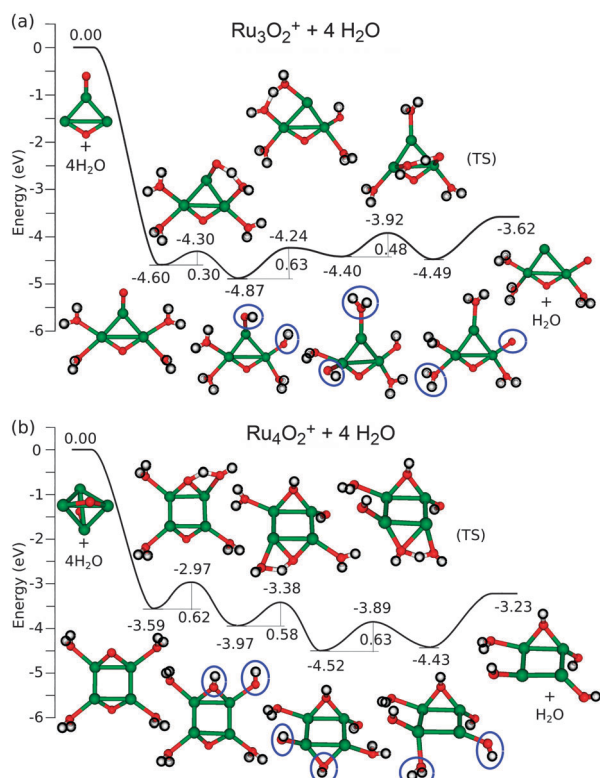


Fig. 6 Calculated energy profiles for doublet ground states of possible reaction pathways for the [1,3] shift hydrogen transfer reaction of (a) $\text{Ru}_3\text{O}_2^+ + 4\text{H}_2\text{O}$ and (b) $\text{Ru}_4\text{O}_2^+ + 4\text{H}_2\text{O}$ including the lowest energy isomers depicted in Fig. 4e and h, respectively. Ru, O, and H atoms are indicated by green, red, and white spheres, respectively. The blue circles indicate the OH-groups resulting from the stepwise hydrogen shifts. The inclusion of the calculated zero-point vibrational energies does not influence substantially the stabilization of the ruthenium oxides by water, as well as the relative energies of the minima and barriers along the reaction pathways.

mass of 20 amu, identical ion mass distributions would be expected after the reaction with each of these two molecules. However, Fig. 5 shows that the mass spectra obtained in the presence of H_2^{18}O are shifted by 4 amu to higher masses. This shift can only be explained by an exchange of the two ^{16}O atoms of $\text{Ru}_{3,4}\text{O}_2^+$ with two ^{18}O atoms of H_2^{18}O , thus, providing unambiguous experimental evidence that water is activated (the H–OH bonds are broken) by the ruthenium oxides $\text{Ru}_{3,4}\text{O}_2^+$.

To complement these findings we present in Fig. 6 calculated energy profiles for the reactions of Ru_3O_2^+ as well as Ru_4O_2^+ with four H_2O each. Each pathway represents a distinct example for one possible exchange reaction mechanism involving the lowest energy structures. The energetics of the first reaction steps after water adsorption in Fig. 6a and b have already been discussed in connection with the structural assignment of the mass spectra in Fig. 4e and h (Section 3.2). From Fig. 6 it is apparent that the oxygen isotope exchange relies on the facile transfer of hydrogen atoms *via* [1,3] shift reactions³³ between the oxygen atoms of the complexes due to the relatively low barriers involved (all reaction barriers are below 0.65 eV). An alternative hydrogen atom transfer reaction pathway containing two [1,2] shifts *via* a metal center was calculated to be substantially more energy demanding.

The next step would now be to investigate, whether these water activating reaction steps might open a feasible route toward water oxidation. For this purpose the formation of an O–O bond and the subsequent elimination of the oxidation products (either H_2O_2 or O_2) are required which involves the breaking of Ru–O bonds. However, the binding strength of oxygen atoms to ruthenium is comparably high. For example, the binding energy of Ru–O has been measured to be 5.48 eV.²⁹ For comparison, a cluster system where water oxidation and H_2O_2 liberation was observed is Mn_2O_2^+ (ref. 35 and 36) and the Mn–O binding energy amounts only to 4.17 eV.²⁹ Despite this strong bonding of oxygen to ruthenium, preliminary theoretical results indicate that the formation and elimination of H_2O_2 on Ru_3O_2^+ and Ru_4O_2^+ with four water molecules might be feasible. This stimulates further theoretical and experimental investigations of the important issue of water oxidation by ruthenium oxide clusters which are currently in progress in our laboratories.

4. Conclusions

Water activation and catalytic oxidation by the “blue dimer” complex and related compounds all containing either bare ruthenium or ruthenium oxide centers represents a very active area of research.^{2–7} In the present contribution we have demonstrated that also free isolated Ru_xO_y^+ clusters are able to activate water in a strongly size and composition dependent fashion. Our DFT calculations and oxygen isotope exchange experiments conclusively establish an [1,3] hydrogen shift from the water molecules to the oxygen atoms of the ruthenium oxide clusters as mechanism for water activation in these complexes. These findings have important implications for the future design of molecular systems which can serve as catalysts for water oxidation.

Acknowledgements

We gratefully acknowledge financial support by the Fonds der Chemischen Industrie (FCI). In particular, S.M.L. is grateful to the European Social Fund (ESF) Baden-Württemberg for a Margarete von Wrangell fellowship.

Notes and references

- 1 S. W. Gersten, G. J. Samuels and T. J. Meyer, Catalytic oxidation of water by an oxo-bridged ruthenium dimer, *J. Am. Chem. Soc.*, 1982, **104**, 4030.
- 2 H. Yamazaki, A. Shouji, M. Kajita and M. Yagi, Electrocatalytic and photocatalytic water oxidation to dioxygen based on metal complexes, *Coord. Chem. Rev.*, 2010, **254**, 2483.
- 3 X. Sala, I. Romero, M. Rodríguez, L. Escriche and A. Llobet, Molecular catalysts that oxidize water to dioxygen, *Angew. Chem., Int. Ed.*, 2009, **48**, 2842.
- 4 M. Yagi and M. Kaneko, Molecular catalysts for water oxidation, *Chem. Rev.*, 2001, **101**, 21.

- 5 K. S. Joya and H. J. M. de Groot, Biomimetic molecular water splitting catalysts for hydrogen generation, *Int. J. Hydrogen Energy*, 2012, **37**, 8787.
- 6 I. Romero, M. Rodríguez, C. Sens, J. Mola, M. R. Kollipara, L. Francás, E. Mas-Marza, L. Escriche and A. Llobet, Ru complexes that can catalytically oxidize water to molecular dioxygen, *Inorg. Chem.*, 2008, **47**, 1824.
- 7 R. Cao, W. Lai and P. Du, Catalytic water oxidation at single metal sites, *Energy Environ. Sci.*, 2012, **5**, 8134.
- 8 Y. V. Geletii, B. Botar, P. Kögerler, D. A. Hillesheim, D. G. Musaev and C. L. Hill, An all-inorganic, stable, and highly active tetraruthenium homogeneous catalyst for water oxidation, *Angew. Chem., Int. Ed.*, 2008, **47**, 3896.
- 9 A. Sartorel, M. Carraro, G. Scorrano, R. De Zorzi, S. Geremia, N. D. McDaniel, S. Bernhard and M. Bonchio, Polyoxometalate embedding of a tetraruthenium(IV)-oxo-core by template-directed metalation of $[\gamma\text{-SiW}_{10}\text{O}_{36}]^{8-}$: A totally inorganic oxygen-evolving catalyst, *J. Am. Chem. Soc.*, 2008, **130**, 5006.
- 10 H. Dau, C. Limberg, T. Reier, M. Risch, S. Roggan and P. Strasser, The mechanism of water oxidation: From electrolysis *via* homogeneous to biological catalysis, *ChemCatChem*, 2010, **2**, 724.
- 11 G. K. Koyanagi, D. K. Bohme, I. Kretzschmar, D. Schröder and H. Schwarz, Gas-phase chemistry of bare V^+ cation with oxygen and water at room temperature: Formation and hydration of vanadium oxide cations, *J. Phys. Chem. A*, 2001, **105**, 4259.
- 12 M. del Carmen Michelini, N. Russo and E. Sicilia, Gas-phase chemistry of actinides ions: New insights into the reaction of UO^+ and UO^{2+} with water, *J. Am. Chem. Soc.*, 2007, **129**, 4229.
- 13 S. Feyel, D. Schröder and H. Schwarz, Gas-phase chemistry of vanadium oxide cluster cations V_mO_n^+ ($m = 1-4$; $n = 1-10$) with water and molecular oxygen, *Eur. J. Inorg. Chem.*, 2008, 4961.
- 14 D. W. Rothgeb, E. Hossain, J. E. Mann and C. C. Jarrold, Disparate product distributions observed in $\text{Mo}_{(3-x)}\text{W}_x\text{O}_y^-$ ($x = 0-3$; $y = 3-9$) reactions with D_2O and CO_2 , *J. Chem. Phys.*, 2010, **132**, 064302.
- 15 J.-B. Ma, Y.-X. Zhao, S.-G. He and X.-L. Ding, Experimental and theoretical study of the reactions between vanadium oxide cluster cations and water, *J. Phys. Chem. A*, 2012, **116**, 2049.
- 16 T. M. Bernhardt, Gas phase reaction kinetics of small gold and silver clusters, *Int. J. Mass Spectrom.*, 2005, **243**, 1.
- 17 T. M. Bernhardt, J. Hagen, S. M. Lang, D. M. Popolan, L. Socaci-Siebert and L. Wöste, Binding energies of O_2 and CO to small gold, silver, and binary silver-gold cluster anions from temperature dependent reaction kinetics measurements, *J. Phys. Chem. A*, 2009, **113**, 2724.
- 18 R. Keller, F. Nöhmeier, P. Spädtke and M. H. Schönenberg, Cordis – an improved high-current ion source for gases, *Vacuum*, 1984, **34**, 31.
- 19 A. D. Becke, Density-functional exchange-energy approximation with correct asymptotic behavior, *Phys. Rev. A: At., Mol., Opt. Phys.*, 1988, **38**, 3098.
- 20 A. D. Becke, Density-functional thermochemistry. III. The role of exact exchange, *J. Chem. Phys.*, 1993, **98**, 5648.
- 21 C. Lee, W. Yang and R. G. Parr, Development of the Colle-Salvetti correlation-energy formula into a functional of the electron density, *Phys. Rev. B: Condens. Matter Mater. Phys.*, 1988, **37**, 785.
- 22 D. Andrae, U. Haeussermann, M. Dolg, H. Stoll and H. Preuss, Energy-adjusted *ab initio* pseudopotentials for the second and third row transition elements, *Theor. Chim. Acta*, 1990, **77**, 123.
- 23 F. Weigend and R. Ahlrichs, Balanced basis set of split valence, triple zeta valence and quadrupole zeta valence quality for H to Rn: Design and assessment of accuracy, *Phys. Chem. Chem. Phys.*, 2005, **7**, 3297.
- 24 A. Schäfer, H. Huber and R. Ahlrichs, Fully optimized contracted gaussian basis sets of triple zeta valence quality for atoms Li to Kr, *J. Chem. Phys.*, 1994, **100**, 5829.
- 25 G. E. Johnson, R. Mitric, V. Bonačić-Koutecký and A. W. Castleman Jr, Clusters as model systems for investigating nanoscale oxidation catalysis, *Chem. Phys. Lett.*, 2009, **475**, 1.
- 26 D. R. Justes, R. Mitrić, N. A. Moore, V. Bonačić-Koutecký and A. W. Castleman Jr, Theoretical and experimental consideration of the reactions between V_xO_y^+ and ethylene, *J. Am. Chem. Soc.*, 2003, **125**, 6289.
- 27 G. E. Johnson, R. Mitric, M. Nössler, E. C. Tyo, V. Bonacic-Koutecký and A. W. Castleman Jr, Influence of charge state on catalytic oxidation reactions at metal oxide clusters containing radical oxygen centers, *J. Am. Chem. Soc.*, 2009, **131**, 5460.
- 28 R. Kang, J. Yao and H. Chen, Are DFT methods accurate in mononuclear ruthenium-catalyzed water oxidation? An *ab initio* assessment, *J. Chem. Theory Comput.*, 2013, **9**, 1872.
- 29 J. B. Pedley and E. M. Marshall, Thermochemical data for gaseous monoxides, *J. Phys. Chem. Ref. Data*, 1983, **12**, 967.
- 30 V. Blagojevic, E. Flaim, M. J. Y. Jarvis, G. K. Koyanagi and D. K. Bohme, Nitric oxide as an electron donor, an atom donor, an atom acceptor, and a ligand in reactions with atomic transition-metal and main-group cations in the gas phase, *J. Phys. Chem. A*, 2005, **109**, 11224.
- 31 S. M. Lang, I. Fleischer, T. M. Bernhardt, R. N. Barnett and U. Landman, Size-dependent self-limiting oxidation of free palladium clusters, *J. Phys. Chem. A*, 2014, **118**, DOI: 10.1021/jp502736p.
- 32 K. Koszinowski, M. Schlangen, D. Schröder and H. Schwarz, Formation, structure, and reactivity of gaseous Ni_2O_2^+ , *Eur. J. Inorg. Chem.*, 2005, 2464.
- 33 M. Brönstrup, D. Schröder and H. Schwarz, Reactions of bare FeO^+ with element hydrides EH_n ($\text{E} = \text{C}, \text{N}, \text{O}, \text{F}, \text{Si}, \text{P}, \text{S}, \text{Cl}$), *Chem. – Eur. J.*, 1999, **5**, 1176.
- 34 S. M. Lang, T. M. Bernhardt, R. N. Barnett and U. Landman, Methane activation and catalytic ethylene formation on free Au_2^+ , *Angew. Chem., Int. Ed.*, 2010, **49**, 980.
- 35 B. Chiavarino, M. E. Crestoni and S. Fornarini, Gas-phase dioxygen activation by binuclear manganese clusters, *Chem. – Eur. J.*, 2002, **8**, 2740.
- 36 S. M. Lang, I. Fleischer, T. M. Bernhardt, R. N. Barnett and U. Landman, Dimensionality dependent water splitting mechanisms on free manganese oxide clusters, *Nano Lett.*, 2013, **13**, 5549.

MARJAN KRSTIĆ

Date of birth: April 27th, 1987

Place of Birth: Split, Croatia

Nationality: Croatian

EMPLOYMENT:

February 2012 – present Teaching assistant at Faculty of Science, Department of Physics, University of Split, Split, Croatia

October 2011 – present Junior Researcher at Interdisciplinary Center for Advanced Science and Technology (ICAST) at University of Split, Split, Croatia

EDUCATION:

December 2011 - present PhD student of the Doctoral school of Biophysics at Faculty of Science at University of Split, Split, Croatia

Thesis: "Modeling and simulation of mechanical systems in engineering practice"

October 2008 – September 2010 Master student in Engineering physics, Mechanical systems at Faculty of Science, University of Split, Split, Croatia

October 2005 – September 2008 Bachelor student in Engineering physics at Faculty of Science, University of Split, Split, Croatia

October 2001 – June 2005 High school, Gymnasium "Don Frane Bulić", Split, Croatia

MARJAN KRSTIĆ

1. I. Russier-Antoine, F. Bertorelle, Ž. Sanader, M. Krstić, C. Comby-Zerbino, Ph. Dugourd, P.-F. Brevet, V. Bonačić-Koutecký, and R. Antoine: Ligand-Core NLO-phores: a combined experimental and theoretical approach of the two-photon absorption and two-photon excited emission properties of small ligated silver nanoclusters, submitted, **2016**
2. A. Zavras, M. Krstić, Ph. Dugourd, V. Bonačić-Koutecký, R. A. J. O'Hair: Selectivity Effects in Bimetallic Catalysis: Role of the Metal Sites in the Decomposition of Formic Acid into H₂ and CO₂ by the Coinage Metal Binuclear Complexes [dppmMM'(H)]⁺, submitted, **2016**
3. M. Krstić, A. Zavras, G. N. Khairallah, Ph. Dugourd, V. Bonačić-Koutecký, R. A. J. O'Hair: "ESI/MS Investigation of Routes to the Formation of Silver Hydride Nanocluster Dications [Ag_nH_{n-2}L_m]²⁺ and Gas-phase Unimolecular Chemistry of [Ag₁₀H₈L₆]²⁺", *Int. J. of M. Spec.* **2016**, doi:10.1016/j.ijms.2016.05.022
4. A. Zavras, G. N. Khairallah, M. Krstić, M. Girod, S. Daly, R. Antoine, Ph. Maitre, R. J. Mulder, S.A. Alexander, V. Bonačić-Koutecký, Ph. Dugourd and R. A. J. O'Hair: "Ligand-induced Substrate Steering and Reshaping of [Ag₂(H)]⁺ Scaffold for Selective CO₂ Extrusion from Formic Acid", *Nature Communication*, 7:11746, **2016**
5. Ž. Sanader, M. Krstić, I. Russier-Antoine, F. Bertorelle, Ph. Dugourd, P.F. Brevet, R., Antoine, V. Bonačić-Koutecký; "Two-photon absorption of ligand-protected Ag₁₅ nanoclusters. Towards a new class of nonlinear optics nanomaterials", *Phys. Chem. Chem. Phys.* , DOI: 10.1039/c6cp00207b, **2016**
6. S. Daly, M. Krstić, A. Giuliani, R. Antoine, L. Nahon, A. Zavras, G. N. Khairallah, V. Bonačić-Koutecký, Ph. Dugourd, R. A. J. O'Hair: "Gas-phase VUV photoionisation and photofragmentation of the silver deuteride nanocluster [Ag₁₀D₈L₆]²⁺ (L= bis(diphenylphosphino)methane). A joint experimental and theoretical study", *Phys. Chem. Chem. Phys.* 17 (39), 25772-25777, **2015**
7. M. Girod, M. Krstić, R. Antoine, L. MacAleese, J. Lemoine, A. Zavras, G. N. Khairallah, V. Bonačić-Koutecký, Ph. Dugourd, and R. A. J. O'Hair: "Formation and characterisation of the silver hydride nanocluster cation [Ag₃H₂((Ph₂P)₂CH₂)]⁺ and its release of hydrogen", *Chemistry-A European Journal* 20 (50), 16626-16633, **2014**
8. S. M. Lang, T. M. Bernhardt, M. Krstić, V. Bonačić-Koutecký: "Water activation by small free ruthenium oxide clusters", *Phys. Chem. Chem. Phys.* 16 (48), 26578-26583 **2014**
9. S. M. Lang, T. M. Bernhardt, M. Krstić, V. Bonačić-Koutecký: "The Origin of the Selectivity and Activity of Ruthenium-Cluster Catalysts for Fuel-Cell Feed-Gas Purification: A Gas-Phase Approach", *Angew. Chem. Int. Ed.* 53 5467-5471, **2014**
10. S. M. Lang, S. U. Förtig, T. M. Bernhardt, M. Krstić, V. Bonačić-Koutecký: "Gas-Phase Synthesis and Structure of Wade-Type Ruthenium Carbonyl and Hydrido Carbonyl Clusters", *J. Phys. Chem. A* 118 (37), 8356-8359, **2014**

11. I. Fleischer, D. M. Popolan, M. Krstić, V. Bonačić-Koutecký, T. M. Bernhardt: "Composition dependent selectivity in the coadsorption of H₂O and CO on pure and binary silver-gold clusters", *Chem. Phys. Lett.* 565, 74, **2013**